1993

Experimental studies of fluid-borne noise generation in a marine pump.

McGee, David Michael.

EXPERIMENTAL STUDIES OF FLUID-BORNE NOISE GENERATION IN A MARINE PUMP

by
David Michael McGee
B.S., United States Naval Academy (1986)

Submitted to the Department of Ocean Engineering and the Department of Mechanical Engineering in Partial Fulfillment of the Requirements for the Degrees of

NAVAL ENGINEER
and
MASTER OF SCIENCE IN MECHANICAL ENGINEERING
at the
MASSACHUSETTS INSTITUTE OF TECHNOLOGY
May, 1993

EXPERIMENTAL STUDIES OF FLUID-BORNE NOISE GENERATION IN A MARINE PUMP

by

David Michael McGee

Submitted to the Department of Ocean Engineering and
the Department of Mechanical Engineering in May 1993
in Partial Fulfillment of the Requirements for the Degrees of
Naval Engineer and Master of Science in Mechanical Engineering

ABSTRACT

Experimental studies were carried out to determine the influence of pump rotational speed, flow rate, and the addition of long-chain polymers on the broadband and tonal noise generated from the fluid flow in a centrifugal water pump.

A theoretical model is presented which relates the tonal noise generation to the static pressure field at the impeller discharge. Using the pump in its original casing, measurements were made of the static pressure distribution at impeller exit under various operating conditions. Attempts were made to correlate the static pressure field at impeller exit with the observed acoustic spectra at pump inlet under these conditions. The results showed fair agreement with the theory at shaft and blade passage frequencies as well as some of the other harmonics. However, the unusually invariant flow conditions at the impeller exit over a wide range of conditions limited the number of conclusions which could be drawn from the experiments.

To further test the theory, an experimental diffuser was designed for the pump which could be used to isolate the effects of interest. The diffuser was designed such that pressure disturbances were far removed from the impeller, which resulted in more uniform conditions at the impeller exit. Results indicate that tonal noise levels at shaft and blade passage frequencies are significantly reduced with the reduction of static pressure non-uniformities. Broadband noise levels did not differ appreciably between the two geometries. A means was provided for imposing various pressure distributions on the impeller exit but initial results were inconclusive.

Thesis Supervisor: Dr. Alan H. Epstein
Title: Professor of Aeronautics and Astronautics

Acknowledgments

This thesis could not have been completed without the support of many people. I would like to offer sincere thanks to the following individuals who made this work possible:

Professor Alan H. Epstein, for his practical insight and guidance throughout the project. His own enthusiasm and encouragement provided the motivation to accomplish more in a limited period of time than I had imagined possible.

Professors K. Uno Ingard and Ian Waitz, for their patience and continuing support throughout the year. They aided immeasurably in the interpretation and understanding of the results and played a large role in making the experience an enjoyable one.

The Staff of the M.I.T. Gas Turbine Laboratory. In particular, Bill Ames, Victor Dubrowski, and Jimmy Letendre for all of their help in setting up the experimental facility and in troubleshooting and correcting the numerous problems which arose. Also, thanks to Holly Rathbun and Robin Courchesne for their assistance with purchasing and logistics.

Finally, this thesis is dedicated to my wife, Linda, whose unselfishness allowed me to pursue this endeavor and whose constant support kept me going through a difficult three years. This work is truly the culmination of a joint effort.

Table of Contents

List of Figures

1. Introduction and Background

The aim of this study is to gain a better understanding of the fluid-borne noise generated in a centrifugal pump. Pump quieting is important whether to create a tolerable environment for people or to enhance stealth for military operations. It is also an important indicator of pump performance. The generation of noise is an indication of inefficient operation in that noise production tends to vary inversely with efficiency. Therefore, a decrease of noise generally has the secondary benefit of increasing efficiency of the machine. Hydraulic noise, in the form of pressure fluctuations, can also interact with the pump casing and impeller, causing them to vibrate and can possibly result in increased erosion and fatigue of pump components.

Noise and vibration in a hydraulic machine may arise from two sources: mechanical unbalance or through the unsteady flow of the working fluid. In the past, mechanical vibrations were the dominant noise source and thus received most of the attention in pump quieting. Consequently, mechanical quieting techniques experienced great advances in recent years. These techniques had little effect, however, in reducing hydraulic noise transmitted through the water; so that in recent years, fluid-generated noise has become a subject of much greater interest.

This is especially true for military stealth purposes because underwater acoustic detection capabilities have also improved dramatically over time, thus lowering acceptable noise levels for shipboard machinery. Ships and submarines can be detected, classified, and localized by radiated machinery noise signatures. The radiated noise can also act as a source to detonate acoustic mines and can interfere with own ship and friendly ship sonars. It is clear, then, that reducing the ship's acoustic signature is critical to maintaining an operational advantage at sea.

Although the design of quiet turbomachinery has received much attention in the engineering community, the mechanisms responsible for fluid noise generation in pumps are not fully understood. This study will investigate the effects of several parameters on

the noise generated by a centrifugal seawater pump. More importantly, it will examine the fundamental physics of fluid noise generation in centrifugal pumps. A thorough understanding of these mechanisms is critical to designing quieter machines.

Lastly, it should be pointed out that this study concentrates mainly on the fluid-borne noise which propagates upstream of the pump. In shipboard applications, this noise is almost always more critical than the downstream noise due to the layout of a typical pumping system. Normally, the pump takes suction directly from the sea through a sea chest on the skin of the ship. Pump noise in the inlet piping travels through a comparatively short length of piping and propagates directly into the surrounding ocean where it can be detected by hostile submarines. The noise in the downstream side of the pump, on the other hand, follows the flow in the discharge piping, which is typically much longer than the inlet piping. The acoustic waves must also pass through one or more heat exchangers before reaching the discharge. Much of the acoustic energy attenuates as it travels down the pipe and is often reflected at flow boundaries, thereby presenting a lesser problem to naval operations.

1.1. General Description of Pump Noise

Pump fluid-borne noise spectra are a superposition of two components: broad band noise and discrete frequency noise. Broadband noise (sometimes referred to as white noise, random noise, or vortex noise) originates from several sources:

1. Turbulent boundary layers and wakes.
2. Vortex shedding from solid surfaces such as impeller blades or diffuser blades.
3. The impingement of initially turbulent flow on solid surfaces.
4. Cavitation (often treated separately).

Hydrodynamic shearing of the working fluid creates swirling eddies with corresponding dynamic sound pressure fluctuations. The amplitude, frequency, and phase of these sources fluctuate within wide limits due to the random nature of turbulence.

Discrete noise frequencies, on the other hand, are easily predicted. They are normally the pure tones and harmonic tones at multiples of the rotational frequency. The shaft tone occurs at the frequency associated with the rotational speed of the pump. The blade passage tone occurs at a frequency equal to the shaft frequency times the number of impeller blades. The amplitudes of these tones are typically several orders of magnitude greater than the broad band noise level and thus dominate the noise spectra. Discrete or rotational noise sources include:

1. Rotating pressure fields attached to the rotor blades which represent a fluctuating pattern for a stationary observer. Noise from this source is sometimes called lift noise and is an unavoidable requirement for the transfer of energy between a working fluid and the moving components of any turbomachine.
2. Interaction between the non-uniform velocity field of the flow and the solid surfaces (stationary or rotating) of the pump. The source of the non-uniform velocity fields can be any solid object in the flow field of the working fluid.[1]
3. Pressure and velocity patterns rotating about the pump annulus at speeds differing from the shaft speed. Rotating stall is the prevalent example of this phenomena of fluid instability.

1.2. Previous Work

A survey of the open literature reveals dozens of studies devoted to fluid-borne turbomachinery noise. The vast majority, however, deal with aerodynamic machinery such as turbines, compressors, fans, and blowers; few deal with the characterization of hydraulic pump noise. Still, there are several studies which are relevant to the present work. These works are summarized briefly in the paragraphs that follow. Note that some research in turbomachinery aeroacoustics did provide useful guidance. Although quantitatively much different from those in hydraulic machines, the noise generating mechanisms of centrifugal compressors, fans, and blowers are qualitatively similar.

The fluid noise in pumps was studied in detail by Simpson, et al.[2-4], in a series of papers published between 1966 and 1970. The authors presented a theoretical model using potential flow analysis of fluctuating flow through a series of blade cascades. The model predicted the pump noise level in the discharge ducting and attempted to estimate the effects of pump load, net positive suction head (NPSH), cutwater position, and pump speed on the noise generated. The theoretical model was then compared to a series of experimental studies on six different volute and diffuser pumps and showed satisfactory agreement. The studies showed that the noise level varied directly as the square of the pump speed. They also showed that the noise level passed through a minimum close to the duty point as pump load was changed.

In 1977, Deeprose and Bolton[5] conducted experiments with nine different pumps, taking acoustic measurements on both the inlet and outlet sides. They concluded that the overall sound pressure level was minimized at the best efficiency point of the pump as compared to other flow rates. They also attempted to reduce the tonal noise in pumps by

1) increasing the volute-impeller clearance distance and 2) using asymmetric impellers. Neither method resulted in reduced tonal noise levels. Their conclusion was that tonal noise reduction was best realized by reducing impeller speed and better hydrodynamic design of the impeller inlet.

Using a pump impeller with air as a working fluid, Yuasa and Hinata[6] conducted experiments on a volute-type centrifugal pump in an anechoic chamber. They investigated the fluctuating flow behind the impeller in an attempt to explain the noise generating mechanisms. The pressure fluctuations were produced by the interaction between fluctuating flow behind the impeller and the cutwater, and the authors showed that these pressure fluctuations were closely related to the tonal noise at blade passage frequency. They also measured dynamic and static pressure fluctuations along a vaneless diffuser and attempted to determine the sources of each. Dynamic pressure fluctuations were attributed to the circulation of blades and to the viscous blade wakes; static pressure fluctuations were predominantly caused by the circulation of the blades.

Lastly, they investigated the effect of varying the operating point of the pump. The amplitudes of the static pressure fluctuations at blade passage frequency and its harmonics decreased with decreasing flow rate in reverse tendency of the time mean value of static pressure. The amplitudes of the dynamic pressure fluctuations, on the other hand, increased with decreasing flow rate. The total pressure fluctuations were unaffected by flow rate.

Most recently, Choi, Bent, et al.[7,8], conducted experiments using a centrifugal pump impeller in air in an attempt to determine the mechanisms responsible for noise generation. Choi, et al.[7], conducted experiments with the pump discharging into open atmosphere. The authors showed that a mild rotating stall pattern which developed at the impeller exit was responsible for the predominant harmonic tones of the radiated noise. They explained the stall pattern as a result of the highly diffusive impeller channel inducing a thick turbulent boundary layer or separated flow near the exit. The noise was generated as a result of the interaction of this strong flow instability interacting with the trailing edge of the impeller blades.

Bent, et al.[8], using the same impeller as Choi, added various parallel-walled, vaneless radial diffusers at the impeller exit. They also postulated that a rotating stall-like instability creates disturbances with which the impeller blades interact. Sharp peaks in the noise spectra are produced if the disturbance corresponds to azimuthal modes that are integer multiples of the number of impeller blades. For these modes, each impeller blade responds to the flow disturbance at the same time, thus enhancing the noise level at these frequencies. A second mechanism of noise generation is the interaction of the

impeller blades with the turbulent flow field convecting from the impeller discharge. This mechanism produces much broader peaks due to the broad range of turbulence scales and smaller regions of coherence.

1.3. Factors Affecting Fluid Noise

It is clear from the above discussion that the generation of fluid noise in a centrifugal pump is a complex phenomenon influenced by many factors. This research will attempt to aid in a more fundamental understanding of noise generation by isolating some of these factors and observing their influence on the inlet sound spectrum. Moreover, it is postulated that the tonal responses may be largely attributed to a single variable: the impeller exit static pressure profile. The relationship between impeller exit static pressure distribution and noise generation has never been explicitly studied to the knowledge of the author. It is evident, however, that there have been many studies, including several of the aforementioned works, which have implicitly touched upon this relationship. Investigations into the effects of speed, volute geometry, and operating point all have bearing on this issue.

The central hypothesis of the present study is that the tonal noise generated in a centrifugal pump is closely related to the non-uniformity of the static pressure field at impeller exit. To understand the motivation for such a hypothesis, it is necessary to recognize the relationship between pump geometry and operational parameters and the pressure distribution imposed upon the pump impeller. These issues are addressed in many turbomachinery analyses[6,9-16] and are discussed briefly below.

1.3.1. Fluid Flow in a Centrifugal Pump Volute

Volute-type pumps are the second most common type of single stage pumps built in the United States. They consist of two principal parts: the impeller and the volute. The impeller imparts a rotary velocity to the liquid, increasing its kinetic energy. The purpose of the volute is to diffuse the high velocity of the working fluid discharged by the impeller into static pressure rise. A typical centrifugal pump volute is shown in Figure 1.1. The hydraulic characteristics of the volute are determined solely by its geometry: the volute area distribution, the volute angle, and the volute width. The design of these elements is based upon both practical and theoretical considerations. The main points are summarized briefly below.

Referring to Figure 1.1, it is clear that the total pump capacity must pass through the volute throat; only part of the total flow passes through any other section. Thus the flow area should increase linearly from the volute tongue to the throat. The average velocity in the volute is estimated from Bernoulli's equation with an experimental factor to account for losses:

$$V_v = K_v\sqrt{2gH}$$

where H is the pump head in feet, g is the acceleration due to gravity, and K_V is an experimentally derived design factor and varies with specific speed.

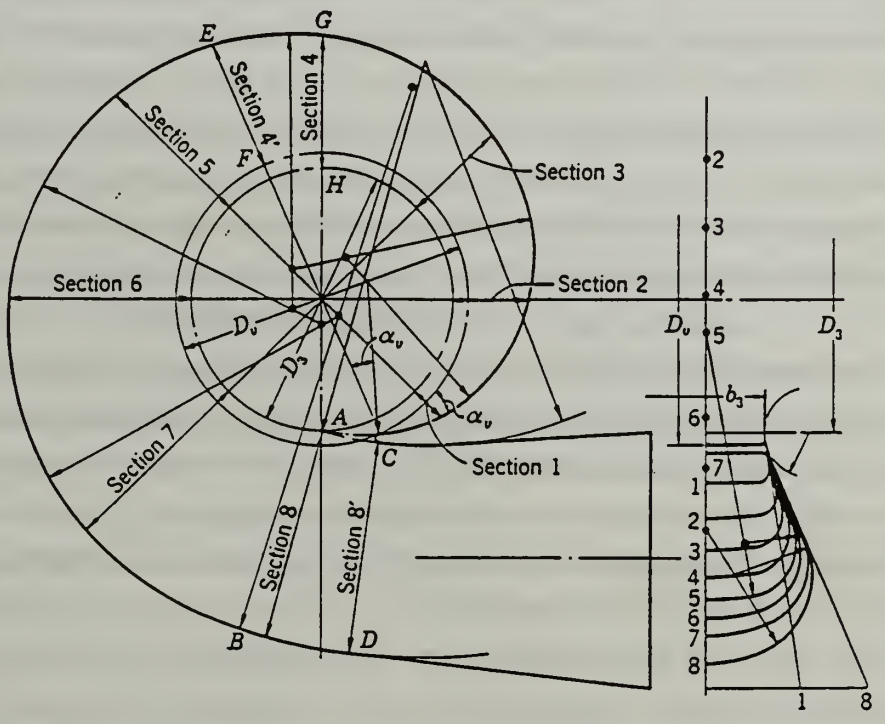

Figure 1.1. Typical Centrifugal Pump Volute (from Stepanoff[9])

However, the velocity distribution across any volute section is not uniform. As with any internal flow, wall friction and the resultant boundary layer distribution have some effect on the flow pattern. The tangential flow has a high velocity core driven by the impeller and decreases toward the volute walls. There is also a radially outward component of velocity which results in a secondary swirling pattern in the flow. The superposition of these two flow components causes a spiral motion along the volute from tongue to exit.

The volute width is normally chosen to minimize losses due to the above flow pattern. Losses will be lessened if the high velocity flow from the impeller discharges into a rotating flow rather than against the stationary volute walls. Another consideration is that the casing should normally be designed to accommodate impellers of different diameters and widths. The volute angle is chosen to match the angle of flow at the impeller discharge in the absolute reference frame to avoid separation loss.

1.3.2 Pump Operating Point

At design conditions, the average velocity across all sections of a well-designed volute will be approximately uniform. This results in a pressure which also remains the same in all volute sections around the impeller. Empirical observations have shown that for a volute pump operating at its best efficiency point, the static pressure at impeller exit is typically on the order of 75% of the pump's head. This value is uniform around the impeller periphery with the exception of the area just prior to the tongue where there may be some deviation of a few percent of the total head. As the operating point moves away from the design point, the variation of pressure around the periphery increases. For example, a typical pump operating at 50% of its design capacity might have a range of pressures about its impeller of approximately 40% of the total head.[9]

An explanation of this effect is offered by Van Den Braembussche and Hände[10]. At higher than optimal mass flows, the fluid enters the volute with larger radial velocity. This results in a large cross-sectional swirl. The tangential velocity is too small to transport the fluid through the volute and so increases in magnitude from the tongue to exit. This results in a pressure decrease along the volute circumference and a discontinuous rise at the volute tongue.

At low flow rates, the opposite occurs. The tangential velocity decreases away from the volute, resulting in a pressure rise around the periphery from tongue to exit with a similar discontinuity in the region of the tongue.

In addition to the spatial variations discussed above, there are also periodic fluctuations of velocity and pressure behind the impeller. In their work described earlier, Yuasa and Hinata took detailed measurements of these fluctuations at blade passing frequency and its harmonics. Their results showed that the amplitude of the pressure fluctuations was also affected by position along the volute. Amplitudes were greater near the cutwater than at other locations due to the close proximity of the impeller in this region.

1.4. Project Goals

The goal of this study is to investigate and understand the fundamental fluid mechanisms responsible for noise generation in a centrifugal pump. The approach taken in this investigation is summarized by the following objectives:

1. Using the existing acoustic pump facility at the M.I.T. Gas Turbine Laboratory, conduct experiments to determine the influence of the following parameters on the inlet noise spectra:
    a. Variation of the pump's rotational speed,
    b. Variation of pump capacity, or flow rate, at constant speed,
    c. Drag-reducing polymers.

Correlate the data from the above experiments and give possible explanations for the phenomena observed.

2. Develop a theoretical model to predict the influence of the impeller exit static pressure distribution on the pump inlet noise spectrum.
3. Design and construct an experimental facility by which the static pressure distributions at impeller exit can be varied in a controlled manner in order to measure their influence on the inlet acoustic spectra.
4. Conduct experiments utilizing this facility to experimentally determine the validity of the model and to correlate the spatial distribution of the impeller exit static pressure field (created by obstructions in the exit flow) with the harmonic tones in the inlet noise spectra.
5. Suggest possible quieting strategies for pump designs based on the observations gained from the above experiments and calculations.

1.5. Thesis Organization

The remainder of this thesis is divided into six chapters. In Chapter 2, the experimental approach is described, including a detailed description of the acoustic pump facilities used to conduct the parametric studies. In Chapter 3, a theoretical model of the centrifugal pump as a tonal noise generating mechanism is presented. In Chapter 4, the parametric studies with the production pump geometry are described in detail. The results are presented and analyses provided to attempt to explain these results. Chapter 5 outlines the experimental approach used to test the model presented in the previous chapter. The experimental goals are outlined and the design of the modifications to the

experimental facility are described. Chapter 6 contains the results of the second set of experiments and an analysis of the modified diffuser. Finally, Chapter 7 discusses conclusions which can be drawn from this study and recommendations for future study.

2. Experimental Approach: The M.I.T. Gas Turbine Laboratory Pump Acoustics Facility

2.1. Description of Pump

The pump used for this study was an auxiliary seawater pump used on a since-retired U.S. Navy submarine. The pump was built in 1961 by the Worthington Corporation. It was originally designed for two speed operation, but was delivered with a single-speed motor. The motor is rated at 15 hp and has a rotational speed of 1780 RPM. The power supply was 440V, 60 Hz A/C electricity.

Variable speed operation was achieved through installation of a Mitsubichi Freqrol Z300 variable speed drive in parallel to the direct A.C. line. The drive was operated from a Parameter Unit mounted directly to the drive.

The distinguishing feature of the pump is that it is mechanically quiet. That is, the pump motor and impeller were precisely balanced to limit mechanical vibrations. The impeller and casing were also designed to be hydraulically quiet. However, the design methodology was purely empirical and information concerning the pump's impeller and casing geometries and how they affected noise production was not available. No drawings of either component were provided.

Pump performance in the acoustic pump loop differed from the operating curve provided with the pump. The original pump was designed to give a 40 psi head rise at a flow rate of 400 GPM and at full speed had a maximum efficiency operating point of 350 GPM with a total head rise of 102 feet (44 psid). The actual performance measured in the test loop was much lower, possibly because the original impeller may have been replaced without updating the performance curve supplied with the pump. Figure 2.1 gives the pump's full speed performance over the range of operating points encountered in this study. Note that this performance curve is only valid for the initial test configuration, which will be described in section 2.2.

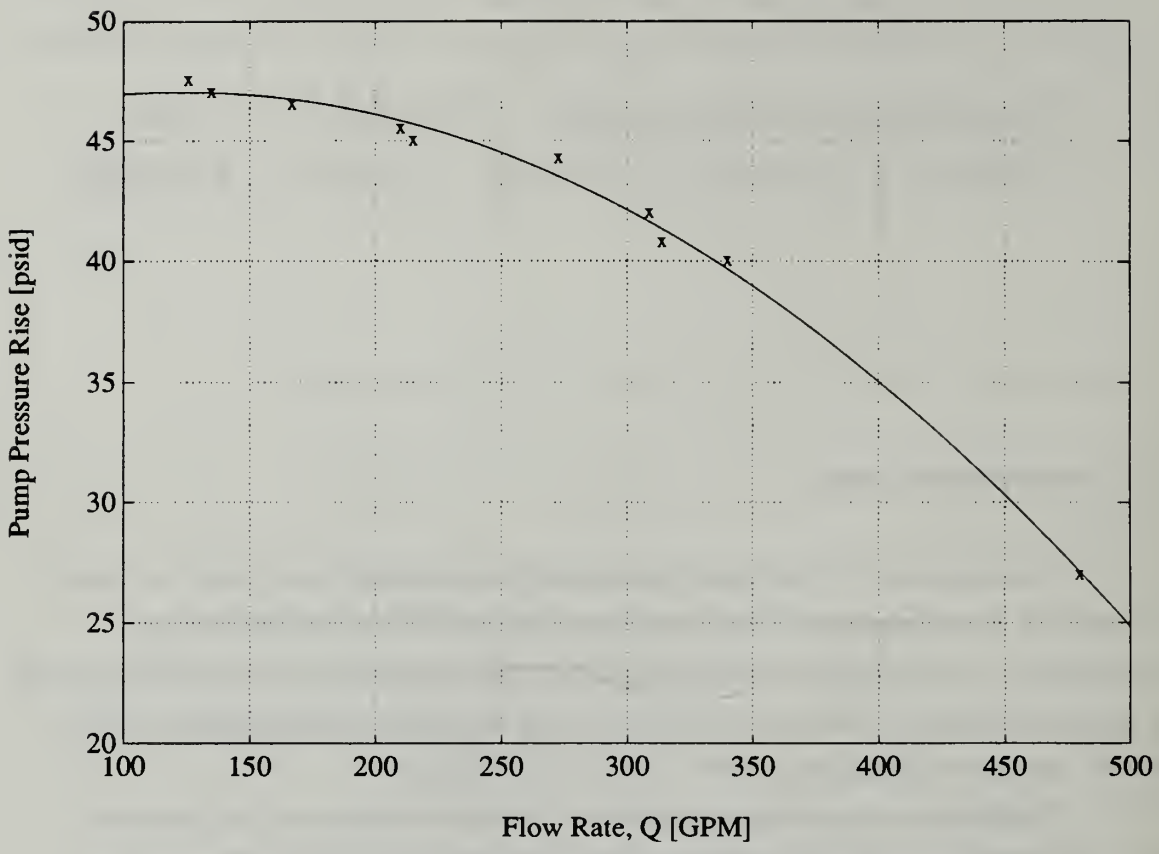

Figure 2.1 Pump Performance Curve, 100% Speed

2.1.1. Pump Impeller

The pump impeller is a fully shrouded design which made it very difficult to ascertain the exact blade geometry. It is known that the impeller has seven backward sloped blades with an exit angle of approximately 22° from tangential as shown in Figure 2.2. Using measurements at the inlet and exit ends, the blades were approximated by a logarithmic spiral shape, although the validity of this assumption is impossible to verify. The impeller diameter is 9.75 inches and the flow passage height is 0.84 inches at exit.

The impeller exit velocity diagram is shown in Figure 2.3. The figure depicts the velocity diagram for 100% speed at a flow rate of 340 GPM. It shows that the pump was designed for high swirl flow. For flow rates between 125 and 480 GPM, the exit flow angle in the absolute frame is between 82.9 and 88.5 degrees from the normal at normal operating speed. This range of angles remains fairly constant for varying speeds of operation. The slip factor was based on the following estimate from Shepherd[17].

$$\mu_s = \frac{V_{u2,actual}}{V_{u2,ideal}} \approx 1 - \frac{\pi u_{tip} \sin \beta_2}{V_{u2,ideal} z_b}$$

where z_b = the number of impeller blades.

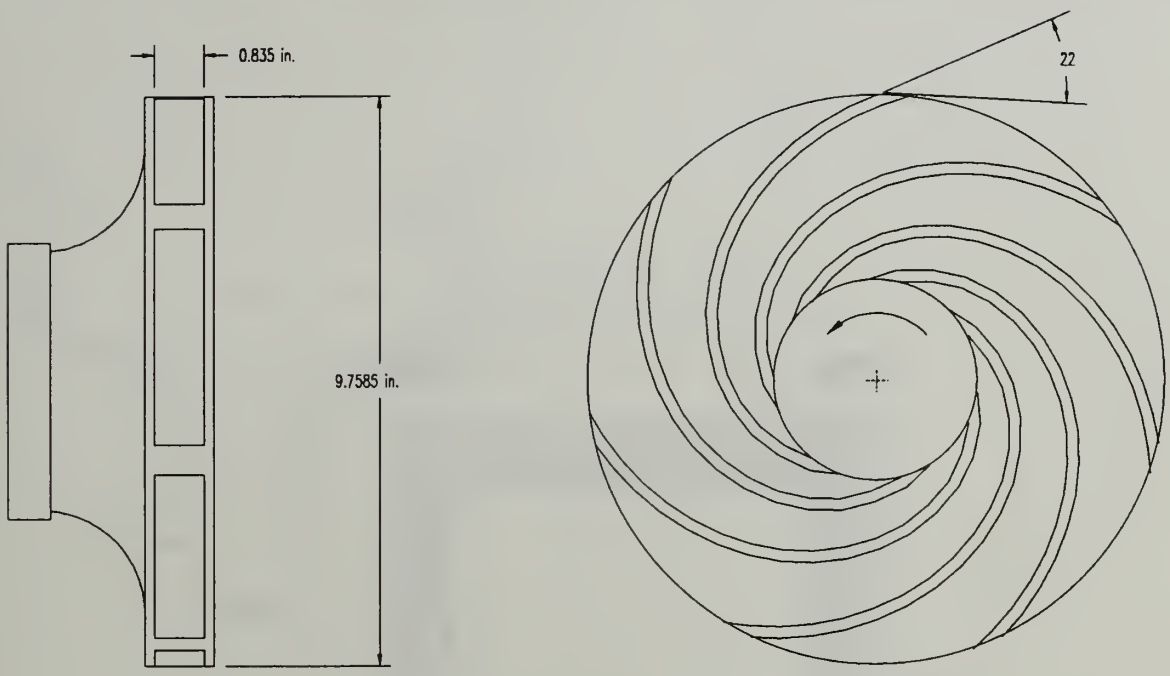

Figure 2.2. Pump Impeller

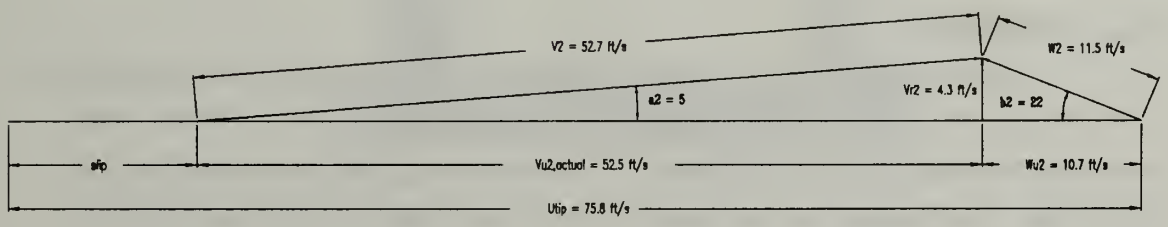

Figure 2.3. Impeller Exit Velocity Diagram

2.1.2. Pump Casing

The pump casing, shown in Figure 2.4, is of the volute type with a single discharge. The casing was cast from a bronze alloy. The volute is different from the description of a standard volute given earlier in section 1.3 in that it is approximately toroidal in shape. That is, the flow area does not increase with angular distance from the tongue. The outermost diameter of the volute remains constant at 14.1 in. for 320° in the

direction of rotation from the tongue. The discharge section occupies the remaining 40°. The depth of the volute at the impeller exit diameter is approximately 3.1 in. and also remains constant around the periphery. The flow exits the volute through a straight conical diffuser, carrying the flow into the four inch exit piping.

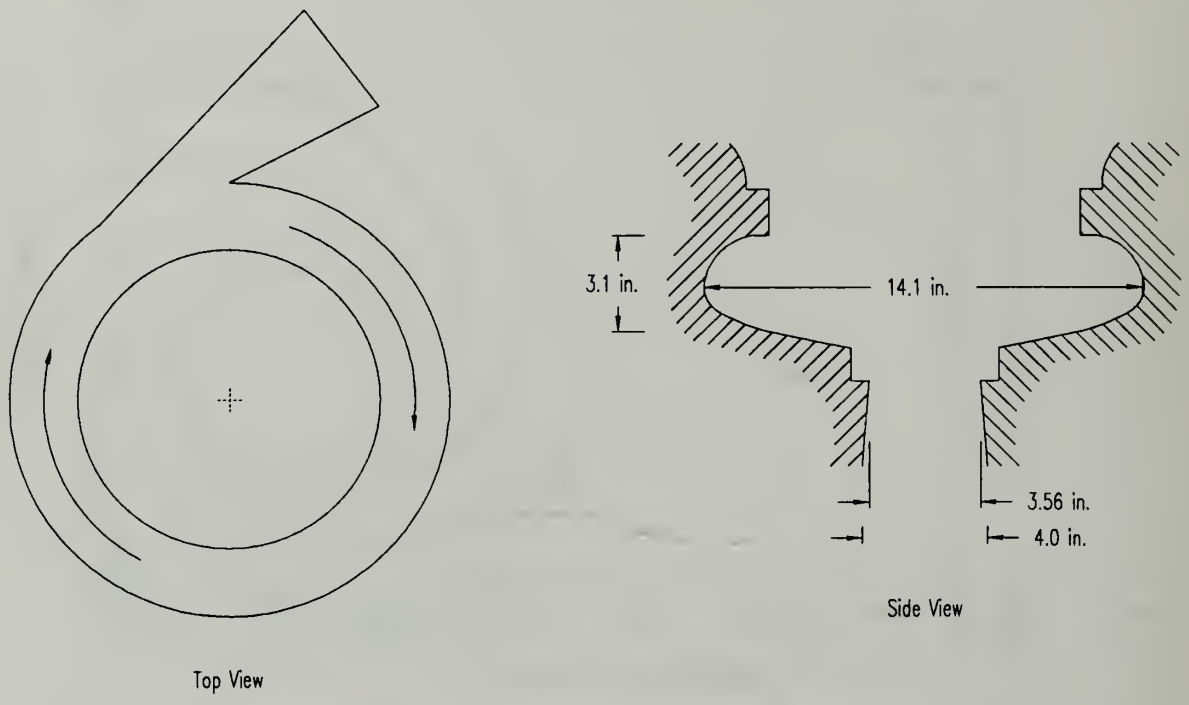

Figure 2.4. Pump Casing

2.1.3. Pump Mount

In order to isolate the pump from outside vibrations, the pump was mounted on four Navy model 7E450 resilient mounts on a frame of 4 in. x 2 in. x 3/16 in. thick mechanical tubing as shown in Figure 2.5. The mounting plate was made from 1 in. thick steel. The framing was mounted on an elevated platform above the cell floor.

2.2. The Acoustic Pump Loop

The M.I.T. Gas Turbine Laboratory acoustic pump loop was originally designed by Barton[18] in 1991 to study the influence of inlet flow distortion on pump noise generation. This same facility, with some modifications, was used to conduct the

parametric studies outlined in Chapter 1. Much of the discussion that follows is taken from Barton and a more detailed description can be found therein.

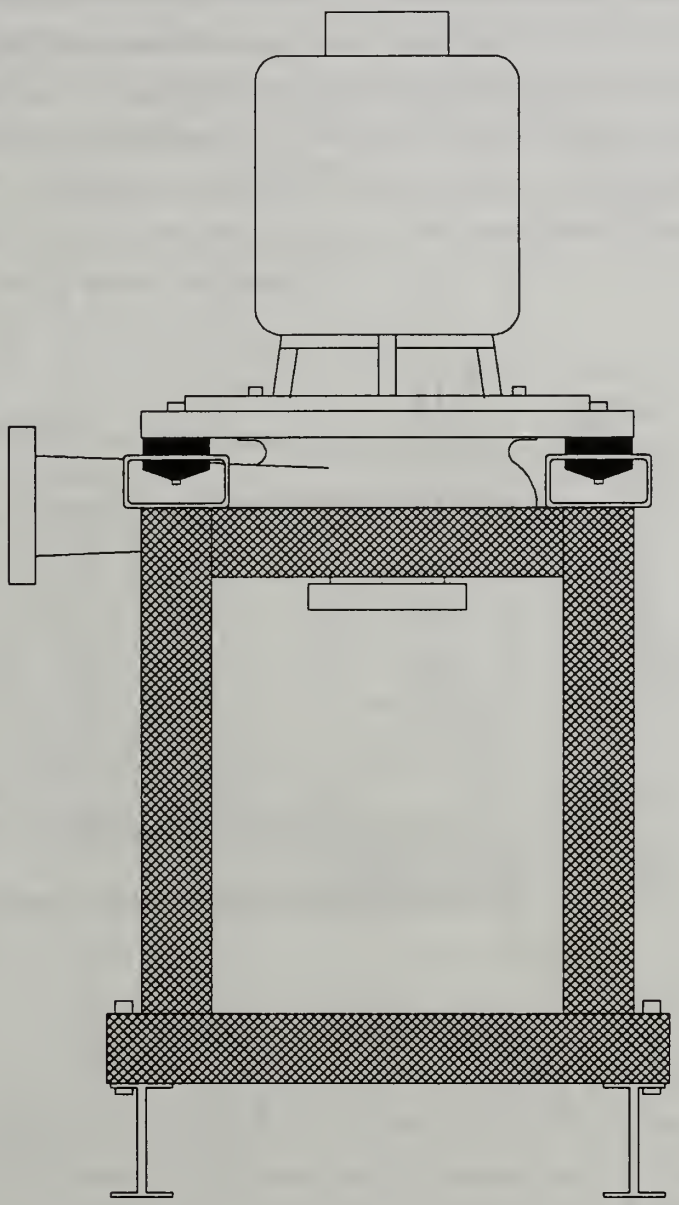

Figure 2.5. Pump Mounting Assembly

The acoustic pump loop used for the parametric studies is shown in Figure 2.6. The system consisted of the pump, a 600 gallon stainless steel tank, 300 feet of 4 inch I.D. rubber hose, 20 feet of 4 inch I.D. stainless steel pipe, a 1-1/2 inch I.D. variable length throttle hose, two 4" to 1-1/2" flow reducers, an 11 gallon expansion tank, a vacuum pump, and measurement and recording devices.

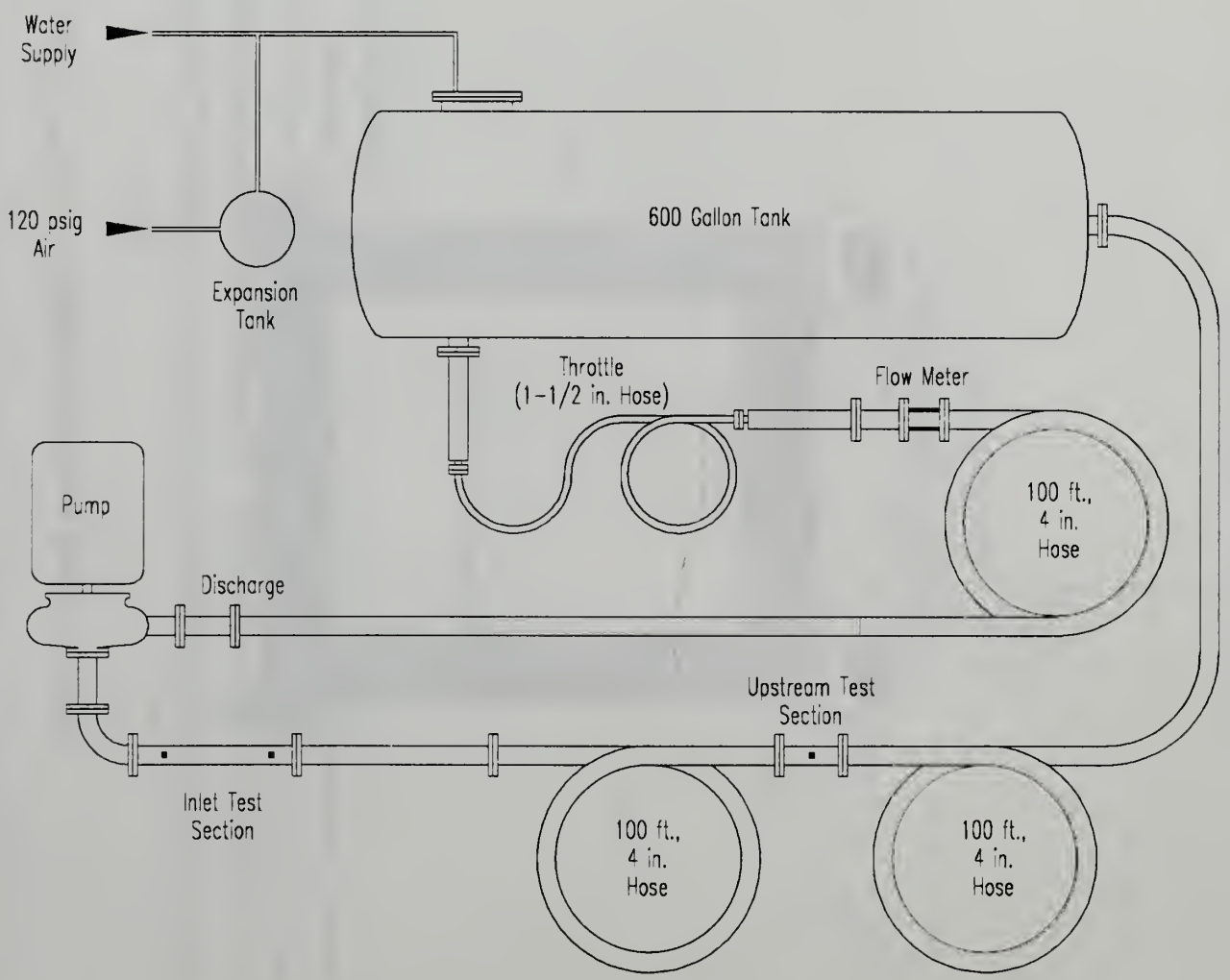

Figure 2.6. Acoustic Pump Loop

The pump took suction from the tank through 200 feet of four inch rubber hose. Both the tank and the pump were located on the same level in the facility. The pump discharged back to the tank through another 100 feet of the rubber hose. Prior to entering the tank, the flow passed through a section of the 1-1/2 in. throttle hose. The transition from one pipe size to the other was accomplished gradually through use of the nozzle/diffuser pair shown in Figure 2.7. The total included angle of convergence/ divergence was 3°. This angle is within well-known experimentally established limits for stable diffusion. This ensured that flow separation would not occur in the transition from the 1-1/2 in. piping to the 4 in. piping.

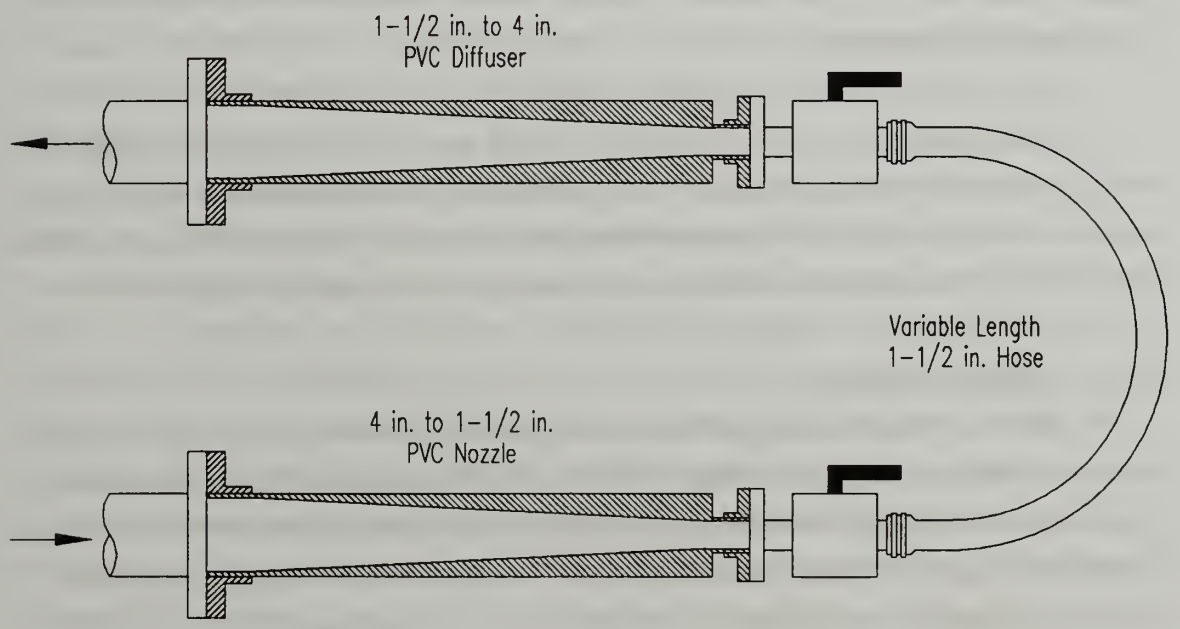

Figure 2.7. Variable Throttle

The loop was filled using filtered water from the city supply line connected to the 600 gallon tank. Prior to testing, the system was de-aerated using a Cenco Hypervac vacuum pump connected to the 600 gallon tank. Isolation valves at the tank suction and return lines were closed to eliminate the compliance of the hose. The vacuum pump suction passed through an intermediate collection tank located between the tank and pump. After a time, the vacuum pump was shut off, the collection tank drained, and the centrifugal pump run at low speed to circulate the water through the system and to trap remaining air in the tank. This process was repeated several times to ensure adequate removal of entrapped air and to allow uniform test conditions between data sets - although the success of this procedure is difficult to determine.

The loop was pressurized to 75 psig using the low pressure air expansion tank. This created a net positive suction head (NPSH) for the pump and eliminated cavitation noise in the pump inlet. More importantly, it eliminated cavitation in the throttle, which proved to be more difficult to control. A pressure regulator was added to the system between the LP air supply line and the expansion tank to maintain a constant mean loop pressure throughout the data collection period.

Acoustic test sections were located just prior to pump inlet and between the two 100 foot hose lengths upstream of the pump as shown in Figure 2.6.

2.3. Acoustic Isolation

In designing the acoustic pump loop, efforts were made to isolate the pump from outside noise and vibration sources. It was also desired to eliminate noise and vibration sources within the loop itself so that acoustic measurements would not be interfered with. Some of the techniques used to accomplish these goals are described briefly below.

2.3.1. Acoustic Attenuation

The main fluid carrying portion of the pump loop was comprised of 4 inch I.D. Goodyear Flexwing rubber petroleum hose. The hose was selected for its attenuating properties. A main goal in the design of the loop was to eliminate sound waves traveling around the loop and forming a standing wave. The rubber hose is significantly more elastic than stainless steel piping and acoustic waves attenuate much more rapidly in ducting with soft walls than in rigid ducting.

In order to validate the acoustic attenuation predictions made by Ingard during the design, the transmission loss through one 100 ft. length of the rubber hose was measured. Measurements were taken at both the inlet and upstream test sections as shown in Figure 2.6. The results showed that noise levels at shaft and blade passage frequencies were attenuated by about 30 dB and 40 dB, respectively. The upstream noise levels were also compared to levels of turbulent boundary layer noise in water in papers published by Clinch[19] and Rogers[20]. The noise levels showed fair agreement with those reported by Clinch and were about 6 dB higher than reported by Rogers.

As a second measure, the coherence between the inlet and upstream signals was also calculated. The results showed low coherence levels (on the order of 0.1) throughout the frequency domain with the exception of a a few of the pump shaft harmonics where the coherence was somewhat higher. Only the blade passage frequency

showed a coherence above 0.9. That the acoustic signal was largely non-coherent across the rubber hose was to be expected. If the hose is effectively attenuating the pump signal, turbulence noise will begin to dominate the spectra far upstream, which results in very low coherence measurements due to the random nature of turbulent fluctuations.

2.3.2. Reflection and Standing Waves

Because the acoustic test sections were of stainless steel, it was necessary to minimize the reflection of noise due to the impedance mismatch at the steel-rubber interface. During studies made by Barton[18], it was found that a standing wave was present in the inlet and outlet of the steel piping. This standing wave becomes resonant at frequencies determined by the characteristics of the steel piping and the reflection coefficients at the boundary. The wave energy attenuates very slowly due to the properties of the steel pipe.

It was attempted to ameliorate the problem by decreasing the reflection coefficient at the steel-rubber interface by providing a gradual transition of acoustic impedance from the steel to rubber. This was accomplished through use of longitudinal steel bars compressing the rubber hose using steel hose clamps as shown in Figure 2.8. The number of bars was decreased in two steps. Details of the procedure and measurements are contained in Barton's thesis. Unfortunately, these efforts were not successful; the magnitude of the reflection coefficient, R, which is defined as the transfer function between incident and reflected waves, remained near 0.5. No further efforts were made to eliminate the problem and analysis of the results must take into account the presence of a standing wave.

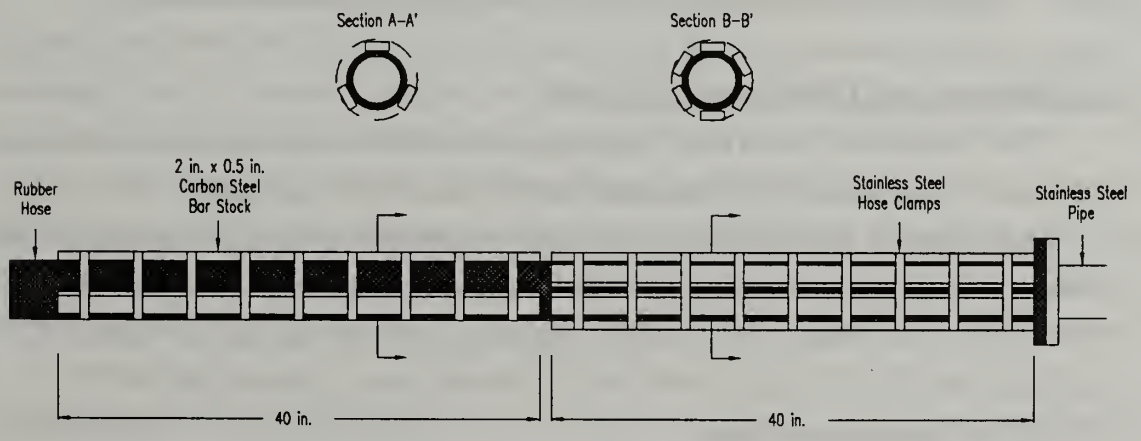

Figure 2.8. Steel-Rubber Boundary Treatment

2.3.3. Vibration

Another potential problem making acoustic measurements in water is the potential for vibro-acoustic interaction between the fluid and its surrounding structure. This is an inherent difficulty in hydroacoustics brought about by the closely matched acoustic impedances of water and its surrounding structure. There are two means by which this interaction could affect the acoustic measurements: 1) the hydrophones could be measuring pipe vibrations directly, or 2) pipe vibrations could be transmitted into the fluid and then detected as acoustic pressure perturbations.

Potential for the first type of interaction was reduced significantly by the selection of hydrophones with extremely low acceleration sensitivity. The sensitivity is given by the manufacturer as varying between 0.0002 and 0.0009 psi/g.

More importantly, Barton measured the vibration spectrum using the accelerometers to be described in section 2.4.3. The results showed that the measured ratio of fluid pressure to structural vibration was up to seven orders of magnitude higher than the specified sensitivity and at no point was lower than 0.1 psi/g. The vibration levels were therefore insignificant when compared to the acoustic pressure levels measured and it was concluded that any vibrations transmitted and measured by the hydrophones did not significantly corrupt the acoustic measurements.

The coupling between structural vibration and acoustic wave propagation was also investigated. An analysis based upon shell theory was presented and showed that the fluid and the pipe wall respond primarily in single and differing spatial modes: a symmetric (n = 0) mode for the fluid and an asymmetric (n = 1) for the pipe. This analysis was verified experimentally and the results showed good agreement with the theory. It was therefore shown that very little coupling exists between the two.

2.3.4 Elimination of Other Acoustic Sources

The throttle used in the loop was designed to minimize flow separation as a noise source in the loop. The throttle was comprised of a nozzle/diffuser pair shown in Figure 2.7. The small angle of divergence in the diffuser minimizes problems of separation and cavitation typically found in valve throttles. In addition, the loop was operated at a static pressure sufficiently large so as to prevent cavitation in the throttle and elsewhere.

2.3.5 Noise Propagation in Pipes

Sound propagation in pipes is highly dependent upon the compressibility of the medium in which it travels. The speed of sound in water is approximately 1465 m/s, much greater than that in air (340 m/s). This illustrates the importance of removing air

from the system, as air has a compressibility on the order of 1×10^5 times that of water. The presence of air can have a major impact on the behavior of the sound field in the system.

Since $\lambda = c_0/f$, the wavelengths of sound waves in water are on the order of meters for frequencies below 1000 Hz. One consequence of this fact is that small discontinuities in pipe geometry will have little effect on sound propagation. In order to affect the sound waves traveling in the piping, geometry changes must be on the order of the wavelength. For the acoustic test loop used for this study there were no such variations.

This also impacts the modes with which sound will travel. Each mode has a frequency below which it cannot propagate. For a 4 inch ID water pipe, the cutoff frequency for higher order modes is on the order of several kilohertz. Any acoustic sources with frequencies below this cutoff frequency will attenuate rapidly. This means that a few pipe diameters from the noise source, the acoustic field will consist entirely of zeroth order, planar waves.

2.4. Instrumentation

2.4.1. Experimental Conditions Monitoring

The test conditions were monitored using various measuring devices located throughout the test loop. All of the test conditions were monitored on a central instrumentation panel located on the lower level of the facility.

The rate of flow through the system was measured by a Sparling FM625 Tigermag magnetic flow meter. The flow meter was located downstream of the pump discharge, just prior to the system throttle. It was calibrated to 400 gallons per minute full scale and is accurate to within ±1% full scale.

Static pressure taps were located at the 600 gallon tank and at pump inlet and discharge sections. This allowed monitoring of the static pressures at each of these locations as well as the pressure rise across the pump and pressure drop across the throttle.

Water temperature was measured using an Omega ICIN-14U-18 thermocouple mounted on a 1/2" tap on the tank.

2.4.2. Pump Impeller Exit Pressure

The original pump casing was drilled and tapped for 1/8 in. N.P.T. fittings as shown in Figure 2.9. The taps were located every 45° except in the region of the volute cutwater where the angular spacing was reduced to 15° in anticipation of increased spatial pressure gradients in this region. The pressure taps were mounted flush with the inner wall of the volute to minimize their impact on the volute flow field.

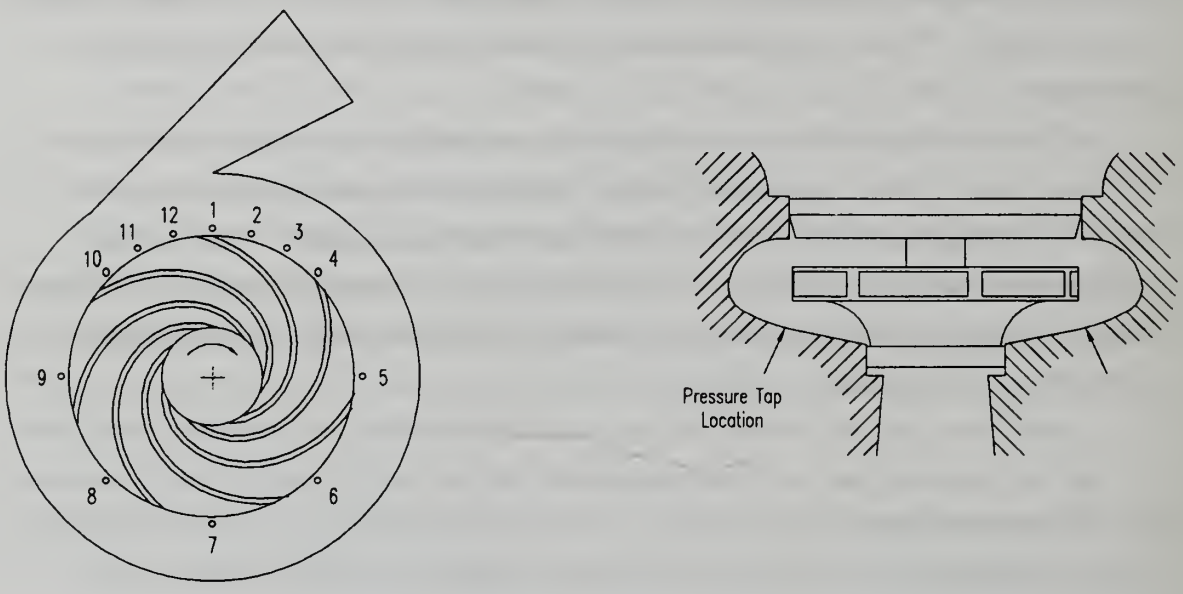

Figure 2.9. Pressure Tap Locations

The spatial pressure distribution was obtained using a Scanivalve pressure measuring system, shown schematically in Figure 2.10. The system consists of a Scanivalve model DSS-48C/Mk4 Double Scanivalve System, a Scanivalve Digital Interface Unit (SDIU), a Validyne Model P305 differential pressure transducer, and an IBM PC-AT personal computer.

The Scanivalve DSS-48 is a pneumatic scanner capable of multiplexing differential pairs of static and slowly changing pressures. It may be used to scan up to 48 differential pressure pairs or 96 individual pressures at rates of up to 8 ports/second. The system contains two synchronously driven precision rotary pneumatic selectors with extremely low internal volume and thus requires minimal settling time between individual readings.

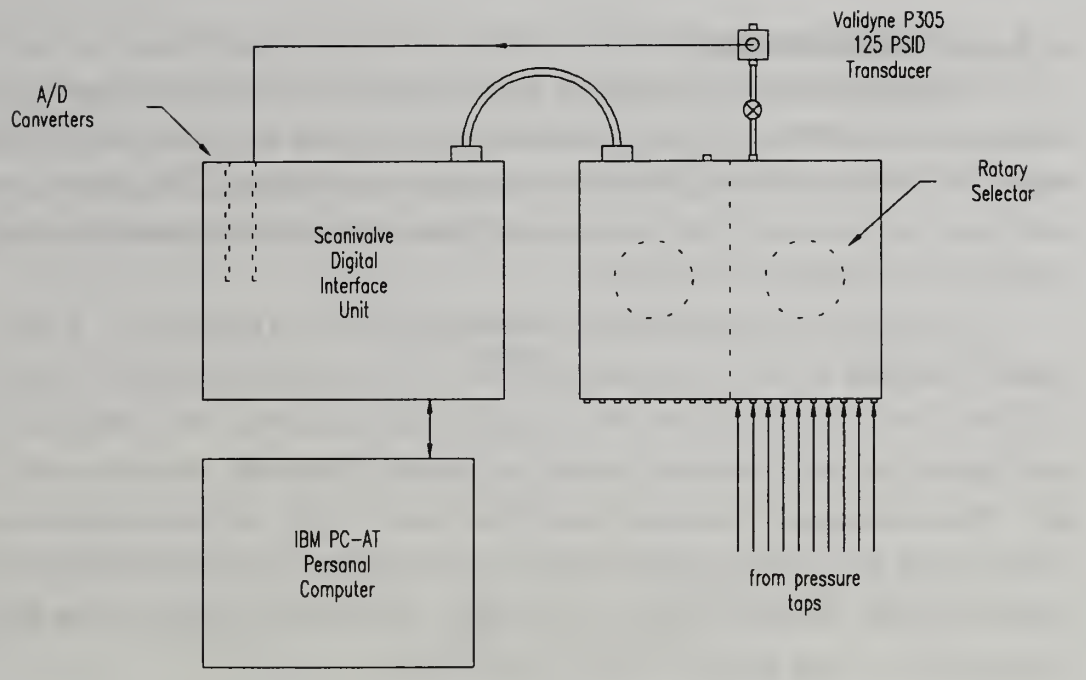

Figure 2.10. Scanivalve Pressure Measuring System

The pressure transducers used in this system were externally mounted. For this experiment, a single Validyne Model P305D differential transducer was used. The transducer has a wet-wet capability with two stainless steel pressure cavities. It accepts an 11-32 VDC input signal and outputs a 5 VDC full scale output signal proportional to the differential pressure across its ports. The diaphragm was selected to provide a maximum range of 125 psid. Zero and span adjustments were provided directly on the transducer. The transducers are accurate to within ±0.25% full scale and can withstand over-pressurization up to 200% full scale with less than 0.5% zero shift.

The Scanivalve Digital Interface Unit (SDIU) interfaced between the rotary Scanivalve and the host computer via an IEEE-488 connection. The SDIU provides the ability to control and read the Scanivalve position and two Analog to Digital (A/D) converters allow analog transducer signals to be digitized and retained in on-board memory. Each pressure reading is identified by a "module" and "port" number. The SDIU can be programmed to correct each reading for zero offset and span shifts for various transducers, thus allowing calibration of the entire pressure monitoring system as a whole.

2.4.3. Acoustic Measurements

Three stainless steel test sections were built on which hydrophones and accelerometers could be mounted. The test sections were 12 in., 28 in., and 100 in. in length. For these studies, only the first two sections were utilized. They are shown in their respective positions in the pump loop in Figure 2.6. A more detailed sketch of the inlet test section is given in Figure 2.11.

Hydrophone and accelerometer mounting are shown in Figure 2.12. A 3/4" diameter hole was drilled through the pipe wall. A brass hydrophone adapter was fit inside the hole and was flush with the inside pipe wall, as shown. The hydrophone itself was threaded into the hydrophone adapter and was also flush with the inside wall of the pipe. The accelerometer mounting bracket was located on top of the hydrophone adapter as shown with the accelerometer mounted atop the bracket. The accelerometers were used in the initial validation studies to investigate vibro-acoustic interactions as described in section 2.3.3. They were not utilized in this study.

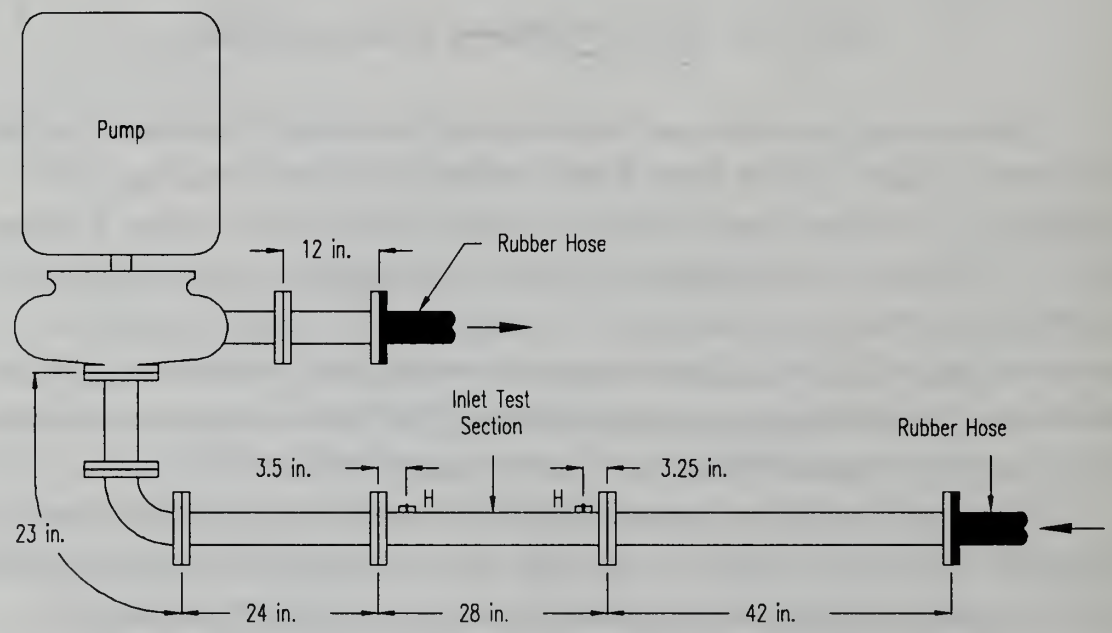

Figure 2.11. Inlet Acoustic Test Section

Acoustic profiles were obtained from pressure field measurements from PCB 105B piezoelectric hydrophones. The hydrophones have a dynamic range of 215 dB re 1 μPa and a nominal sensitivity of 300 mV/psi. The electric signal from the hydrophone was amplified using a PCB model 483B08 voltage amplifier. Vibration measurements were taken with Endevco model 7701-50 accelerometers with a nominal sensitivity of 50

pC/g and a dynamic range of more than 2000g. The accelerometer signals were amplified using Endevco model 2721B charge amplifiers with an output range of 10 to 1000 mV/g. Hydrophone and accelerometer signals were filtered through a Frequency Devices 744PL-4 low pass filter and digitized via a Data Translation DT2821 analog to digital board on an NEC 386SX personal computer.

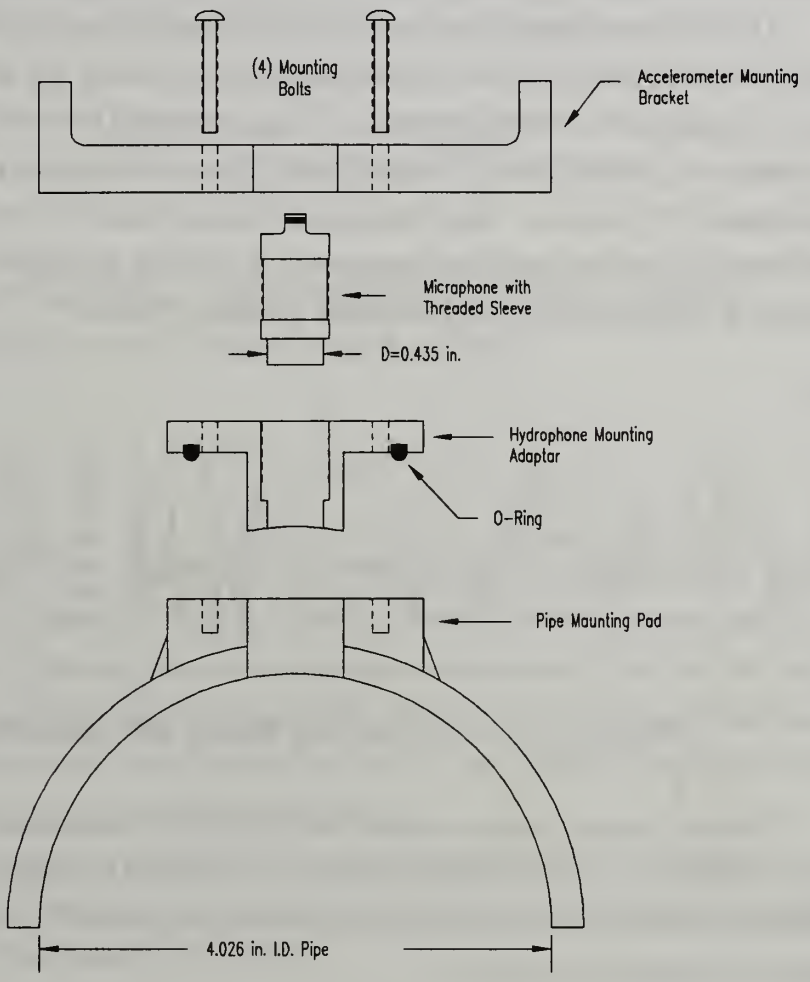

Figure 2.12. Hydrophone/Accelerometer Mounting Assembly

2.5 Data Acquisition and Processing

Acoustic data was acquired through a DT2821 Analog to Digital board and ILS Station spectral processing software. Data were acquired at a sampling rate, f_s, of 5000 Hz per channel. This results in a Nyquist cutoff or folding frequency

$$f_c = \frac{f_s}{2} = 2500\text{Hz}.$$

In order to avoid aliasing, the cutoff frequencies of the analog filters were set at 1000 Hz. Frequencies above this level were not of interest for this study.

The raw time domain data was collected, demultiplexed into the individual channel data, and converted into engineering units (psi) using ILS software programs. The time domain data for each channel was then converted into MATLAB format for processing using MathWorks PRO-MATLAB. The total sampling time was approximately 131 seconds. Spectral analysis was performed on the data using the Welch method of power spectrum estimation. A detailed description of this method is contained in Oppenheim[21]. The procedure is outlined below.

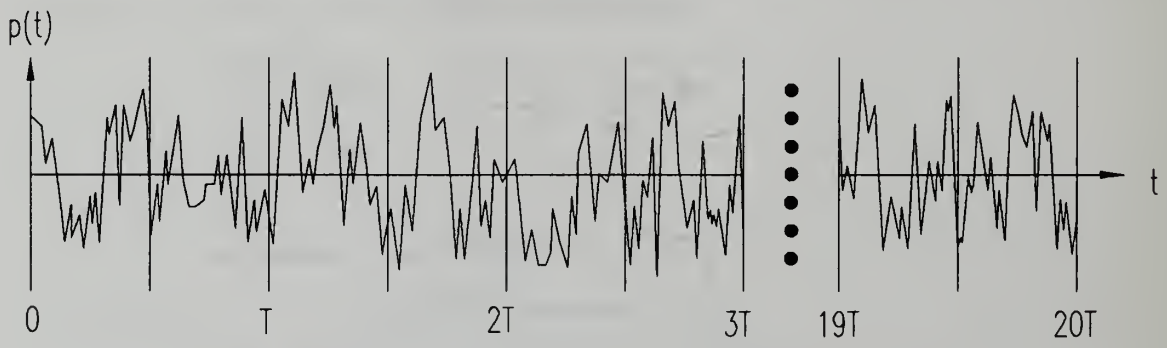

Figure 2.13. Division of Time History into Sample Records

The time history of each channel was subdivided sequentially into 39 overlapping records of length $T \cong 6.55$ seconds as shown in Figure 2.11. Each record contained N = 32768 data points and overlapped each neighboring record by $N/2$ = 16384 points. The resolution bandwidth is given by

$$B_e = \Delta f = \frac{1}{T} = \frac{1}{N\Delta}$$

where Δ = the time between samples = $1/f_s$. Successive records were then windowed using a Hanning, or cosine, taper and transformed using 32768 point Fast Fourier Transforms (FFT).

The Fourier transform-inverse pair is defined by the following:

$$X_K = X(k\Delta f) = \sum_{n=0}^{N-1} x_n e^{-2\pi i k n/N}$$

$$x_n = x(n\Delta) = \frac{1}{N}\sum_{k=0}^{N-1} X_K e^{2\pi i k n/N}$$

where N = the number of points.

The power spectral density (PSD) or autospectral density is estimated for each record by

$$P_{xx}(f) = \frac{2}{N\sum_{n=1}^{N}|w_n(N)|^2 \Delta f}|X_k(f)|^2$$

where $w(N)$ represents the N point window function. For example, applying a rectangular window, or no window, results in the following:

$$P_{xx}(f) = \frac{2}{N^2 \Delta f}|X_k(f)|^2$$

The units of P_{xx} are psi^2/Hz. The result is normalized such that it satisfies the energy theorem described in Marple[22]. This theorem is a direct result of the more familiar Parseval's Theorem. It dictates that the total power in one period T must be obtained by rectangular integration of the area under the PSD curve. This definition differs from many textbook definitions by the additional factor $1/\Delta f$ and explicitly incorporates the dependence of the PSD on the sampling interval Δ.

The reported pressure spectral density represents an ensemble average of the PSDs of each of the 39 individual records. Results for this study are presented in terms of spectrum density level which is defined by

$$\text{spectrum density level} = 10\log\frac{P_{xx}}{p_0^2}, \text{ dB}$$

where p_0 = 1 μPa which is the standard acoustic reference pressure for water applications. Note also that a reference bandwidth of 1 Hz is implied in the equation in order to satisfy proper dimensionality.

An uncertainty analysis was performed by Barton to account for measurement uncertainties (associated with the hydrophone, amplifier, analog filter, and A/D converter) and spectral processing errors (random and bias errors associated with the

FFT). Measurement equipment was identical to that used in these studies. The analysis methods were also the same with the following exceptions: 1) the number of sample records was increased from 35 to 39 in the present study, and 2) the Hanning taper was used, where none had been used previously. These differences result in negligible differences in the analyses.

The uncertainty in the spectrum density level was shown to be about 4.0 dB. The details of the analysis can be found in Barton[18].

3. A Theoretical Model of Tonal Noise Generation in Centrifugal Pumps

The discussion that follows was first presented by K.U. Ingard[23] in an informal note on sound generation in centrifugal pumps.

3.1. The Whirling Pipe Model

As a simplified model of a centrifugal pump, consider a pipe of length ℓ whirling about a a fixed axis as shown in Figure 3.1. Let the pipe rotate at a constant angular velocity Ω.

The equation of fluid motion is given by the Navier-Stokes equation:

$$\frac{\mathrm{D}\mathbf{u}}{\mathrm{D}t} = -\frac{1}{\rho}\nabla p + \nu\nabla^2\mathbf{u}$$

where $\frac{\mathrm{D}}{\mathrm{D}t}$ denotes the substantial derivative.

In order to transform the equation of motion from the inertial frame of reference to a rotating reference frame, centrifugal and Coriolis forces must be introduced:

$$\left(\frac{\mathrm{D}\mathbf{u}}{\mathrm{D}t}\right)_{\mathrm{I}} = \left(\frac{\mathrm{D}\mathbf{u}}{\mathrm{D}t}\right)_{\mathrm{R}} + \Omega\times(\Omega\times\mathbf{r}) + 2\Omega\times\mathbf{u}_{\mathrm{R}}$$

$(\mathrm{D}\mathbf{u}/\mathrm{D}t)_{\mathrm{R}}$ is the acceleration relative to the rotating frame and can be expanded:

$$\left(\frac{\mathrm{D}\mathbf{u}}{\mathrm{D}t}\right)_{\mathrm{R}} = \frac{\partial\mathbf{u}_{\mathrm{R}}}{\partial t} + (\mathbf{u}\cdot\nabla\mathbf{u})_{\mathrm{R}}$$

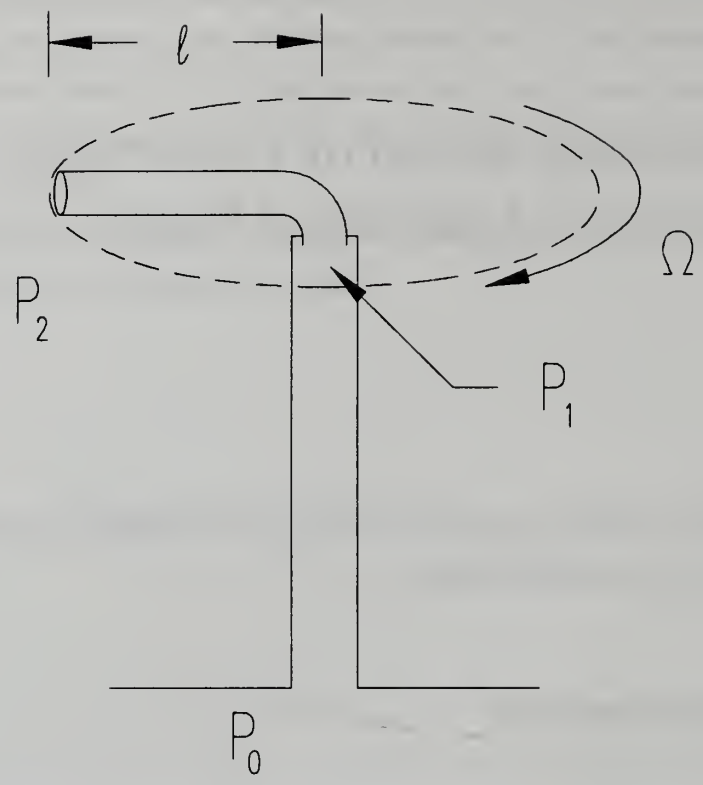

Figure 3.1. Whirling Pipe Model of a Centrifugal Pump

Neglecting viscosity, the *r*-component of the equation of motion can then be written as follows:

$$\rho\left(\frac{\partial U}{\partial t}+\frac{\partial\left(U^2/2\right)}{\partial r}\right)=-\frac{\partial p}{\partial r}+\rho\Omega^2 r \qquad [3.1]$$

During steady state operation, the flow in the pipe should be independent of time. The flow can also be assumed incompressible and from continuity, the flow is independent of *r*. With a uniform pressure gradient along the path of the pipe exit, integration of equation 3.1 between $r = 0$ and $r = \ell$ yields

$$P_2 - P_1 = \frac{\rho\Omega^2\ell^2}{2} \qquad [3.2]$$

Now, suppose the pressure along the path of the pipe exit is non-uniform. The flow then becomes time dependent in the relative frame. The exit pressure non-uniformity can be expressed as a function of the dynamic head and of the angular position ϕ by

$$P_2 = \overline{P_2} + \beta(\phi)\rho U_0^2/2$$

where $\overline{P_2}$ denotes the average pressure around the periphery.

As a result of the pressure non-uniformity, an unsteady component of velocity, u, will be introduced:

$$U = U_0 + u(t)$$

The pressure non-uniformity will cause a piston-like oscillatory flow superposed on the mean flow in the pipe as it rotates through the non-uniform exit pressure field. It is important to recognize that this unsteady flow is considered incompressible within the pipe and thus is not a function of radial position. This assumption is only valid when the length, ℓ, of the pipe is small compared to the wavelength of sound in the range of frequencies of interest. This assumption cannot, for example, be extended to include the region of the inlet pipe, which is assumed to have length $L >> \ell$.

The oscillatory component of velocity will generate sound pressures p_1 and p_2 at the inlet and exit ends of the pipe, respectively. Integration of equation 3.1 under these conditions and elimination of the mean flow terms using equation 3.2 yields

$$(p_2 - p_1) + \rho\ell\frac{\partial u}{\partial t} = -\beta(\phi)\frac{\rho\Omega^2\ell^2}{2} \qquad [3.3]$$

3.2. The Area Function

In anticipation of expanding the model to account for more realistic pump geometries, an area function, $A(\phi')$, is introduced to describe the position of the pipe exit flow area. Here, ϕ' denotes an angle in the rotating frame ranging from 0 to 2π radians. For a single pipe, this function is trivial. If the axis of the rotating frame is selected to

coincide with the pipe center, the area function will look something like that shown in Figure 3.2.

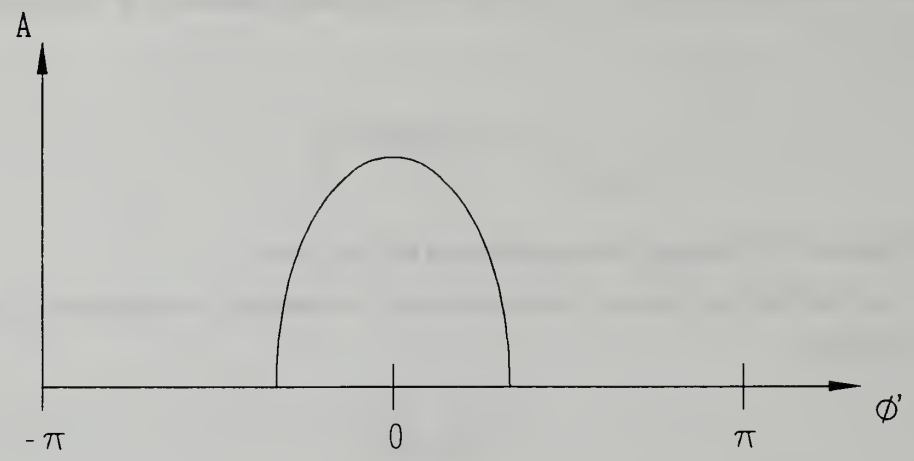

Figure 3.2. Sample Area Function for a Single Pipe "Pump"

If the angle ϕ' is extended from $-\infty$ to $+\infty$, the area function becomes periodic in ϕ' with period 2π. It can then be expanded in a Fourier series as follows:

$$A(\phi') = \sum_{-\infty}^{\infty} A_m e^{im\phi'}$$
$$A_m = \frac{1}{2\pi}\int_{-\pi}^{\pi} A(\phi')e^{-im\phi'}d\phi' \qquad [3.4]$$

where $A_{-m} = A_m^*$ is the complex conjugate of A_m.

3.3. The Unsteady Velocity Component

The circumferential pressure distribution may be considered periodic in the fixed reference frame with period 2π and can also be expanded in a Fourier series:

$$\beta(\phi) = \sum_{-\infty}^{\infty} \beta_n e^{in\phi}$$
$$\beta_n = \frac{1}{2\pi}\int_{-\pi}^{\pi} \beta(\phi)e^{-in\phi}d\phi$$

This series can be expressed in the rotating reference frame using the Galilean transformation

$$\phi = \phi' + \Omega t$$

where $t = 0$ is chosen as the time when the axes of the two frames coincide. This yields

$$\beta(\phi', t) = \sum_{-\infty}^{\infty} \beta_n e^{in\phi' + in\Omega t}$$

In a similar manner, the sound pressures p_1 and p_2 and velocity u may be expressed in analogous Fourier series:

$$p_1(\phi', t) = \sum_{-\infty}^{\infty} p_{1n} e^{in\phi' + in\Omega t}$$

$$p_2(\phi', t) = \sum_{-\infty}^{\infty} p_{2n} e^{in\phi' + in\Omega t}$$

$$u(\phi', t) = \sum_{-\infty}^{\infty} u_n e^{in\phi' + in\Omega t}$$

Substituting these Fourier expansions into Equation 3.3 and simplifying yields

$$p_{2n} - p_{1n} + i\rho\ell n\Omega u_n = \beta_n \frac{\rho U_0^2}{2} \qquad [3.5]$$

Next, note that the sound pressures are related to the unsteady velocity perturbations by the acoustic radiation impedances $\rho c\varsigma_1$ and $\rho c\varsigma_2$ at inlet and exit as follows:

$$p_{1n} = -\rho c\varsigma_1 u_n \quad \text{and} \quad p_{2n} = \rho c\varsigma_2 u_n .$$

Inserting these relations into Equation 3.4 and rearranging yields:

$$u_n = -\frac{\beta_n \rho(\ell\Omega)^2/2}{\rho c(\varsigma_1 + \varsigma_2) + in\rho\ell\Omega} \qquad [3.6]$$

3.4. Pump Geometry Considerations

At this point, it is useful to consider the effects of more realistic pump geometries on the analysis presented thus far. The single rotating pipe represents a single impeller passage in an actual pump. If there are B impeller blades, we represent this with B identical pipes rotating about the axis. The area function given by equation 3.4 will have coefficients, A_m, which are non-zero only for values of m which are integer multiples of B.

Next, consider the impeller blade geometry in an actual pump. A typical pump impeller passage is a diffuser with a mean path that may or may not be radial. The blades on most centrifugal pumps, including the one used in the present work are swept back from the direction of rotation. More complex geometries necessitate refinement of the governing equation 3.3. Here, the $\rho\ell$ term must be replaced by an equivalent mass within the impeller passage. This is done by considering the total kinetic energy of the unsteady flow within an impeller passage. Assuming a 2-dimensional passage, the total kinetic energy of the flow between blades with respect to the rotating reference frame is given by

$$K.E. = \iint_A \frac{\rho}{2} u^2(r,\theta) dA$$

and is equated to the kinetic energy of an equivalent fluid slug with velocity u_2. The velocity u_2 can be selected as the total exit velocity or the normal component of the exit velocity. The acceleration term in the governing equation is then replaced by $m\frac{du_2}{dt}$. In practice, the flow within the pump impeller is non-uniform and requires computational analysis to describe accurately. Such an analysis is beyond the scope of this work and will thus be neglected.

3.5. The Total Time Dependent Velocity and Sound Pressure

As discussed previously, we are interested in the sound field which propagates upstream of the pump. Denote the area of the inlet pipe by S. The time dependent

velocity component in the inlet pipe, $w(t)$, is obtained by integrating the product of the velocity $u(\phi',t)$ and the area function over angle ϕ'

$$w(t) = \frac{1}{S}\int_0^{2\pi} A(\phi')u(\phi',t)\mathrm{d}\phi'$$

Substituting the Fourier series expansions given in equations 3.4 and 3.6 and rearranging yields

$$w(t) = \frac{1}{S}\sum_{m=-\infty}^{\infty} A_m \left\{ \sum_{n=-\infty}^{\infty} u_n e^{in\Omega t} \int_0^{2\pi} e^{im\phi'} e^{in\phi'} \mathrm{d}\phi' \right\}$$

The integral is identically equal to zero unless $n = -m$ in which case it is equal to 2π. This means that the mth harmonic is produced solely by the mth spatial Fourier component of the exit static pressure distribution. The total velocity in the main duct then simplifies to

$$w(t) = \sum_{-\infty}^{\infty} w_m e^{-im\Omega t}$$
$$w_m = \frac{2\pi}{S} A_m u_{-m} \qquad [3.7]$$

where the coefficients A_m and u_{-m} are obtained from equations 3.4 and 3.6 respectively.

It is important to note that if there are B identical blades, the coefficients w_m will be non-zero only when m is an integer multiple of B. This means, in essence, that the fundamental frequency for the tonal noise produced by this model will be the blade passage frequency, $B\Omega$, and not the shaft frequency, Ω. In practice, non-uniformities in the impeller will result in non-zero area function coefficients, A_m, for values of m which are not integer multiples of B, but we would expect these coefficients to be much smaller than for those values of m which are.

The corresponding sound pressure at the inlet is given by the product of each harmonic component of the total velocity and the radiation impedance of the main duct at each frequency $\omega_m = m\Omega$. The total sound pressure at the entrance to the main duct is thus

$$\Pi(t) = \sum_{-\infty}^{\infty} \Pi_m e^{-m\Omega t}$$
$$\Pi_m = -\rho c \varsigma_1(m\Omega) w_m \qquad [3.8]$$

where $\rho c \varsigma_1(m\Omega)$ denotes the specific radiation impedance at the pump inlet.

The total radiated acoustic power is given by the sum of the power contributions from each harmonic:

$$W = \sum_{-\infty}^{\infty} \Pi_m \omega_m^*$$

3.6. Acoustic Impedance at Pump Inlet and Outlet

The specific radiation impedances at the pump inlet and outlet consist of a resistance and a reactance: $\varsigma \equiv \theta + i\chi$. For the case presented in the model with the pump discharging into free space, ζ_2 will generally be negligible compared to ζ_1 at the inlet. For an impeller discharging into a diffuser or volute, this will not be the case. The situation also simplifies when the inlet pipe is very long. As the length of the pipe goes to infinity, $\zeta_1 = 1$.

The quantity $-im\rho\ell\Omega$ in equation 3.6 is the mass reactance of the fluid in the impeller which is added to radiation impedance. The reactance of the fluid in the impeller can be normalized by the characteristic impedance ρc:

$$\frac{-im\Omega\rho\ell}{\rho c} = -im\frac{U_0}{c} = -imM_0$$

where M_0 is the Mach number of the flow in the pipe. This term may be neglected for small values of m when the length of the inlet pipe is very long. However, when the inlet pipe is short and terminates in free field, the mass reactance of the fluid in the impeller may become significant. This is especially true when the inlet pipe has a length which is an integer number of half wavelengths. (See Ingard[24].)

3.7. An Example

Consider the case of a seven bladed impeller rotating through a static pressure field which is uniformly increasing with angular distance from the volute tongue as shown in Figure 3.3. There is a discontinuity in the pressure field at the tongue where the pressure perturbation drops from its maximum value of β_{max}. Such a pressure distribution is similar to that encountered in volute pumps operating below design capacity.

Expanding the pressure distribution into a Fourier series, the coefficients β_n are given by the following:

$$\beta_n = \frac{i\beta_{max}}{2\pi n}(-1)^n \qquad \text{for n = ...-3, -2, -1, 1, 2, 3...}$$

For this example, let $\beta_{max} = 0.1$ (a pressure variance equal to 10% of the dynamic head).

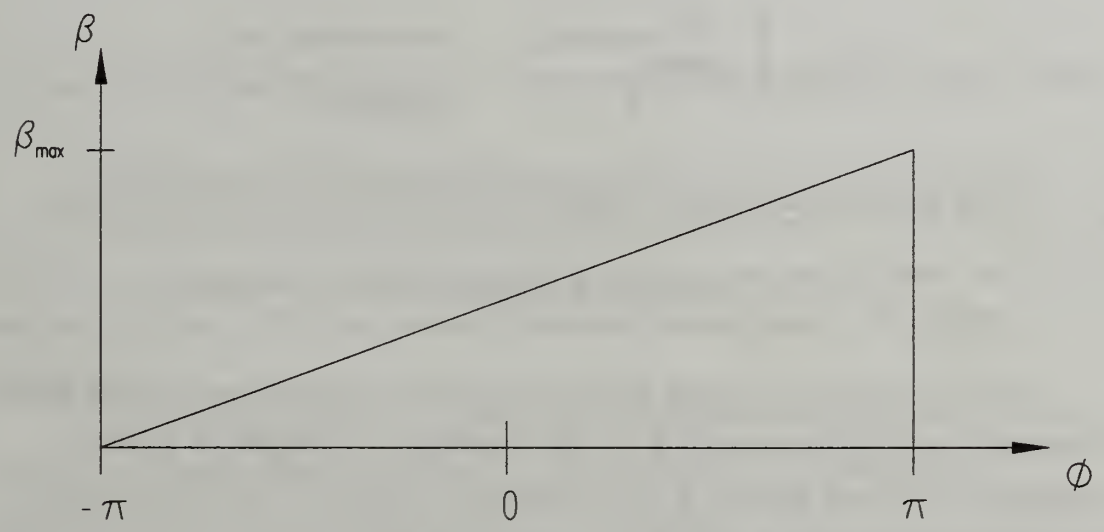

Figure 3.3. Sample Pressure Distribution Function

Let the total flow area at the exit of the pump impeller be S_{exit}.; the flow area between each blade, $S_p = S_{exit}/7$. Denote the angular separation between blades by α. (Note that for most pumps, $\alpha \approx 2\pi/B$, where B is the number of blades.) The area function can then be approximated using rectangular forms as shown in Figure 3.4 below.

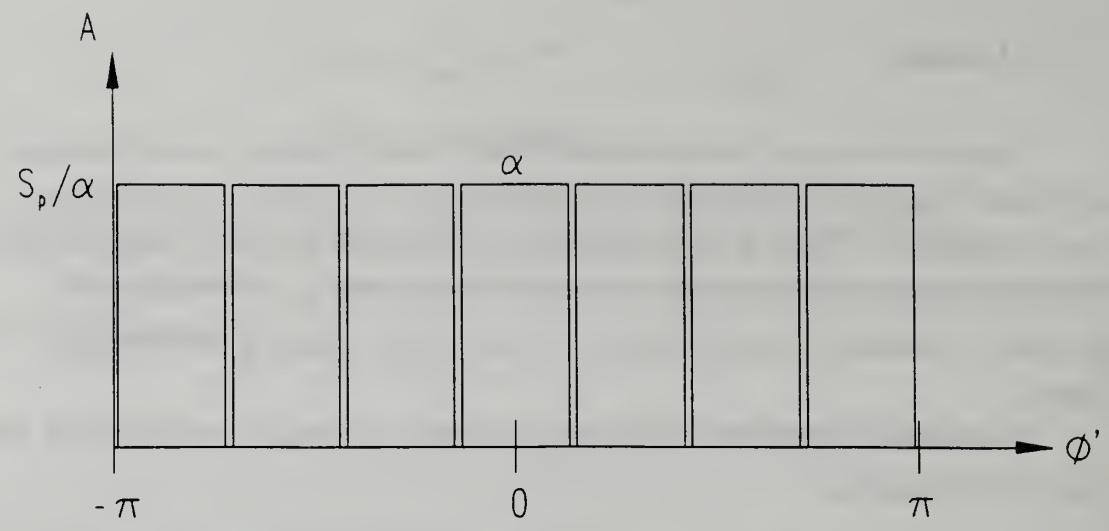

Figure 3.4. Sample Area Function for a Seven Bladed Impeller

The expansion coefficients for the area function are given by:

$$A_m = \begin{cases} \dfrac{7S_p}{m\pi\alpha}\sin(m\alpha/2) & \text{for } m \text{ multiple of } 7 \\ 0 & \text{otherwise} \end{cases}$$

Select the other parameters to match the characteristics of the M.I.T. pump:

$$S_p = 3.4 \text{ in}^2, \alpha = 48°, \Omega = 1780 \text{ rpm, and } \ell = r = 4.9 \text{ in.}$$

Next, for simplicity, assume that the inlet pipe is infinitely long and that the exit impedance is negligible compared to the inlet impedance. Equation 3.8 gives the magnitude of the sound pressure at each component frequency. The resulting spectra predicted for this example is show in 3.4. Results are given in terms of spectrum density level.

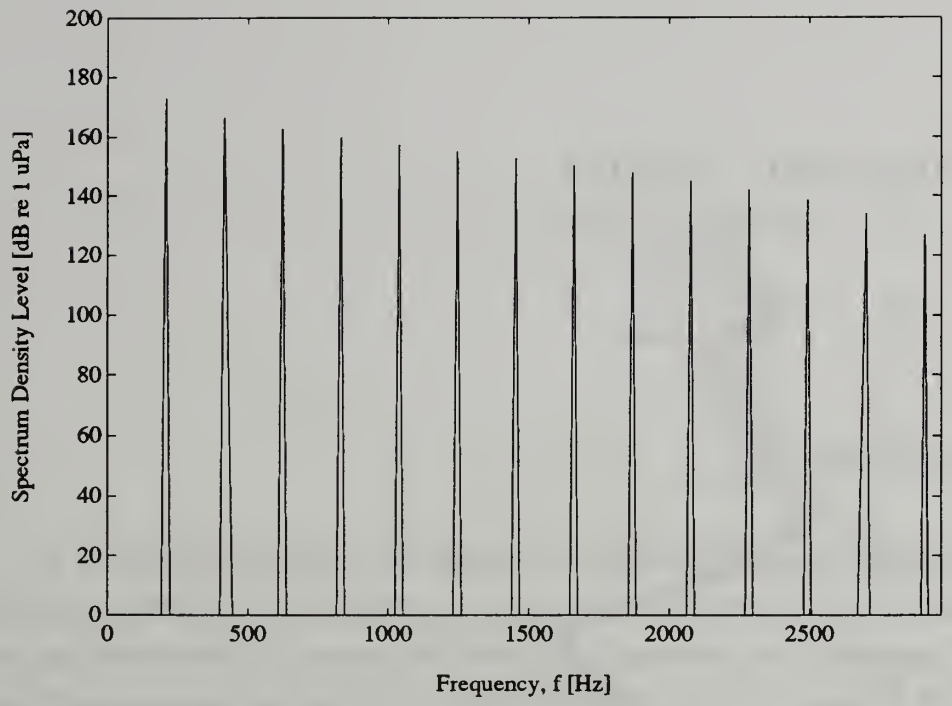

Figure 3.5. Predicted Harmonic Noise Levels in the Inlet Piping for Example Problem

Note that tones are produced only at harmonics of blade passage frequency (~210 Hz). That the harmonic levels decrease so slowly with frequency is an artificiality of the problem. In practice attenuation increases with frequency so that the peak levels drop off much more rapidly. The mass reactance term also becomes significant at higher frequencies.

This problem is not meant to show the simplicity of using the model. To the contrary, it illustrates the complexity of acoustic predictions. The large number of variables and their interdependence make it very difficult to obtain analytical solutions without making many simplifications. However, this does not diminish the utility of the model in gaining an understanding of the physical phenomena involved in the noise generating process.

4. Parametric Studies

4.1. General Discussion

Prior to discussing the results of the individual parametric studies, it is appropriate to consider the effects of the acoustic phenomena described in section 2.3 on a typical spectrum. An understanding of these phenomena is critical to the proper analysis of the data. For the following discussion, refer to the typical acoustic spectrum presented in Figure 4.1

The broadband noise floor of the spectrum varies significantly with frequency and is dominated by turbulent pressure fluctuations. The turbulent fluctuations are highest at very low frequencies and drop off considerably above 10 Hz. At higher frequencies, the turbulent energy level is lower and attenuation is more rapid. The residual noise level with the pump off is below 120 dB over all frequencies and below 100 dB for frequencies above 50 Hz except for spikes of about 120 dB corresponding to 60 Hz and its harmonics. The source of these tones is assumed to be a 60 Hz transformer on the roof above the test cell.

The sharp peaks contained in the spectrum are pure tones at shaft frequency and its harmonics. These peaks are marked with circles on Figure 4.1. Note that the highest peak corresponds to $7 \times f_{sh}$, (~205 Hz)which is the blade passage frequency, f_{bp}, defined previously. Note also that there are many sharp peaks which do not correspond to shaft harmonics. Most of these occur in the region above 500 Hz where the broadband noise level is much lower.

4.1.1. Turbulence Noise

Fluid flow in the acoustic pump loop was in the turbulent regime for all of the studies reported herein. The Reynold's number based on pipe diameter ranged between 25,000 and 400,000, well above the laminar limit for all cases. Because turbulent

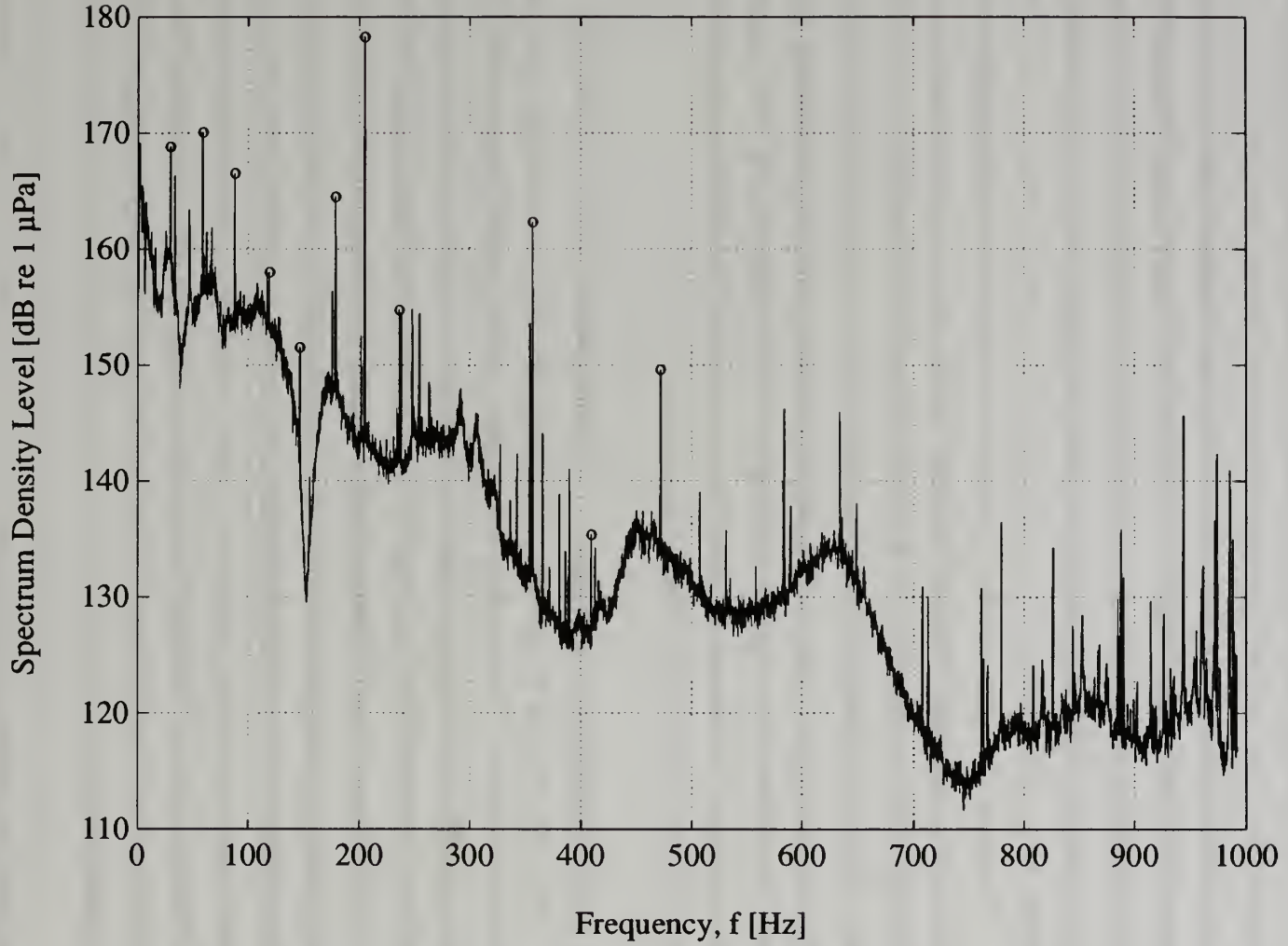

Figure 4.1 Typical Inlet Noise Spectrum

pressure fluctuations can be detected by the hydrophones used in this work, it was necessary to ensure that these fluctuations were not corrupting the acoustic spectra presented. The energy produced by turbulence is not acoustic; it does not travel at the speed of sound, but has been shown to propagate at a speed of about 0.8 times the mean flow speed.[18]

Barton showed that these fluctuations were not a dominant source of noise in the studies by using a coherence argument. Turbulent fluctuations are non-coherent. By showing that the pressure field near the pump inlet was strongly coherent over a long length of pipe, it was deduced that turbulence did not significantly corrupt the data presented.

The pump inlet pressure field coherence was measured across a straight 100 in. test section at pump inlet. The results showed that, for the most part, the entire spectrum was strongly coherent. In particular, the shaft harmonics had coherence levels very close to unity. The notable exception to this was the shaft frequency itself which showed slightly lower coherence for the inlet piping arrangement used for these studies. Other areas of low coherence were around the frequencies where the standing wave pattern produced nodes at the location of one of the microphones. In these instances, the turbulent energy levels dominated the measurements.

4.1.2. Reflection and Standing Waves

The noise floor of the spectrum is strongly affected by the standing wave pattern in the inlet test section. The standing wave pattern is a function of frequency, the reflection coefficient at the steel-rubber interface, and the position of the hydrophones relative to the wave maxima and nodes. It is possible to predict the standing wave structure and this was done for this pump loop configuration by Louie[25]. The calculated standing wave spectrum showed reasonable agreement with the measured spectra. Louie's calculations showed resonant peaks at frequencies near 200 and 600 Hz. In the measured spectra, broadband peaks were located around 450 and 650 Hz and a narrower peak often appeared near 250 Hz. The importance of the calculations however, is that they show that such a pattern can exist and that the noise floor level is strongly affected by the wave structure.

4.1.3. The Effects of Air in the System

Prior to taking any acoustic measurements, efforts were made to remove all entrapped from the system using the de-aeration methods described in section 2.2. During the course of the experiments, it became apparent that certain aspects of the

acoustic spectra could not be explained by any of the aforementioned phenomena. An example is the sudden drop in the noise floor which occurred on many of the spectra at frequencies between 150 and 200 Hz. A possible cause may be the presence of air in the system.

Air in the pump loop will be transported through the loop with the flow and will tend to settle at higher locations and small cavities. The pump volute may be a possible location for small quantities of air to settle. The air "bubble" has a natural frequency associated with it. Small pressure perturbations (i.e., sound waves) occurring at this frequency will be absorbed by the air bubble, thereby attenuating the perturbations very rapidly. The resonant frequency of the air pocket may be estimated using the analysis contained in Appendix A.

In this instance, we wish to know what size bubble corresponds to a resonant frequency of ~ 200 Hz. Using equation A.3, the approximate size of a bubble which corresponds to this frequency is ~ 1.5 inches in diameter. If the air is in the form of a thin layer, this frequency corresponds to a layer of about 0.125 in. thickness and covering an area of 5 $in.^2$ or to a layer of 0.25 in. thickness covering an area of 1.3 $in.^2$. The presence of water bubbles of this size in the rig is clearly possible.

4.2. The Effect of Long Chain Polymers

4.2.1. Experimental Procedure

In an attempt to gain some information about the nature of the broad-band noise radiated from the centrifugal pump, the water in the loop was treated with a long chain polymer additive. Experiments by Sedov[26] and Paterson[27] have shown that the polymers act to reduce the drag on the flow in small diameter pipes by appreciably altering the turbulent flow behavior of the fluid. Their effects on flow in the laminar regime is not as marked.

The mechanism by which this phenomenon is produced is not well understood. Van Driest[28] hypothesized that the drag reduction is caused by the damping of turbulent fluctuations by the interspersed polymer chains. This suppresses the generation of turbulence in the viscous sub-layer of the flow. He also attempted to show that increasing the polymer concentration increases the size of the eddies which are damped. It is well known that turbulent fluctuations are one of the main sources of broad band noise generated by turbomachines so it seemed a reasonable expectation for the polymers to have some effect on the broad band noise produced by the pump.

The loop was filled with water and then treated with a polyethylene oxide (Poly-Ox) additive. The Poly-Ox additive was a WSR-301 grade water soluble resin with a molecular weight of 4×10^6 grams/mole. The resin was predispersed in a solution of propylene glycol, a water-miscible non-solvent. The mixture was injected into the loop through the blind flange on the top of the 600 gallon tank. Several different concentrations of polymer were used: 100, 500, and 1000 ppm by weight. After each set of experiments, the loop was drained and flushed several times to ensure that all traces of the polymer were removed from the test loop prior to re-testing. The experimental conditions for the polymer enhanced and pure water base cases are summarized in Table 4.1 below.

Table 4.1 Polymer Treatment Experimental Conditions

Concen. [PPM]	Speed [RPM]	ΔP_{pump} [PSI]	$\Delta P_{throttle}$ [PSI]	Flow Rate [GPM]
100	1038	14.5	13.5	195
---	1038	14.5	12.5	192
100	1780	42	37	338
---	1780	40	33	340
500	1038	14.5	14	190
---	1038	14.5	12.5	192
500	1780	41.5	38	343
---	1780	40	33	340
1000	1038	14.5	14.5	155
---	1038	15.5	14.5	154

The polymers proved difficult to work with in the large quantities required to treat the entire pump loop. Most of the work in this area found by the author dealt with much smaller-scale use of the polymer additives. In this study, it was desired to mix the solution evenly throughout the 800 gallon loop. It was, however, extremely difficult to ensure uniform mixing due to the tendency of the polymer solution to agglomerate. Baffle plating at the bottom of the tank added to the difficulty. In order to enhance mixing, the pump was run at low speeds while adding the polymers. The degree of success is impossible to ascertain. However, the observed flow rate was steady

throughout the data collection period which is a fair indication that the solution was evenly-mixed.

The other problem associated with the polymers is that they have a limited period of effectiveness. Paterson[27] showed that polymers degrade due to the rupture of molecular valence bonds caused by shearing forces in the solution which result in molecular scission. The shear forces exerted on the fluid by the pump impeller causes the chains to be broken, thus reducing the effectiveness of the solution. Therefore there was an attempt to balance, on the one hand, the desire to achieve thorough mixing while, on the other hand, ensuring the effectiveness of the polymers was not diminished prior to taking the acoustic measurements.

The general effect of the polymers was to increase the flow rate through the pump loop for the same throttle setting. It also appears that the performance of the pump may have improved slightly with the polymer additives. That is, there was an increase in the flow rate without a corresponding decrease in the pump head rise. The opposite occurred when the polymer concentration was increased to 1000 ppm. In this case, the flow rate actually decreased from the water only case for the same throttle setting. Again, there was no change in the pump head rise.

The phenomenon of an overall loss of drag-reducing effectiveness at high concentrations has been observed in the past. Van Driest[28] showed that at sufficiently high concentrations of polymer, the fluid drag may actually increase from the pure solvent case due to an increase in laminar friction which ultimately overtakes the effect of turbulent drag reduction. However, this is not a likely explanation for the reduced flow observed in this case as the concentration levels required for such a crossover are about 7000-8000 ppm. A more detailed accounting of the behavior of polymeric solutions can be found in Van Driest.

Comparisons between the polymer-treated water and the base cases were made on an equal operating point basis. This was achieved by lessening the length of the throttle for the water runs until the flow rate matched that of the polymer-enhanced solution. As cited above, for the 1000 ppm comparison the throttle hose actually had to be lengthened.

4.2.2. Results

The general effect of the polymer treatment was to lower the broadband noise level measured at pump inlet. Figure 4.2 below shows a typical result of the polymer addition on the inlet noise spectrum. In the case presented, the effect of the polymers is more pronounced for frequencies above 150 Hz. In this frequency domain, the overall

noise floor is about 3 dB lower with the polymer treatment than for the corresponding water case.

The remaining inlet spectra results are contained in Appendix B and show that the effect of the polymers appears to increase with increased concentration of polymer. With 1000 ppm of Poly-Ox, the broadband noise level was reduced by about 5 dB from the water-only baseline over the entire range of frequencies. The noise reduction is about the same for the 100% speed cases for the same concentration. Tonal noise appears to have been unaffected by the addition of polymers.

The reader should note that in several of the spectra presented, there is a range of frequencies from 150 to 200 Hz in which there is a more pronounced difference between the polymer-treated and water-only noise levels. This phenomenon is not attributed to the addition of polymers, but to the presence of air in the system as discussed in section 4.1.3.

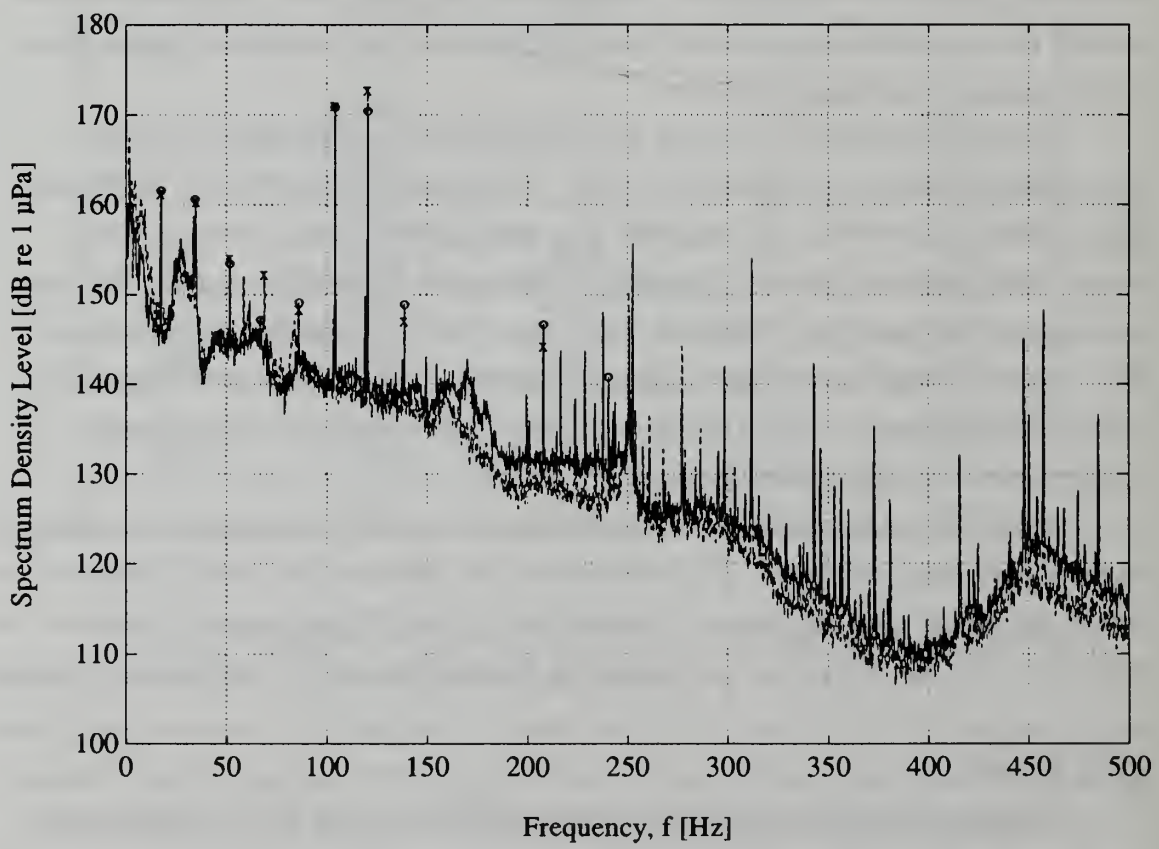

Figure 4.2. Inlet Noise Spectra, 58% Speed, Water and 100 ppm Polymer
(———, o : water only; — —, x : polymer treated)

Figure 4.3 shows an example comparison of the far upstream spectra for the water of polymer cases. Somewhat surprisingly, the polymers appear to have had no effect on the noise measured far upstream. The noise spectra in this region is dominated by turbulent flow noise and it was expected that the drag reducing polymers would have had some impact on the broad band noise measured at that location.

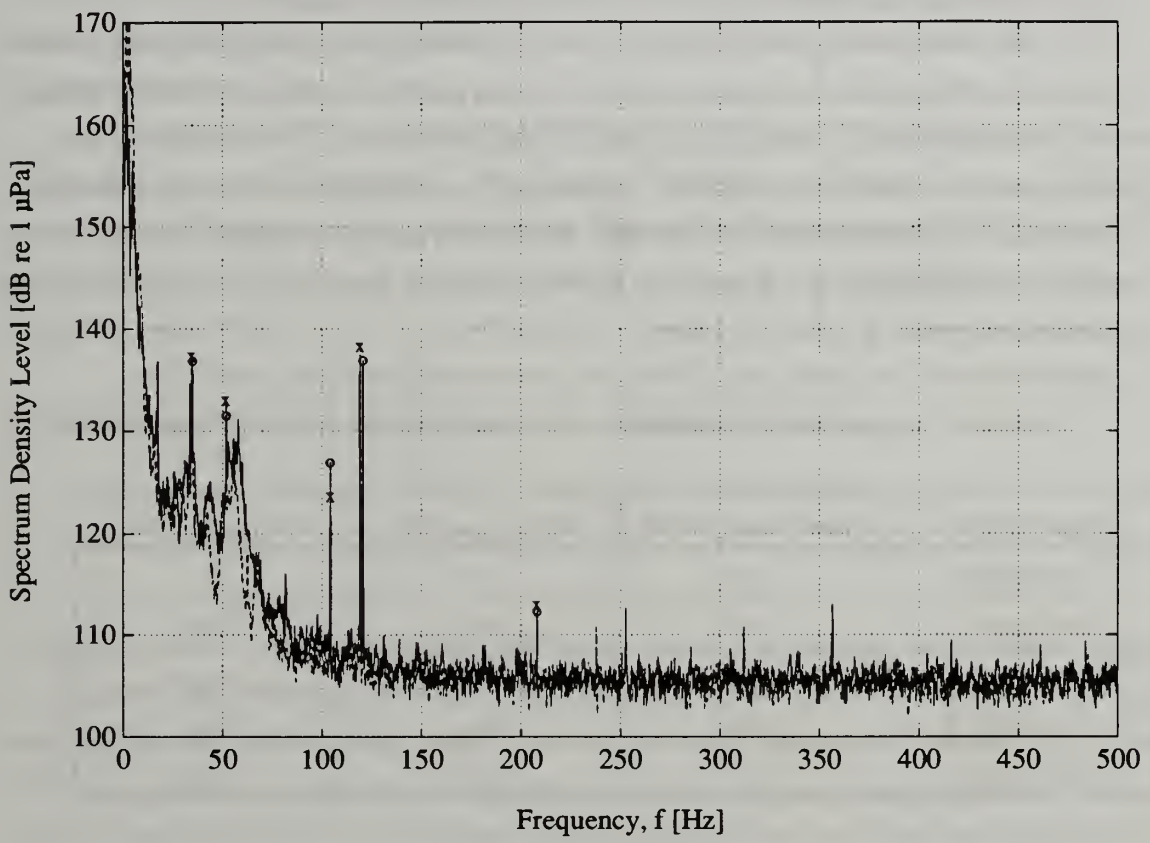

Figure 4.3. Upstream Noise Spectra, 58% Speed, Water and 100 ppm Polymer
(———, o : water only; — —, x : polymer treated)

These results indicate that the addition of long chain polymers to the working fluid has the potential for a minor reduction of the turbulent noise level. The effect is most likely due to suppression of the turbulent fluctuations in the flow, but more studies are required to better understand the physics of the situation.

4.3. Broadband Noise Studies

This section investigates the factors affecting broadband noise generation. The section is divided into two sections: 1) the effect of pump rotational speed on broadband noise in the pump inlet and far upstream, and 2) the effect of flow rate on the noise spectra in the same regions.

4.3.1. The Effects of Pump Speed on Broad Band Noise Generation

One of the stated goals of this study was to determine the effect of pump speed on both the broadband and tonal noise produced by the pump. It was impossible to isolate the effect of speed variations from all other effects due to the close coupling between pump speed, flow rate, and head rise. By making large changes to the throttle length, however, it was possible to obtain acoustic data for the pump operating on an equal flow basis at several different pump speeds. The experimental conditions for each of the cases presented are given in Table 4.2 below.

Table 4.2. Experimental Conditions for Constant Flow, Varying Speed Trials

Speed (RPM)	Flow Rate (GPM)	ΔP_{pump}(psi)	$\Delta P_{throttle}$(psi)
445 (25%)	~155	2	2
890 (50%)	155	10.5	10
1038 (58%)	154	15.5	14.5
1335 (75%)	155	26	25
1780 (100%)	167	46.5	46

Note that the experimental conditions for the 25% speed case were very difficult to measure accurately due to instabilities in the loop. This low frequency instability was present under all operating conditions but was much worse in this particular case. The operating point for this case was achieved by removing the throttle section entirely, thereby eliminating most of the flow resistance in the loop. The effect was an amplification of the loop instability which caused wild fluctuations of the pressure gages and an unsteady flow rate through the loop. The flow rate given in the table above represents a best estimate based on long period of observation but confidence in its accuracy is low.

The noise spectra for each of these cases are given in terms of spectrum density level for both the inlet test section and the far upstream section in Appendix C. In order to better interpret the results, it was desirable to plot the spectra on the same graph. However, the large variations about the noise floor made it difficult to distinguish between the different spectra. To facilitate differentiating between plots, the spectra were passed through a third order, low-pass Butterworth filter with a cutoff of 0.033 seconds. This eliminated tonal information and smoothed the noise floor without affecting its mean level. By eliminating all of the pump harmonics and some of the sharper broadband peaks, the procedure serves to highlight the phenomenon of interest, the overall broadband noise level.

The inlet acoustic spectra for the 100%, 75%, 50%, and 25% speeds are shown in Figure 4.4. The plot indicates that at the pump inlet the broadband noise signature of the pump is strongly dependent on pump speed. The spectral density levels differ by as much as 30 to 35 dB between the highest and lowest speed cases, with the intermediate speeds falling between the two bounding cases.

Correlation of the broadband noise level with pump speed was attempted using a non-dimensional pressure spectral density, S_p, defined as follows:

$$S_p \equiv \frac{P_{xx} U}{q^2 d}$$

where, for the inlet spectra, U is the impeller tip velocity, q is the dynamic pressure based on velocity U and d is the hydraulic diameter of the volute (in this case, estimated as the height of the volute at impeller exit). A more appropriate characteristic velocity may be the mean exit flow velocity from the impeller, but for this particular pump, the flow velocity was dominated by the tip speed of the pump and the two values were equivalent to within 25%. More importantly, the flow velocity scaled roughly with tip speed. The spectral density is thus scaled by a factor of $1/U^3$. This is has been shown to be the proper scaling of the power spectral density, P_{xx}, for undisturbed turbulent wall fluctuations and for published levels of turbulent boundary layer noise in water pipes.[19,20,29]

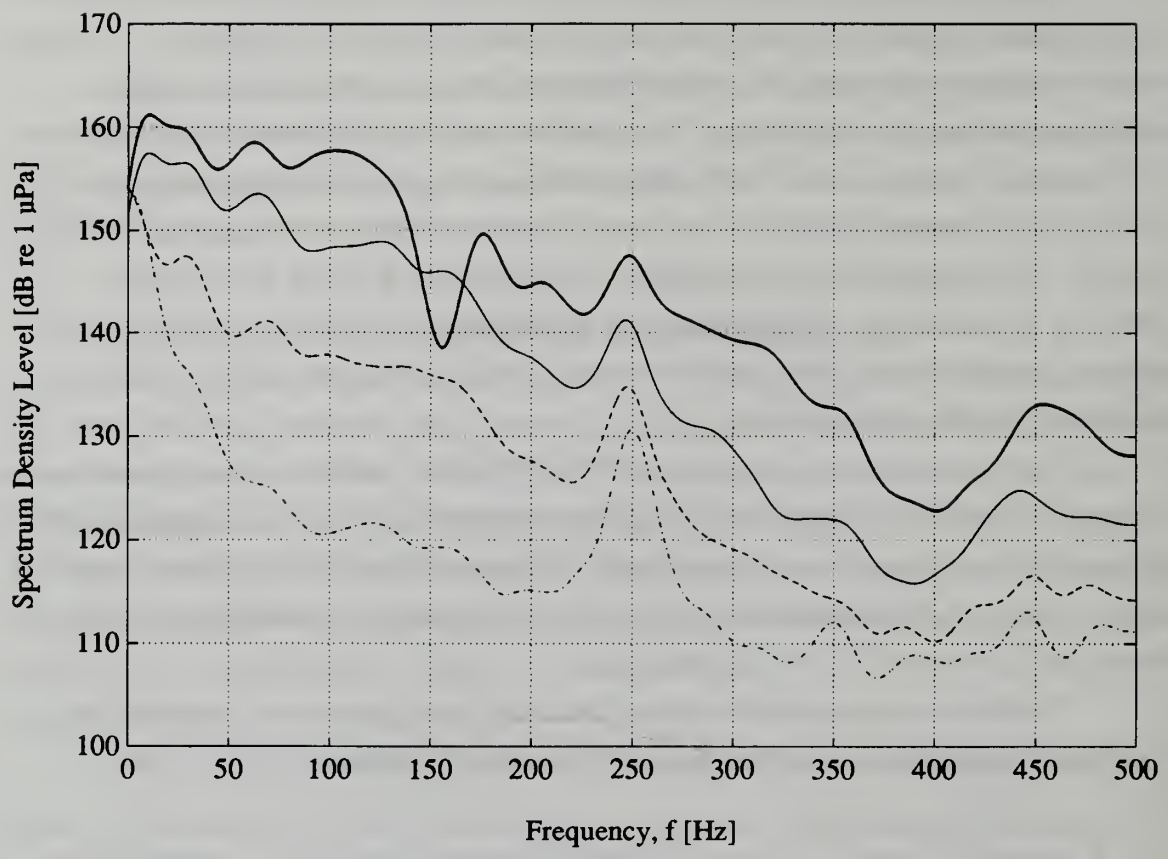

Figure 4.4. Inlet Noise Spectra, ~160 GPM, Varying Speed
(—— : 100% Speed, —— : 75% Speed, — — : 50% Speed, — · — : 25% Speed)

The non-dimensional pressure spectral densities (again filtered for ease of interpretation) are given in Figure 4.5. The scale on the ordinate matches that in Figure 4.3 (the distance between grid lines is equivalent to 10 dB with 7 divisions on each plot). The inlet noise levels are more closely matched using the non-dimensional value, but there is still some discrepancy between the individual plots.

Because the shape of the noise floor also changes from one case to the next, it would be difficult to determine the proper scaling of the pressure spectral density unless these effects could be isolated. It is also likely that there are multiple sources of sound within the pump which are affected by the pump's rotational speed and that the measured sound field is a superposition of these sources. The conclusion drawn, then, is that the broadband noise phenomenon is more complicated than can be described with a single non-dimensional parameter.

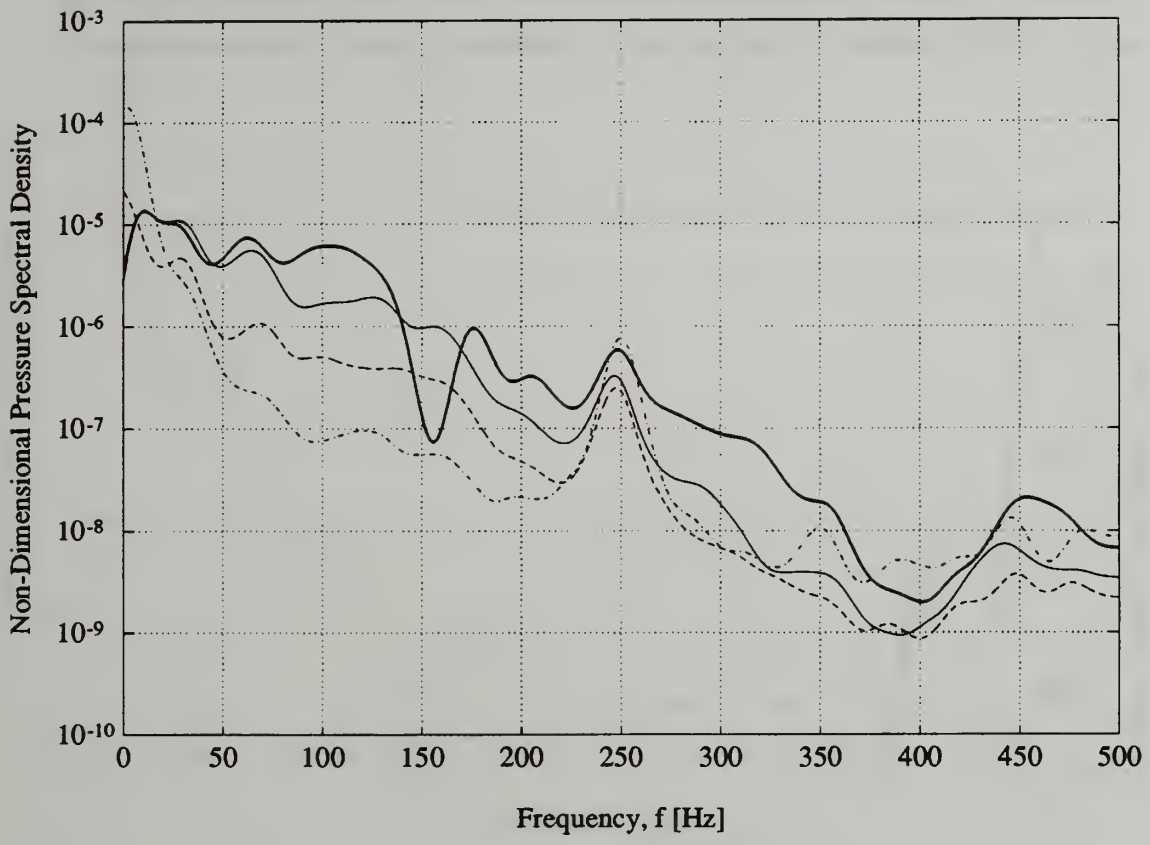

Figure 4.5. Non-Dimensional Inlet Noise Spectra, ~160 GPM, Varying Speed
(——: 100% Speed, ——: 75% Speed, — —: 50% Speed, — · —: 25% Speed)

The pressure spectral density levels for the far upstream test section are presented in Figure 4.6. As expected, the far upstream noise levels are more closely matched because the spectra are dominated by turbulent flow noise. The noise due to turbulence is highly dependent upon the flow velocity through the pipe which remains constant for all the cases presented.

For frequencies above 150 Hz, the spectrum levels are equal within the experimental uncertainty. Below 150 Hz, there is some variation with speed, with higher noise levels as speed increases. These results were somewhat expected. Acoustic wave attenuation scales with the wavelength, λ. Thus, higher frequency waves will attenuate more rapidly than lower frequencies. Since the hydrophone, in this case, was separated from the dominant noise source in the loop (the pump) by more than 100 feet of rubber hose, higher frequency waves were fully attenuated at the upstream test section. For frequencies below 150 Hz, a small amount of acoustic energy was still present far

upstream - enough to dominate the turbulent flow noise in this frequency range. An analysis of the coherence of the inlet and far upstream signals by Barton supports this argument.

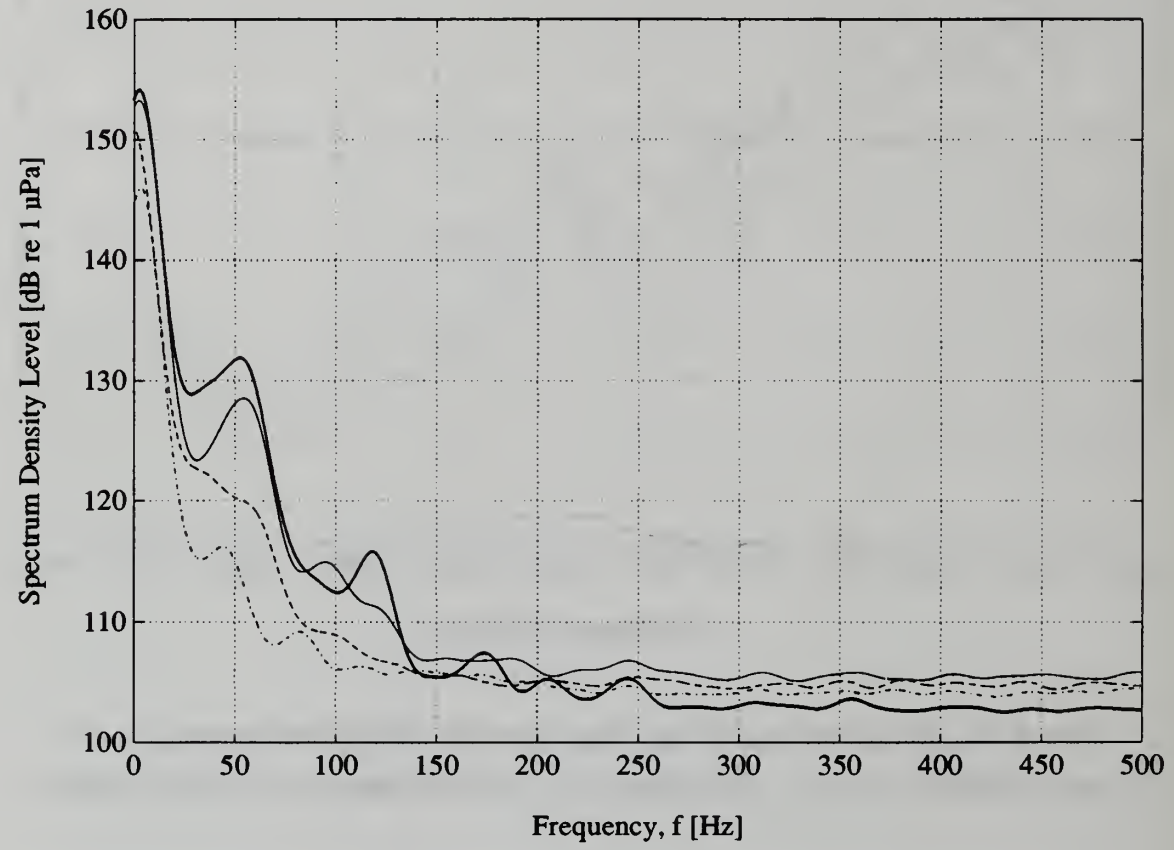

Figure 4.6. Upstream Noise Spectra, ~160 GPM, Varying Speed
(—— : 100% Speed, —— : 75% Speed, — — : 50% Speed, — · — : 25% Speed)

A comparison of the non-dimensional pressure spectral densities is shown in Figure 4.7. Again, the characteristic velocity used for scaling was the impeller tip speed. Here, the spectra collapse quite well for frequencies below about 80 Hz and begin to diverge as the frequency increases beyond this point. This behavior supports the above arguments that pump noise dominates the acoustic spectra at lower frequencies while turbulent flow noise dominates the spectra at higher frequencies.

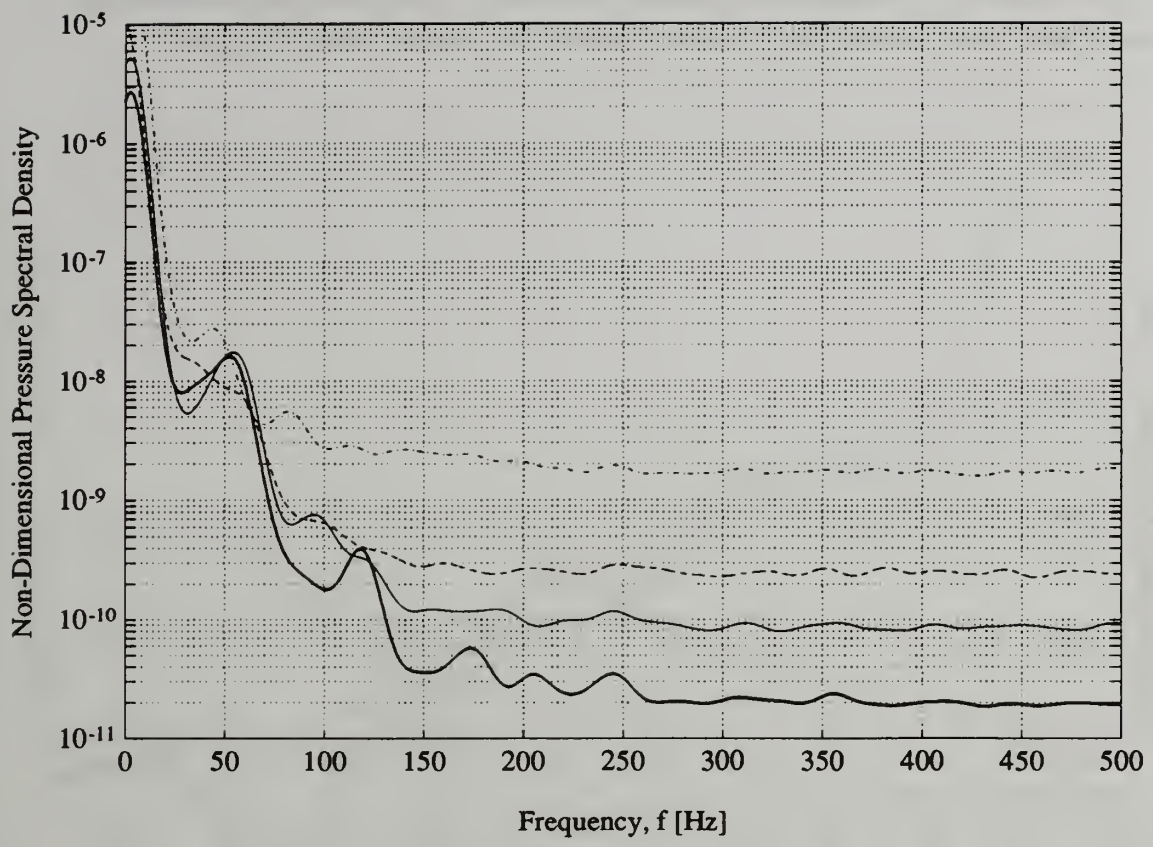

Figure 4.7. Non-Dimensional Upstream Noise Spectra, ~160 GPM, Varying Speed
(—— : 100% Speed, —— : 75% Speed, — — : 50% Speed, — · — : 25% Speed)

4.3.2. The Effects of Flow Rate on Broad Band Noise Generation

Using different throttle settings also provided data for the pump's acoustic performance at different operating points on the pump curve for a fixed speed. The results, provided in Appendix C, showed that the pump operating point had little effect on the broadband noise generated by the pump. A sample plot is given in Figure 4.8 below for 100% pump speed. The figure depicts the pressure spectral density level for flow rates of 126 GPM, 210 GPM, 333 GPM, and 480 GPM.

The sound profiles are nearly identical for the three lower flow rates. The high flow rate spectrum is also very close to the other three over most of the frequency domain with one notable exception. For low frequencies (below 50 Hz), the spectrum density level for the high flow condition is 15 to 20 dB higher than for the other conditions. Similar results were found for the other pump speeds tested. In each case,

the inlet spectra were nearly identical except in the low frequency region where the sound level was much higher when the throttle was removed from the loop.

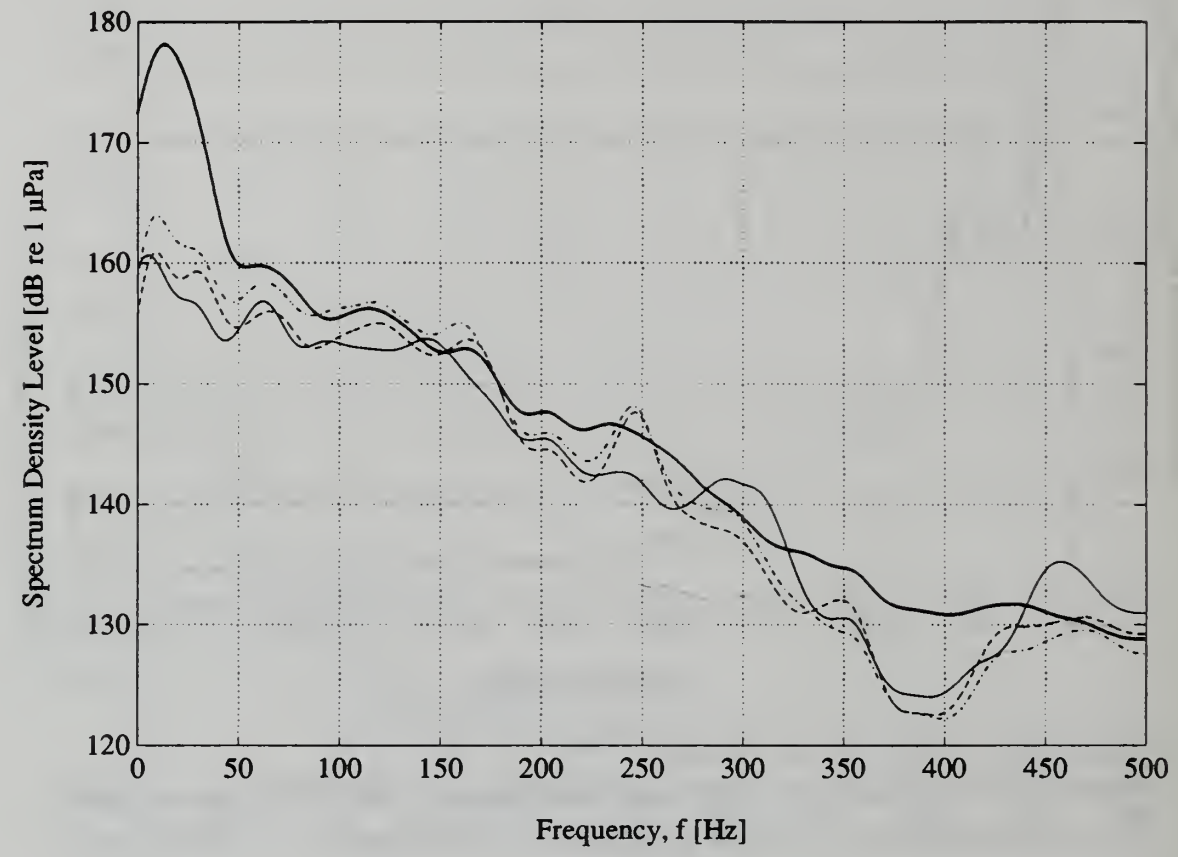

Figure 4.8. Inlet Noise Spectra, 100% Speed, Varying Flow Rate
(—— : 480 GPM, —— : 333 GPM, — — : 210 GPM, — · — : 126 GPM)

Note that these results could also be non-dimensionalized by using the total flow velocity at impeller exit, vice the impeller tip speed. However, between the highest and lowest flow rate cases, the total velocity changes by less than 10%. This equates to only 1 dB when translated to the non-dimensional pressure spectrum scale and would not noticeably affect the results presented. Therefore, with the noted exceptions, it is concluded that the broadband noise level of the pump is independent of the flow rate.

Far upstream noise levels for each of the test conditions given in Table 4.2 above are shown in Figure 4.9. Here, one would expect the power spectrum to scale with the cube of the flow velocity through the four inch pipe. Figure 4.10 shows the upstream non-dimensional spectral densities for these cases, calculated as before except with

$U = U_{pipe}$ and $d = d_{pipe}$. Surprisingly, the results do not support this assertion.

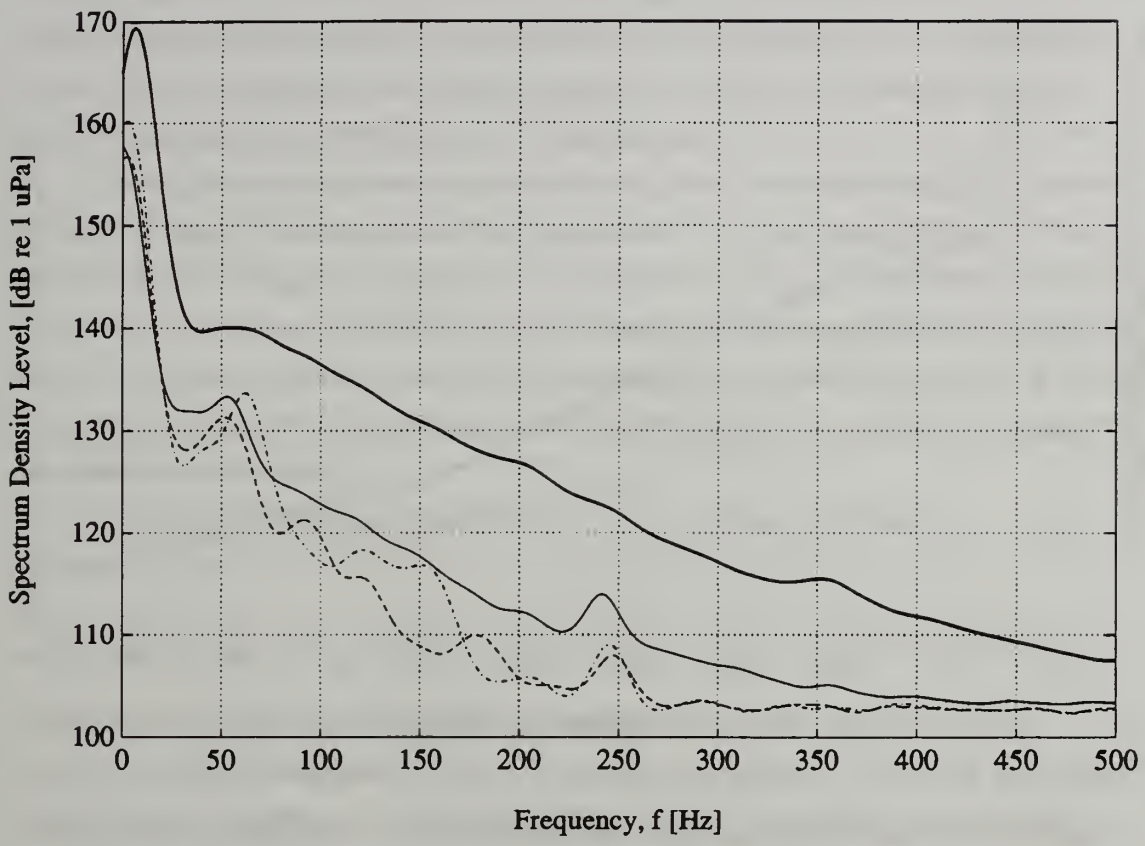

Figure 4.9. Upstream Noise Spectra, 100% Speed, Varying Flow Rate
(——: 480 GPM, ——: 333 GPM, — —: 210 GPM, — · —: 126 GPM)

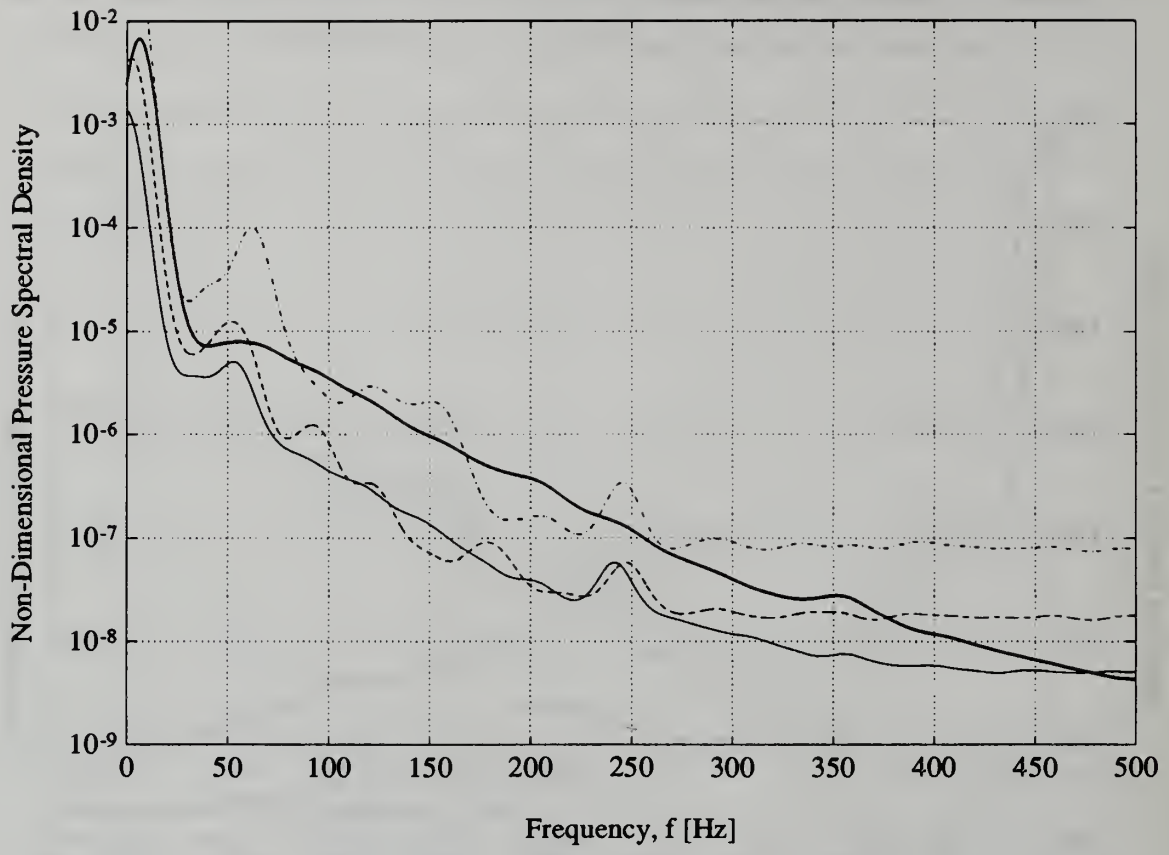

Figure 4.10. Non-Dimensional Upstream Noise Spectra, 100% Speed, Varying Flow
(——: 480 GPM, ——: 333 GPM, — —: 210 GPM, — · —: 126 GPM)

4.4. Harmonic Noise Studies

The other issue to be addressed in this chapter involves the harmonic tones produced by the pump. Specifically, how are harmonic noise levels affected by changes in pump speed and flow rate? By simultaneously measuring the spatial pressure distribution about the impeller discharge, attempts were also made to correlate the harmonic noise levels with the impeller exit pressure field and to test the model presented in Chapter 3.

4.4.1. Impeller Discharge Pressure Profile

In Chapter 3, a model was proposed which predicted the influence of the circumferential pressure distribution at impeller exit on the tonal noise produced by the

pump. The theory can be tested using the static pressure data and the corresponding acoustic spectra. The theory predicts that the *m*th harmonic of the acoustic pressure will be determined by the *m*th spatial Fourier component of the azimuthal pressure distribution about the impeller. By decomposing the 2π periodic pressure distribution into its Fourier components, the relative magnitudes of the sound harmonics can be predicted and compared with the actual measured levels.

Static pressure measurements about the impeller were taken using the Scanivalve pressure measuring system as described in section 2.4.2. Data was collected for four separate throttle settings at pump speeds of 100%, 75%, 50%, and 25% of the rated speed of the motor. Data were typically acquired using the maximum scan rate of 8 ports per second. Validation studies proved that the measurements were not dependent on the scan rate. Fifty readings were taken at each port and an average and standard deviation were computed for each location.

The random error associated with the sample average is given by

$$\sigma_\mu \cong \sigma/\sqrt{N}$$

where σ is the sample standard deviation and N is the number of sample points. Typically, this error was about 0.02 psi for full speed conditions. The 95% confidence interval for a given mean value is on the order of $\mu \pm 0.04$psi where μ is the sample mean. The confidence interval is typically less than 5% of the range of the mean pressures around the impeller.

It is interesting to note that the static pressure field in the volute was unsteady. The oscillations resulted in a standard deviation which did not converge to zero as the number of samples was increased. For random sampling of a periodic signal, the standard deviation converges to the rms value of the signal. To verify this observation, an oscilloscope was connected to the transducer output. It was found that the amplitudes of the oscillations were consistent with those predicted by the statistical analysis. The amplitudes of the fluctuations were typically on the order of 5-10% of the difference between the highest and lowest average pressures and were, therefore, significant but not too large compared to the spatial variations to invalidate the measurements. An analysis of the origin and effects of this unsteadiness were outside the scope of the present work and no further analysis was performed. The interested reader is referred to the previously discussed study by Yuasa and Hinata[6].

Static pressure data were recorded for sixteen different operating conditions: four different throttle settings with four speeds of operation at each setting. The average pressures for each of the sixteen operating conditions are given in Figure 4.11. Note that throttle setting A corresponds to highest throttle setting and C, the lowest. For example, at 100% speed the no throttle flow rate was 480 GPM. The flow rates for throttle settings A, B, and C were 314 GPM, 210 GPM, and 126 GPM, respectively. The data are plotted in terms of the head coefficient, Ψ, defined by

$$\Psi \equiv \frac{2(P - P_{inlet})}{\rho U_{tip}^2}$$

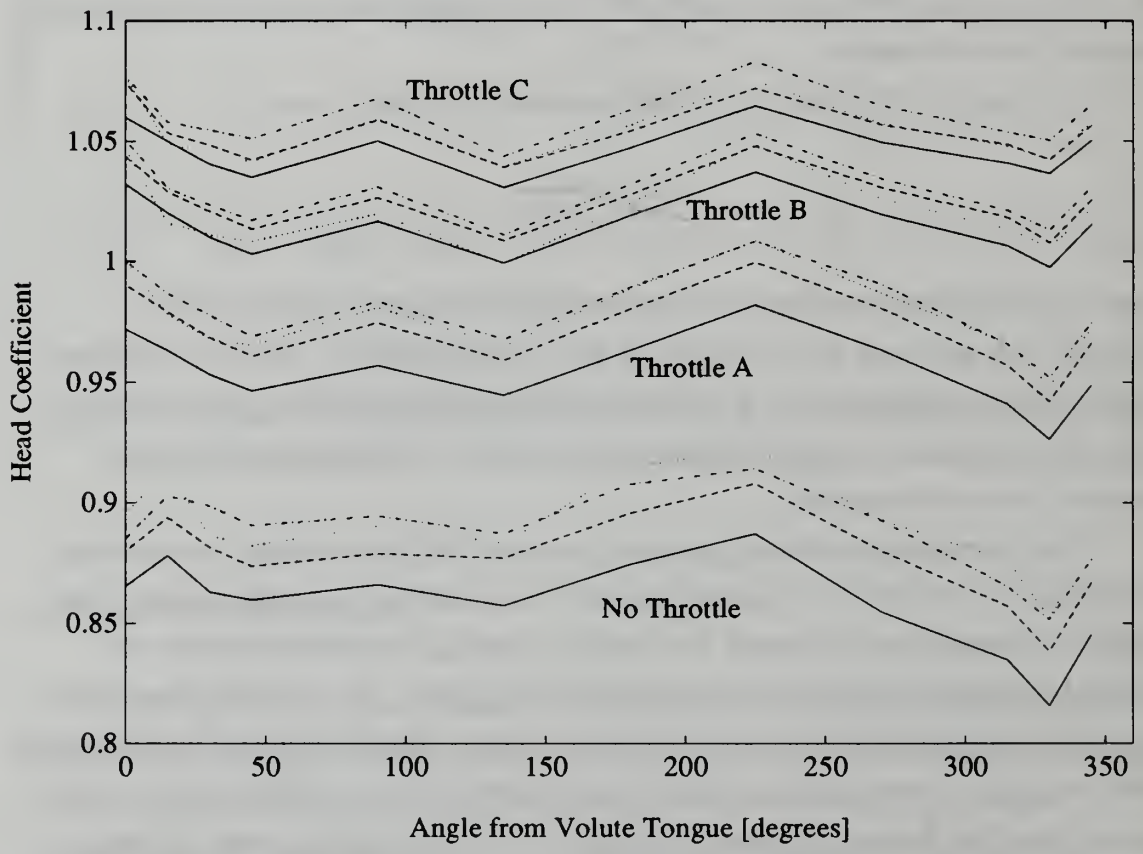

Figure 4.11. Static Pressure Profile at Impeller Discharge
(—— : 100% Speed, —— : 75% Speed, — — : 50% Speed, — · — : 25% Speed)

Noting the small range of values represented on the y-axis, the figure shows that there was very little variation in the static pressure distributions. For a given throttle

setting, this is expected. Changing the speed of the pump does not change the fluid conditions other than to scale all of the important flow parameters so that pump conditions at different speeds are dynamically similar. This is reflected in the closely matched results in each of the four groups of throttle settings.

The fact that varying flow rate through the pump (for a set speed) also had little effect on the pressure profile is unique to this particular pump. Because of the high exit swirl from the impeller, the velocity triangles did not change appreciably from one flow rate to the next. Therefore, changing the flow rate also did very little to alter the fluid dynamics in the volute.

At all of the conditions, the pressure measurements showed surprisingly little spatial variation. The amplitude of the non-dimensional pressure spatial fluctuations was constant for each throttle setting. For a given speed, the pressure differentials scaled roughly with the square root of the flow rate: at the lowest throttle setting (Throttle C), the range of measured values was about 2.5% of the pump head and with no throttle, the range was about 4.6% of the total head. The remaining two throttle settings fell between these two cases. As mentioned earlier, previous studies[9,15] have found spatial variations as high as 40% of the total head for off-design operation. The high swirl of the exit flow, which was invariant over all ranges of operation, is the reason for this pump's invariant pressure distribution.

4.4.2. Fourier Decomposition of Static Pressure Measurements

The pressure pattern in the volute can be expressed in terms of its spatial Fourier components by using a Discrete Fourier Transform (DFT). Calculations were carried out for a typical set of data. Due to the similarity between all of the test cases, a single example is representative of the whole.

The pressure at each of the twelve tap locations is represented by the following discrete Fourier series:

$$P_n = \sum_{k=-11}^{12} \beta_k e^{ik\theta_n}$$

Here, the pressure values are known and we desire to know the coefficients of the discrete Fourier series which reproduces these twelve values. Since there were only twelve discrete sample values, the Nyquist cutoff was at $k = 6$ and only the first six components of the series can be determined. Note also that since the pressure taps were

not evenly spaced, the individual elements of the location vector, θ, had to be explicitly stated.

A simple program was written which took the twelve average pressure values and produced the six Fourier coefficients. Conditions for the case presented were closest to the best efficiency point of the pump: throttle setting A, 100% speed, 314 GPM. Figure 4.12 shows the Fourier representation of the measured pressure and the magnitude of the coefficients.

Because the number of data points is small, the accuracy of this representation is highly suspect. According to the analysis, the third and fourth spatial harmonics were dominant, but confidence in these results is low. More pressure taps would yield a more accurate analysis.

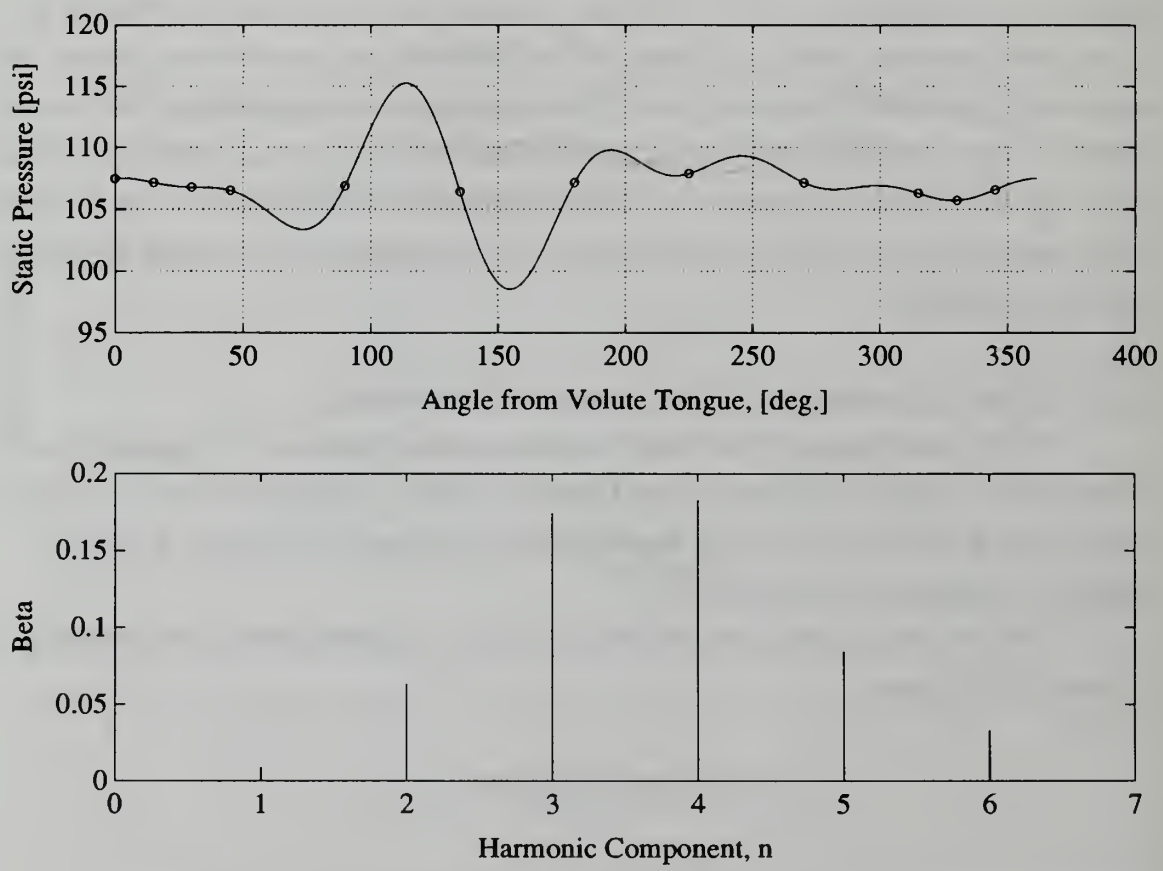

Figure 4.12. Fourier Representation of Static Pressure Field at Impeller Exit

4.4.3. The Effects of Pump Speed on Harmonic Noise Generation

Tonal noise produced by the pump is dependent on the pump rotational speed in two ways. The first is obvious: the frequencies of the tones are strictly determined by the shaft rotation rate. In order to compare the pressure amplitudes of the spectra produced by two different speeds of operation, dynamic similarity is required. The Strouhal Number, St, provides such a similarity parameter and for the analyses contained in this thesis, may be considered a non-dimensional frequency. The Strouhal number is defined by

$$St = \frac{fd}{U}$$

where f is the frequency, d is the impeller diameter and U is the impeller tip speed. A factor of π is removed from the value of tip speed for convenience. This results in a Strouhal number at f_{sh} equal to unity. The blade passage frequency then corresponds to a Strouhal value of 7. This will facilitate interpretation of the results in that the nth harmonic of shaft frequency will be plotted with an ordinate, $St = n$.

As discussed in Chapter 1, previous studies[2-5] have shown that the tonal noise produced by a centrifugal pump increases with rotational speed or, more specifically, with the square of the pump speed. The model presented in Chapter 3 attributes the tonal noise levels to the spatial pressure non-uniformities at the impeller exit.

Applying the model to the static pressure measurements taken at different rotational speeds with a fixed throttle setting supports the assertion that tonal noise is dependent on the rotational speed. For a given throttle setting, the magnitude of the spatial static pressure differentials scaled with pump speed as evidenced by the close matching of the non-dimensional pressure profiles for a given throttle setting. In terms of the model, this equates to the function $\beta(\phi)$ being the same for all different speeds. The sound pressures are then proportional to the square of the impeller speed.

However, the above argument only holds when the mass reactance term in Equation 3.6. is small compared to the radiation impedances at pump inlet and exit. When this is not the case, the sound pressure dependence on pump speed is lowered and tends toward a linear relationship.

In terms of the spectral density level, a second order dependence of the sound pressures on pump speed is indicated by a 12 dB increase in corresponding harmonic

levels when pump speed is doubled. A 6 dB increase is expected when the relationship is linear.

The inlet noise spectra for each of the 16 test cases are included in Appendix D. To aid in analysis of the data, the shaft tones are circled. The peaks correspond to $n \times f_{sh}$ with n = 1, 2, 3, 4, 5, 6, 7, 8, 12, 14, and 16. These were the peaks most consistently seen in the spectra.

Comparison of the harmonic levels is facilitated by non-dimensionalizing the frequency axis using the Strouhal number, as defined above. For the four speeds at throttle setting A, the peak values at the above harmonics were extracted from each of the spectra and plotted together in Figure 4.13. Similar plots were prepared for the other three throttle settings and are included in Appendix D.

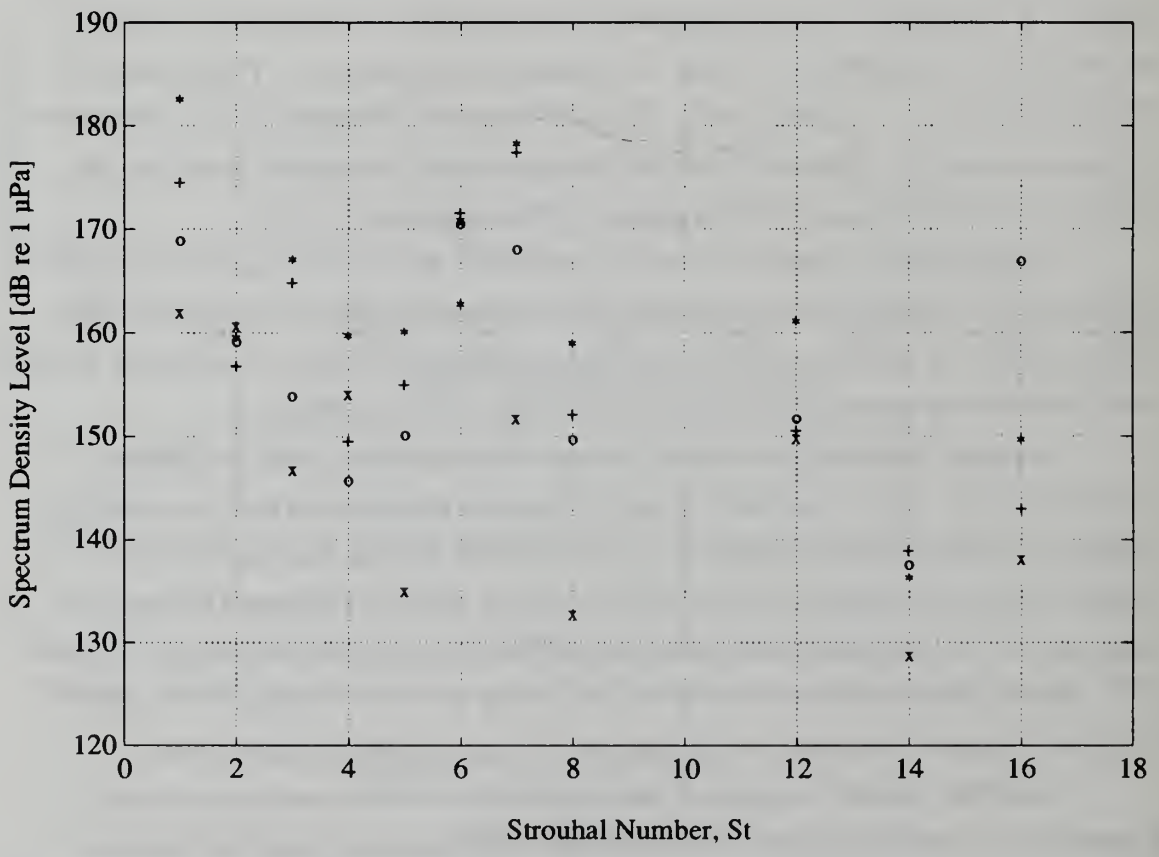

Figure 4.13. Tonal Noise Levels, High Throttle, Varying Speed
(* : 100% Speed, + : 75% Speed, o : 50% Speed, x : 25% Speed)

Each of the four sets of results show that the shaft tone level is strongly dependent on the rotational speed. The level of the shaft tone was increased by just over 20 dB going from 25% speed to 100% speed, except in the case of the lowest throttle settings where the increase in noise level was not as substantial. Doubling the shaft speed from 25% to 50% or from 50% to 100% results in an increase in the shaft tone level by an average of about 7 dB and 13 dB, respectively.

A similar dependence is found in the third, fifth, seventh, and eight harmonics. In order to illustrate this dependence, the harmonic levels for the shaft and blade passage frequencies, as well as the third and fifth harmonics of shaft frequency, are plotted against pump speed in Figure 4.14. The curves represent best-fit second order polynomials (with linear term forced to zero) for harmonic sound pressure dependence on pump speed. Such a relationship is expected when the mass reactance term in Equation 3.6 is negligible compared with the inlet and exit impedances. Note that the curves appear biased toward the higher speed data points. This is a result of the logarithmic scale on the ordinate.

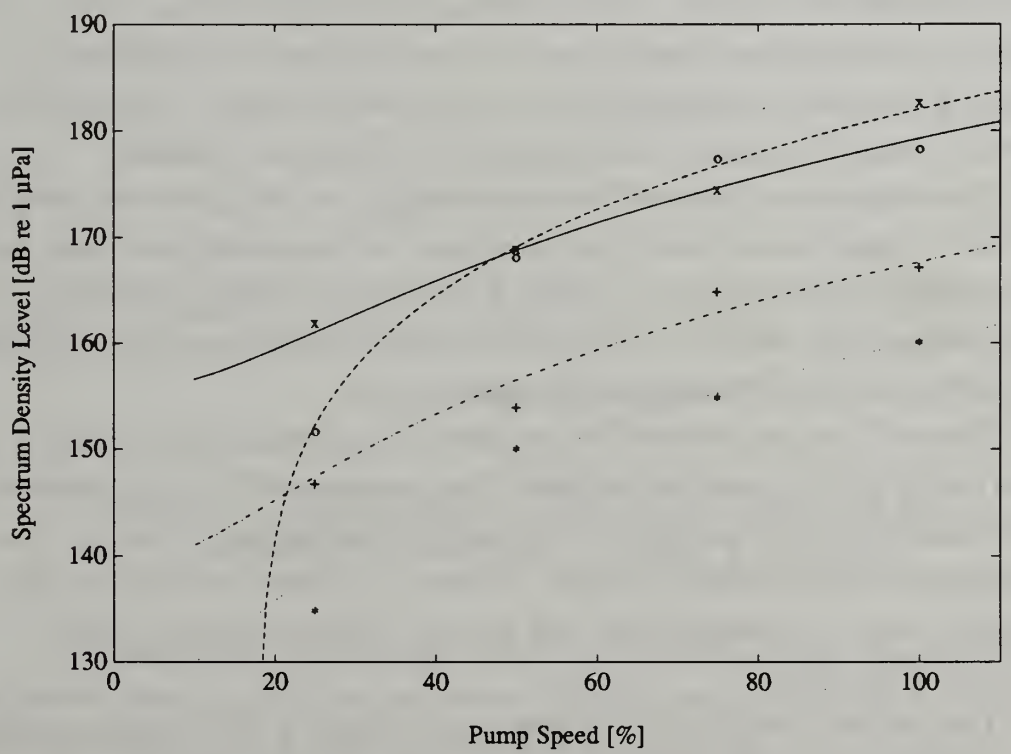

Figure 4.14. Variation of Selected Tonal Noise Levels with Pump Speed
(— —, x : f_{sh}; — · —, + : $3\times f_{sh}$; · · · ·, * : $5\times f_{sh}$; ——, o : f_{bp})

The second, fourth, sixth, and higher harmonic levels did not show any trends. It is possible that the Fourier coefficients for the spatial pressure distribution were lower for these harmonics and the noise levels were thus dominated by some other frequency-dependent phenomenon, but since the average levels of these harmonic tones are not lower than the other harmonics, this explanation is not entirely consistent. More studies are required to satisfactorily explain these observations.

In summary, the harmonic noise produced by the pump does appear to be dependent on the rotational speed. For the shaft and blade passage tones as well as the 3rd, 5th, and 8th harmonics, the coupling between pump speed and harmonic levels appears to be very strong. For the other harmonics, pump noise levels did not correlate with pump speed.

4.4.4. The Effects of Flow Rate on Harmonic Noise Generation

For a given rotational speed, the model predicts that the amplitudes of the tones in the inlet sound spectrum are a function of the combined effect of the shape of the geometry function and the shape of the exit pressure distribution function. The pressure distribution coefficients have already been discussed. In general, the coefficients maintain the same relative amplitudes from one flow rate to the next. This is a result of the constant shape of the pressure distribution for all operational conditions.

The magnitudes of the coefficients scale roughly with the square root of the flow rate. This is a phenomenon found in this pump only. As has already been stated, the pressure distribution in conventional designs is usually more strongly dependent on the pump operating point. Such was not the case with this design as the relative magnitudes of the coefficients were unchanged by the operating point.

Therefore, applying the model to the present pump characteristics, Equation 3.6 predicts that for a given speed, the harmonic sound pressures will scale approximately with the square root of the mass flow. The strength of each harmonic relative to the other harmonics should remain unchanged. In terms of spectrum density level ,this means that a factor of 4 increase in the flow rate will result in an increase in each harmonic level by 3 dB.

The harmonic levels for the four flow rates examined at 100% speed are plotted together in Figure 4.15. Similar plots were prepared for 75% speed, 50% speed, and 25% speed and are included in Appendix D. Although in this case the frequencies are the same for each harmonic on the plot, the Strouhal number is still used to facilitate the description of the results.

With reference to Figure 4.15 and to the other plots in Appendix D, it is clear that for most of the harmonics, the sound levels change very little for different flow rates. This is the result predicted by the model. From the highest to lowest flow cases, the flow rate was only changed by a factor of four. As such, the model predicts a 3 dB difference in spectrum density level between these extremes which is consistent with the data at about half of the harmonics.

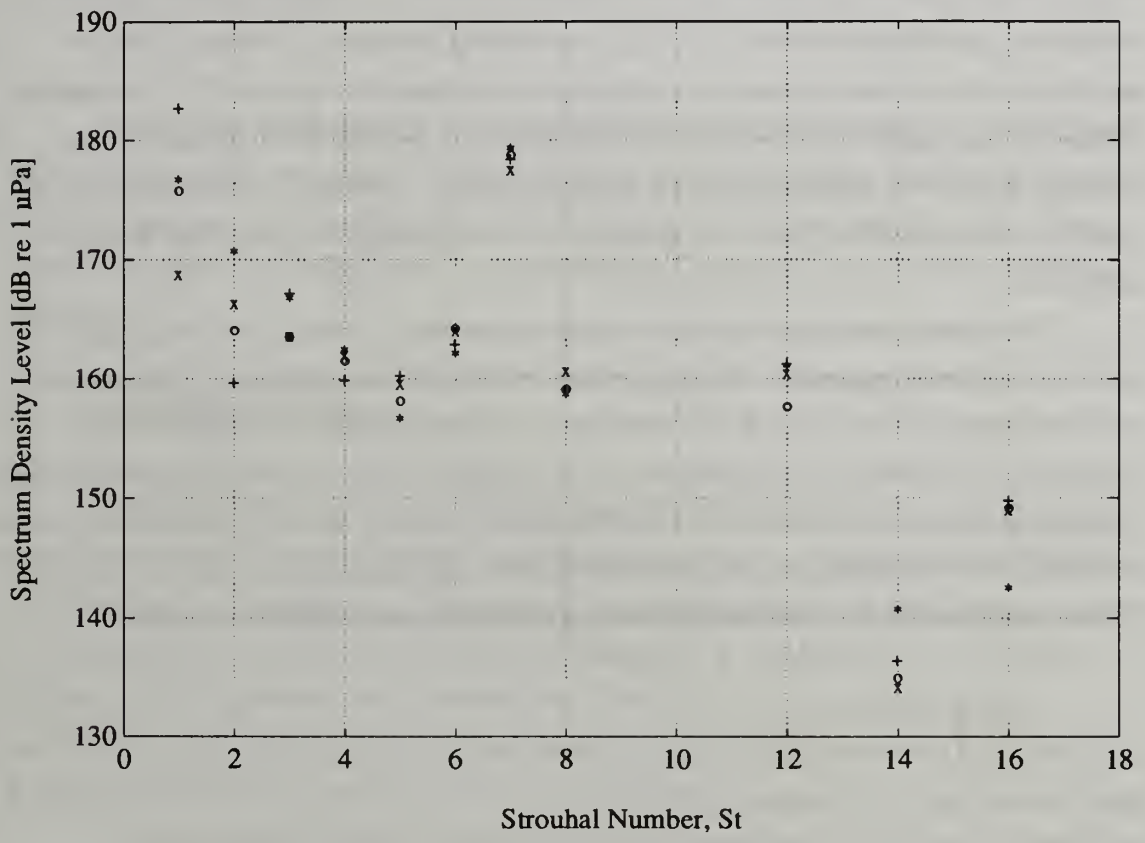

Figure 4.15. Tonal Noise Levels, 100% Speed, Varying Flow Rate
(* : 480 GPM, + : 314 GPM, o : 210 GPM, x : 126 GPM)

The data matches the model particularly well at blade passage frequency for all four speeds. In no instance is the maximum difference between harmonic levels greater than 15 dB and in all but five of the 44 harmonics analyzed, the difference between extreme values is well under 10 dB. Also, note the model also correctly predicts that the relative amplitude of the harmonics should remain about the same and this assertion is

also supported by the data. There is a noticeable trend in the spectrum density levels from one harmonic to the next and this trend is about same for all flow rates.

Lastly, it would be interesting to compare the relative strength of each harmonic with those predicted by the model, but this was not feasible for this project. If the pump impeller is assumed to be well designed such that the blades are all identical and perfectly spaced, then the area function will have non-zero components, A_m, only for m = 7, 14, 21, ...etc. Since each sound pressure component is a function of the product of the area coefficients and the pressure distribution coefficient, β_n, estimates of the pressure distribution coefficients for n = 7, 14, 21, ...etc would be needed. Discrete Fourier transforms only produce expansion coefficients for values of n up to half of the number of known data points. This means that if we desired to predict the first three or four harmonic levels, we would need 42 or 56 pressure taps. With only twelve pressure taps there is no way to predict the sound pressure at blade passage frequency nor any of its harmonics.

What about the shaft frequency and its harmonics? Clearly there are tones produced at these frequencies, but the problem which inhibits prediction of these tones with the current model is a lack of a satisfactory method to quantify impeller non-uniformities such that an area function can be estimated. One can see the potential utility of computational fluid dynamics (CFD) to predict the affects of small disturbances on the flow field. This information could be used to better estimate the area function and its Fourier components, but such an undertaking is beyond the scope of this project.

5. The Modified Pump Acoustics Facility

In order to determine the validity of the theoretical model proposed in Chapter 3, an experimental rig was required which could be used to house the centrifugal pump and in which various pressure distributions could be imposed on the impeller exit. This chapter describes the design goals and methodology, and a discussion of the modified pump loop.

5.1. Vaned Diffuser Design

The initial attempts to design a test apparatus for the above purposes involved a more "conventional" pump diffuser which would produce a circumferentially uniform static pressure at impeller exit. Because the flow must be removed from the pump volute to the exit piping through a finite number of passages, it was impossible to create a diffuser without geometric non-uniformities. The idea was to isolate these non-uniformities such that any pressure disturbances created in the flow were far-removed from the impeller exit space and would be satisfactorily attenuated at impeller exit radius.

A large, parallel-walled, vaneless space was considered. This would allow flow velocities to decrease significantly before encountering obstructions which might result in pressure perturbations. By decreasing the dynamic head of the flow, the magnitude of any such perturbations would be lessened and their effects on the impeller exit conditions minimized

Simple inviscid flow analysis using continuity and conservation of angular momentum shows that the mean flow velocity decreases linearly with radius. To decrease the flow velocity to a nominal level of 10% of the impeller exit velocity, a diffuser with a diameter of over 8 feet was required. The diffusion process could be achieved in a much shorter distance by using vanes, or foils. The vanes direct the flow

toward the radial direction which removes some of the angular momentum in the flow and decreases the flow velocity in a much shorter distance.

The design goal, then, was to create a large, parallel-walled, vane-island diffuser which would allow a slow, controlled diffusion of the flow such that disturbances in the flow were minimized and far removed the impeller. As an initial step, the vanes were designed as triangular wedges. The variables to be optimized were the number of vanes, the leading edge radius, the chord length, the wedge angle, and the angle of attack. These parameters determined the angle of divergence in the flow passage and the rate of diffusion. A simple program was written to select the optimal set of variables to achieved the desired diffusion angle for a fixed inlet and exit radius. The optimal angle of divergence for a two dimensional diffuser has been empirically determined to be about 6°; the optimal ratio of passage length to throat area is about four.

After the completion of the initial studies, it was decided to abandon the design due to difficulties caused by the high swirl condition of the pump. The exit flow angle was such that stall would occur within a small distance from the impeller exit. This phenomenon was first explained by Jansen[30] in 1964 using integral boundary layer analysis. Boundary layers grow on the diffuser walls, thus slowing the flow near the walls. There is a uniform negative radial pressure gradient across the channel. Because of the relatively low radial velocity of the flow (compared to the tangential velocity), the flow in the boundary layer does not have sufficient radial momentum to overcome this pressure gradient. This condition results in reverse flow.

The reverse flow condition can result in rotating stall and flow instability. Jansen correlated the range of stable flow with Reynold's number and exit flow angle. For this pump, with a Reynold's number based on impeller radius of about 2×10^6 and a flow angle of 85° at exit, the flow is predicted to become unstable at a radial distance of less than 2 inches from the impeller. In order to avoid this condition, vanes would have to be placed in the diffuser at a radius inside that which marks the onset of the instability. Moreover, the high swirl could not be suitably removed from the flow with a single row of diffuser blades; a cascade would be required to redirect the flow with enough radial momentum to avoid reverse flow.

Given the difficulties presented and the limited time frame of the project, it was determined that design closure could not be reached in the time allotted. An alternate approach was required which could circumvent the problems caused by the high swirl operating condition of the pump impeller.

5.2. Experimental Diffuser Design

Once it was determined that a suitable vaned diffuser could not be designed without great difficulty, it was necessary to design a completely different type of experimental diffuser. The new goal was to create a reservoir, or dump diffuser, into which the flow from the impeller would be discharged. If the diffuser were large enough, non-uniformities caused by the collection process would not affect the flow from the impeller. The impeller discharge flow would behave as a two dimensional jet exiting into a large dead end channel. The flow field for such a situation is well established from turbulent jet theory and empirical observations.[31]

The location of side and end walls determine jet spreading and the rate of velocity decay in the turbulent region. The velocity in the turbulent region decays with distance from the source and, ideally, the end walls could be placed far enough away from the impeller such that the flow would behave as a jet flowing into an infinite medium. In practice, such a design was not feasible based upon size constraints and the end wall location was fixed based on size limitations in the test cell itself.

The location of the side walls also affects the flow pattern. Although the turbulent core velocity decays more quickly when the side walls are closer together (due to the increased shear flow in the recirculating region), it was felt that such recirculation could result in stall and separation problems similar to those predicted by the vaned diffuser design. The side walls were thus located such that they would not interfere with the spreading of the turbulent region.

At a distance of 30 inches from the origin of the jet, the radial component of the core velocity in the jet was predicted to be on the order of 25% of the initial radial velocity discharged by the impeller. It is this outward velocity component which determines the magnitude of the pressure disturbance created by the end wall obstruction. Since the radial component of the velocity was small compared to the total flow velocity to begin with, this appeared to be reasonable estimate of the size of diffuser required to satisfy the objectives set forth.

5.2.1. The Acoustic Pump Diffuser

The proposed fluid design presented several mechanical problems which had to be overcome. The first problem was caused by the fact that the diffuser was going to have an operating pressure in excess of 100 psi. The diffuser was, in effect, a pressure vessel which required significant mechanical design in order to ensure that it was structurally sound.

The second problem involved the design of a collector. Ideally, flow would be removed from the diffuser uniformly from around its periphery. This would eliminate circumferential non-uniformities from the flow field. In practice, of course, the flow had to be collected at a finite number of points. Because the impeller had seven blades, we wanted to avoid spatial pressure distributions with non-zero seventh Fourier components. By making the disturbance pattern with a spatial period less than $2\pi/7$, it was ensured that the pressure disturbances caused by these non-uniformities would not have a seventh spatial component. The minimum number of collection points required to accomplish this was eight.

The resulting design is shown in its plan view in figure 5.1. The three sectional views marked in Figure 5.1 are shown in Figures 5.2 through 5.5. The main body of the chamber is a cylindrical shell with two flat heads. Eight conical discharges are evenly spaced around the periphery of the shell to collect the flow. A 23 inch I.D. well was inserted through the top head which houses and supports the pump. The pump impeller is centered between the two heads. A smaller 12 in I.D. draft tube penetrates the lower head to accommodate the 4 in. inlet pipe. The entire chamber was constructed of carbon steel in accordance with A.S.M.E. Code and painted with two coats of Navy epoxy to prevent corrosion.

Again, the size of the chamber was limited by the constraints of the acoustic test cell in the M.I.T. Gas Turbine Laboratory and by economic considerations. The inner diameter of the shell is 56 inches with an inside height of 36 inches between heads. The exit nozzles are 18 in. in diameter centered on the cylinder wall, converging to 1-1/2" hose couplings at exit. The angle of convergence is 30 degrees total.

The top and bottom heads were originally designed as 2:1 ellipsoidal heads, which is an inherently stronger geometry. The design was modified to the flat heads in order to facilitate manufacturing and expedite delivery. The bending moments produced in the heads at the inner and outer radii were much larger than those found in the original design, thereby increasing the thickness of plate required. As such, the thickness of the top and bottom heads are 4 in. and 3.5 in., respectively.

The bottom head is flanged as shown and secured by 40 3/4" bolts. This allows the entire lower assembly to be lowered for access to the inside of the chamber. Raising and lowering of the cover is accomplished using four "come-along" devices attached between the upper and lower lifting brackets as shown in Figures 5.3 and 5.4. The total allowable travel is such that the head may be lowered to the cell floor without disconnecting the lift devices.

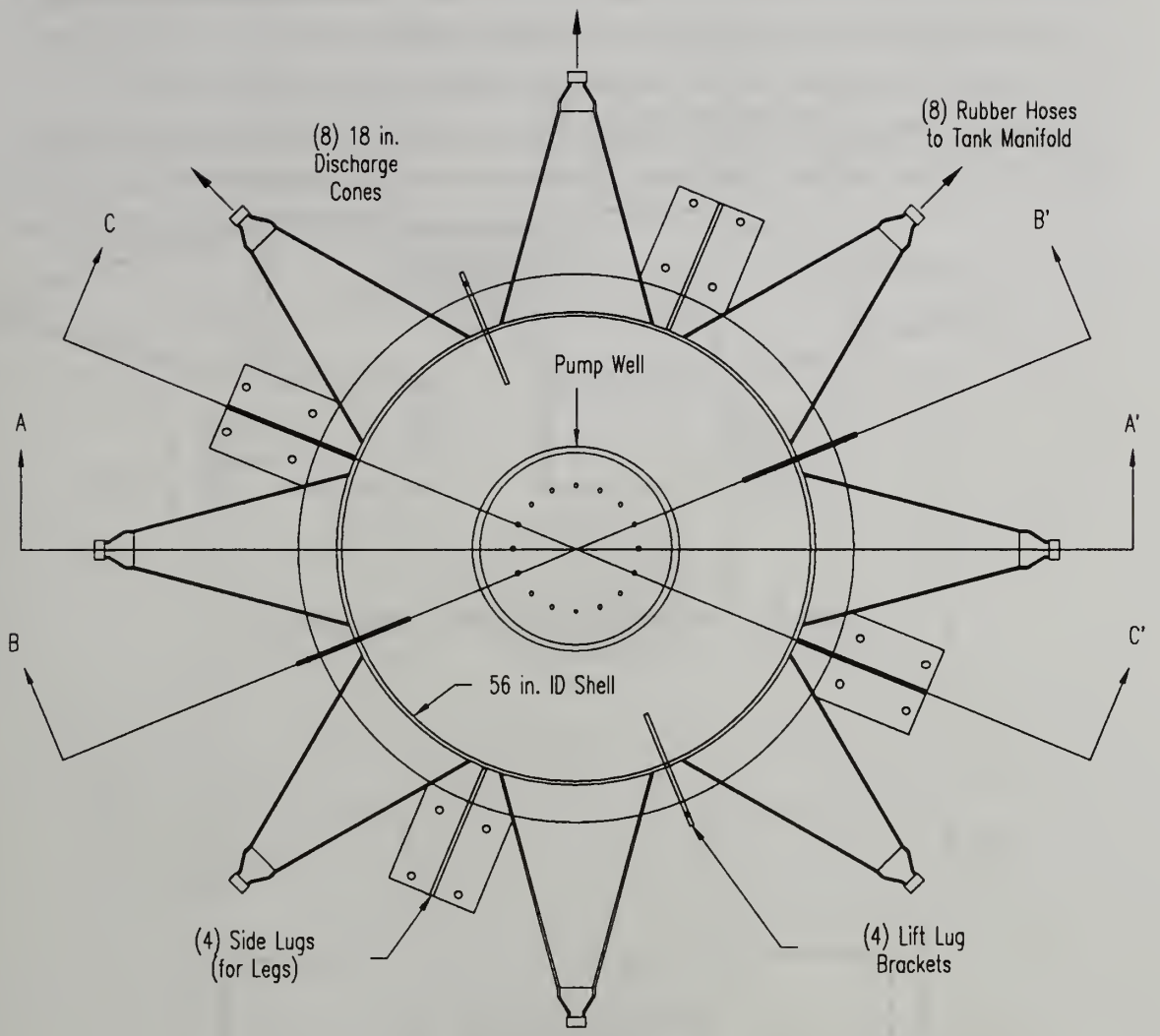

Figure 5.1. Acoustic Pump Diffuser, Top View

Raising of the lower assembly into place requires precision accuracy. The clearance between the rotating impeller inlet and the inlet flange is 0.021 inches. To ensure proper alignment of the impeller and inlet piping, the following measures were taken: 1) The upper flange, or pump flange, was machined to hold the clearance between the flange and the pump mount within 0.005 in. to 0.010 in., 2) the main flange pilot diameter was machined with a 0.015 in. tolerance above the clear bore diameter on the shell flange, and 3) the initial line-up was accomplished using a tightly fitting plug and two dowel pins were inserted on the main flange to mark the proper alignment. The dowels allowed raising of the lower assembly without removing the pump each time.

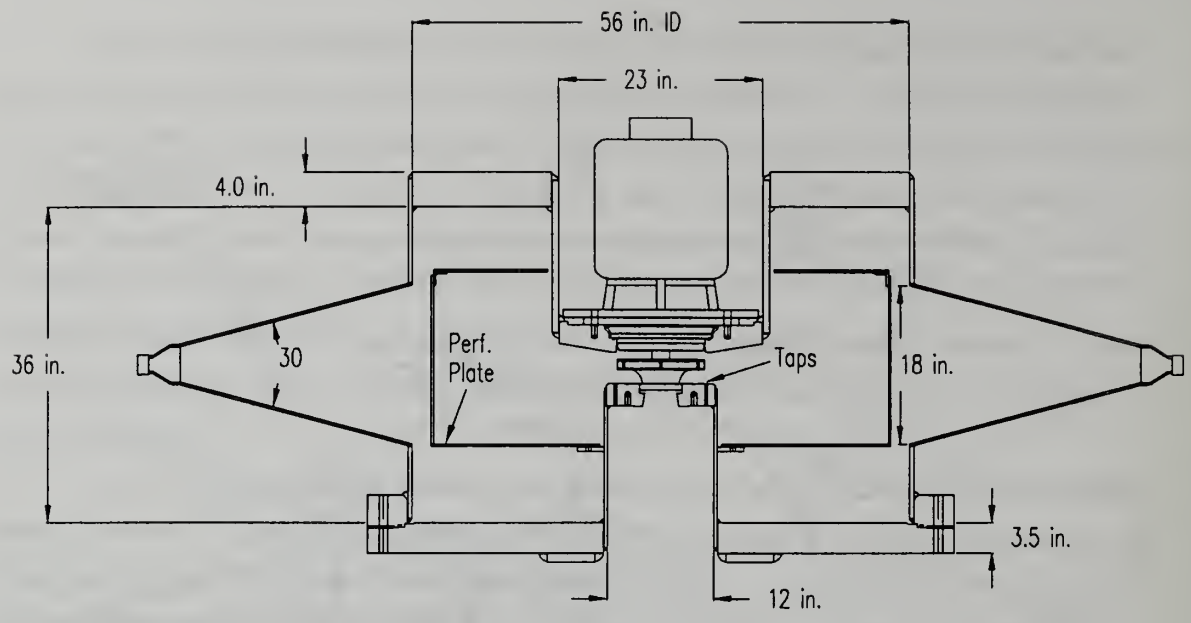

Figure 5.2. Acoustic Pump Diffuser, Section A-A'

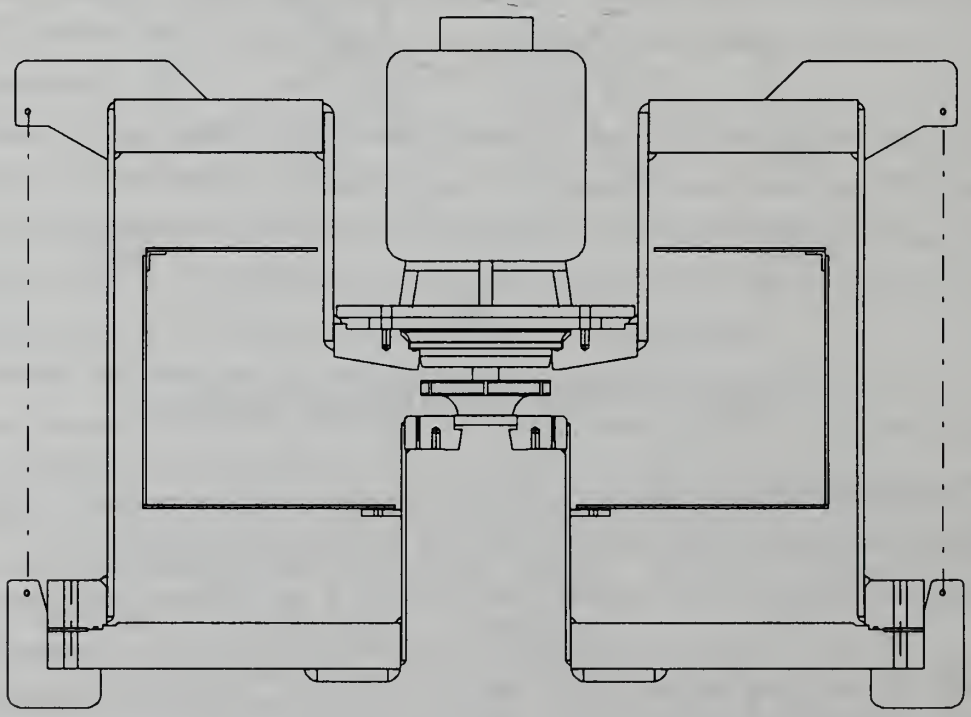

Figure 5.3. Acoustic Pump Diffuser, Section B-B'

The pump flange was machined from a 3.5 in. thick plate. The upper surface was drilled and tapped for the studs which hold the pump in place. The bottom surface of the

flange was tapered as seen in Figure 5.2 to remain clear of the 2-D jet pattern exiting the pump impeller. A 10.5 in. O-ring provides the seal between the flange and the pump.

The lower reverse flange was machined from 2-13/16 in. plate. The inner surface duplicates the geometry of the original pump casing. The lower surface was provided with 8 blind tap holes to support a standard 4 in. pipe flange and has 24 1/8" NPT holes on a 10.25 in. diameter for static pressure taps.

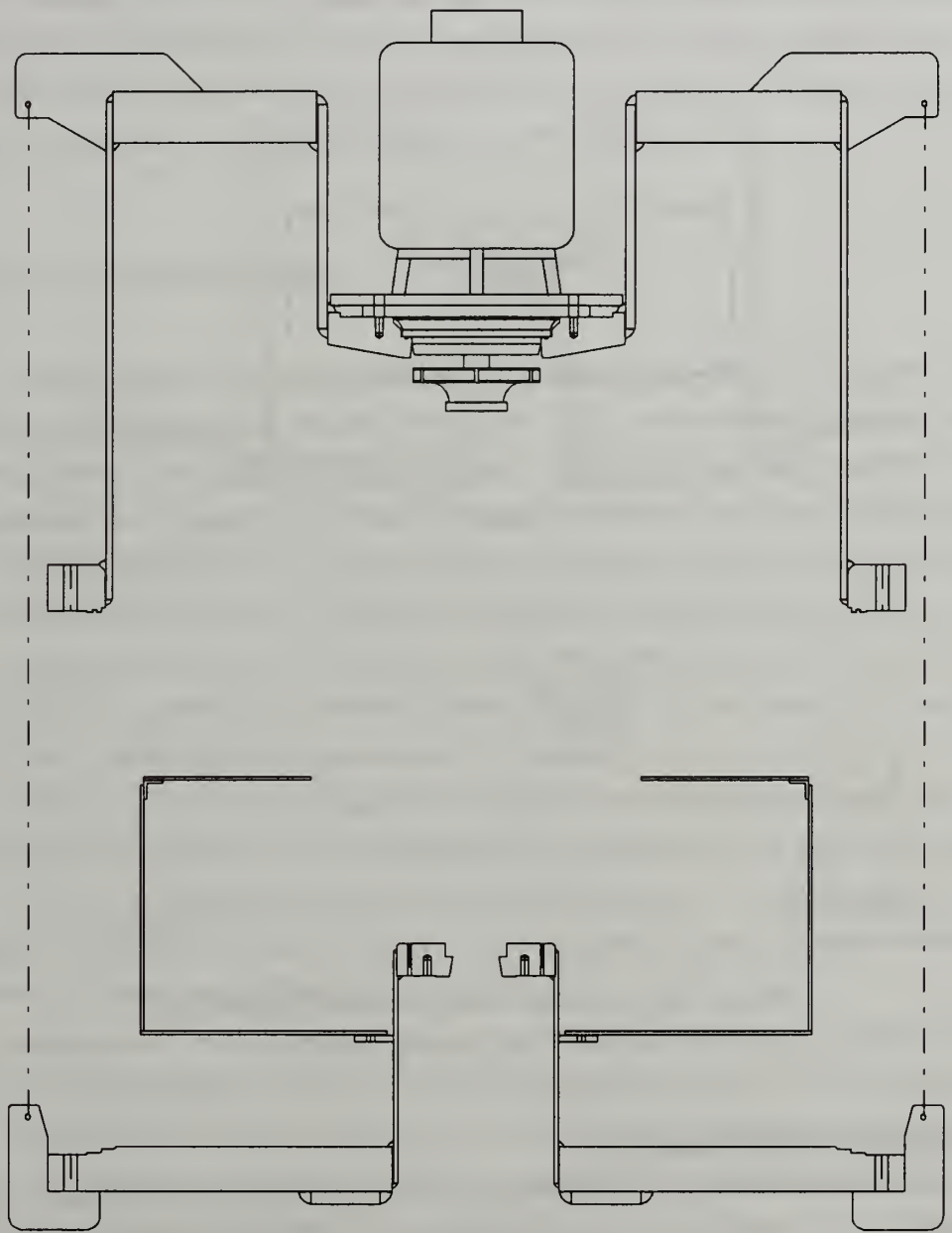

Figure 5.4. Acoustic Pump Diffuser, Section B-B' (cover down)

The top head was drilled and tapped for a 3/4 in. vent to facilitate de-aerating. The bottom head has two 2" NPT instrument connections and one 1-1/2" NPT drain. The instrument connections were not used for this project.

The pump diffuser was mounted on four 10" x 39# H-beam legs, 56 inches in length. The legs were connected to four side lug support assemblies built on to the outer shell between adjacent exit cones. Each leg was welded to a 18" x 18" square plate which served to distribute the load on the test cell floor.

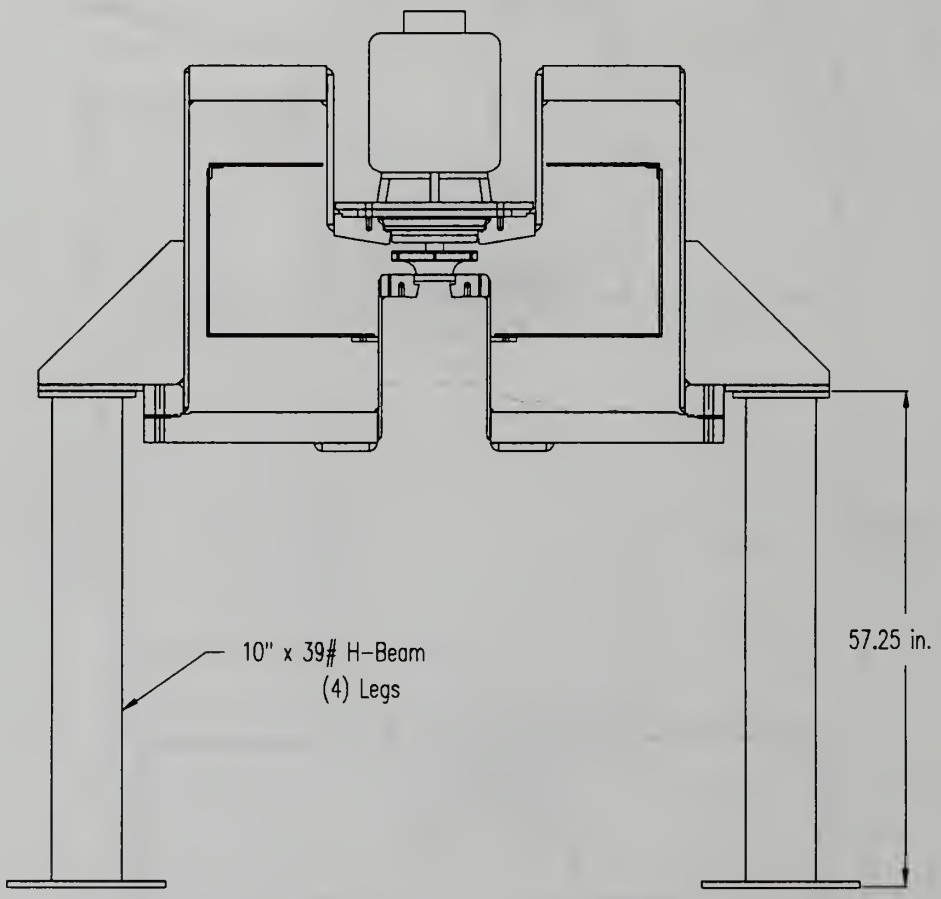

Figure 5.5. Acoustic Pump Diffuser, Section C-C'

5.2.2. Perforated Basket Assembly

Provisions were made for a three-layer basket assembly. The outermost basket is shown in Figures 4.3. The assembly is comprised of 1/4" thick perforated stainless steel plate. The perforated plate has 3/8" diameter holes on 9/16" staggered centers. The open area is 40% of total. The two inner cylinders were 1/8" thick with the same open area.

The perforated plates were built to serve as a mechanical support for screen or filter material. There were three possible uses for screen in the assembly: 1) to isolate the impeller from disturbances caused by the shell area between discharge cones, 2) to create artificial pressure disturbances through non-uniform lining of basket assembly, and 3) to create an additional pressure drop in the system.

The basket assembly is supported by a 1/4 in. thick mounting plate welded to the outside diameter of the inlet pipe draft tube. The lower head of the basket is bolted to the mounting plate with eight 5/8 in. bolts. The intermediate cylinder is bolted to the outermost assembly, and the innermost cylinder was designed to fit snugly over the inlet draft tube unsupported. The entire assembly is removable.

5.3. Pump Loop Modifications

The replacement of the original pump casing with the diffuser described above required modifications to the original pump loop. The most obvious impact was on the discharge piping. The dump diffuser had eight 1.5 in. exit ports from which the flow had to be collected and returned to the tank. In keeping with the stated goal of maintaining an azimuthally uniform flow, it was desirable to maintain an equal flow resistance in each of the parallel exit lines. This was accomplished by cutting eight identical 1.5" I.D. rubber hoses (the same type of hoses used for throttling in the original configuration). The hoses were attached to long shank nipples on the end of each cone by two stainless steel bands. Each hose was approximately 38 feet long.

The eight exit hoses terminated in a manifold on the 600 gallon tank. The manifold, shown in figure 5.6, was fabricated from a standard 12 in. pipe blind flange. Eight 1.5 in. holes were drilled through the blind flange and 1.5 in. N.P.T. hose couplings were welded around the holes on the top of the flange. The hoses attached to long shank nipples threaded into the hose couplings.

Replacement of the discharge piping also eliminated the in-line throttle section used in the original design. The throttle hose represented the main flow resistance in the loop. Although the same hose type of size was used to collect the flow from the acoustic diffuser, the pressure drop was predicted to be much less because the flow is divided equally between the eight hoses. The pressure drop, ΔP, across a section of piping is given by

$$\Delta P \propto \frac{fLQ^2}{d^5}$$

where f is the friction factor of the piping, L is the length of the piping, Q is the volumetric flow rate, and d is the pipe diameter.

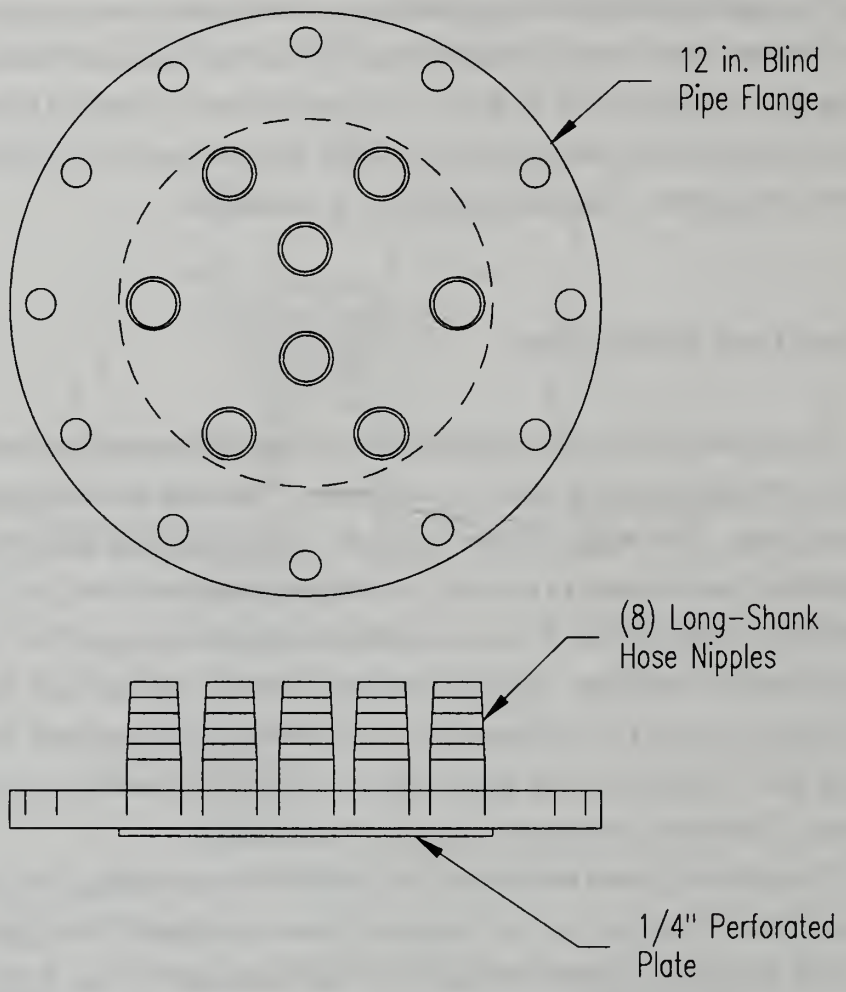

Figure 5.6. Flow Collection Manifold

If the eight hoses have length approximately equal to that of the throttle hose, the only variable which changes from the original throttle to the new discharge configuration is the flow rate, Q. For the same total flow rate, the flow rate through the individual hoses is decreased by a factor of eight from the throttle hose in the initial configuration. This means that the expected pressure drop will be decreased by a factor of 64.

Screens and filters could be used to provide additional flow resistance. A 12 inch diameter perforated plate was tack-welded to the underside of the flange and fit into the

pipe section at the top of the tank as shown in Figure 5.6. The perforated plate was the of same 1/4" thick material used for the basket assembly used in the diffuser. This provided a mechanical support for the screens, and since the manifold was at the highest point in the system, allowed changing the screens without draining the loop.

5.4. Acoustic Considerations

In designing the modifications to the pump loop, one of the goals was to duplicate, as closely as possible, the acoustic properties of the loop outside of the diffuser. This would facilitate comparisons between the noise spectra produced by each pump configuration by minimizing the influence of outside factors. The following is a brief summary of the steps taken to ensure that acoustic conditions were not appreciably altered from the original conditions.

5.4.1. Acoustic Attenuation

The total length of the four inch rubber hose was kept constant to maintain the same sound attenuation. All three 100 foot lengths were connected in series between the tank and the impeller inlet. The flow meter was located between the first two lengths of hose and the upstream test section was positioned between the second two lengths. Thus, the far upstream measurements were taken at the same location relative to the pump.

5.4.2. Reflection and Standing Waves

The overall length of steel piping and the position of the microphones relative to the reflection boundary was kept constant to within about 1/2 inch from the original configuration. This was done in an effort to duplicate as closely as possible the standing wave pattern encountered in the volute arrangement. Figure 5.7 shows the inlet piping dimensions for modified configuration. It can be compared with the original inlet piping configuration shown in Figure 2.11.

5.4.3. De-aeration

The modifications to the pump loop made de-aerating efforts more difficult than in the original configuration. The sensitivity of the system to even small quantities of air has already been discussed. Although air vents were installed on both the 600 gallon supply tank and the pump diffuser, there was no way to ensure that the system was free of significant quantities of air.

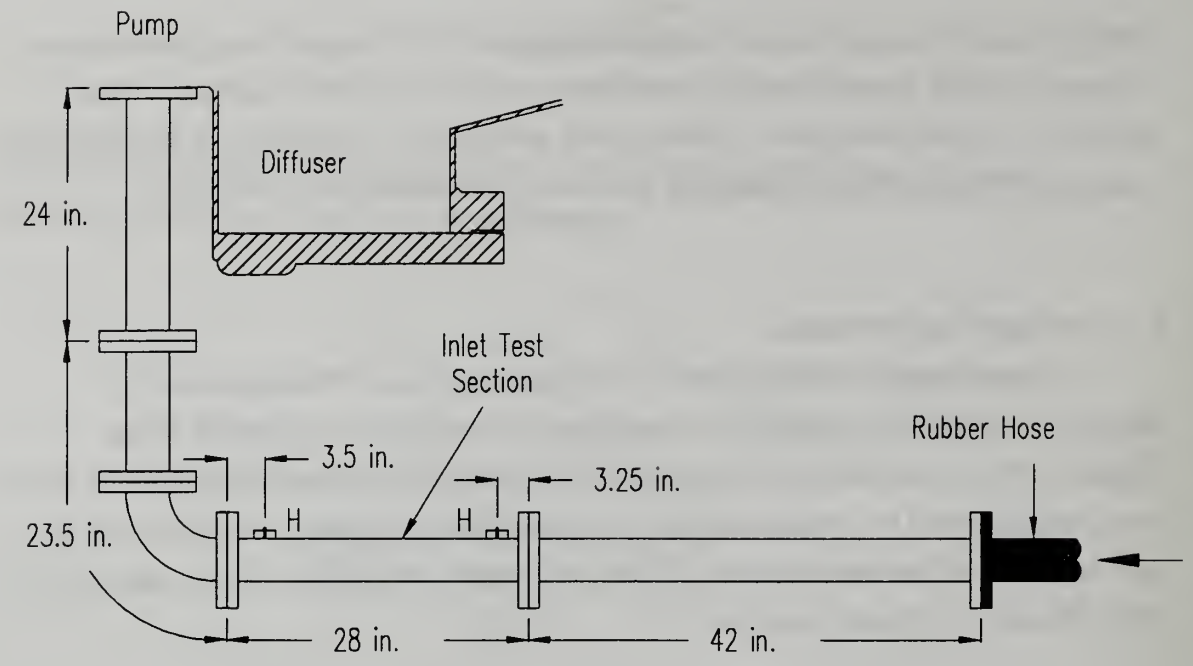

Figure 5.7. Inlet Piping Dimensions for the Modified Pump Loop

Efforts were made to de-aerate by drawing a vacuum on the system as was done in the initial test loop, but the addition of over 300 feet of rubber hose caused great difficulty with this procedure. There were no valves installed on the tank manifold to isolate the hoses and, therefore, eliminate their compliance. When a vacuum was drawn on the system, large quantities of water were pulled from the system as the hoses collapsed.

In spite of the difficulties, every effort was made to remove air from the system prior to taking measurements, but success in this area was questionable. An obvious solution to the problem is to use re-enforced hoses (like the 4 in. Flexwing hose) which could withstand a vacuum. Another solution would be to install eight isolation valves between the tank manifold and the rubber hoses, but the close proximity of the hose couplings to one another added complications to the problem and a lack of time prevented pursuing a solution to the problem.

6. Experimental Diffuser Studies

Before discussing the results of the experiments using the modified pump, it is first instructive to discuss some of the acoustic phenomena introduced with the changes to the pump diffuser. An understanding of the various phenomena involved will aid in interpretation of the results.

6.1. Acoustic Phenomena Associated with the Diffuser

6.1.1. Natural Modes of the Diffuser

Because the modified diffuser has inner dimensions which are of the same order as the wavelength of sound, the natural acoustic modes of the diffuser are significant. Theses modes are characterized by a standing wave pattern which exists across one of its principle dimensions. These modes were not significant with the original volute because the dimensions of the volute were much smaller and the wavelengths of sound associated with such a standing wave correspond to frequencies much higher than the range of interest.

The first mode is characterized by the presence of a standing wave with a positive maximum pressure amplitude on one end and a negative maximum on the other end. The characteristic wave mode between parallel plates such as the axial mode in the cylindrical diffuser, is developed when the distance between the plates, h, is equal to a half wavelength. The fundamental frequency is given by:

$$f_1 = \frac{c}{\lambda_1} = \frac{c}{2h}$$

For a cylinder, the first radial mode is characterized by a wavelength equal to 1.7 times the diameter, d. The dimensions of the acoustic diffuser yield axial and radial fundamental frequencies of 820 Hz and 620 Hz, respectively.

6.1.2. The Diffuser as a Helmholtz Resonator

At sufficiently low frequencies, the diffuser acts like a mass-spring oscillator. The water in the impeller passages acts like a mass slug, while the water in the diffuser corresponds to the spring. (The impeller passages and diffuser correspond to the neck and bottle of the standard Helmholtz resonator.) There are tones associated with this mass-spring system which are excited by pressure fluctuations at the impeller inlet. The tones are the result of resonant oscillations of the fluid within the impeller blade passages superposed on the mean flow. The resonance frequency is given by the following:

$$f = \frac{c_0}{2\pi}\sqrt{A/\ell V}$$

where A is the discharge area of the impeller, ℓ is the length of the impeller passages, and V is the volume of water in the tank. Approximating the length of the impeller passage by the impeller radius, the resonance frequency is approximately 70 Hz. This number is highly dependent upon the content of air in the tank, as just a small quantity of air in the tank will lower the spring constant and thereby lower the resonance frequency.

6.1.3. Sound/Flow Interaction

It will be seen that for many of the noise spectra presented in this section, the shape of the noise spectrum has significant variations even between samples taken under very similar conditions. The content and location of air in the system may account for some of these variations. It can also be explained by the coupling of sound and fluid flow- specifically, the flow over any periodic disturbance such as can be found on the perforated basket assembly. This sound-flow interaction is extremely sensitive to flow speeds. The following paragraphs explain the origin of such a coupling and estimate their effects on the acoustic spectra presented.

Consider a traveling wave moving over a uniform boundary. The equation describing the pressure field is given by

$$p(x,t) = Ae^{ikx-i\omega t}$$

If the boundary is has a periodic perturbation (such as holes or raised surfaces), then the amplitude of the pressure field becomes a function of position:

$$p(x,t) = A(x)e^{ikx-i\omega t}$$

and must be periodic such that it may be expressed by a Fourier series as follows:

$$A(x) = \sum_{m=-\infty}^{\infty} B_m e^{imKx}$$

where $K = 2\pi/L$

The sound field is then given by

$$p(x,t) = \sum_{m=-\infty}^{\infty} B_m e^{imKx} e^{ikx-i\omega t}$$

The above equation shows that the pressure field is then a sum of partial waves

$$B_m e^{i(k+mK)x} e^{-i\omega t}$$

The phase velocity of each of these partial waves is given by

$$c_m = \frac{\omega}{(k+mK)} = \frac{\omega/k}{1+mK/k} = \frac{c_0}{1+m\lambda/L}$$

The partial wave speed , c_m, can be much lower than the characteristic speed of sound in the fluid, c_0, and can be equal to the mean flow speed, U. There is then a strong coupling between the mean flow and the acoustic wave and very strong tones can be produced.

Such a situation is possible inside the pump diffuser when one or more layers of the perforated basket assembly are in place. If we estimate the tangential component of velocity at the radial location of each perforated cylinder using conservation of angular momentum, the characteristic frequencies for flow across each of the inner, intermediate, and outer cylinders at 100% speed are estimated at 880 Hz, 360 Hz, and 220 Hz, respectively.

6.2 Test Conditions

In order to obtain information about the pump's performance in the acoustic diffuser, initial tests were run with the diffuser in its delivery configuration: with the outer basket and intermediate cylinder in place. Unless otherwise noted, all of the results reported in this chapter were recorded with the diffuser in this configuration. In addition to obtaining acoustic data, initial testing was required to establish the pump's operating characteristics in the diffuser as well as the characteristics of the modified pump loop. The initial observations are summarized in the paragraphs that follow.

6.2.1. Pump Loop Flow Resistance

Initial tests confirmed design predictions of the inherently low flow resistance in the loop. At full speed, the volumetric flow rate through the loop was above 500 GPM with very little pressure drop across the hoses. In order to increase flow resistance and lower the flow rate, 20 μm, sintered metal fiber filters were installed on the eight return lines on the tank manifold.

Initially, it appeared that the filters would provide an appropriate resistance for the loop; the full speed flow rate was about 400 GPM. However, despite the fact that the city water supply was passed through a 5 μm filter, it was found that small particles collected on the hose filters, further obstructing the flow and causing a slow, continuous decline in the flow rate. After several hours of operation, flow rates were reduced to 120 GPM at full speed.

The city water supply filter was changed and the loop refilled, but the same events occurred. Switching to 40 μm filters slowed down the rate of decrease in the flow, but still did not allow an acceptable equilibrium operating point to be reached. Better results were achieved using a single layer of thin wire screen as flow rates were nearly settled within the normal operating range of 350-400 GPM.

6.2.2. Static Pressure Distribution

The static pressure distribution at impeller exit was measured using the 24 pressure taps on the inlet reverse flange and the Scanivalve Pressure Measuring System described in section 2.4.2. Again, about 50 readings were taken at each port and an average and standard deviation calculated. Note that the measurements taken at the first and second ports are not considered very accurate due to the large change in pressure from the previous port, located at pump inlet. The large change in pressure required a longer transducer settling time prior to taking the measurement. This presented a

problem only when the pressure distribution was intentionally altered. In this case, the readings were obtained manually to ensure their validity.

The results indicate that the pressure distribution was uniform over all of the operating conditions of the pump in its initial configuration. The variation in average pressure between all ports was typically less than 0.1% of the total head rise of the pump. It was also noted that the standard deviations were much lower than those measured in the production volute. This indicates that temporal pressure fluctuations may have also decreased in this diffuser, although no other measurements were made to verify this assertion.

6.2.3. Loop Instability

Somewhat surprisingly, the low frequency instability (referred to in section 4.3.1), which was present in the original pump loop over all operating conditions, was not observed with the current configuration. The flow meter and pressure gages were very steady over the range of operating conditions imposed on the loop.

6.3. Results

Because of time constraints, it was not possible to fully investigate the theory described in Chapter 3. The results reported in this section are not complete and leave many questions unanswered. However, the studies do provide some insight into the acoustic performance of the pump diffuser and will serve as a baseline set of measurements for future studies and further analysis.

6.3.1. A Typical Noise Spectrum

Figure 6.1 presents a typical acoustic spectrum obtained with the experimental diffuser. Peaks corresponding to the shaft frequency tone and its harmonics are circled. The circled harmonics correspond to $n \times f_{sh}$ for n = 1, 2, 3, 4, 5, 6, 7, 8, 12, 14, and 16.

Notice that many of the shaft tones are not sharply defined as they were in the spectra of the production volute. In this particular example, the third, fourth and fifth harmonics were not even noticeable above the noise floor. The highest peak is associated with the sixth harmonic, which was the case in nearly all of the spectra obtained with the diffuser. It is noteworthy that the blade passage tone, which was so dominant in most of the spectra from the original pump configuration, is only a few dB above the noise floor

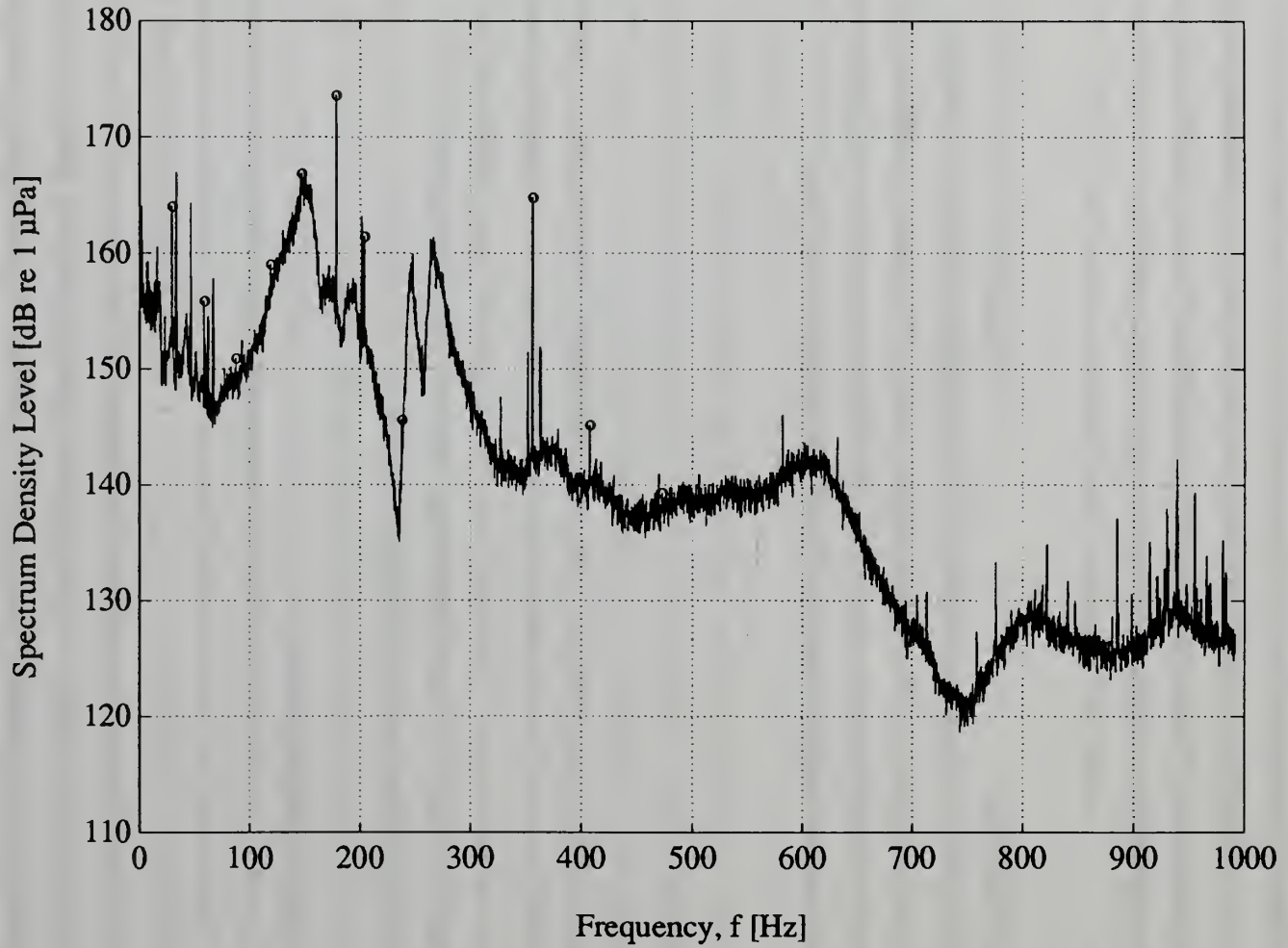

Figure 6.1. Typical Inlet Noise Spectrum, Experimental Diffuser (w/ basket), 100% Speed

in this configuration. This observation is, again, also true for most of the spectra taken with the diffuser in its delivery condition.

The spectrum is also characterized by large variations in the broadband noise level, particularly at frequencies below 400 Hz. There were several sharp drops in the broadband noise level, most notably at a frequency near 240 Hz. This is a common characteristic of nearly all of the spectra. Like the similar drop in the noise floor near 150 Hz on the volute spectra, this is attributed to air in the system.

6.3.2. Comparison of Acoustic Signatures of Diffuser and Original Volute

Comparisons between the noise spectra obtained from each of the two pump configurations were made on an equal speed, equal flow rate basis. Figure 6.2 shows one such comparison for 100% rotational speed and a flow rate of 333 GPM. Other examples are included in Appendix E. With reference to Figure 6.2 and the other figures in Appendix E, it is readily apparent, that the spectra are dominated by very different standing wave patterns. Over most of the frequency domain, the broadband noise level is actually higher in the experimental volute.

Harmonic noise levels were somewhat mixed. The diffuser generally produced lower tones at f_{sh}, f_{bp}, and the 2nd, 3rd, 8th, and 16th harmonics of f_{sh}. The diffuser consistently produced higher tones at the 5th, 6th, and 14th harmonics. In many cases, however, it appears that the higher tonal level is due more to the higher noise floor than to a sharp tone produced by the pump. (See, for example, the fifth harmonic in Figure E.2.

Lastly, it was noted that under nearly equal operating conditions, there was far more variation between measured spectra in the diffuser arrangement than in the initial configuration. That is, the results were much less repeatable using the experimental diffuser than they were with the original volute. It was hypothesized that this was the result of one or more of the acoustic phenomena described in section 6.1. Many of these phenomena are sensitive to fluid flow fields in the diffuser and it is likely that small changes in the flow field could result in easily discernible differences in the acoustic spectra. It is also likely that the air content of the pump loop was not as consistent due to the difficulties in de-aerating described in section 5.4.3.

In an attempt to isolate and identify some of the acoustic phenomena, the entire perforated plate assembly was removed from the diffuser. A single set of data was taken with the pump operating at full speed. The results are presented in Figure 6.3.

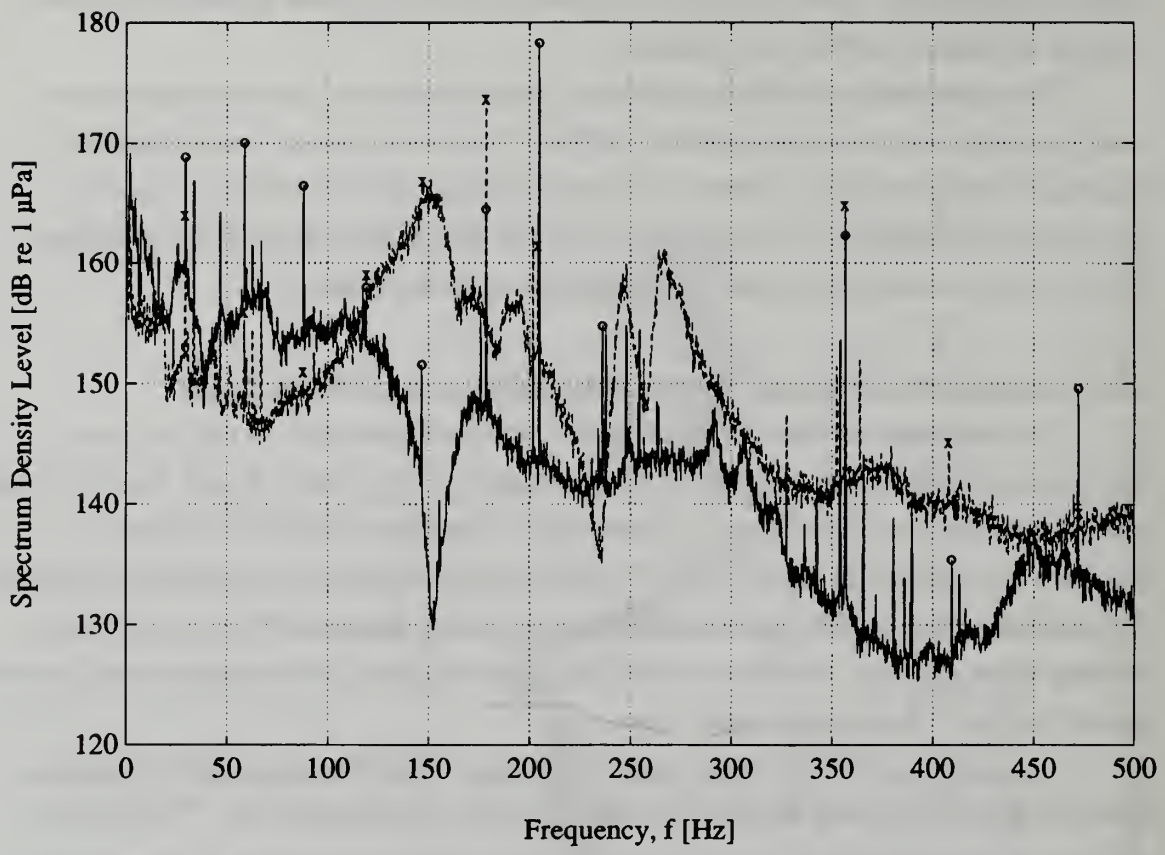

Figure 6.2. Comparison of Inlet Noise Spectra, Volute Pump and Experimental Diffuser (———, o : Volute; — —, x : Experimental Diffuser)

Comparing this figure with Figure 6.1 reveals only minor differences between the two cases. The differences are no greater than those observed between spectra obtained at nearly equal conditions. It is likely, then, that the outer two layers of the basket assembly were not the source of any extraneous noise measured at pump inlet.

6.3.3. Effects of Speed and Flow Rate Variations

As a means of better understanding the acoustic behavior of the pump in the test chamber, speed and flow rate were varied to determine their effect on the noise produced by the pump. The dependence of the acoustic spectra on each of these parameters could then be compared with their effects in the initial studies described in Chapter 4. The goal was to isolate the physical phenomena involved in the process to achieve a better understanding of how these parameters affect fluid noise generation.

The slowly increasing flow resistance due to particle build-up in the filters/throttles provided an opportunity to obtain data at several speed and flow rate

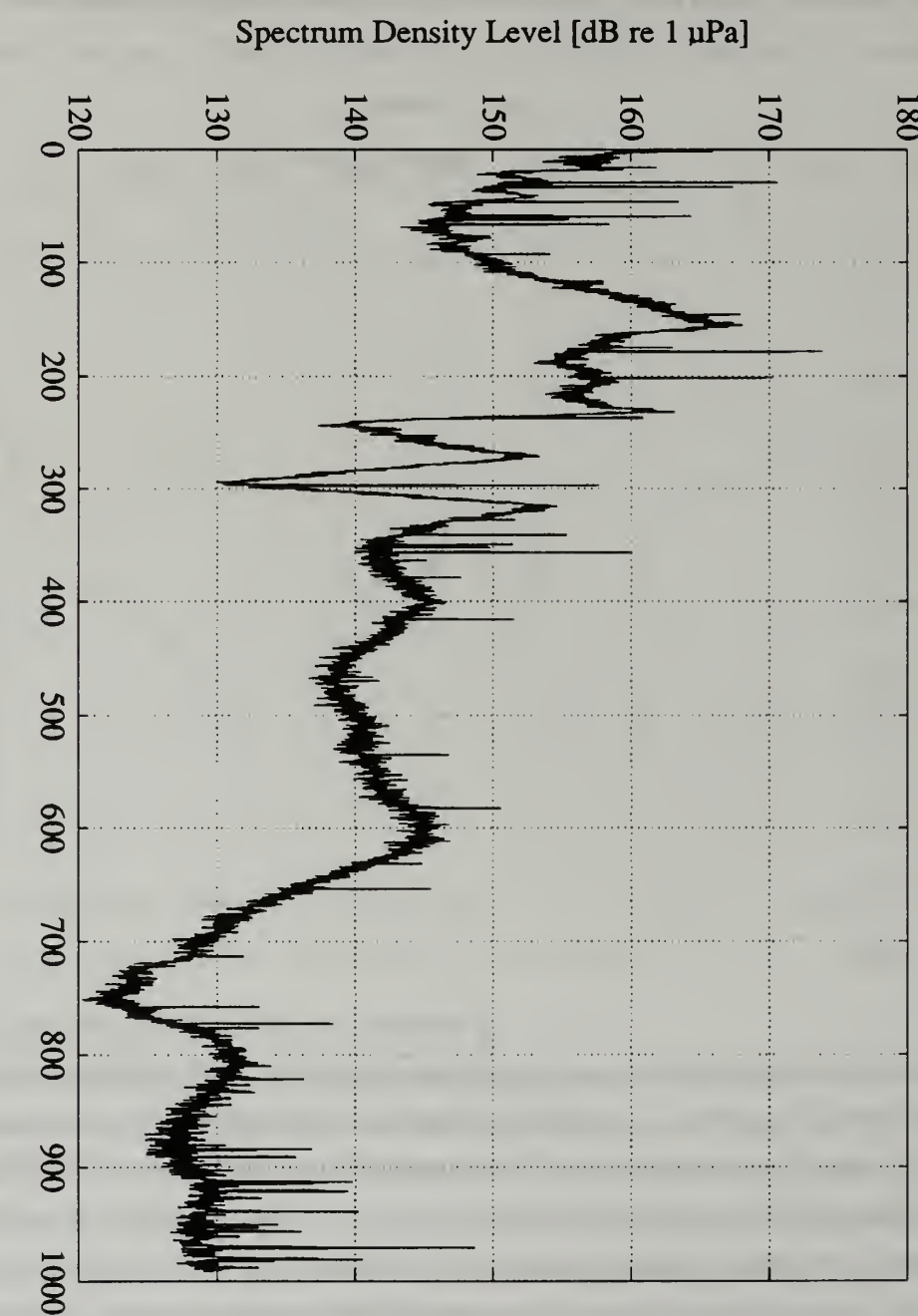

Figure 6.3. Inlet Noise Spectrum, Experimental Diffuser (w/o basket), 100% Speed

combinations. It was expected that both speed and operating point would affect the broadband noise signature, but would have little effect on the tonal noise.

Broadband noise is dominated by turbulent fluctuations which are still present in the turbulent jet emanating from the impeller. Tonal noise, on the other hand, is predicted to be much lower with this arrangement. The model shows that tonal noise is coupled to speed and flow rate only through their concurrent effect on the static pressure profile. Because, in the test diffuser, the static pressure was comparatively uniform around the impeller under all operating conditions, this coupling was very small.

Data was obtained for the pump operating at 100%, 75%, and 50% speeds with the flow rate remaining roughly constant around 240 GPM. The individual spectra for each of these test cases are included in Appendix E.

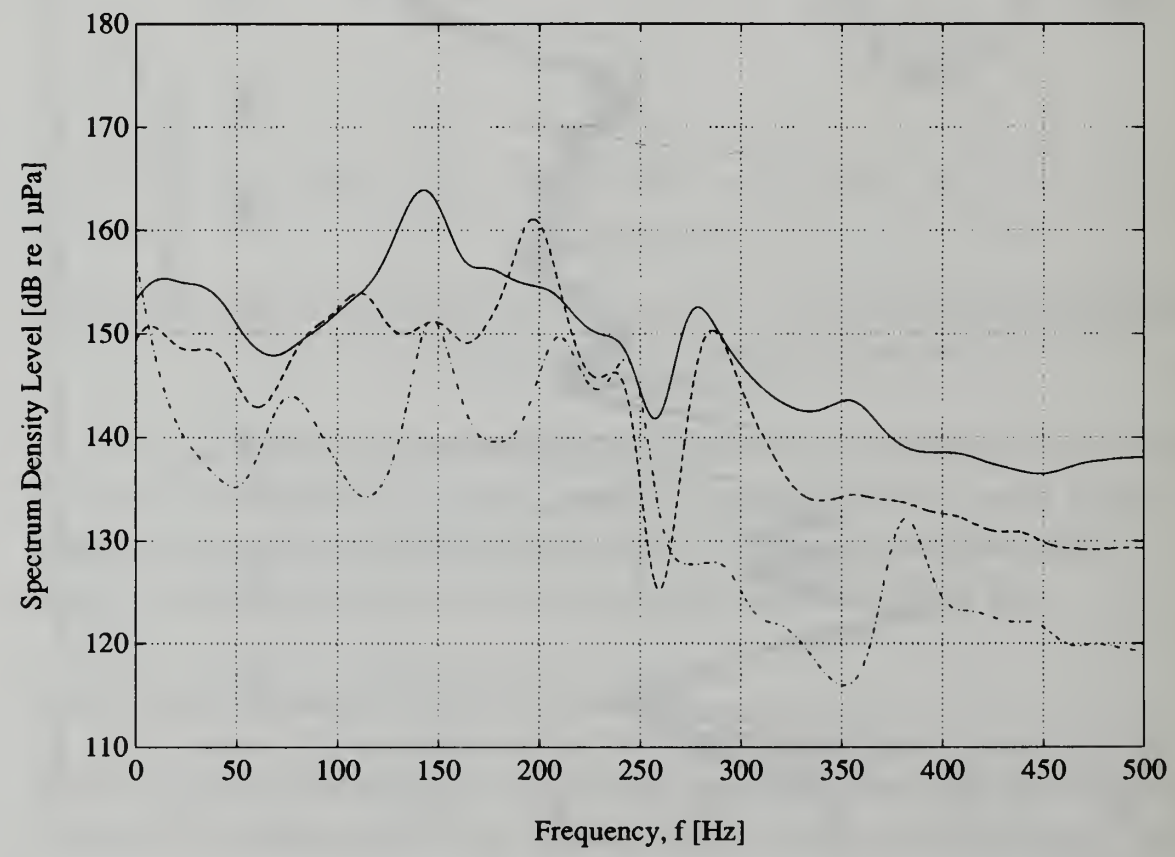

Figure 6.4. Broadband Noise Spectra, Constant Flow Rate (~240 GPM), Varying Speed
(—— : 100% Speed: — — : 75% Speed; — . — : 50% Speed)

In order to facilitate comparisons of broadband and tonal noise for the three cases, separate plots were prepared for each. The broadband plots were filtered using the same lowpass Butterworth filter described in section 4.3.1. The broadband noise floors and shaft harmonics are given in Figures 6.4 and 6.5, respectively.

Figure 6.4 indicates that broadband noise is dependent on pump speed. This is consistent with observations from the volute experiments. A probable explanation is that the broadband noise is dominated by turbulent flow fluctuations which are greatest at the impeller exit. Close to the impeller tip, the velocity dependence on impeller speed is similar to the volute case. The turbulence is the result of hydrodynamic shearing of the flow as it moves past the slower moving fluid in the region outside the core of the jet.

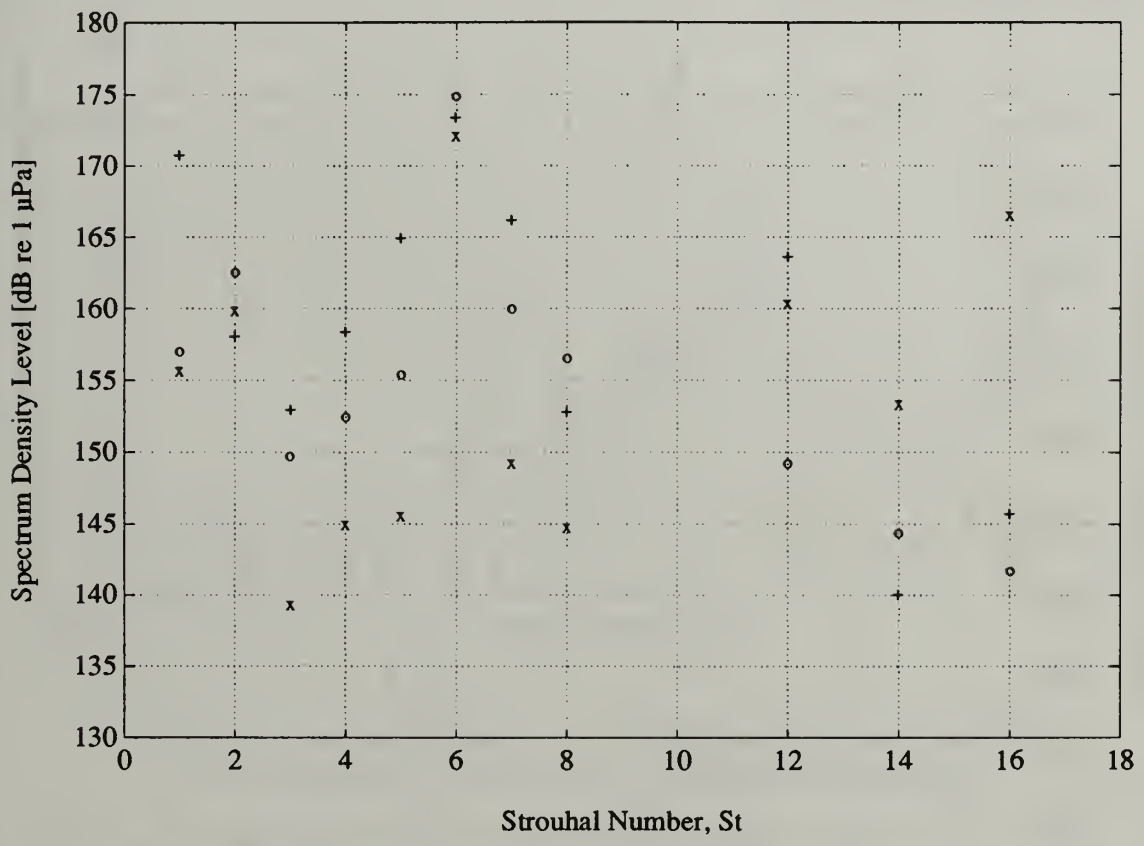

Figure 6.5. Harmonic Noise Levels, Constant Flow Rate (~240 GPM), Varying Speed
(+ : 100% Speed: o : 75% Speed; x= 50% Speed)

Tonal noise levels also appear related to pump speed. In the shaft and blade passage frequencies, as well as in the 3rd, 4th, and 5th harmonics, the tonal noise levels increased by about 15 dB between the 50% and 100% speed cases. There are two possible explanations for this dependence. The first is that the static pressure is not spatially invariant - some non-uniformity still exists. The other explanation is that there exists a different tonal-generating mechanism than the one proposed in the theoretical model.

An example of one such mechanism is a rotating stall pattern was present around the impeller discharge. Such a noise generating phenomenon was observed by Choi, et al.[7], testing a centrifugal pump impeller in an open air configuration. However, a more detailed description of the flow field is required to draw any meaningful conclusions about the source of the tones.

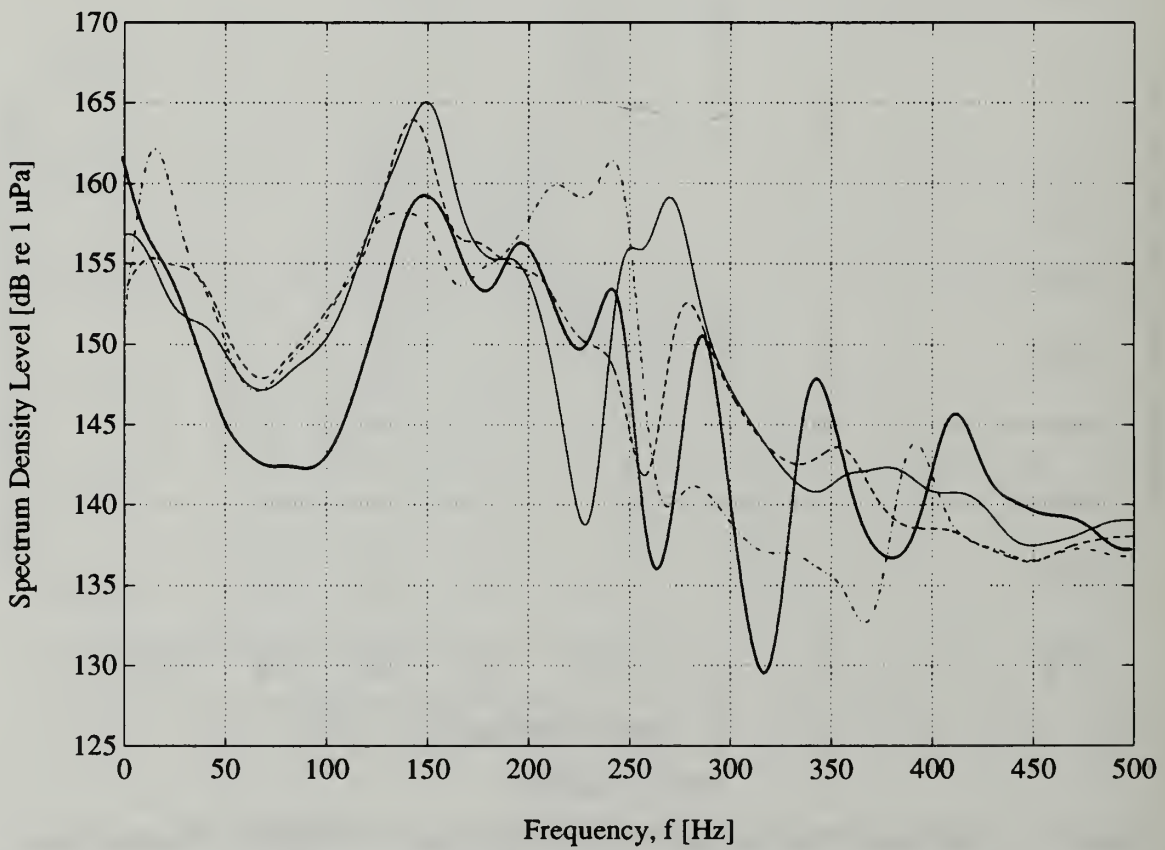

Figure 6.6. Broadband Noise Spectra, 100% Speed, Varying Flow Rate
(—— : 505 GPM; —— : 347 GPM; — — : 224 GPM; — · — : 122 GPM)

The pump operating point appears to have very little effect on either broadband or tonal noise generation. Figures 6.6 and 6.7 show comparisons of the broadband and tonal noise levels for the pump operating over a wide range of capacities at 100% speed. The broadband noise levels vary substantially from one spectrum to the next, but there is no clear trend in the data. It appears that the overall spectrum level remains fairly constant over each of the four cases presented.

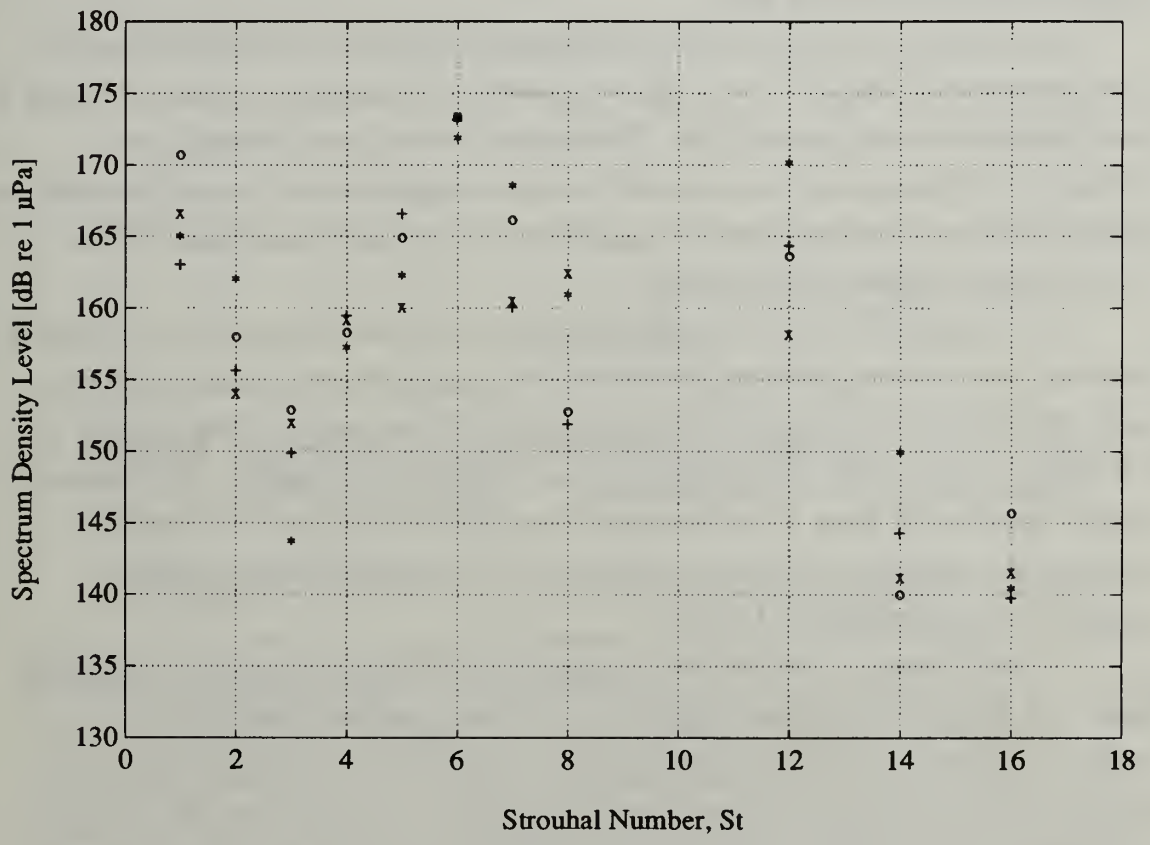

Figure 6.7. Harmonic Noise Levels, 100% Speed, Varying Flow Rate
(* : 505 GPM, + : 347 GPM, o : 224 GPM, x= 122 GPM)

With regard to tonal noise, Figure 6.7 offers little insight. Although there is significant spread in the data at each harmonic, there is no reliable trend in the levels as they changed from case to case.

6.4. The Effects of Static Pressure Field Disturbances on Noise Generation

One of the main reasons for designing the acoustic pump diffuser was to be able to control the pressure distribution at the impeller exit. By beginning with a known, relatively uniform pressure distribution, changes in the discharge geometry could be used to impose the desired pressure profile on the pump impeller exit. The corresponding changes in sound generation could then be measured and correlated to the imposed changes in the static pressure field.

Due to time constraints, it was not possible to complete a thorough study of the theory presented in Chapter 3. As a first step, however, an attempt was made to impose a gross disturbance to the pressure field. The reasons for such an experiment were twofold: 1) to obtain a rough measure of the acoustic significance of non-uniformities in the flow field, and 2) to determine the magnitude of the pressure disturbances which could be easily imposed on the impeller.

To accomplish these goals, a 180° blockage was placed in front of the impeller by installing the innermost perforated cylinder lined on one-half with stainless steel shim stock. The shim stock was pressed up flush against the inner surface of the cylinder and tack welded in place. The inner diameter of the cylinder is 12.84 inches. This represents a radial separation of about 1.5 in. between the impeller and the plate. For reference, recall that the original volute had a diameter of 14.1 in., which equates to a radial separation of approximately 2.1 inches.

A typical pressure distribution obtained from the imposed disturbance is given in Figure 6.8. For comparison, the pressure is non-dimensionalized using the head coefficient, Ψ, and plotted with a typical pressure distribution from the unobstructed diffuser and from the original volute at similar conditions. Note that the 180° blockage was located between 135° and 315° from the reference point. For the original volute, the reference point was defined as the location of the volute tongue. Note also that the first two points of the diffuser plots were corrected using manual readings for reasons outlined in section 6.2.2.

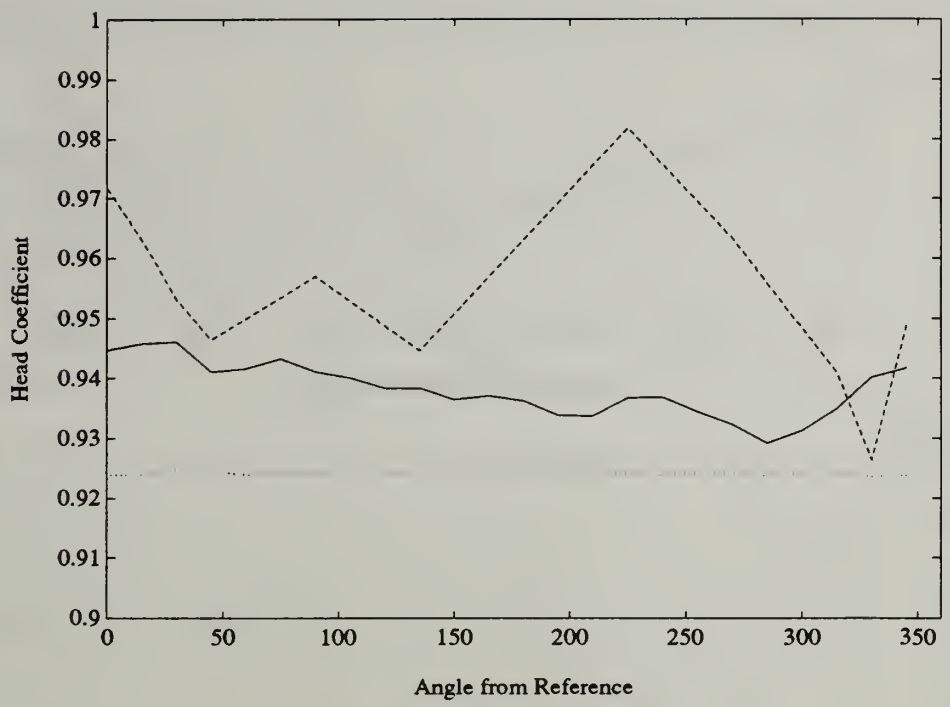

Figure 6.8. Imposed Static Pressure Distribution at Impeller Exit (100% Speed,)
(—— : with 180° blockage, · · · · : unobstructed, — — : original volute)

The figure shows that the blockage pattern had only a small effect on the exit pressure distribution. The range of values was less than 2% of the head rise across the impeller - only about one-fourth of the spatial pressure variation observed in the original volute. The relative insensitivity of the static pressure distribution to changes in discharge geometry is due to the high swirl characteristic of the pump impeller. The pressure disturbance caused by blockage on the cylinder would scale with the normal component of velocity impinging upon the blocked area. For this pump, the radial component of velocity was very small compared to the total.

Larger magnitude disturbances might result from placing a radial blockage close to the impeller. This would directly block the tangential flow of the fluid and the curvature of the streamlines as they approached the blockage would cause a circumferential pressure gradient.

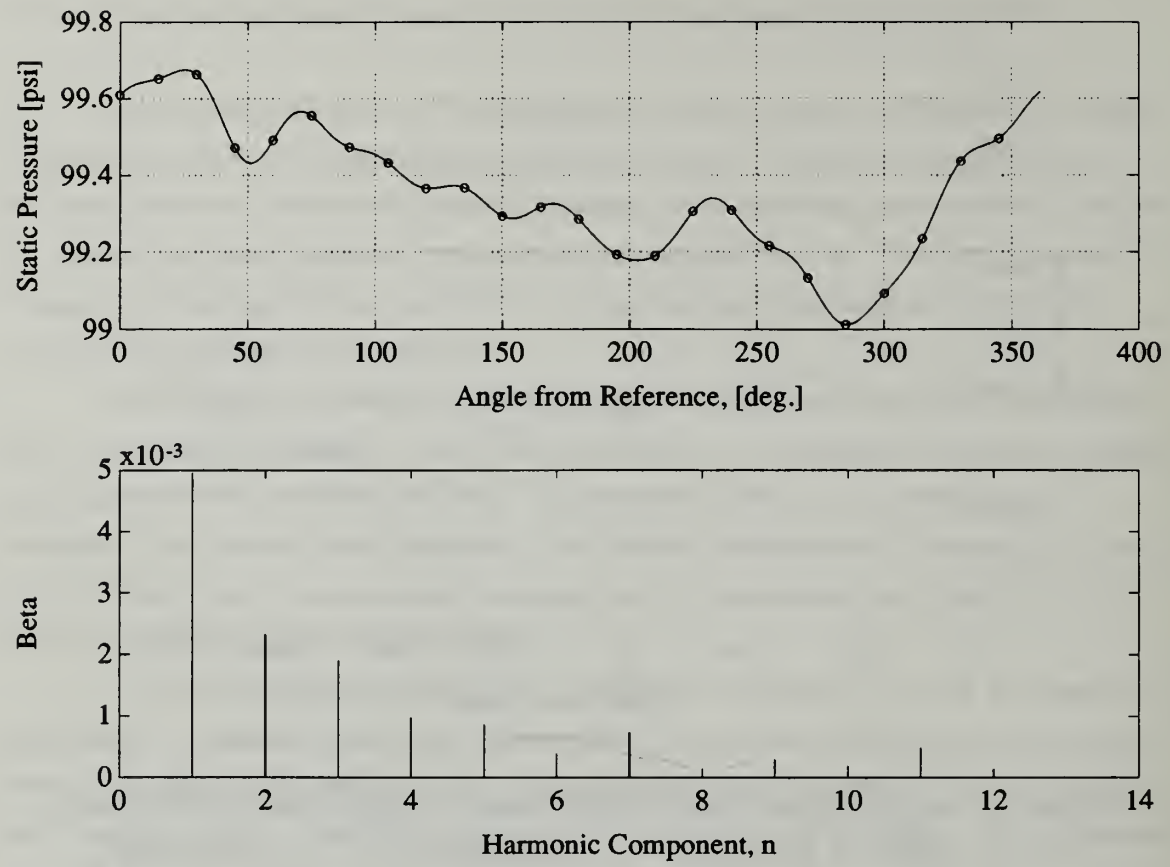

Figure 6.9. Fourier Representation of Impeller Exit Pressure Field (180° Obstruction)

The Fourier representation of the pressure distribution is given in Figure 6.9. Note that the coefficients, β_n, are two orders of magnitude less than those for the volute case, but much of this is attributed to a larger number of coefficients and a closer representation of the true spectra than was obtained with only twelve, unevenly spaced pressure taps.

The acoustic spectra measured with the 180° obstruction at four different speeds was compared with the spectra from the three other configurations under similar test conditions. For the 100% speed case, the filtered broadband plots and tonal noise levels are compared in Figure 6.10 and Figure 6.11, respectively. The individual plots are contained in Appendix E.

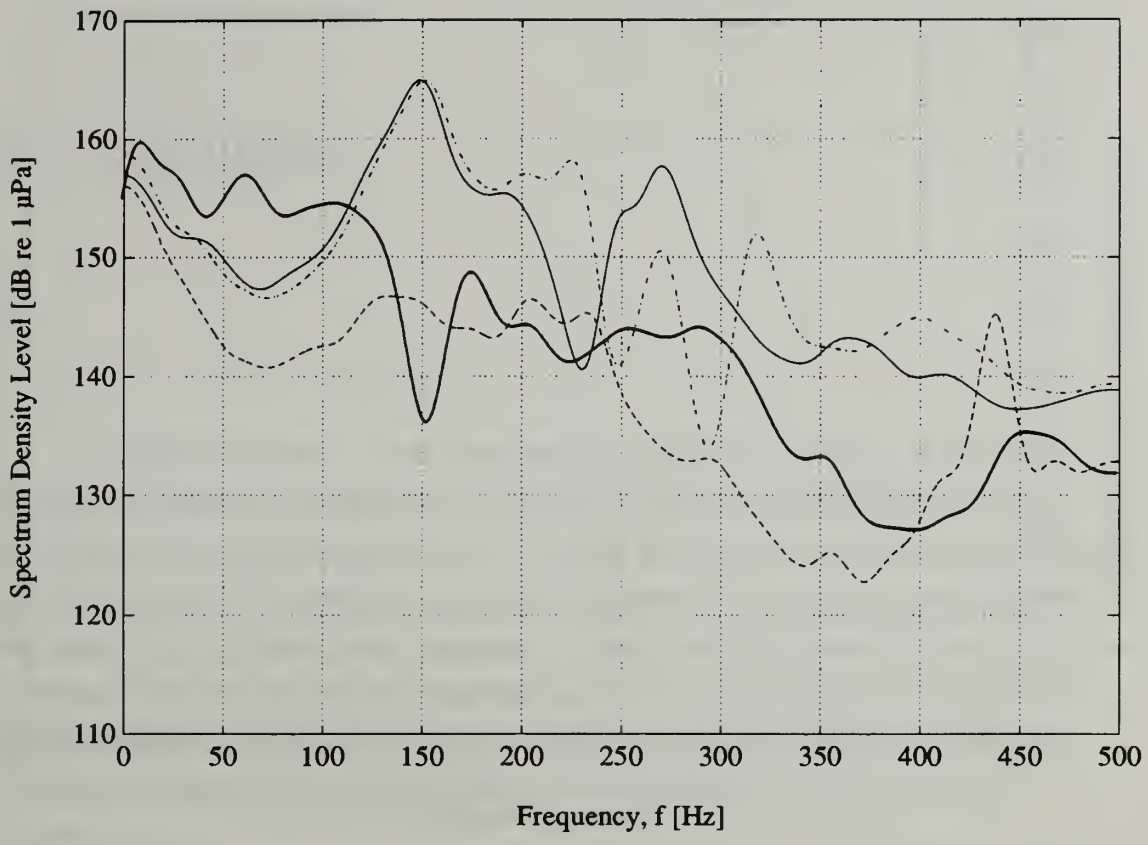

Figure 6.10. Comparison of Broadband Noise for Various Pump Configurations
(——— : Volute, ——— : Diffuser (w/ basket), — — : 180° Obstruction,
— · — : Diffuser (w/o basket))

With reference to Figure 6.10, the following observations are made:

1. The broadband noise level is lowest with the obstructed configuration.
2. The noise floor for the diffuser housing was not altered appreciably with the removal of the perforated basket assembly.
3. The broadband signature of the pump in its original casing is closest to that of the pump in the diffuser with the obstruction.
4. The broadband peaks in the obstructed case spectrum at ~ 440 and 880 Hz (not pictured due to the scale selected to compare results) are attributed to the presence of the close-in perforated cylinder as these occurred only when this cylinder was in place and only at 100% speed. The peak at 880 Hz correlates exactly with the first characteristic frequency of the innermost cylinder, as discussed in section 6.1.3

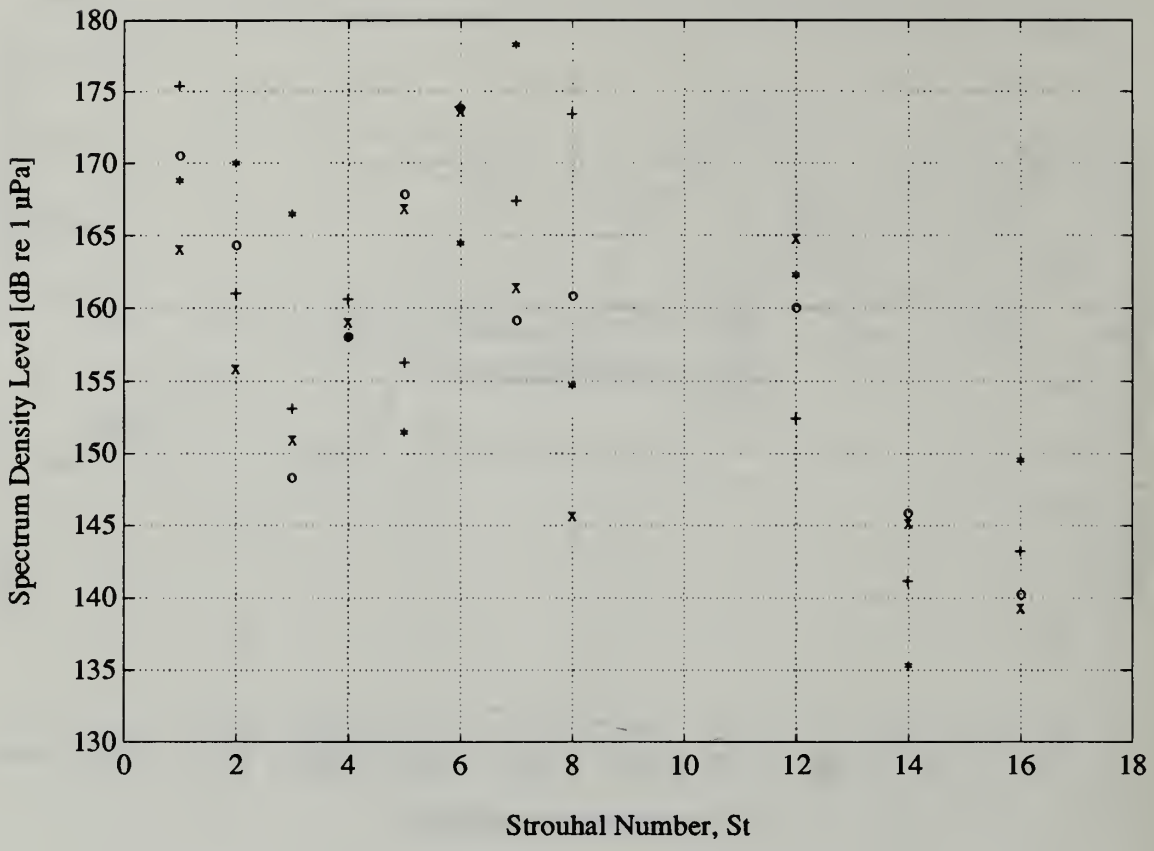

Figure 6.11. Comparison of Tonal Noise Levels for Various Pump Configurations (* : Volute; x : Diffuser (w/ basket); + : 180° Obstruction; o : Diffuser (w/o basket)

Regarding tonal noise, the most significant observation is that the blade passage tone was highest at all speeds with the original volute and that the shaft tone was always highest in the volute and obstructed cases. These observations also support the theory in that the tone levels were dependent on the pressure non-uniformities at impeller exit. The relative strength of the remaining tones varies with the harmonic number. No further trends were identified.

7. Conclusions

Experimental studies were conducted in an attempt to better understand the physical mechanisms which affect the generation of noise in a centrifugal pump. A theoretical model was presented which described the pump as a tonal noise generating mechanism. The model relates the tonal noise generation to the static pressure field at the impeller exit. Studies were conducted to determine the influence of pump rotational speed and flow rate on both the broadband and tonal noise produced. Simultaneous measurements of the pressure profile at impeller exit were taken in an attempt to correlate the tonal noise levels to spatial non-uniformities in the static pressure distribution.

A pump diffuser was designed whereby this pressure distribution could be more closely controlled. Additional experiments were conducted using the diffuser in a modified pump loop to further investigate the influence of the static pressure distribution at impeller exit on harmonic noise levels.

7.1. The Effect of Polymers, Rotational Speed, and Operating Point on Pump Noise

Based on the results presented in Chapter 4, there is evidence that polymers may result in some minor reduction in broadband noise levels produced at pump inlet. The polymers have no noticeable effect on tonal noise levels.

Pump rotational speed impacts both tonal and broad band noise generated by the pump. The broadband noise, as described by the pressure spectral density, scales roughly with the cube of the flow velocity through the volute, although there are complexities in the broadband spectra not accounted for by flow speed alone. Tonal noise levels were found to be dependent on rotational speed for the shaft tone and odd harmonics. At these frequencies, sound pressures showed between first and second order dependence on

rotational speed. These observations agree with previously published results. At other harmonics, no dependence was noted.

For a given speed, flow rate had little effect on the pump inlet sound spectrum. This result is considered a unique consequence of the unusual flow characteristics of the experimental pump and will not generally hold true for other pump geometries.

7.2. The Effect of Impeller Exit Static Pressure Field on Pump Noise

The high swirl flow in the pump volute over a wide range of operating conditions resulted in the volute pressure distribution having only minor dependence on pump operating condition. As such, the predicted effect on the acoustic spectra was small - inside the measurement uncertainty. The results did not contradict this prediction, but, because of measurement uncertainty, neither did they definitively support it.

Using, the experimental diffuser, the pressure non-uniformities were further reduced with the result being a corresponding reduction in the tonal noise levels at f_{sh} and f_{bp}. One attempt was made to impose a non-uniform pressure profile on impeller exit, but was only marginally successful. Nevertheless, the shaft and blade passage tones again responded by increasing in magnitude. Other shaft harmonics showed little dependence on the static pressure distribution.

7.3. Recommendations for Future Work

The results of this study clearly indicate that much work remains to be done. The experimental pump diffuser may be employed to test a wide number of acoustic phenomena in pump noise generation. However, there are a number of problems which must be resolved before any definitive evaluations may be made. As a matter of first course, it would be desirable to positively identify all extraneous noise sources from the diffuser and in the pump loop. These sources could then either be treated and eliminated, or properly accounted for in the analyses. An improved method of removing air from the system would also eliminate some of the uncertainty in the analyses.

In order to more effectively test the theoretical model proposed in this work, it would be desirable to create larger scale pressure disturbances or to use a more sensitive pressure transducer with a known reference pressure . These actions would eliminate the significance of transducer measurement uncertainty. Additional pressure taps could also be used to obtain a finer grid of pressure measurements so that more accurate Fourier analysis could be accomplished.

It may also be possible to change the flow characteristics in the impeller by narrowing the height of the impeller passage. This would result in larger radial components of velocity which would make the flow angle more sensitive to flow rate. It might also increase the magnitude of pressure disturbances created by flow interaction with the volute or with imposed disturbances in the diffuser.

There are a number of other studies which could be undertaken to further refine this work. The development of a computational fluid dynamics code to describe the flow in the impeller and volute would aid in understanding the fluid mechanics involved in the generation of tones. Such a code could also be used to determine the influence of impeller non-uniformities on the exit flow field and the corresponding effect on the inlet sound field. There is also the potential for the study of the unsteady fluctuations in the pump volute and their relationship to the sound field in the inlet piping.

In Barton's investigation of the influence of inlet distortion on tonal noise generation, one of his recommended courses of action was to eliminate extraneous sources of blade passage noise in order to isolate the phenomenon of interest. The diffuser designed for this study can clearly be used to re-evaluate these studies.

Lastly, the diffuser might be used to house other impeller discharge configurations. For example, a pair of parallel plates could be positioned within the diffuser to collect the flow from the impeller. There would then be the potential for adding vanes or foils to the geometry to determine their influence on the noise spectra.

8. References

1. Maroti, L.A., and A.V. Pradhan, "Noise Generation Characteristics of High Speed Centrifugal Fans," ASME Society Paper 69-WA/FE-9, 1969, pp1-8.

2. Simpson, H.C., and T.A. Clark, "Noise Generation in a Centrifugal Pump," ASME Society Paper 70-FE-37, 1970, pp 1-8.

3. Simpson, H.C., R. Macaskill, and T.A. Clark, "Generation of Hydraulic Noise in Centrifugal Pumps," *Proceedings of the Institution of Mechanical Engineers*, Vol. 181, Pt 3A, 1966-67, pp 84-108.

4. Simpson, H.C., T.A. Clark, and G.A. Weir, "A Theoretical Investigation of Hydraulic Noise in Pumps," *Journal of Sound and Vibration*, Vol. 5, No. 3, 1967, pp 456-488.

5. Deeprose, W.M., and A.N. Bolton, "Current Industrial Pump and Fan Fluid-Borne Noise Level Prediction," National Engineering Laboratory, East Kilbride, C251/77, 1977, pp 43-47.

6. Yuasa, Tatsuji, and Tatsuo Hinata, "Fluctuating Flow Behind the Impeller of Centrifugal Pump," *Transactions of the Japanese Society of Mechanical Engineers*, Vol. 22, No 174, 1979, pp 1746-53.

7. Choi, Jong-Soo, D.K. McLaughlin, and D.E. Thompson, "Experiments on the Aerodynamic Noise Sources in Centrifugal Turbomachinery," American Institute of Aeronautics and Astronautics 13th Aeroacoustics Conference, Tallahassee, FL, 1990.

8. Bent, Paul H., Dennis K. McLaughlin, and Donald E. Thompson, "The Influence of Discharge Configuration on the Broadband Noise in Centrifugal Turbomachinery," University Park, PA, 1990.

9. Stepanoff, A.J., Centrifugal and Axial Flow Pumps, John Wiley & Sons, Inc, New York, 1957.

10. Van Den Braembussche, R.A. and B.M. Hände, "Experimental and Theoretical Study of the Swirling Flow in Centrifugal Compressor Volutes," ASME Paper 89-GT-183, 1989.

11. Ayder, E., R. Van den Braembussche, and J.J. Brasz, "Experimental and Theoretical Analysis of the Flow in a Centrifugal Compressor Volute," ASME Paper 92-GT-30, 1992,

12. Brownell, R.B., and R.D. Flack, "Flow Characteristics in the Volute and Tongue Region of a Centrifugal Pump," ASME Paper 84-GT-82, 1984.

13. Badie, R., J.B. Bonker, and T.G. Van Essen, "Calculations on the Time-Dependent Potential Flow in a Centrifugal Pump," ASME Paper 92-GT-151, 1992.

14. Worster, R.C., "The Flow in Volutes and its Effect on Centrifugal Pump Performance," *Proceedings of the Institution of Mechanical Engineers,* Vol. 177, No. 31, 1963, pp. 843-875.

15. Iversen, H.W., R.E. Rolling, and J.J. Carlson, "Volute Pressure Distribution, Radial Force on the Impeller, and Volute Mixing Losses of a Radial Flow Centrifugal Pump," *Transactions of the A.S.M.E. Journal of Engineering for Power*, April, 1960, pp136-144.

16. Csanady, G.T., "Radial Forces in a Pump Impeller Caused by a Volute Casing," *Transactions of the A.S.M.E. Journal of Engineering for Power*, October, 1962, pp. 337-340.

17. Logan, E., Turbomachinery: Basic Theory and Applications, M. Dekker, Inc., New York, 1981, p 34.

18. Barton, Scott Andrew, "An Experimental Investigation of the Influence of Inlet Distortion on the Fluid Borne Noise of a Centrifugal Pump," S.M. Thesis, Massachusetts Institute of Technology, Cambridge, MA, 1991.

19. Clinch, J.M., "Measurement of the Wall Pressure Field at the Surface of a Smooth-Walled Pipe Containing Turbulent Water Flow," *Journal of Sound and Vibration*, Vol. 9 No. 3 1969 pp 398-419.

20. Rogers, W.L., *Transactions of the American Society of Heating and Ventilation Engineers*, Vol. 60, 1965, p 411.

21. Oppenheim, Alan V., and Ronald W. Shafer, Digital Signal Processing, Prentice-Hall, Inc., Englewood Cliffs, NJ, 1975, p. 556.

22. Marple, S. Lawrence Jr., Digital Spectral Analysis with Applications, Prentice-Hall, Inc., Englewood Cliffs, NJ, 1987, pp 34-42.

23. Ingard, K.U., "On Sound Generation in a Centrifugal Pump," Internal Report, Massachusetts Institute of Technology, Cambridge, MA, 1992.

24. Ingard, K.U., "A Note on Sound Radiation from a Water Pump in a Pipe Line with End Reflection," Internal Report, Massachusetts Institute of Technology, Cambridge, MA, 1992.

25. Louie, Lisa Lai Yee, "Active Control of Pipe-Borne Pump Noise," S.M. Thesis, Massachusetts Institute of Technology, Cambridge, MA, 1991.

26. Sedov, L.I., V.A. Ioselevich, V.N. Pilipenko, and N.G. Vasetskaya, "Turbulent Diffusion and Degradation of Polymer Molecules in a Pipe and Boundary Layer," *Journal of Fluid Mechanics*, Vol. 94, Part 3, 1979, pp 561-576.

27. Paterson, R.W., and F.H. Abernathy, "Turbulent Flow Drag Reduction and Degradation with Dilute Polymer Solutions," *Journal of Fluid Mechanics*, Vol. 43, Part 4, 1970, pp 689-710.

28. Van Driest, E.R., "Turbulent Drag Reduction of Polymeric Solutions," *Journal of Hydronautics*, Vol. 4, No. 3, 1970, pp 120-126.

29. Norton, M.P., Fundamentals of Noise and Vibration Analysis for Engineers, Cambridge University Press, Cambridge, 1989.

30. Jansen, W., "Rotating Stall in a Radial Vaneless Diffuser," *Transactions of the A.S.M.E. Journal of Basic Engineering*, December, 1964, pp 750-758.

31. Abramovich, G.N., The Theory of Turbulent Jets, The M.I.T. Press, Cambridge, MA, 1963.

Appendices

A. The Resonance Frequency of an Air Bubble in Water

First, consider a small, pulsating bubble of air with radius a surrounded by an incompressible fluid. The pulsations produce a velocity disturbance in the surrounding water which decays as $1/r^2$ where r is the distance from the air-water interface. The total kinetic energy of the water is obtained from the following:

$$K.E. = \int_a^\infty \frac{\rho}{2} u^2(r)\, 4\pi r^2\, dr$$

Substituting $u(r) = U_0 \left(a/r\right)^2$, the total kinetic energy is then

$$K.E. = 4\pi\rho a^3 U_0^2/2$$

The equivalent mass of the fluid is then given by $4\pi\rho a^3$ which is roughly equivalent to the mass of a layer of water of thickness a around the bubble.

The pressure required to accelerate this mass is given by

$$p = \rho_w a \frac{\partial u}{\partial t} = -i\omega\rho_w a \cdot u \qquad [A.1]$$

where ρ_w is the density of water, u is the outward velocity of the fluid mass, and ω is the frequency of the oscillations.

Next, consider the air inside the bubble. The differential form of mass conservation applied to the air in the bubble is given by:

$$\int_V \frac{\partial \rho_a}{\partial t}\, dV + \int_S \rho_a \mathbf{V} \cdot \mathbf{n}\, dS = 0$$

Substituting $\frac{\partial \rho}{\partial t} = \frac{1}{c_0^2}\frac{\partial p}{\partial t}$ and simplifying yields the following:

$$-i\omega V \frac{1}{c_0^2} p = -\rho_a S\, u \qquad [A.2]$$

where c_0 is the speed of sound in air. Combining equations 4.1 and 4.2, and rearranging gives the resonant frequency of the bubble:

$$f \approx \frac{c_0}{2\pi}\sqrt{\frac{S}{Va}\frac{\rho_a}{\rho_w}} = \frac{c_0}{2\pi}\frac{\sqrt{3}}{a}\sqrt{\frac{\rho_a}{\rho_w}} \qquad \text{[A.3]}$$

The analysis is similar for a bubble which rests on a solid surface. Suppose that the bubble is in the form of a flat layer of radius a and thickness d. It can be shown that the equivalent thickness, t, for the disturbed region outside such a bubble is given by:

$$t = \frac{8}{3\pi}a$$

Following the same procedure as above, the resonant frequency is estimated by:

$$f \approx \frac{c_0}{2\pi}\sqrt{\frac{3\pi S}{8Va}\frac{\rho_a}{\rho_w}} \approx \frac{c_0}{2\pi}\sqrt{\frac{3\pi}{8ad}}\sqrt{\frac{\rho_a}{\rho_w}}$$

B. Polymer Treatment Results

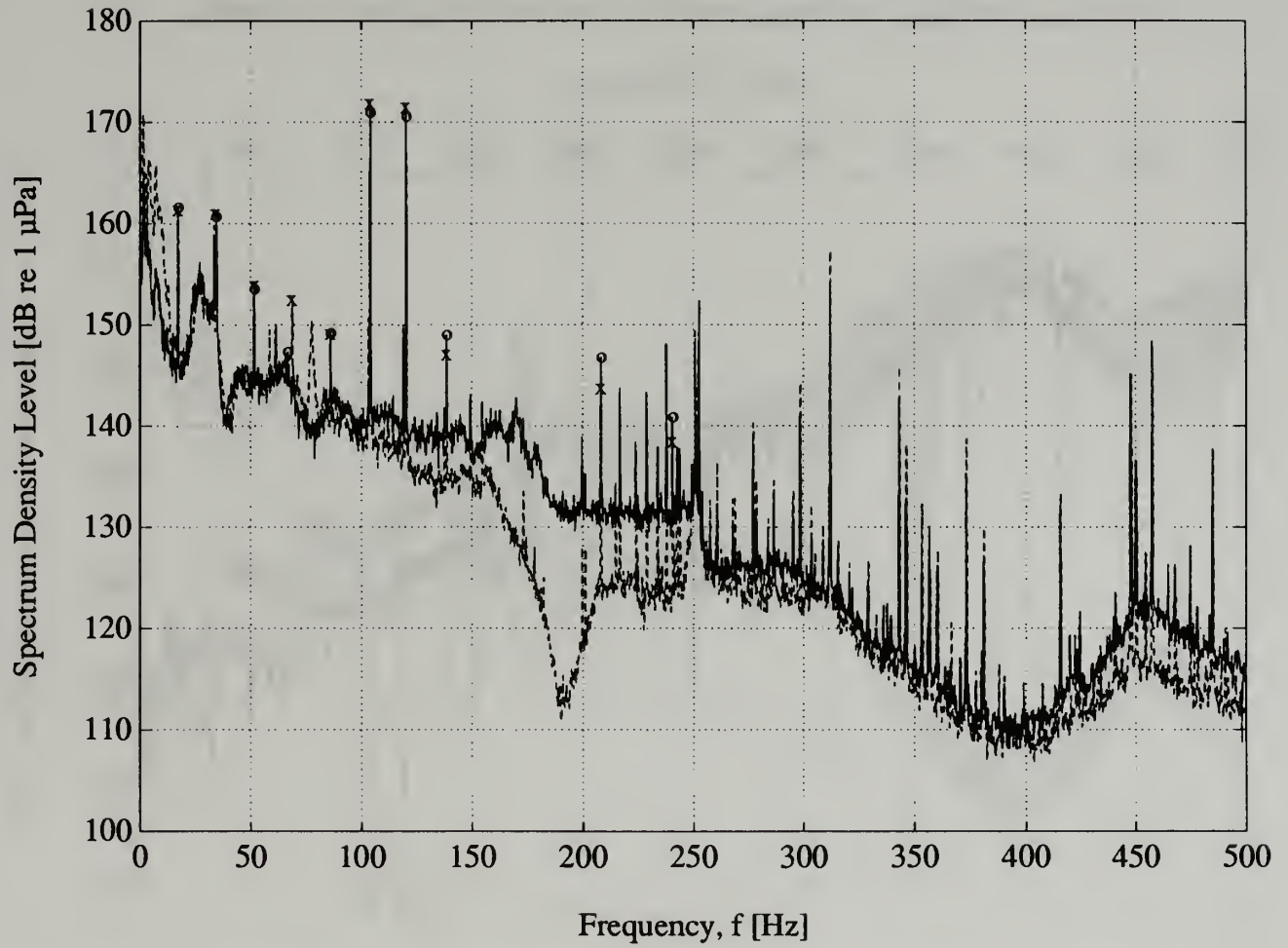

Figure B.1. Inlet Noise Spectra, 58% Speed, Water and 500 ppm Polymer
(——, o : water only; — —, x : polymer treatment)

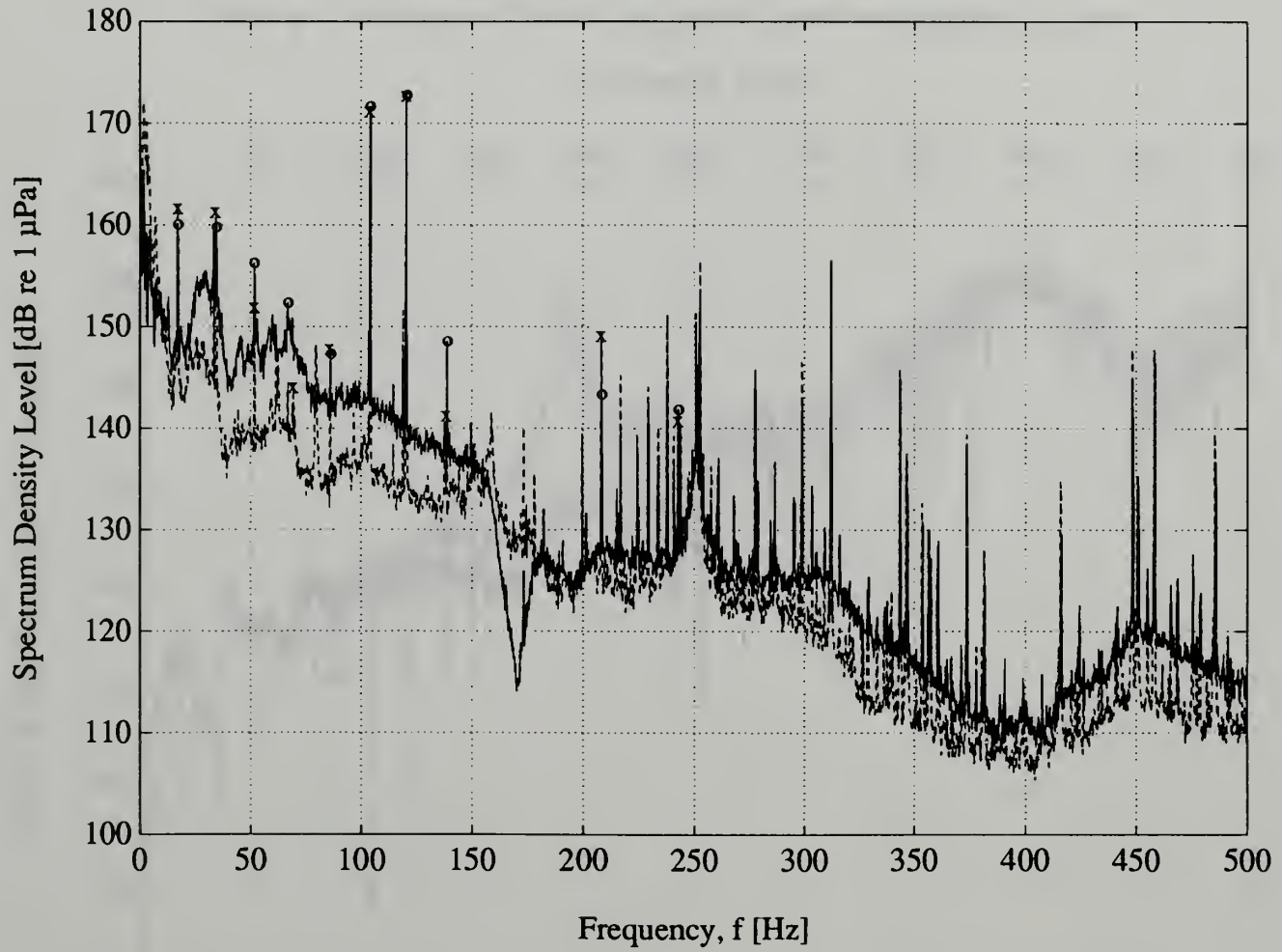

Figure B.2. Inlet Noise Spectra, 58% Speed, Water and 1000 ppm Polymer
(——, o : water only; — —, x : polymer treatment)

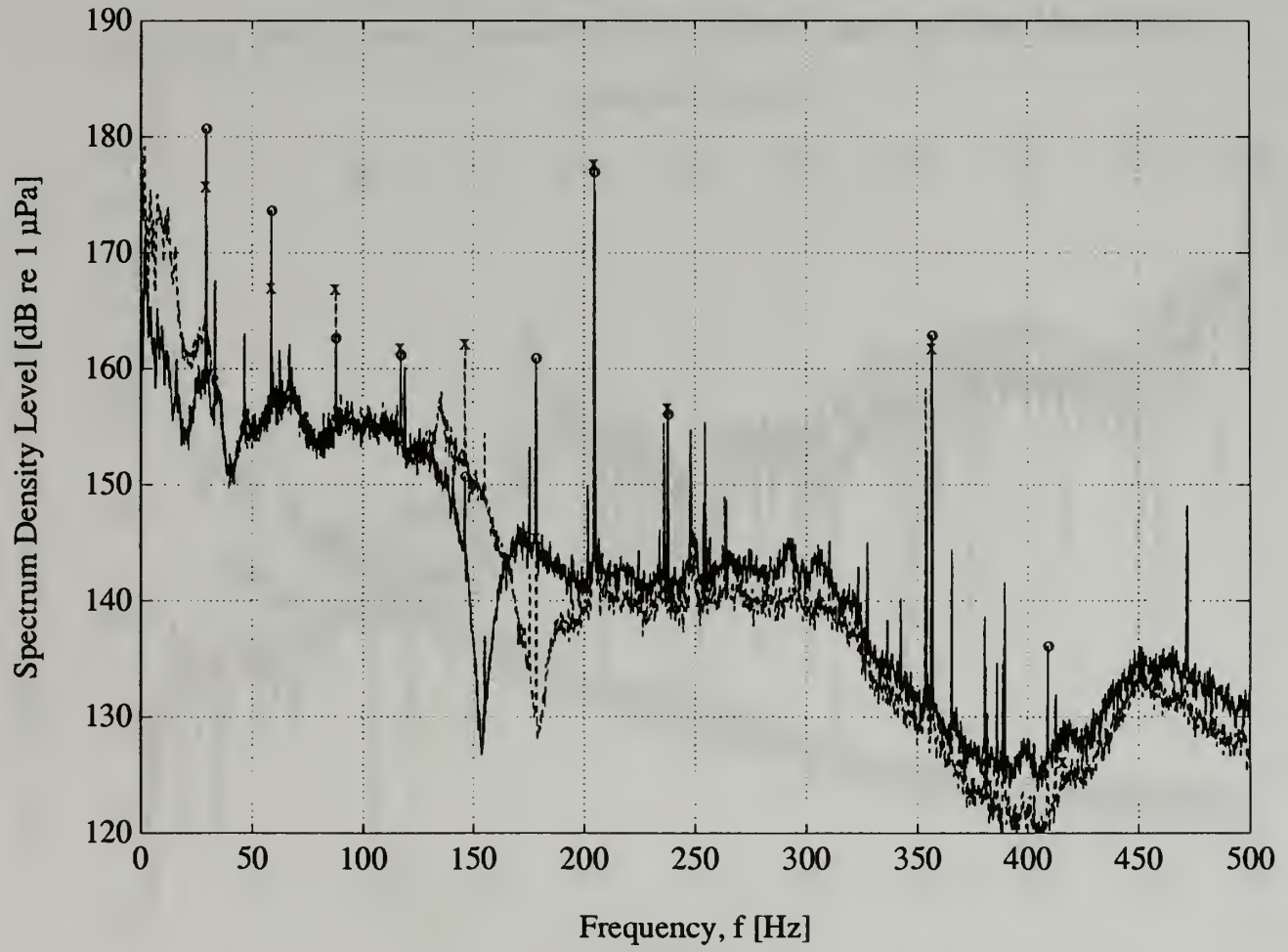

Figure B.3. Inlet Noise Spectra, 100% Speed, Water and 500 ppm Polymer
(——, o : water only; — —, x : polymer treatment)

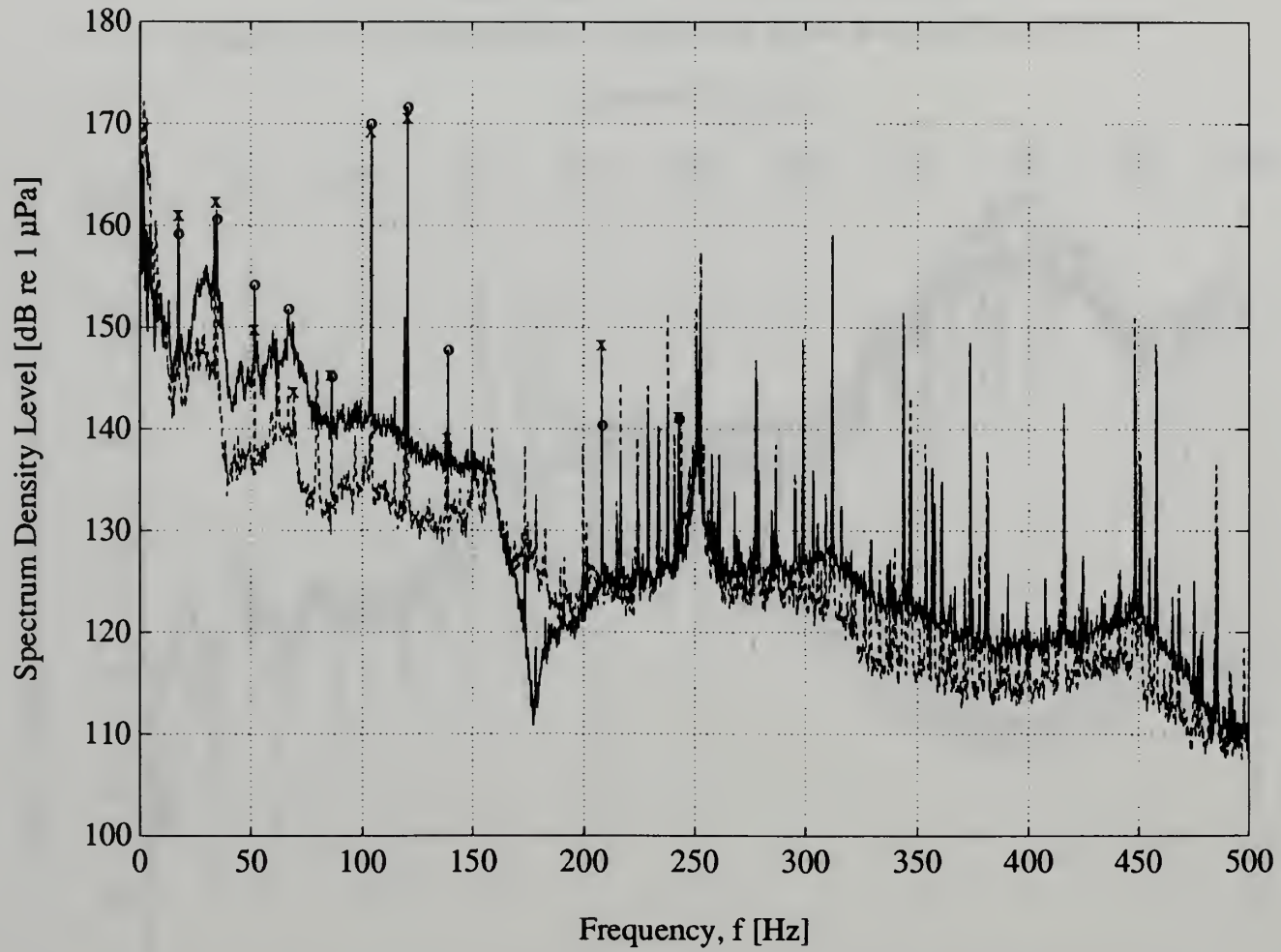

Figure B.4. Inlet (Channel 2) Noise Spectra, 58% Speed, Water and 1000 ppm Polymer
(——, o : water only; — —, x : polymer treatment)

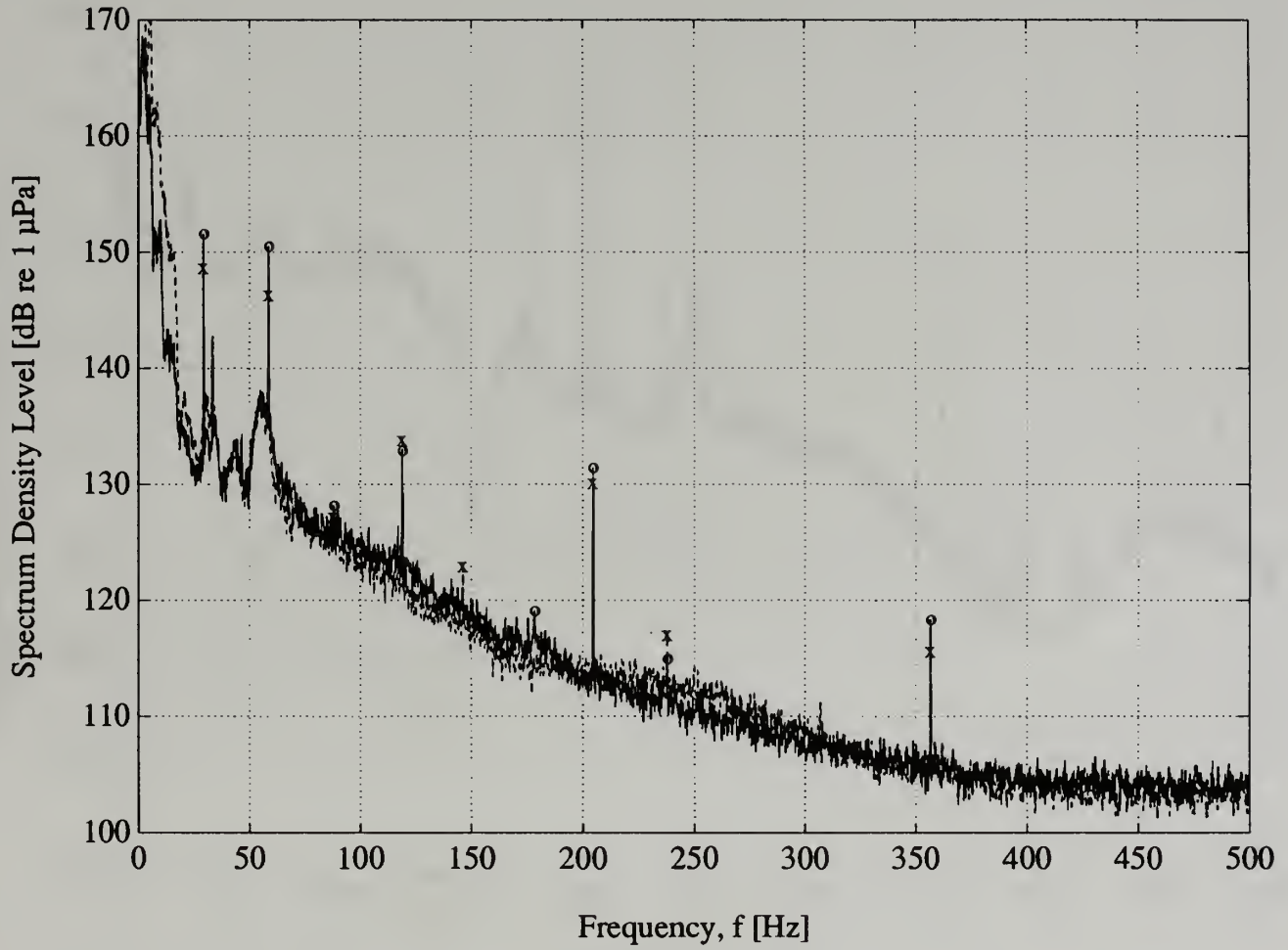

Figure B.5. Far Upstream Noise Spectra, 100% Speed, Water and 500 ppm Polymer
(——, o : water only; — —, x : polymer treatment)

C. Speed/Flow Rate Effects on Broadband Noise

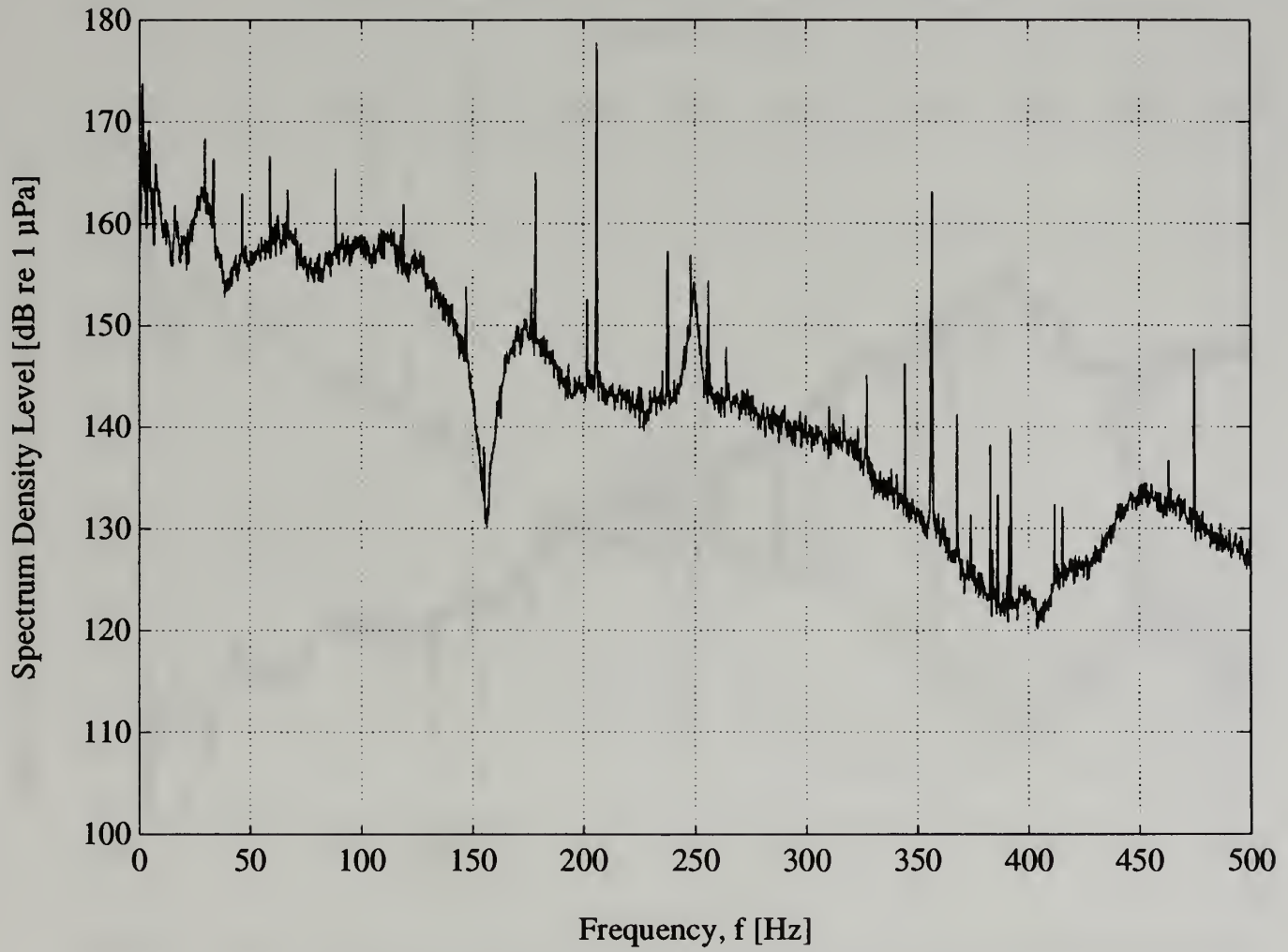

Figure C.1. Inlet Noise Spectrum, 100% Speed, 167 GPM

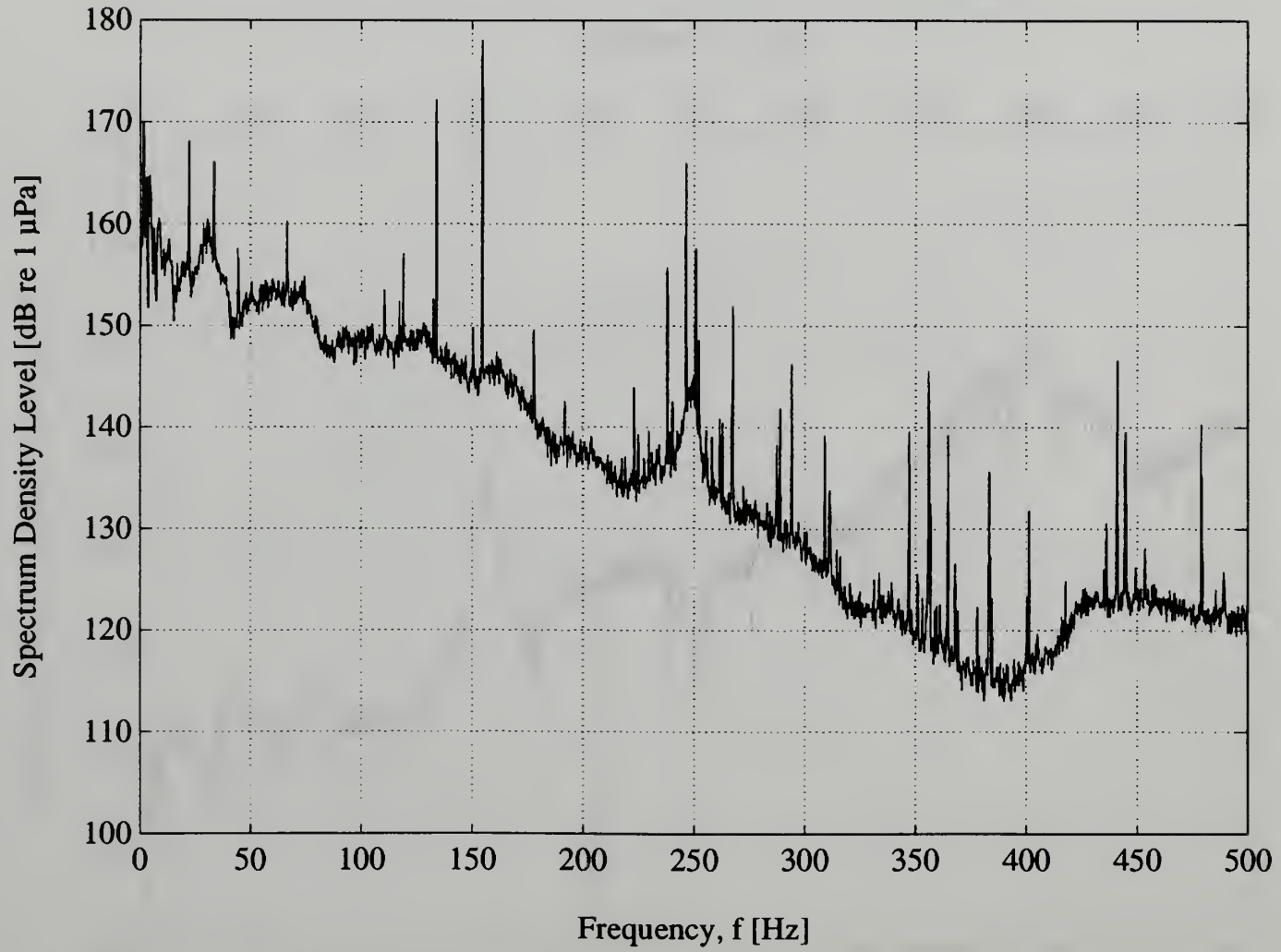

Figure C.2. Inlet Noise Spectrum, 75% Speed, 155 GPM

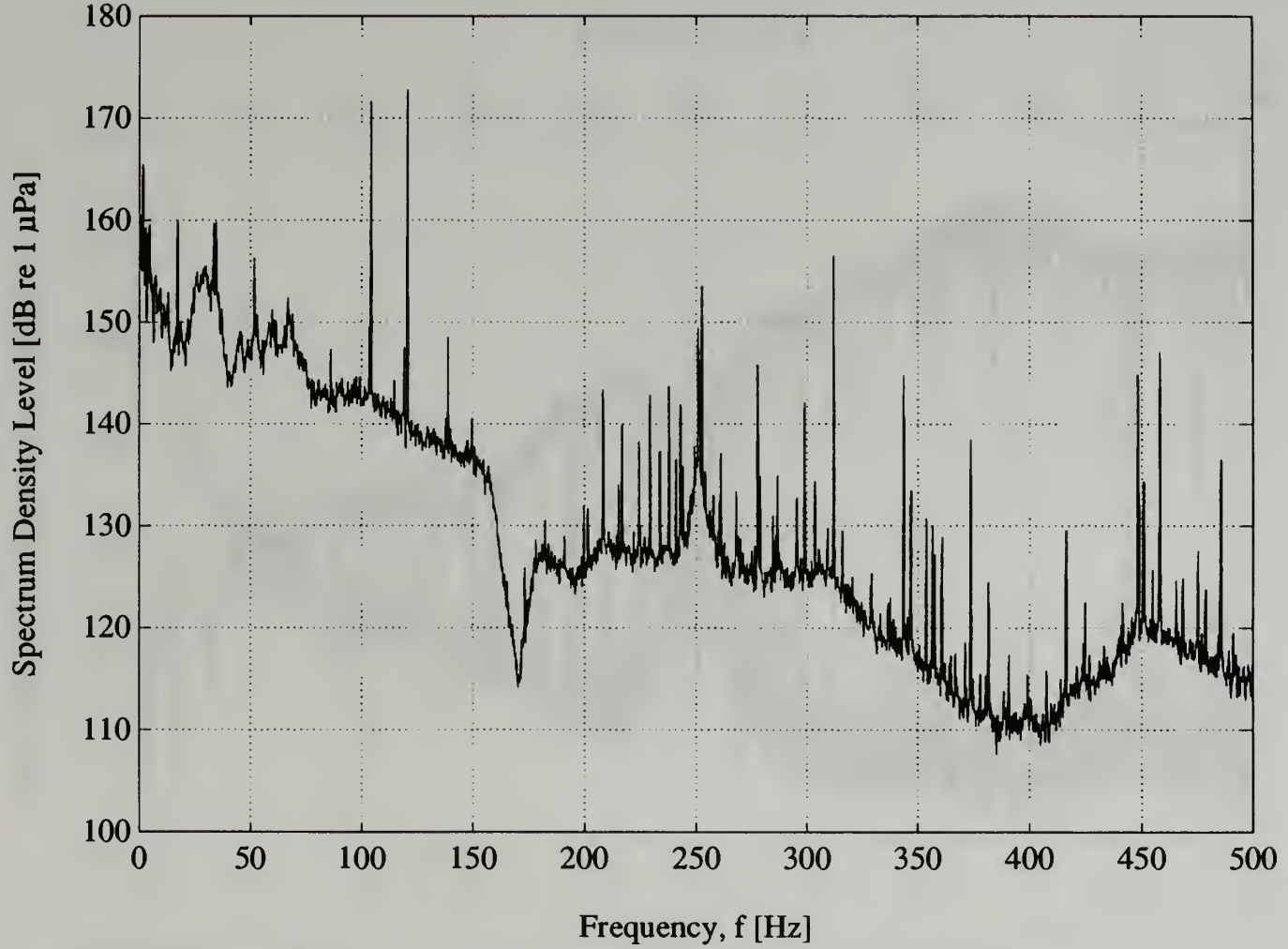

Figure C.3. Inlet Noise Spectrum, 58% Speed, 154 GPM

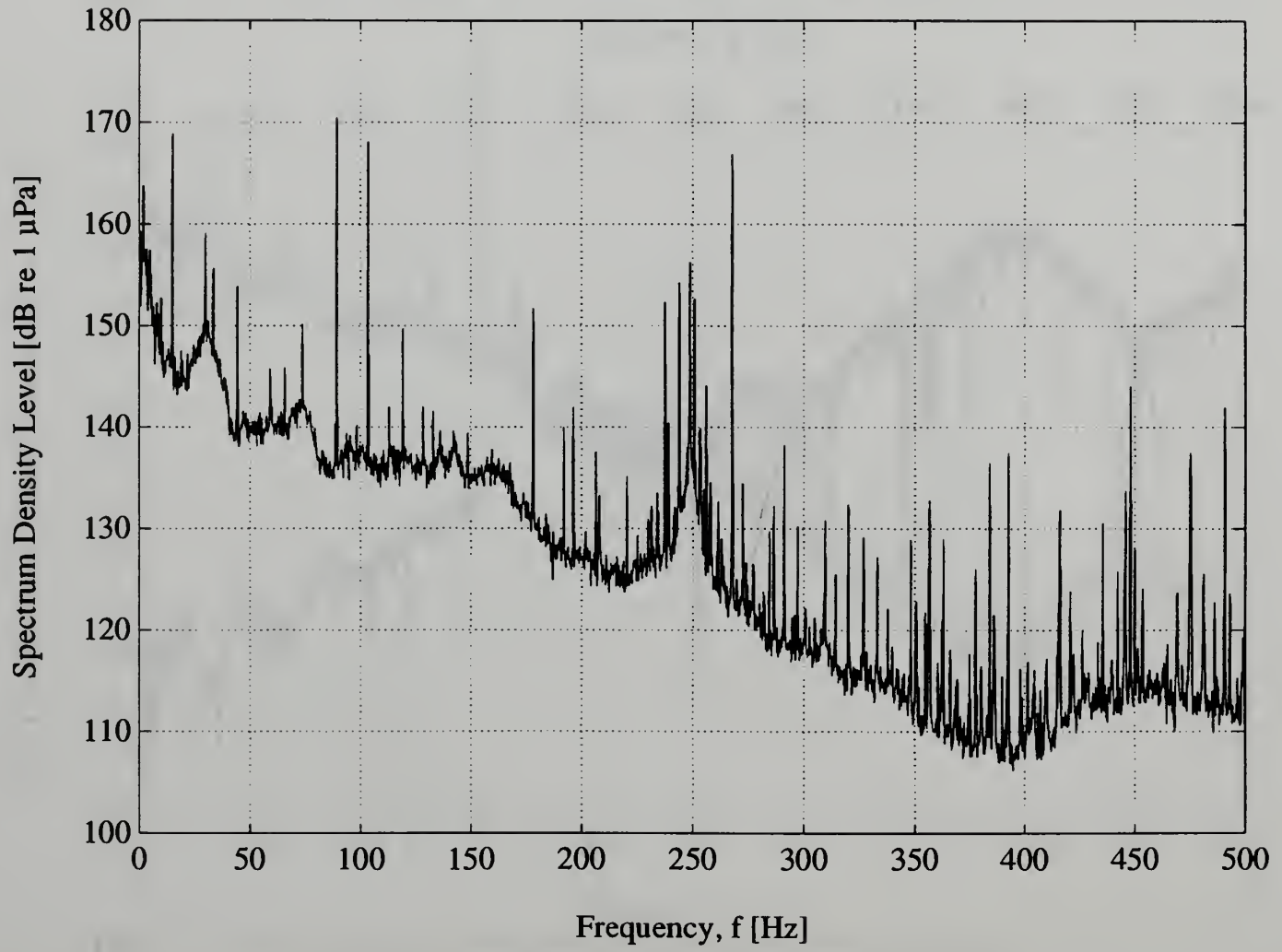

Figure C.4. Inlet Noise Spectrum, 50% Speed, 155 GPM

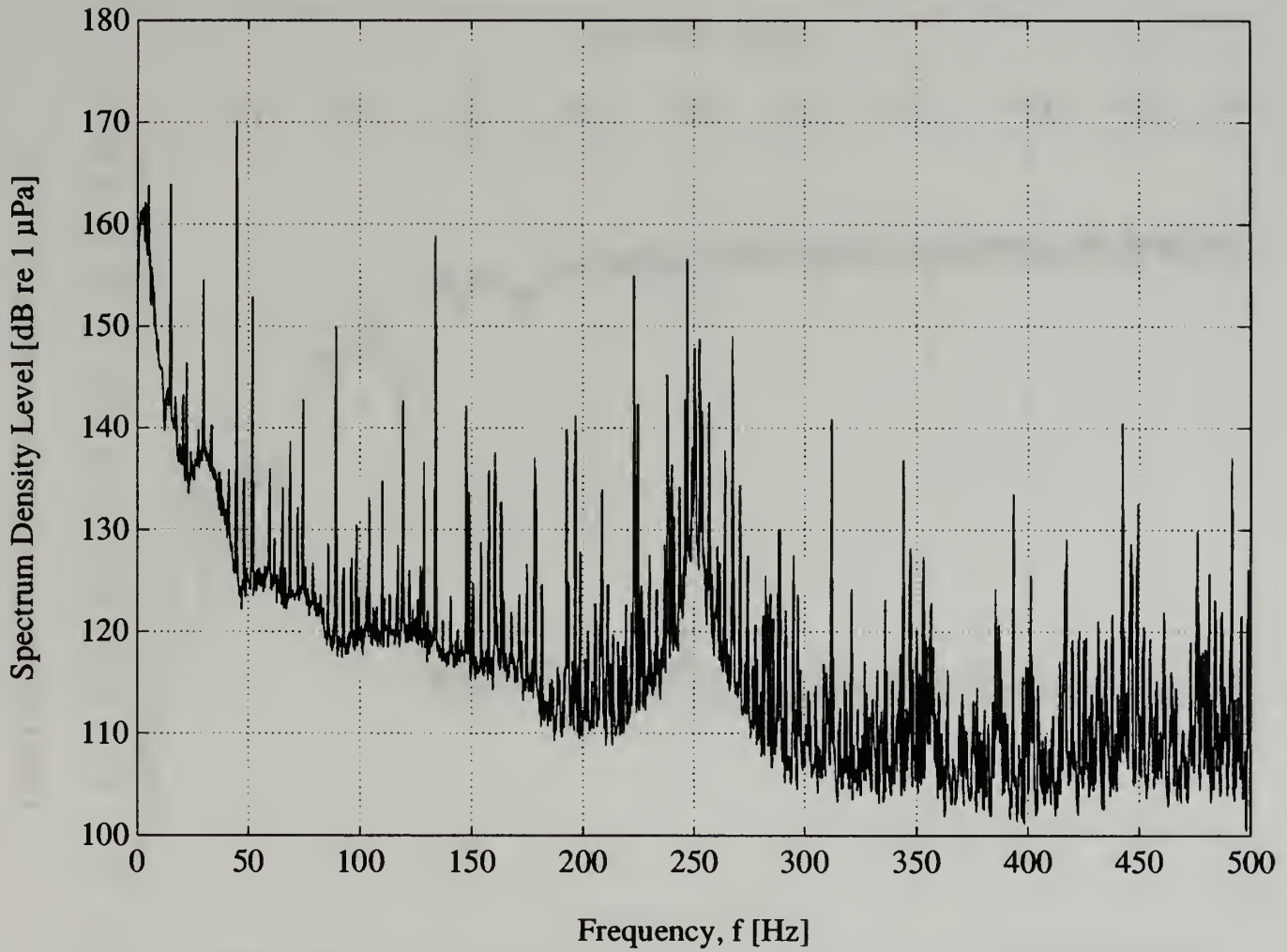

Figure C.5. Inlet Noise Spectrum, 25% Speed, 155 GPM

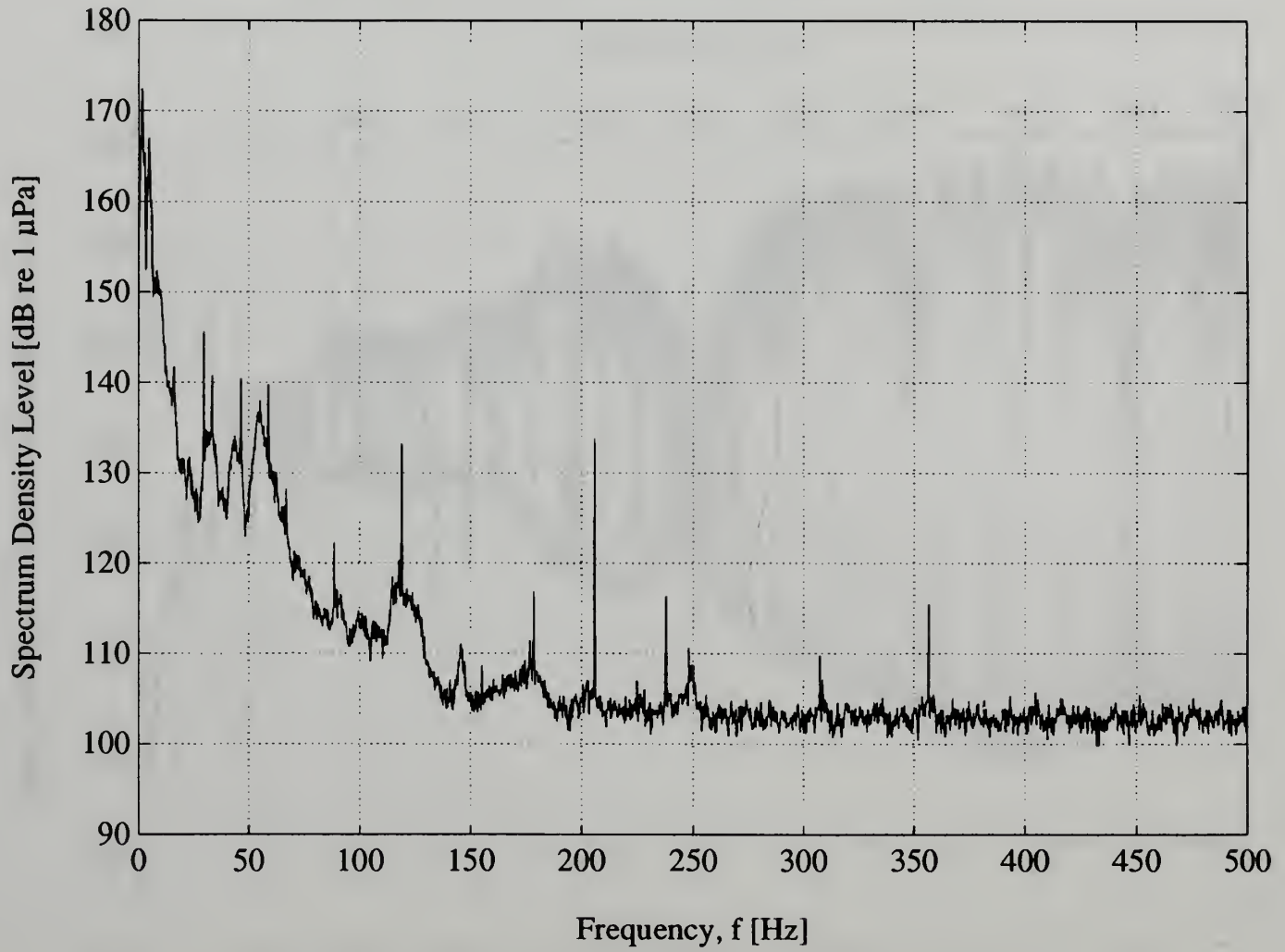

Figure C.6. Upstream Noise Spectrum, 100% Speed, 167 GPM

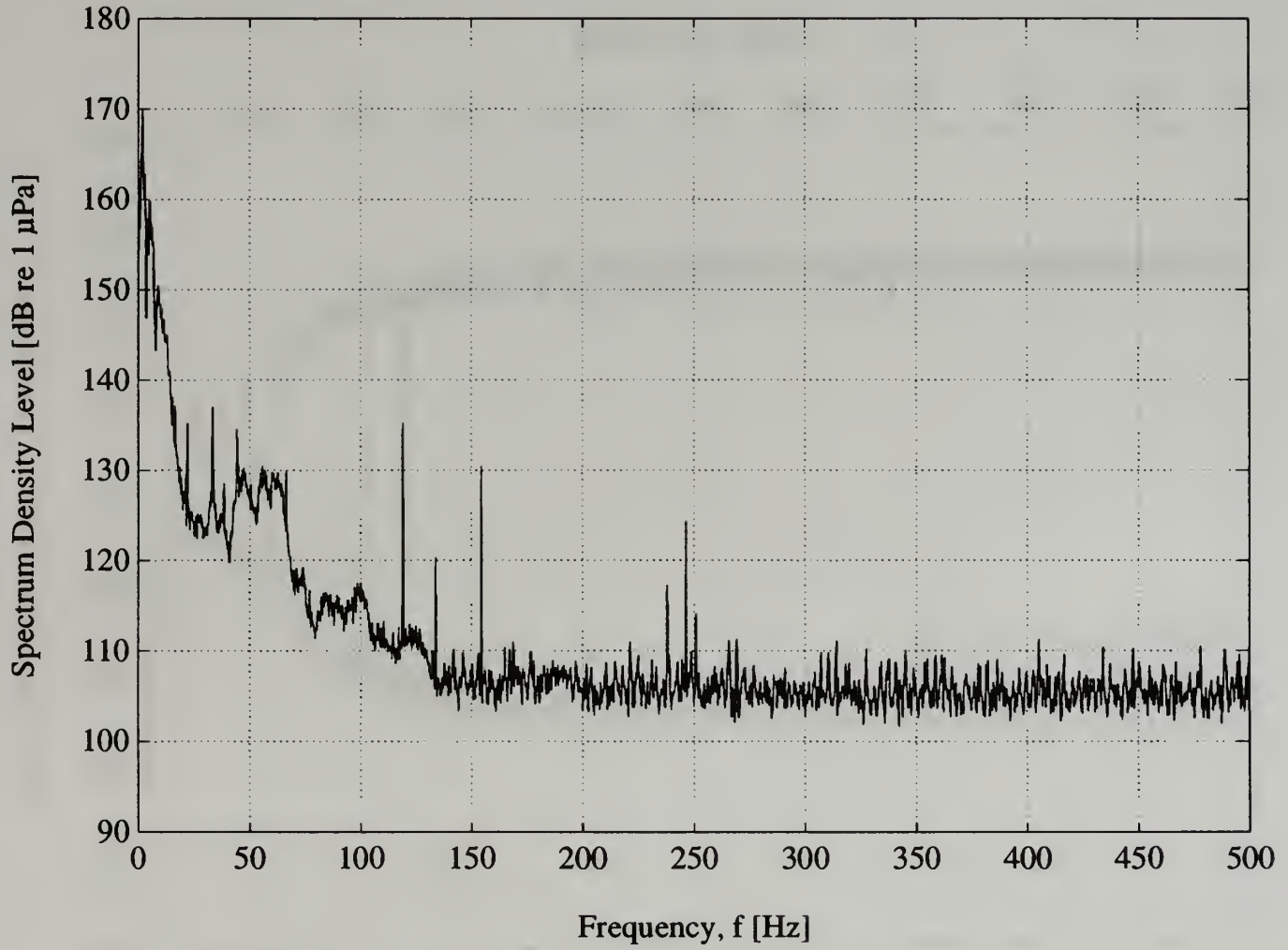

Figure C.7. Upstream Noise Spectrum, 75% Speed, 155 GPM

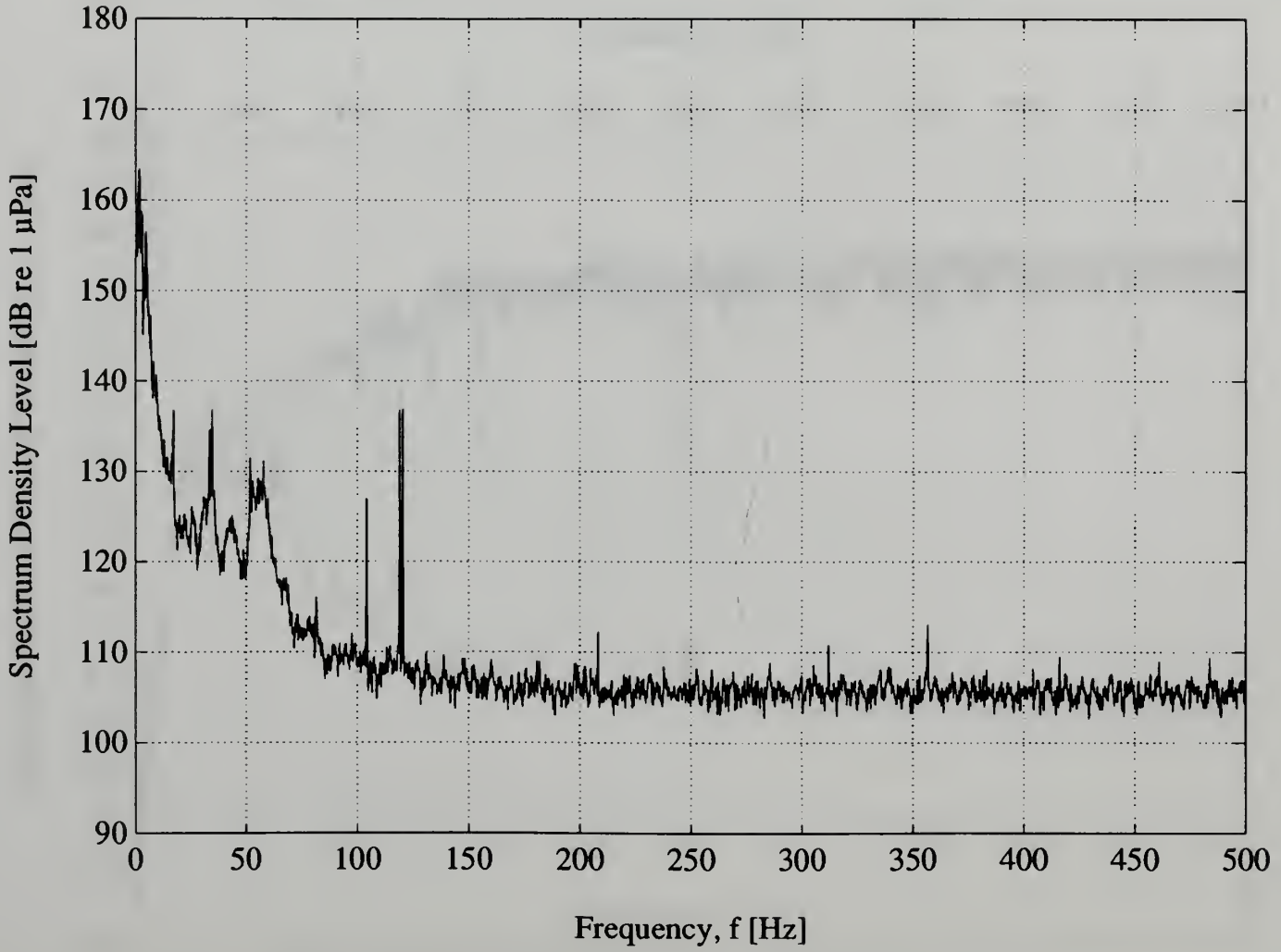

Figure C.8. Upstream Noise Spectrum, 58% Speed, 154 GPM

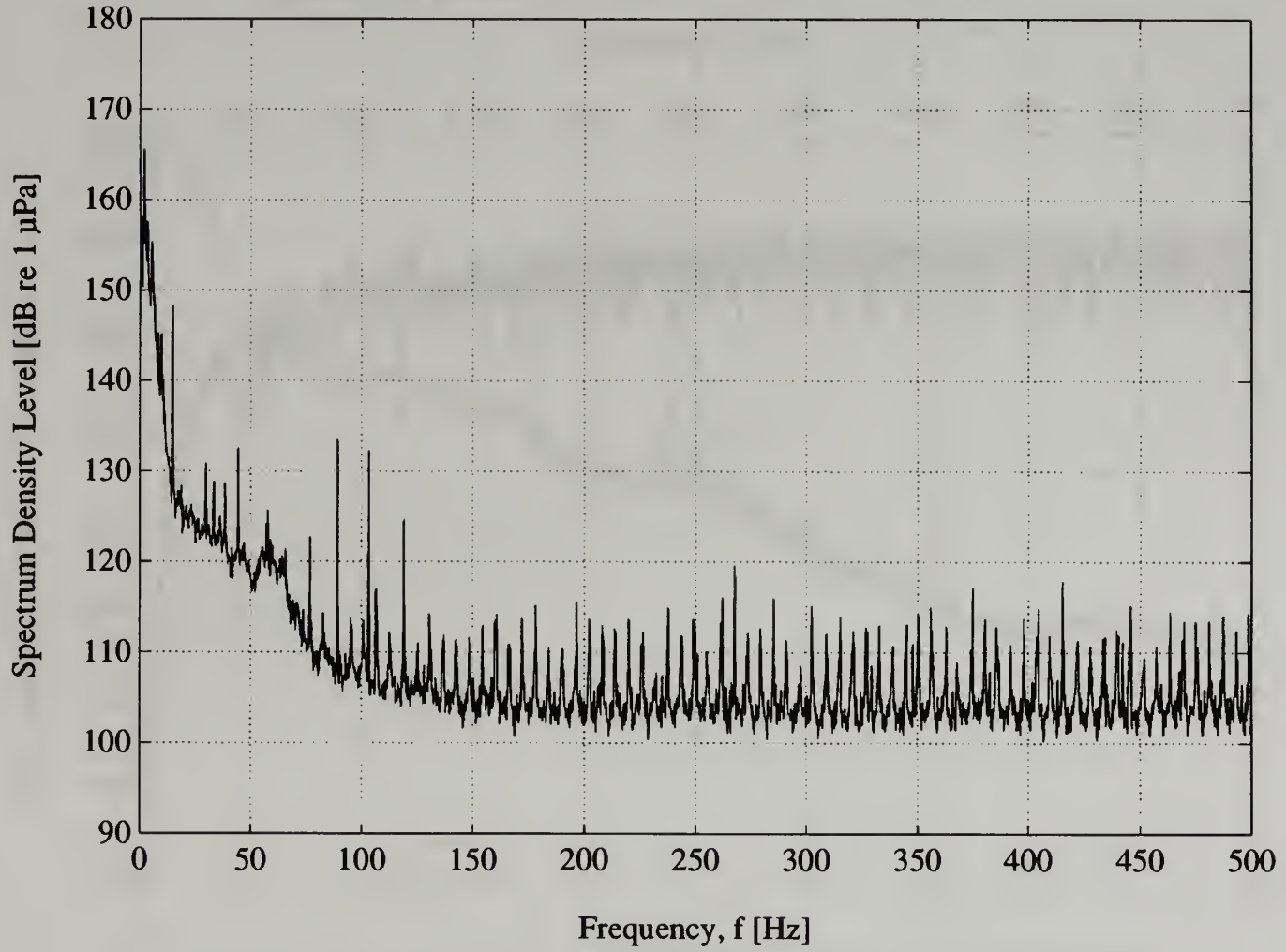

Figure C.9. Upstream Noise Spectrum, 50% Speed, 155 GPM

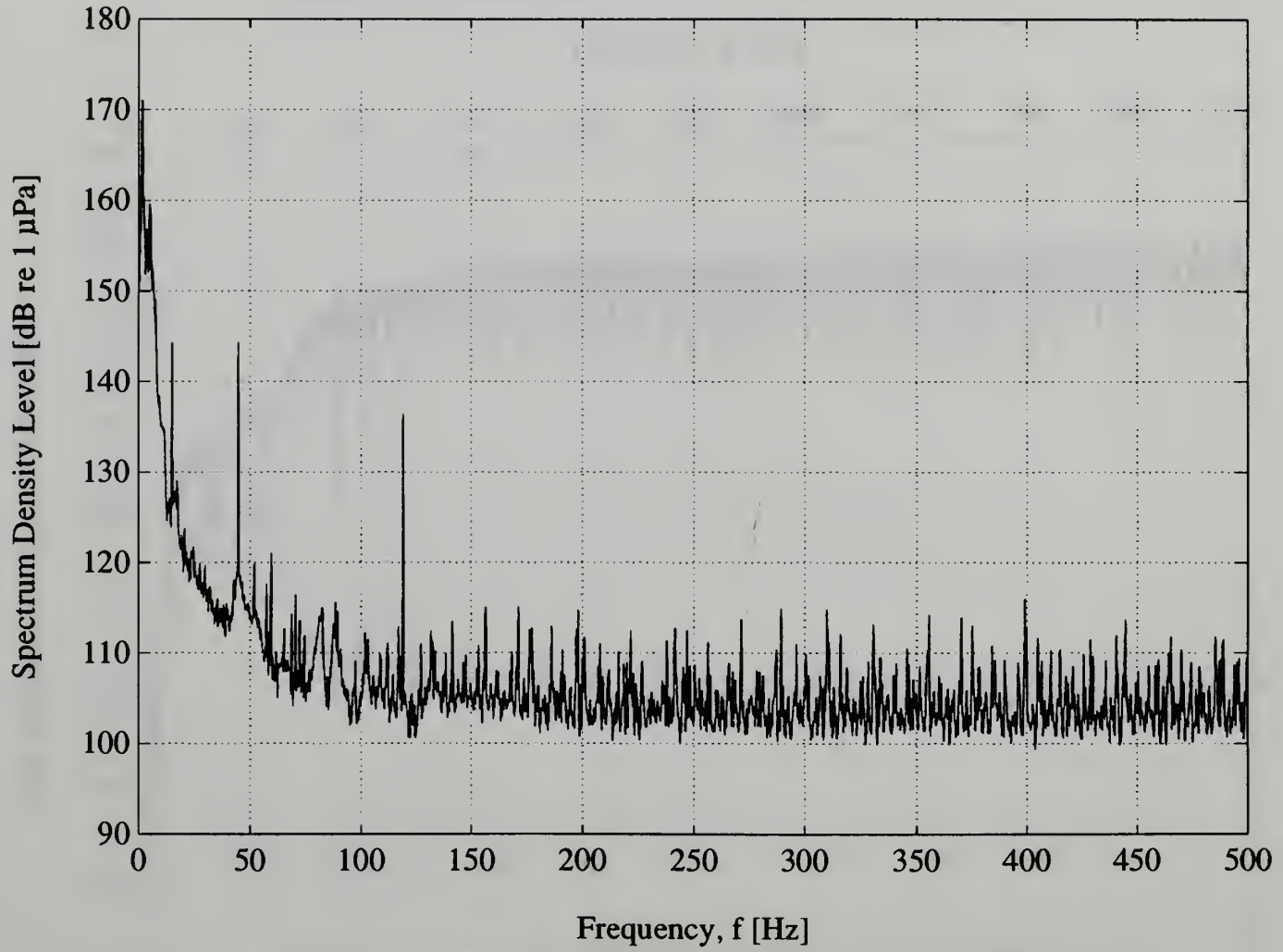

Figure C.10. Upstream Noise Spectrum, 25% Speed, 155 GPM

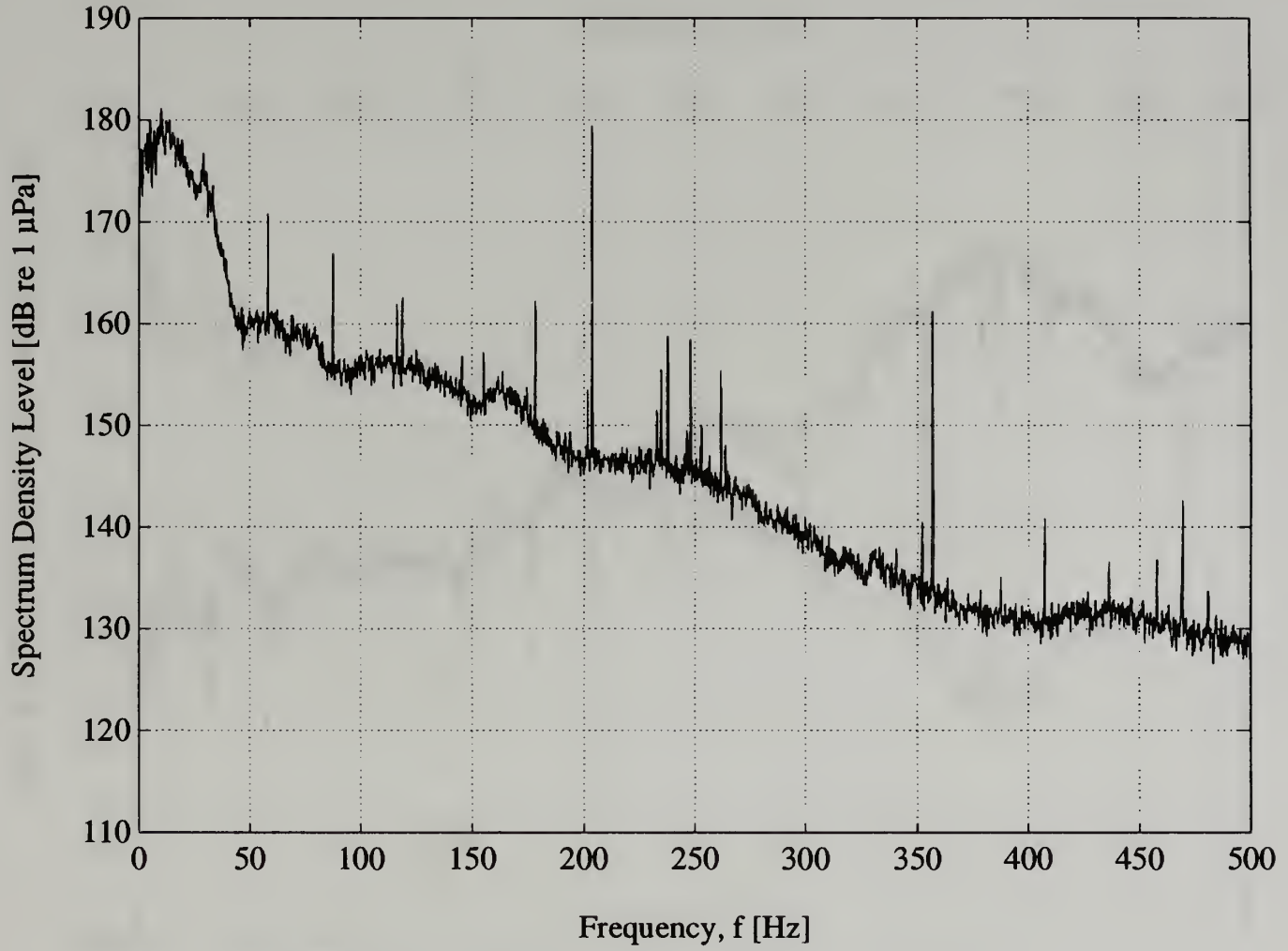

Figure C.11. Inlet Noise Spectra, 100% Speed, 480 GPM

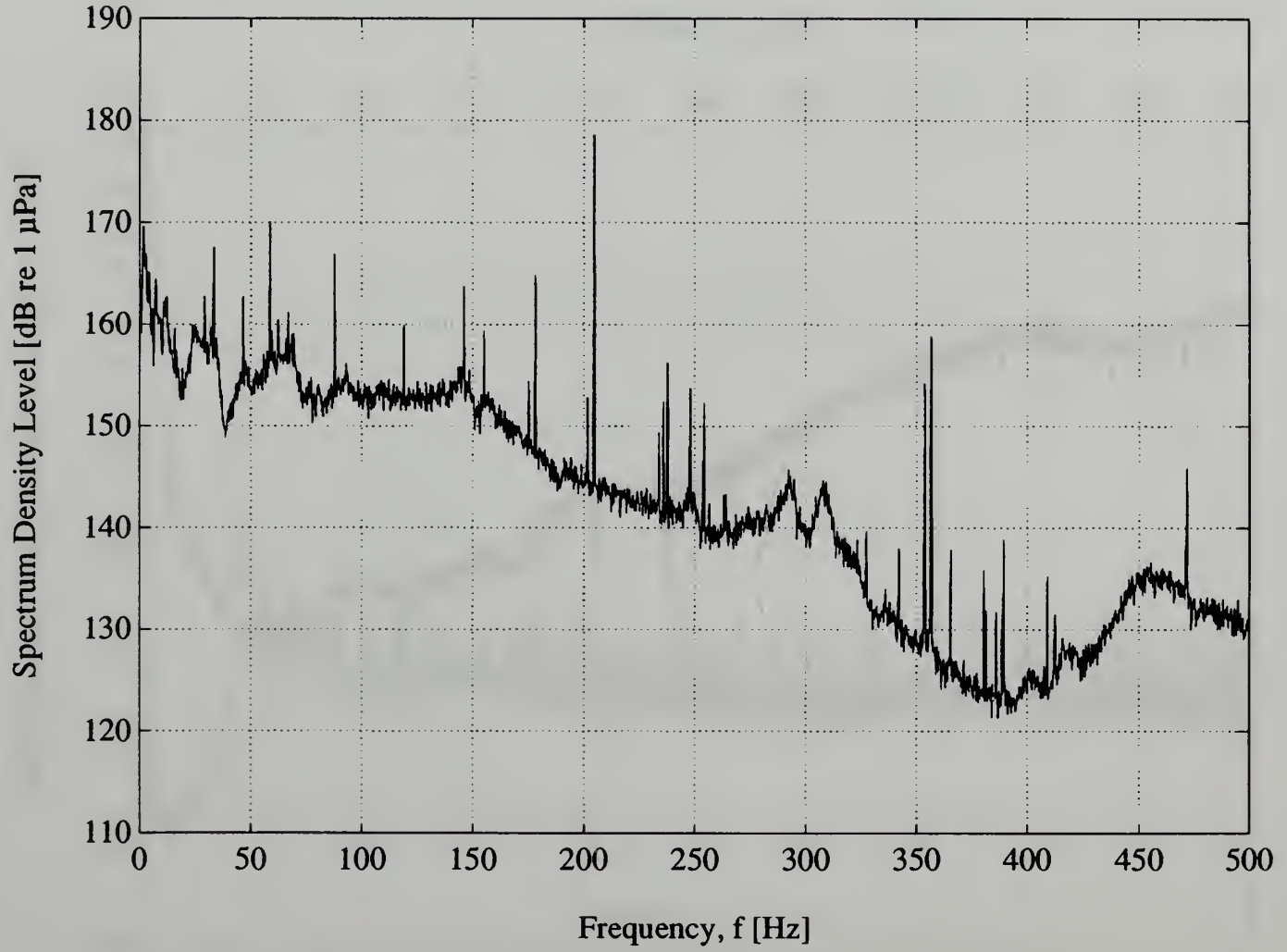

Figure C.12. Inlet Noise Spectra, 100% Speed, 333 GPM

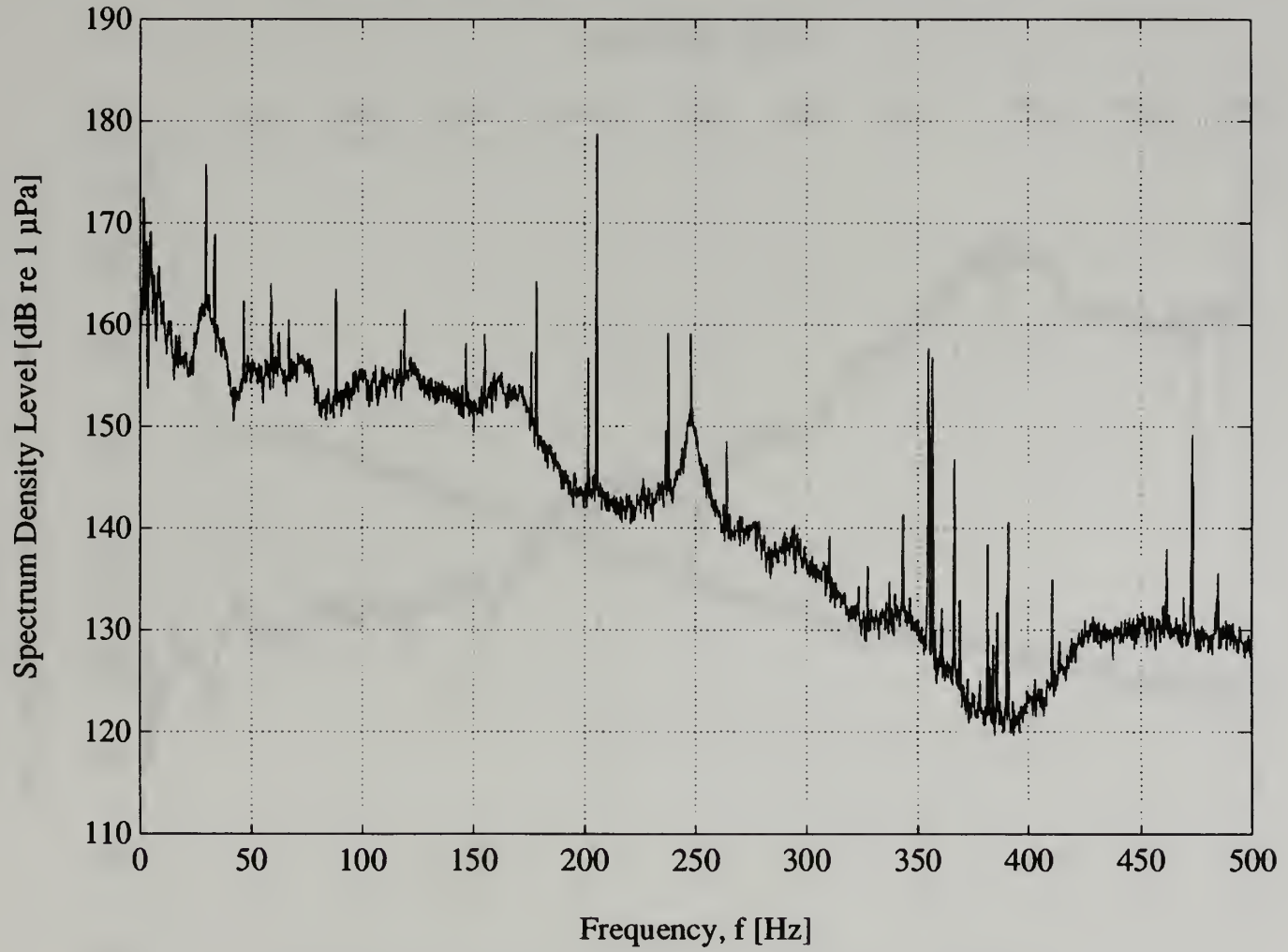

Figure C.13. Inlet Noise Spectra, 100% Speed, 210 GPM

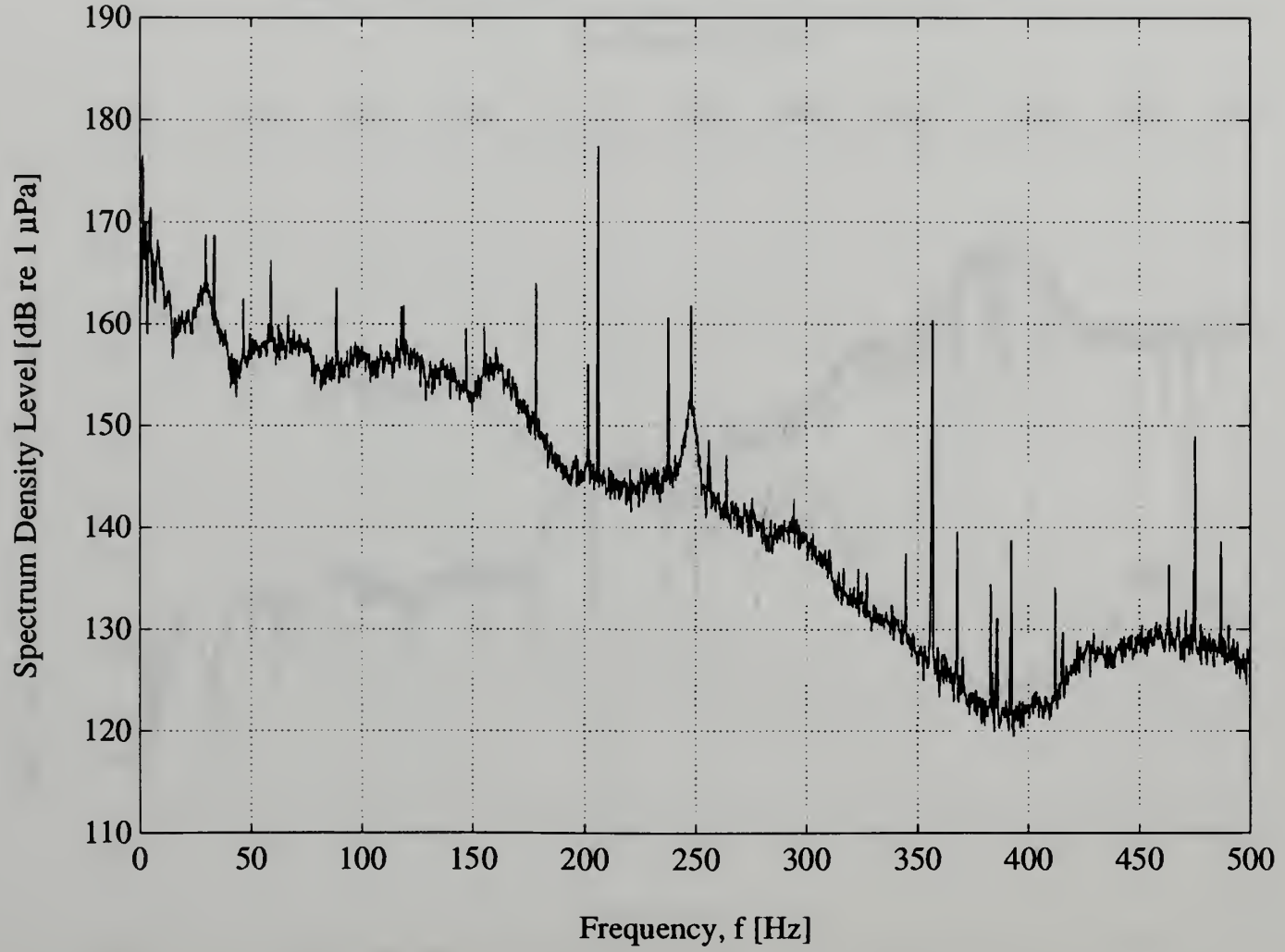

Figure C.14. Inlet Noise Spectra, 100% Speed, 126 GPM

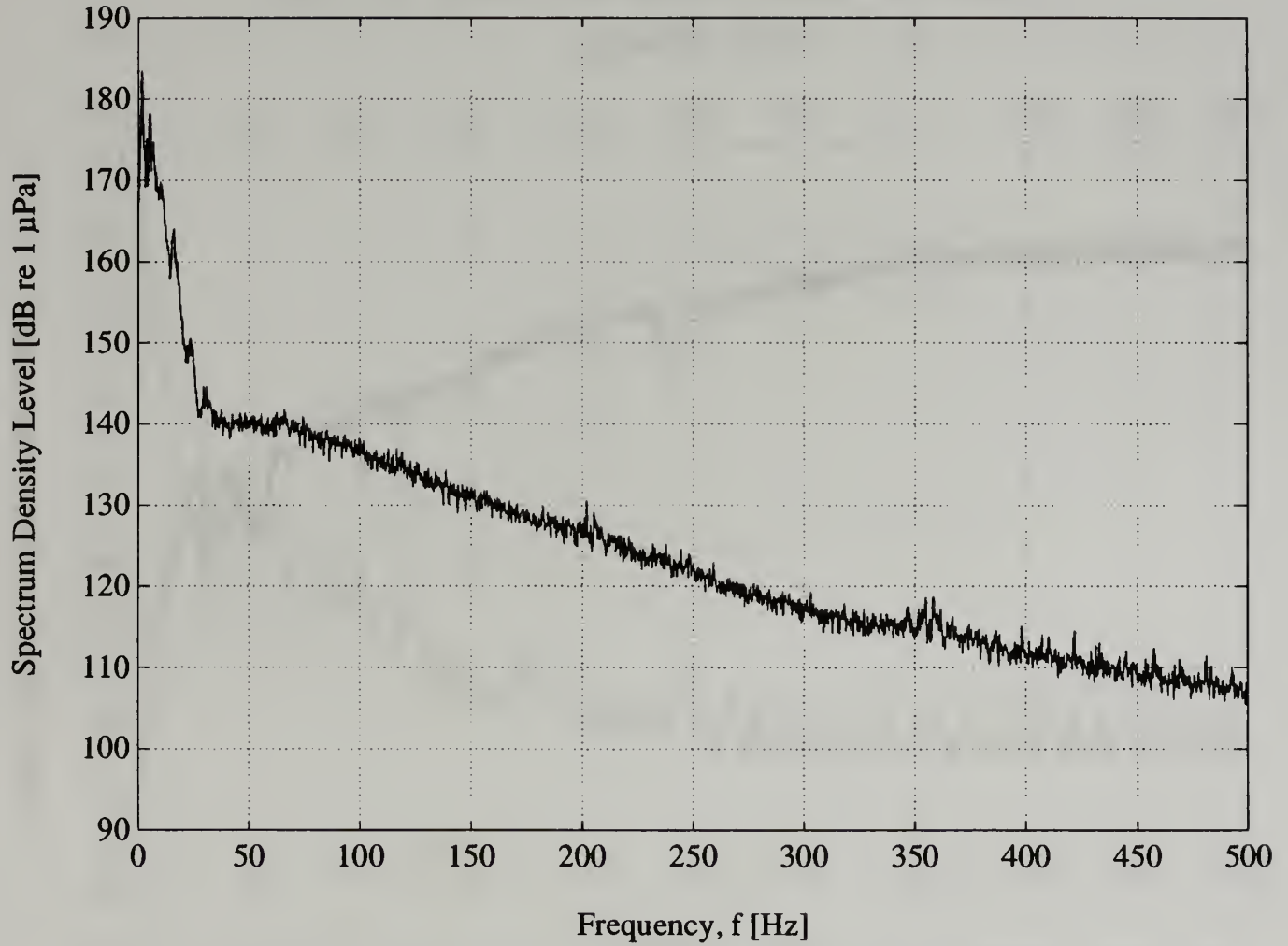

Figure C.15. Upstream Noise Spectrum, 100% Speed, 480 GPM

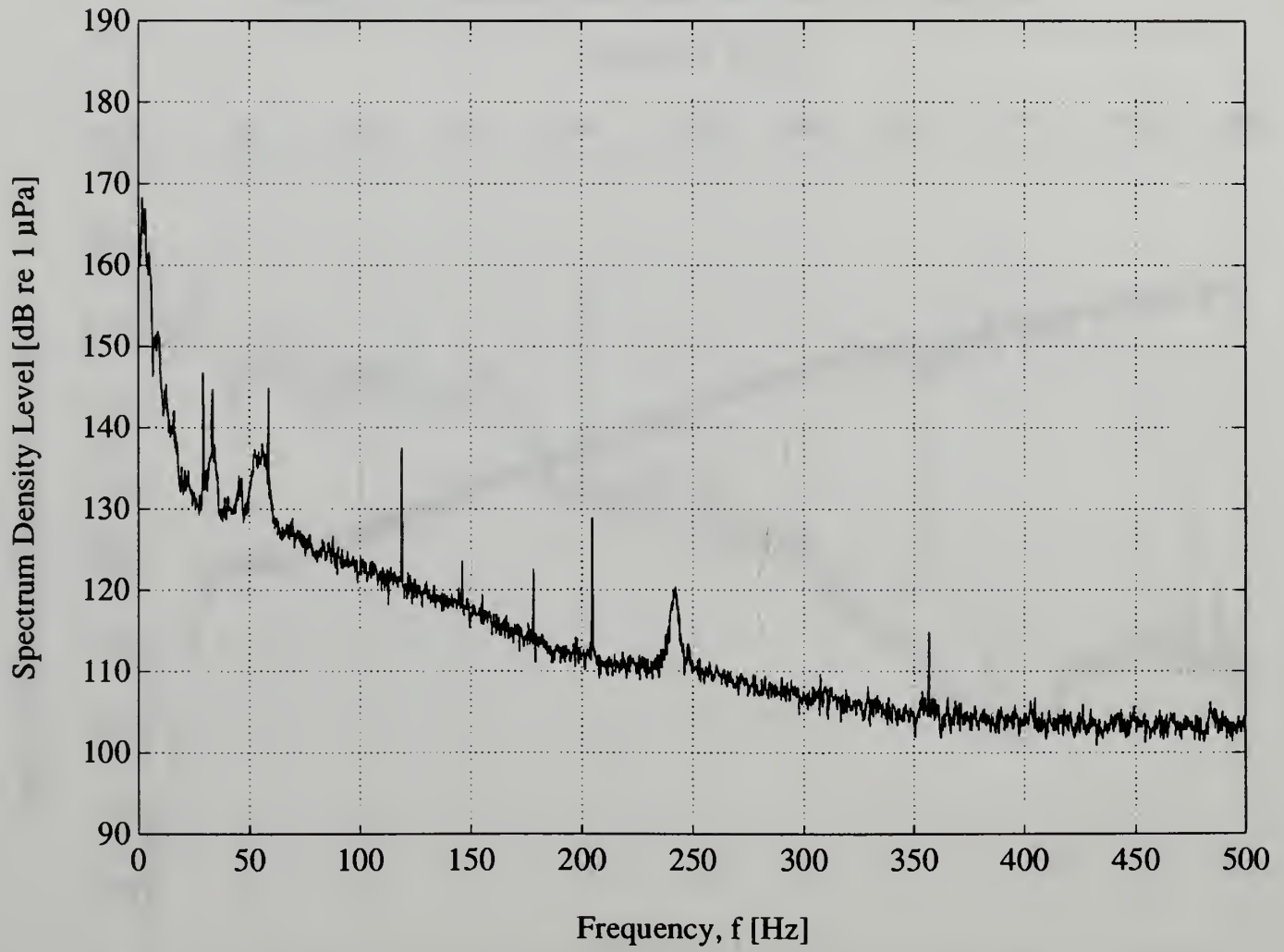

Figure C.16. Upstream Noise Spectrum, 100% Speed, 333 GPM

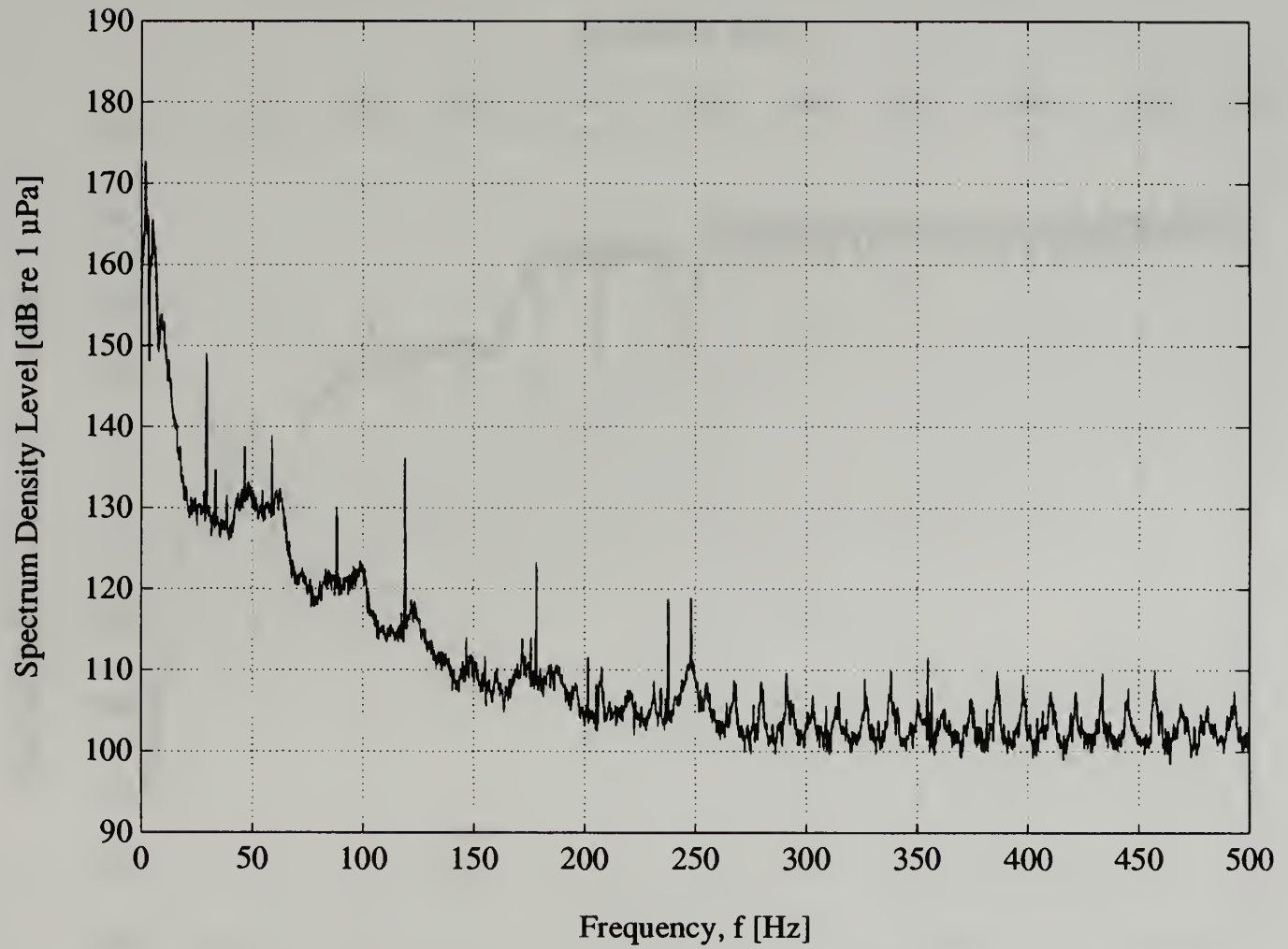

Figure C.17. Upstream Noise Spectrum, 100% Speed, 210 GPM

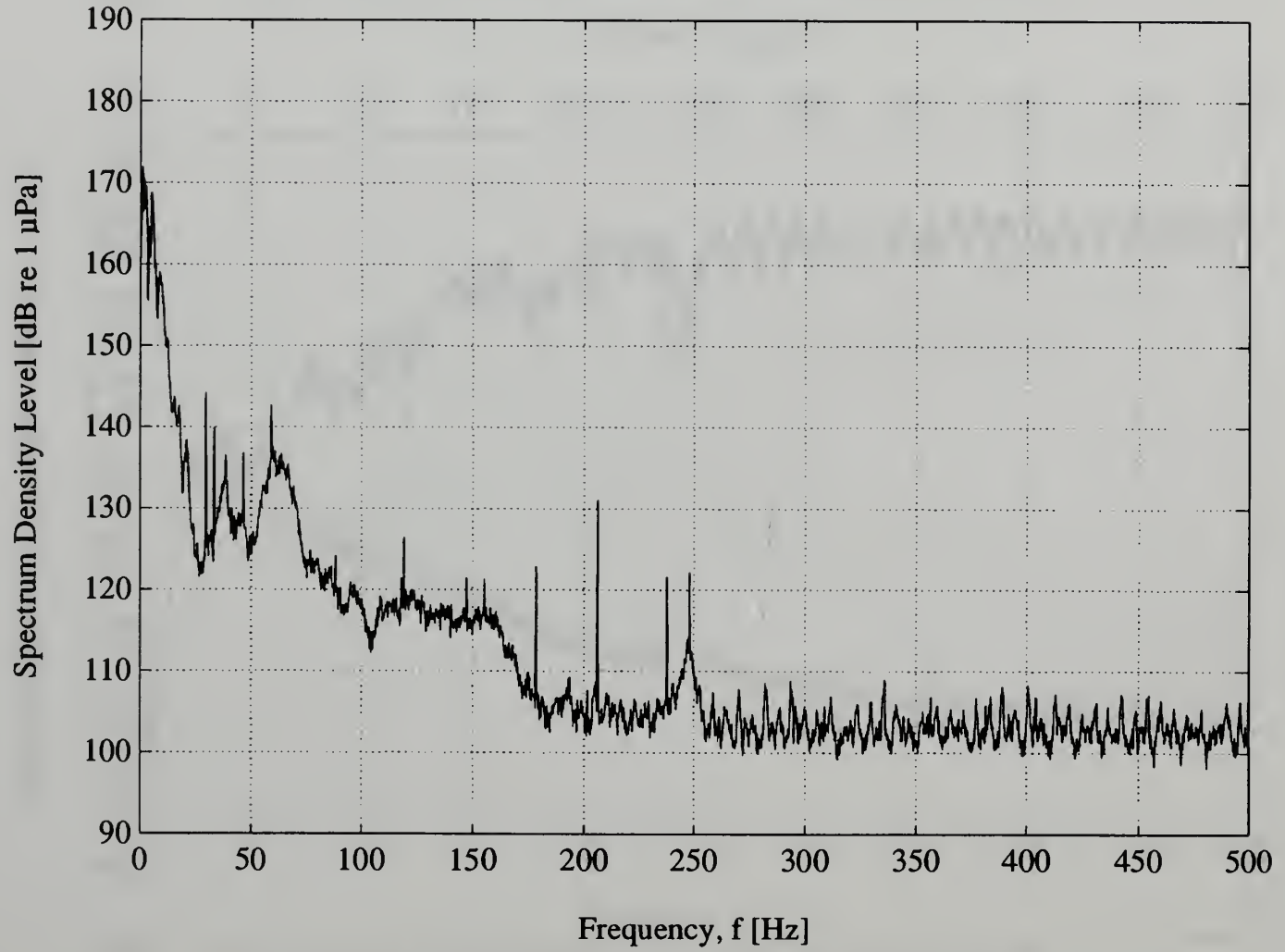

Figure C.18. Upstream Noise Spectrum, 100% Speed, 126 GPM

D. Speed/Flow Rate Effects on Tonal Noise

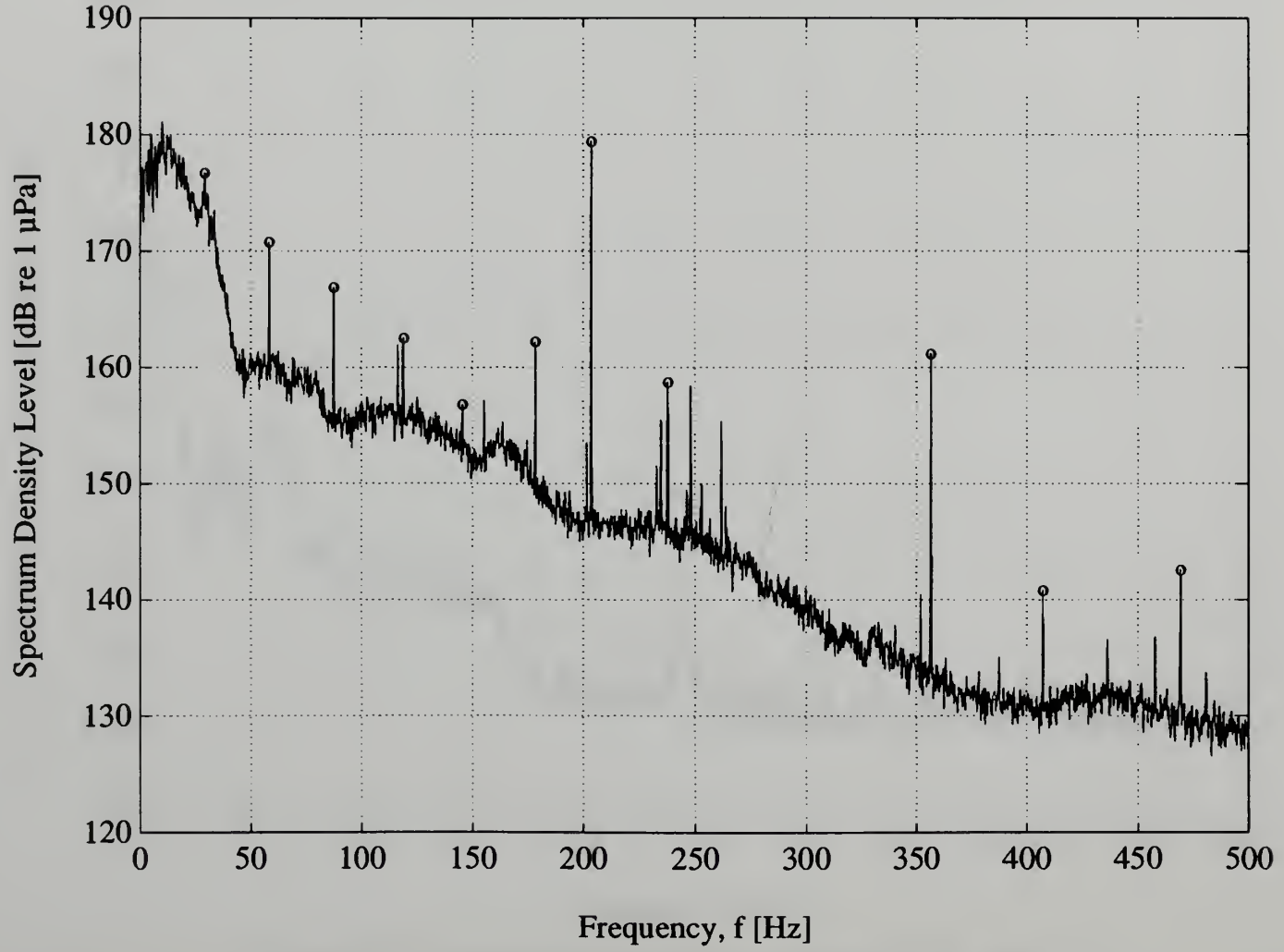

Figure D.1. Inlet Noise Spectrum, No Throttle, 100% Speed, 480 GPM

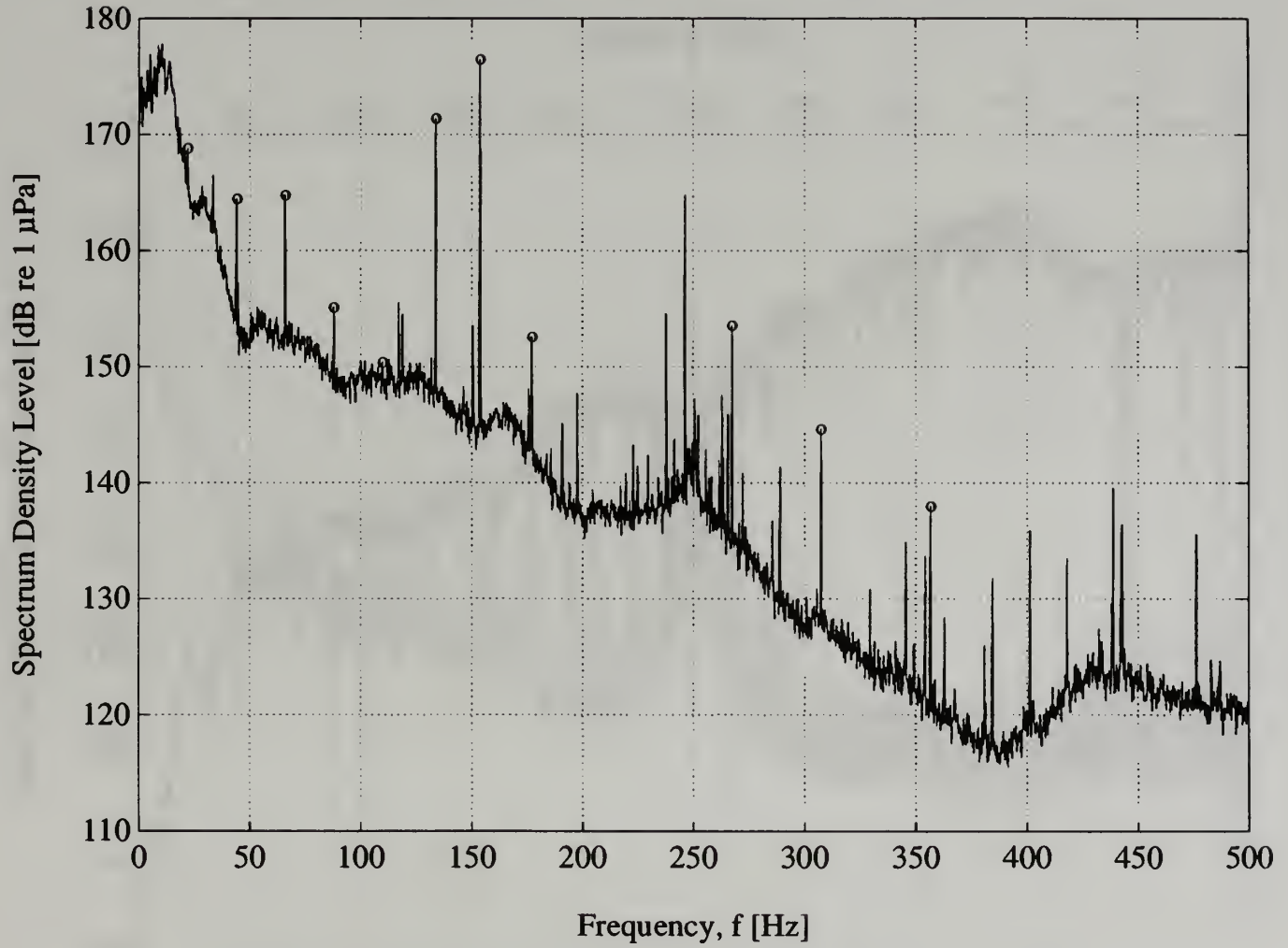

Figure D.2. Inlet Noise Spectrum, No Throttle, 75% Speed, 359 GPM

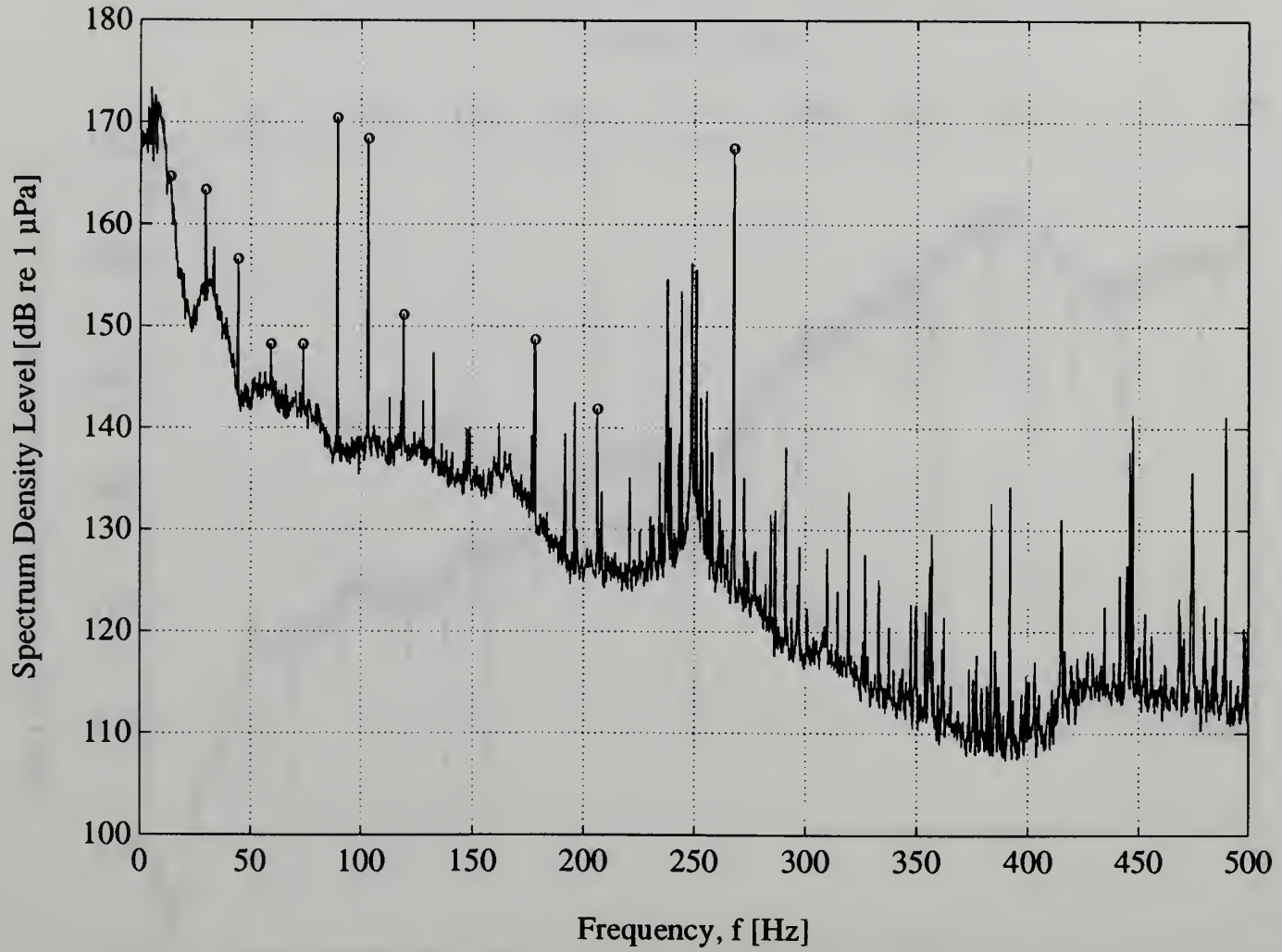

Figure D.3. Inlet Noise Spectrum, No Throttle, 50% Speed, 223 GPM

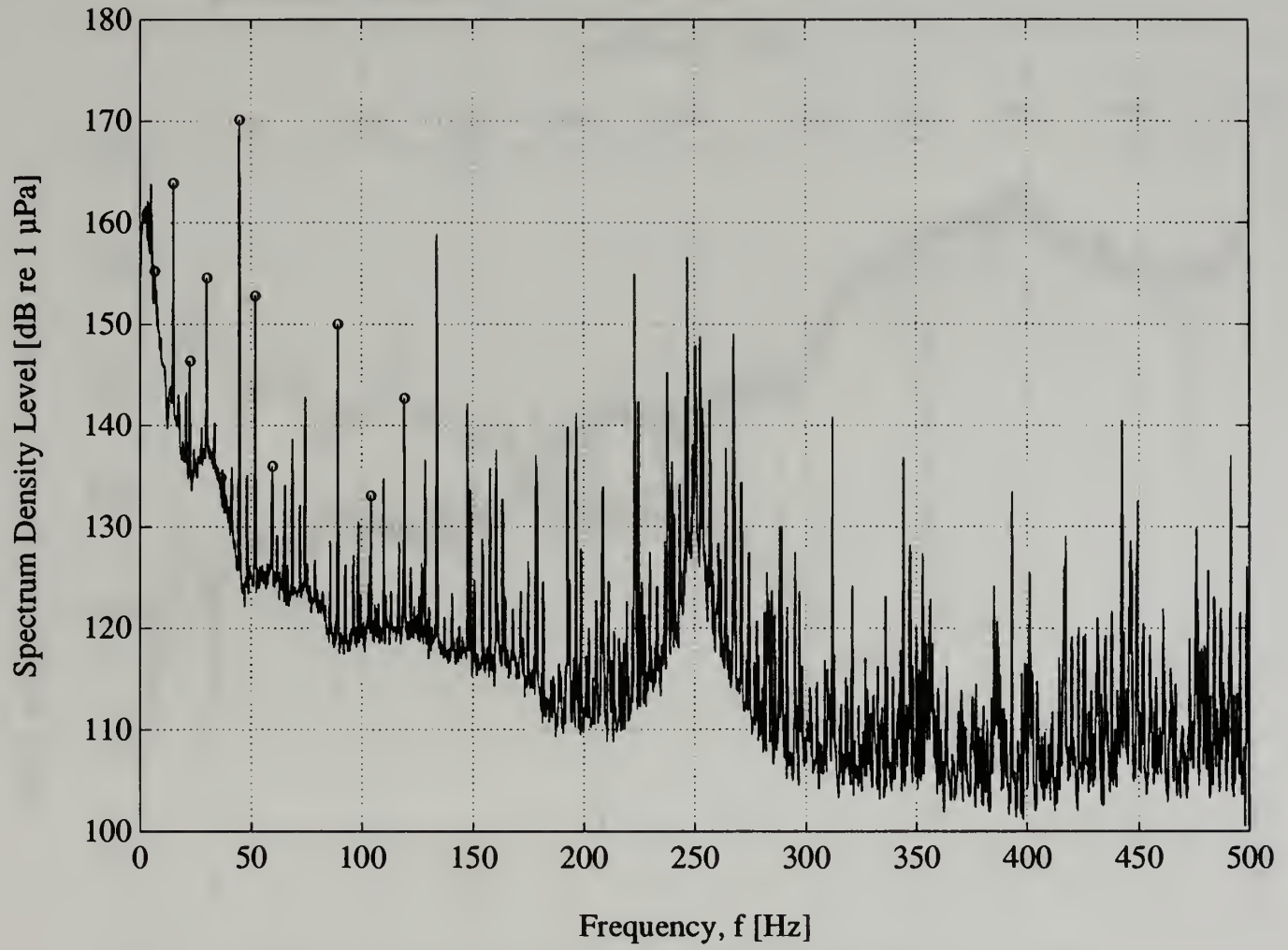

Figure D.4. Inlet Noise Spectrum, No Throttle, 25% Speed, 155 GPM

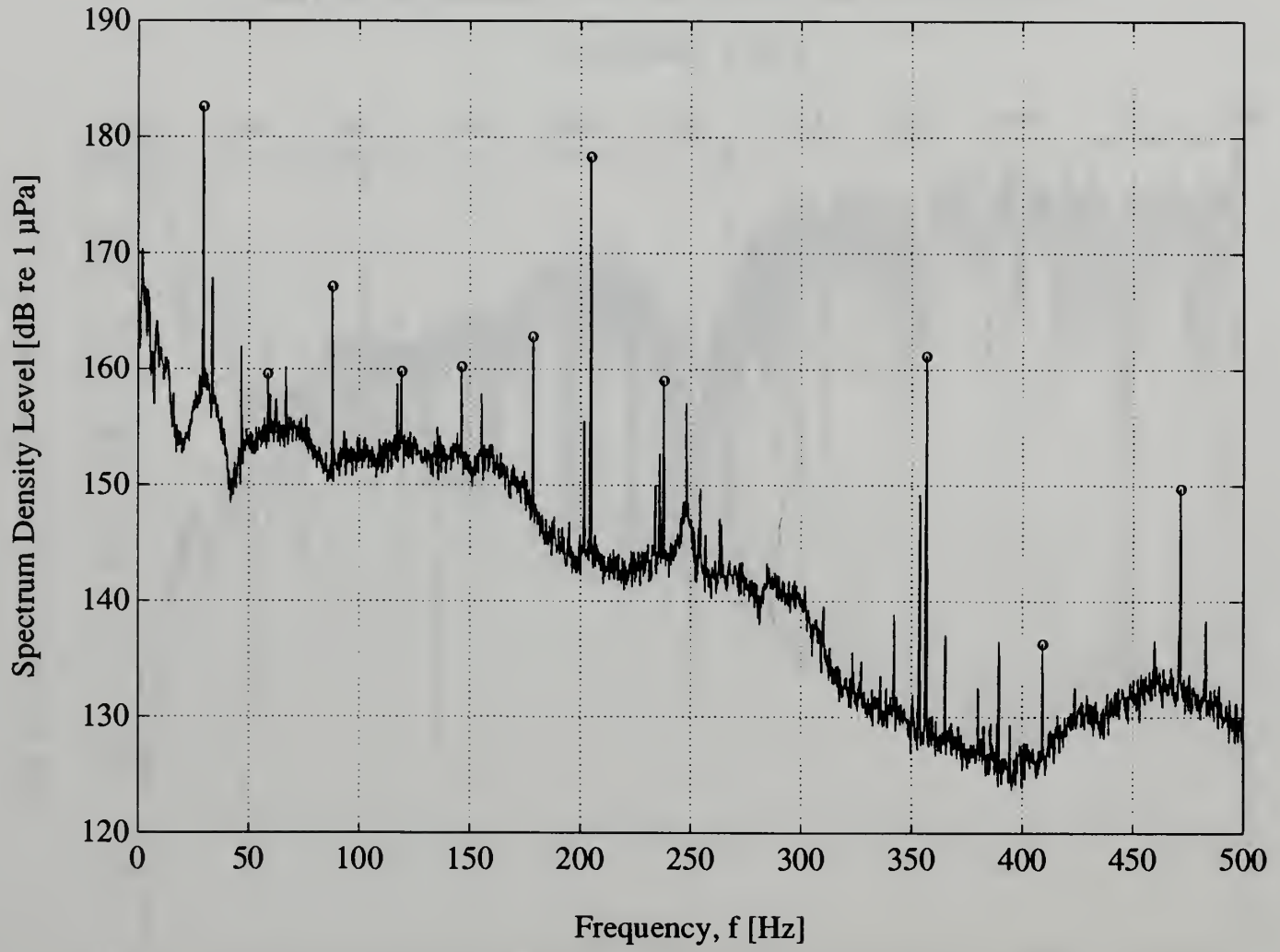

Figure D.5. Inlet Noise Spectrum, High Throttle, 100% Speed, 314 GPM

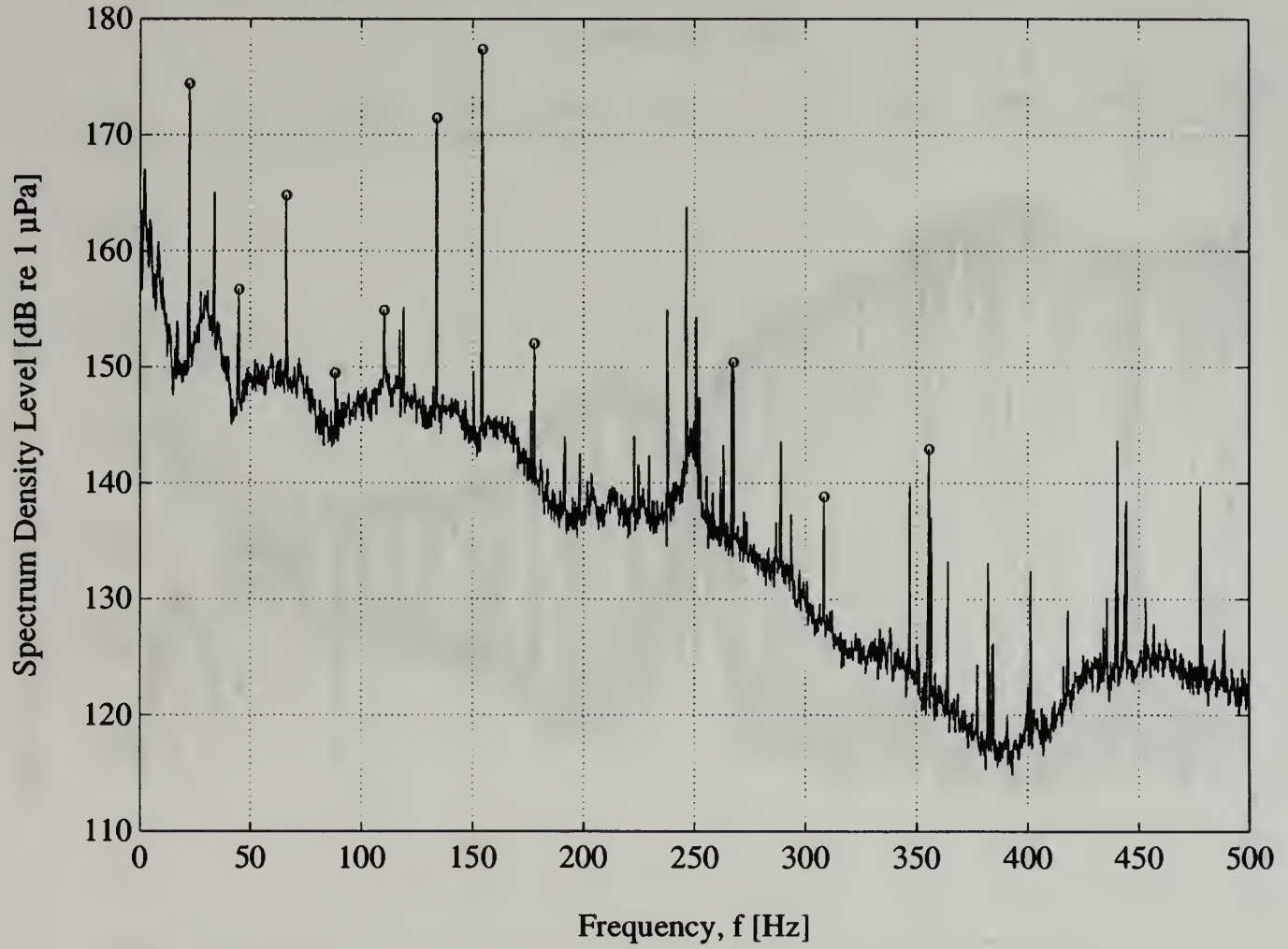

Figure D.6. Inlet Noise Spectrum, High Throttle, 75% Speed, 234 GPM

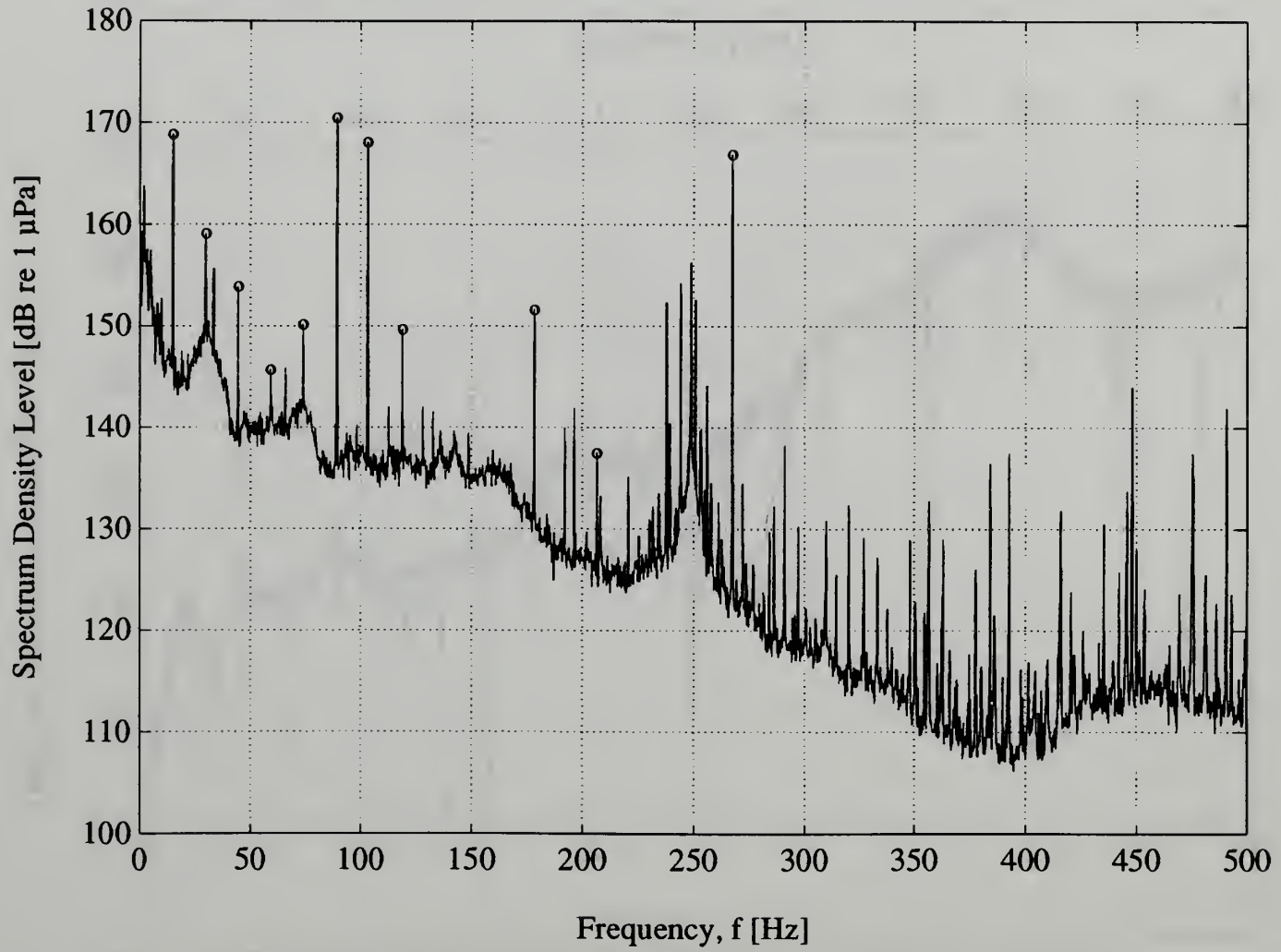

Figure D.7. Inlet Noise Spectrum, High Throttle, 50% Speed, 155 GPM

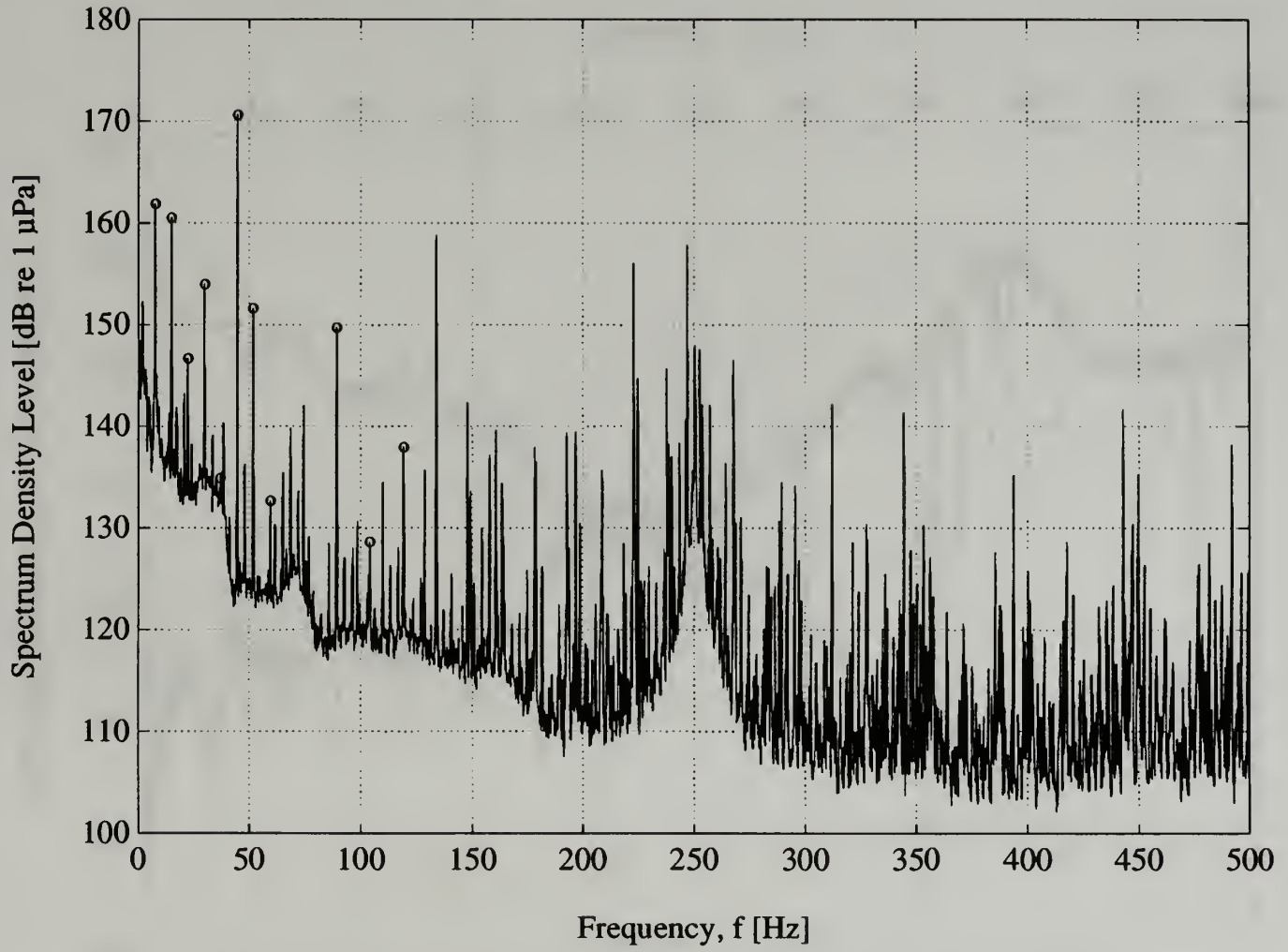

Figure D.8. Inlet Noise Spectrum, High Throttle, 25% Speed, 75 GPM

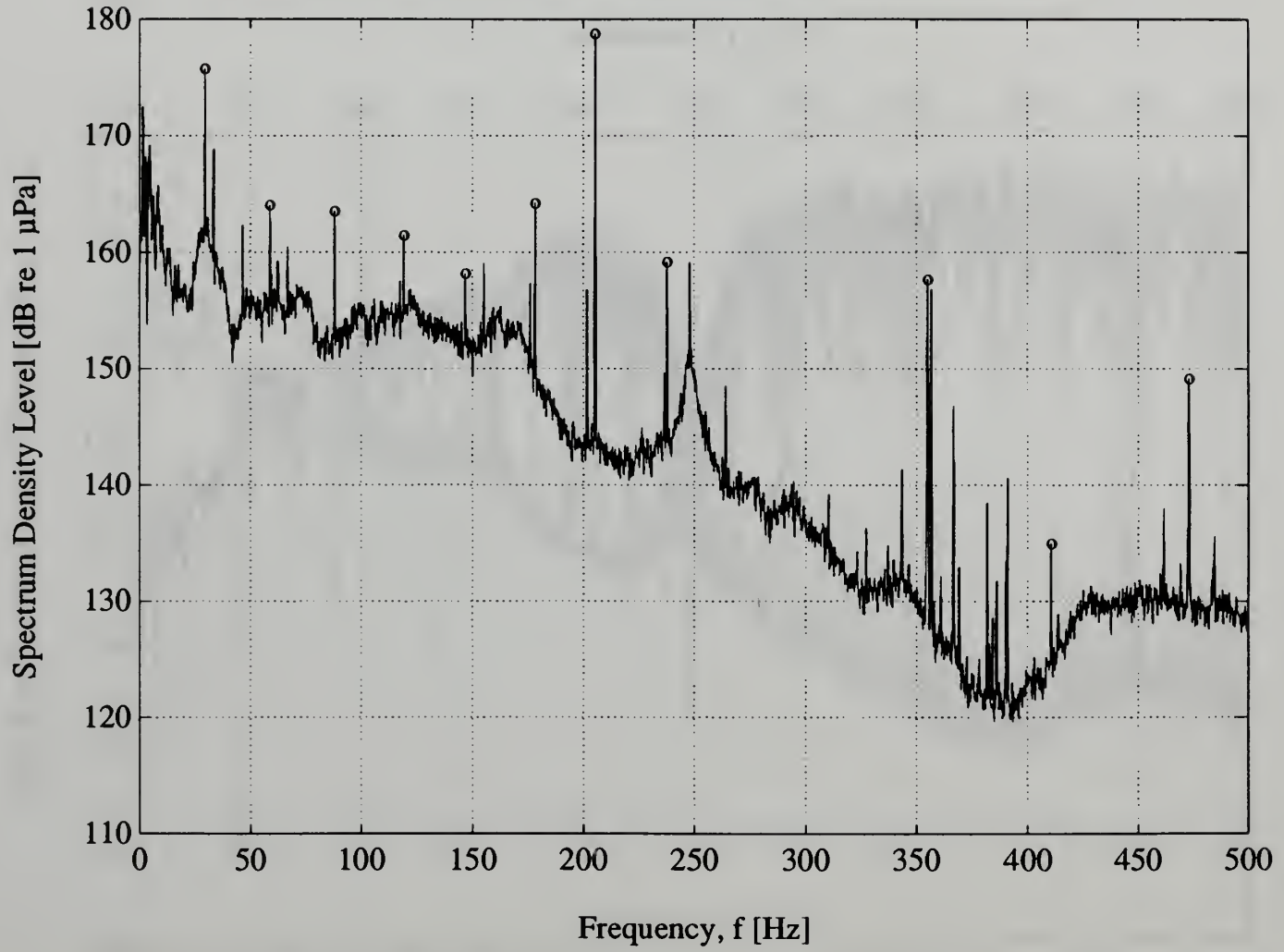

Figure D.9. Inlet Noise Spectrum, Throttle Setting B, 100% Speed, 210 GPM

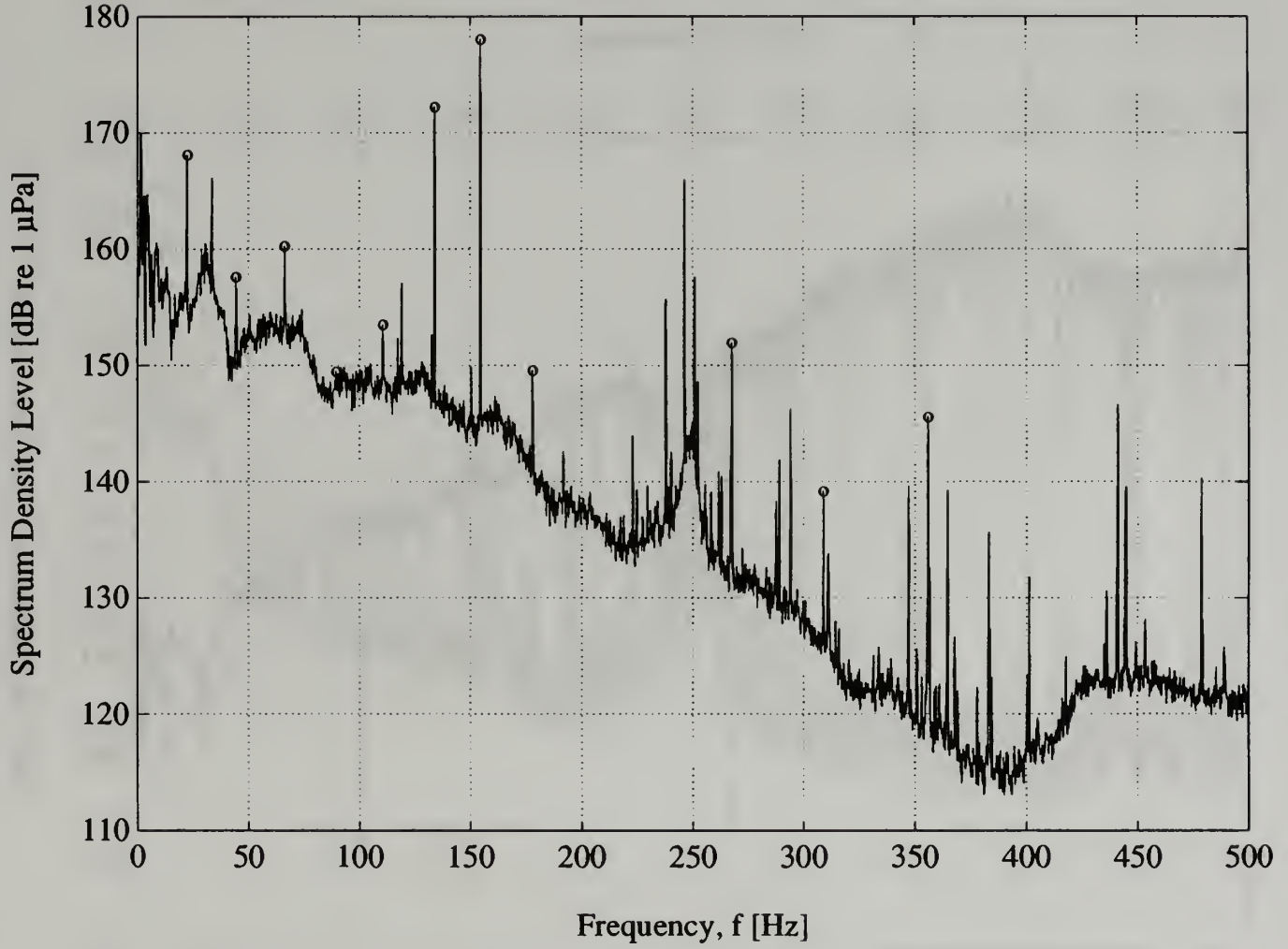

Figure D.10. Inlet Noise Spectrum, Medium Throttle, 75% Speed, 155 GPM

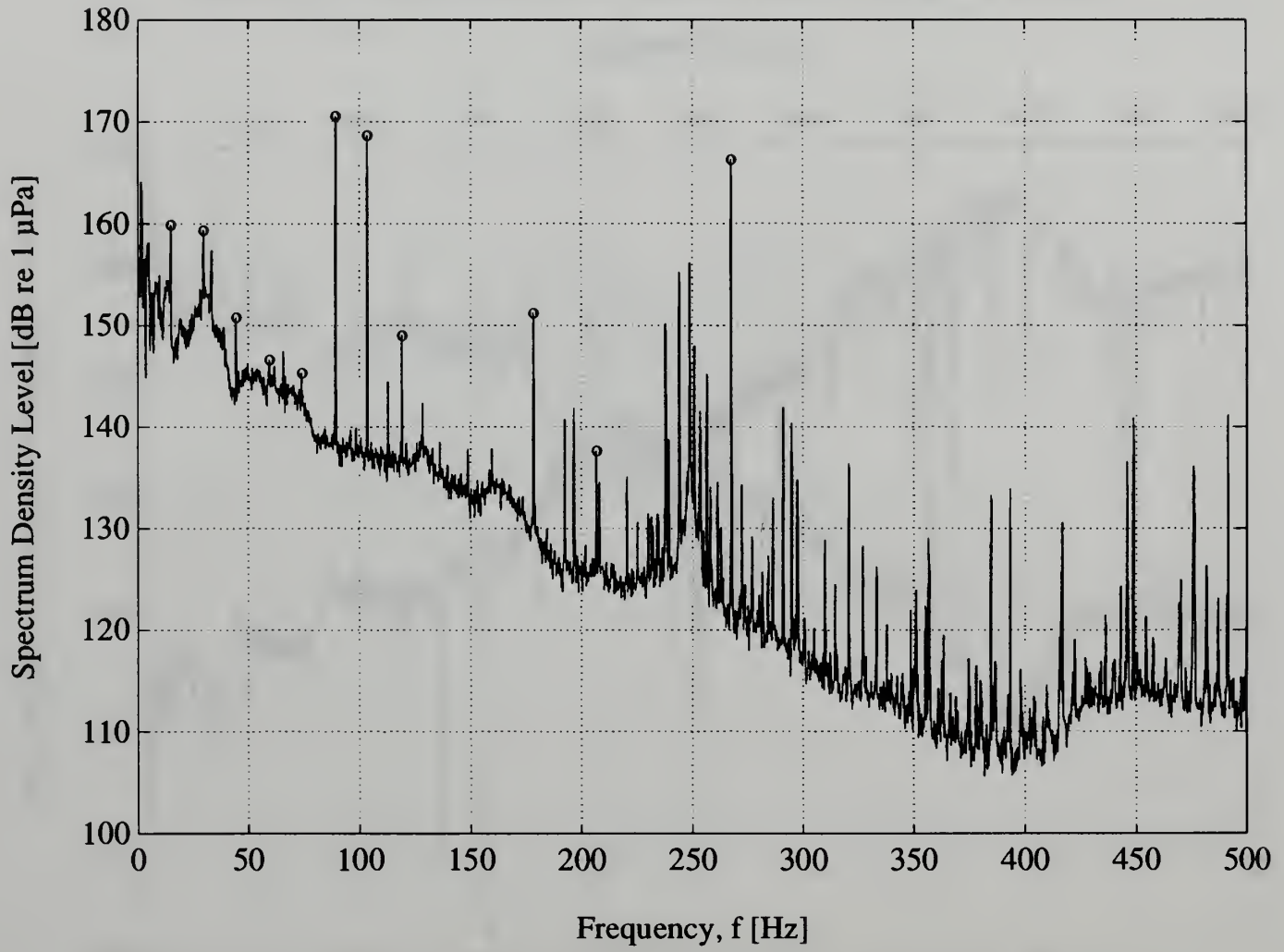

Figure D.11. Inlet Noise Spectrum, Medium Throttle, 50% Speed, 100 GPM

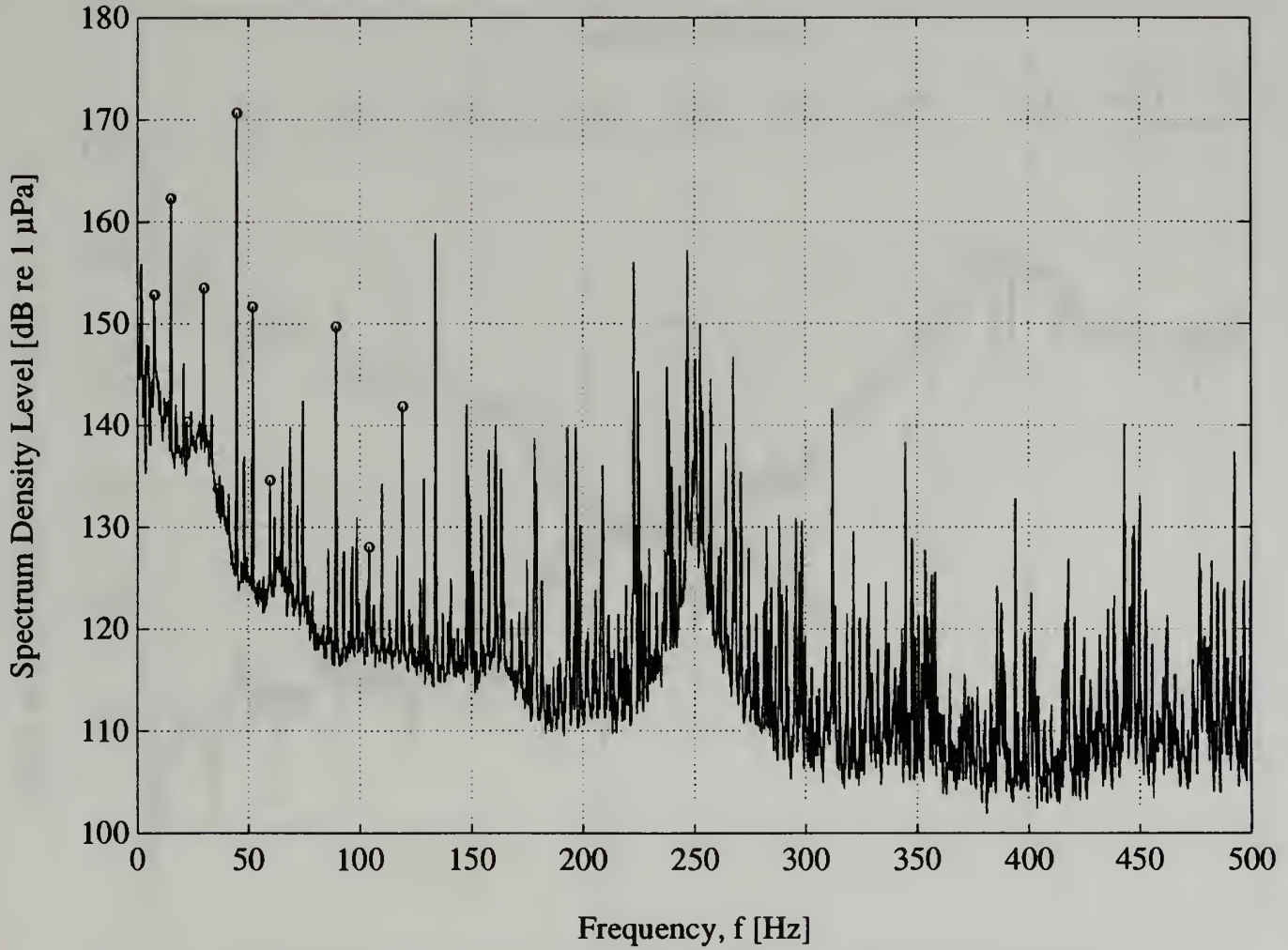

Figure D.12. Inlet Noise Spectrum, Medium Throttle, 25% Speed, 47 GPM

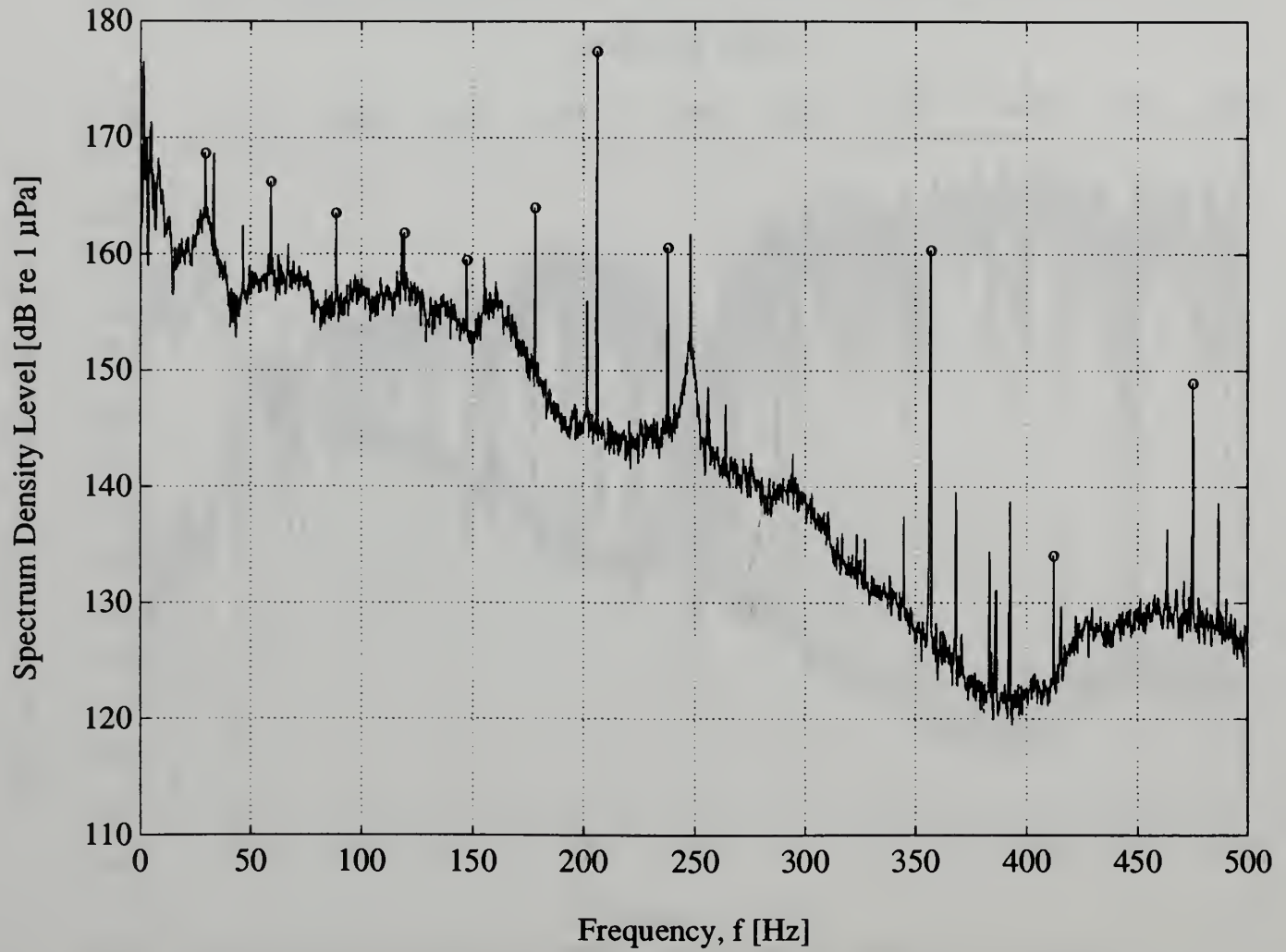

Figure D.13. Inlet Noise Spectrum, Low Throttle, 100% Speed, 126 GPM

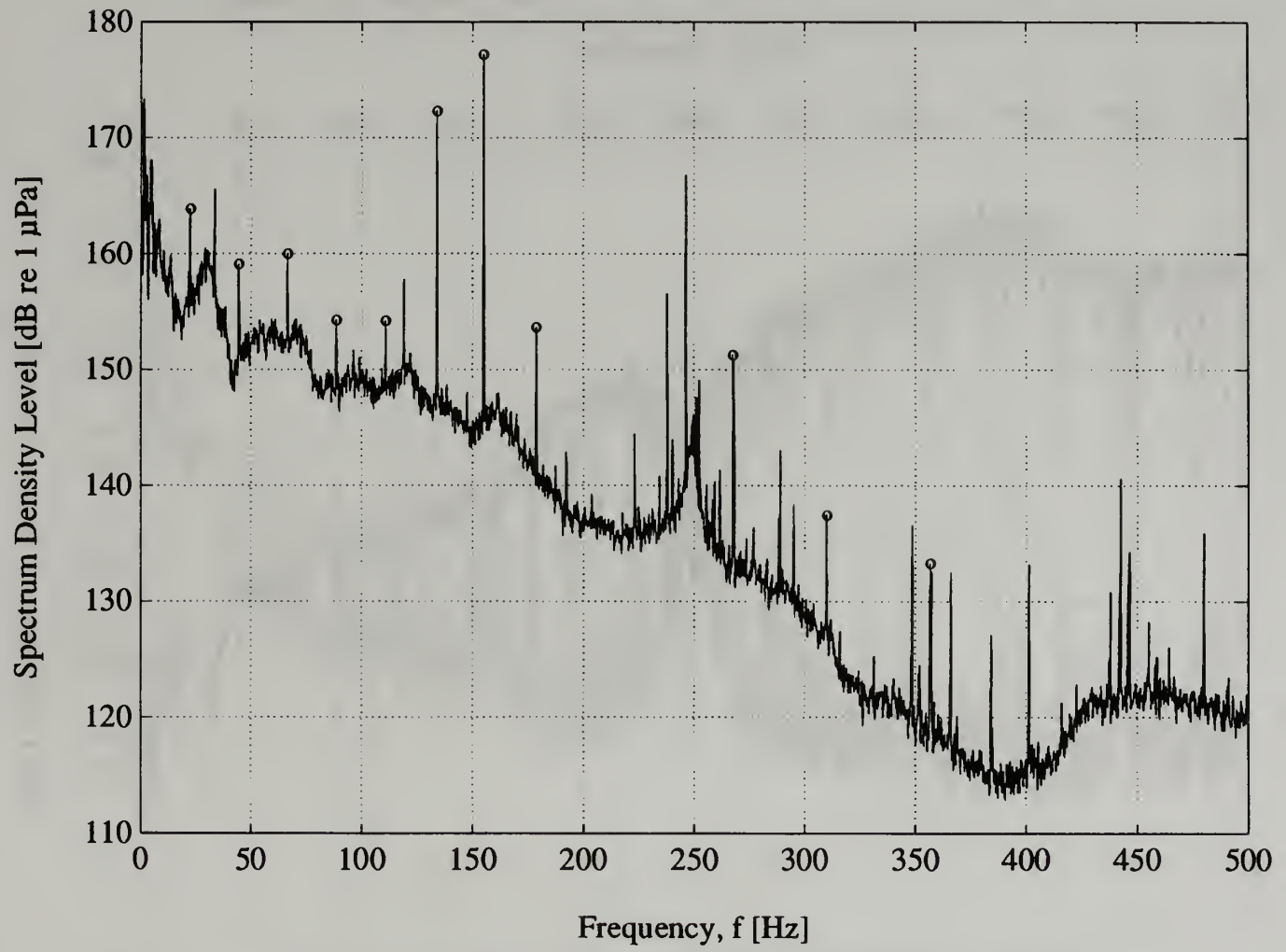

Figure D.14. Inlet Noise Spectrum, Low Throttle, 75% Speed, 92 GPM

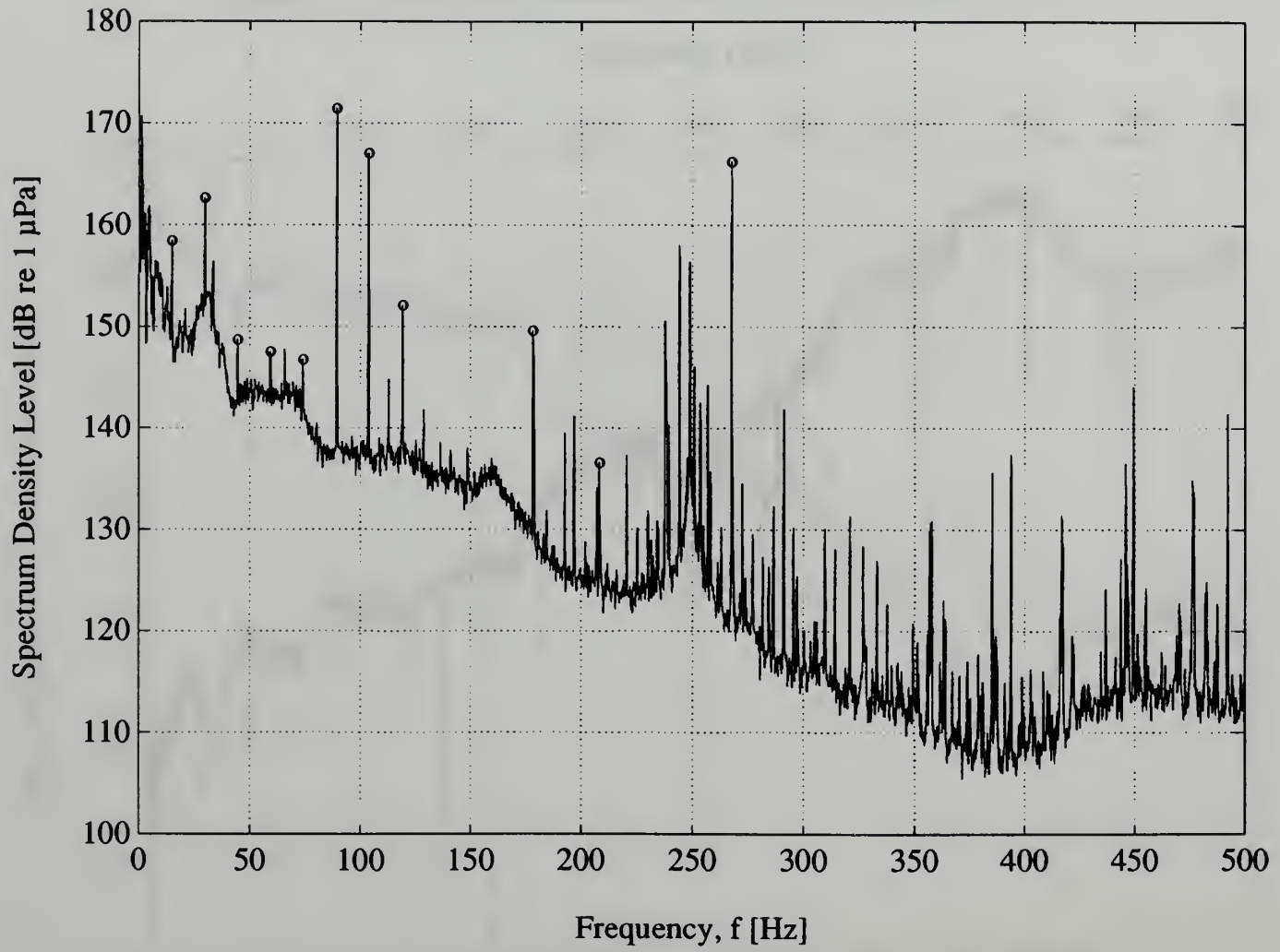

Figure D.15. Inlet Noise Spectrum, Low Throttle, 50% Speed, 59 GPM

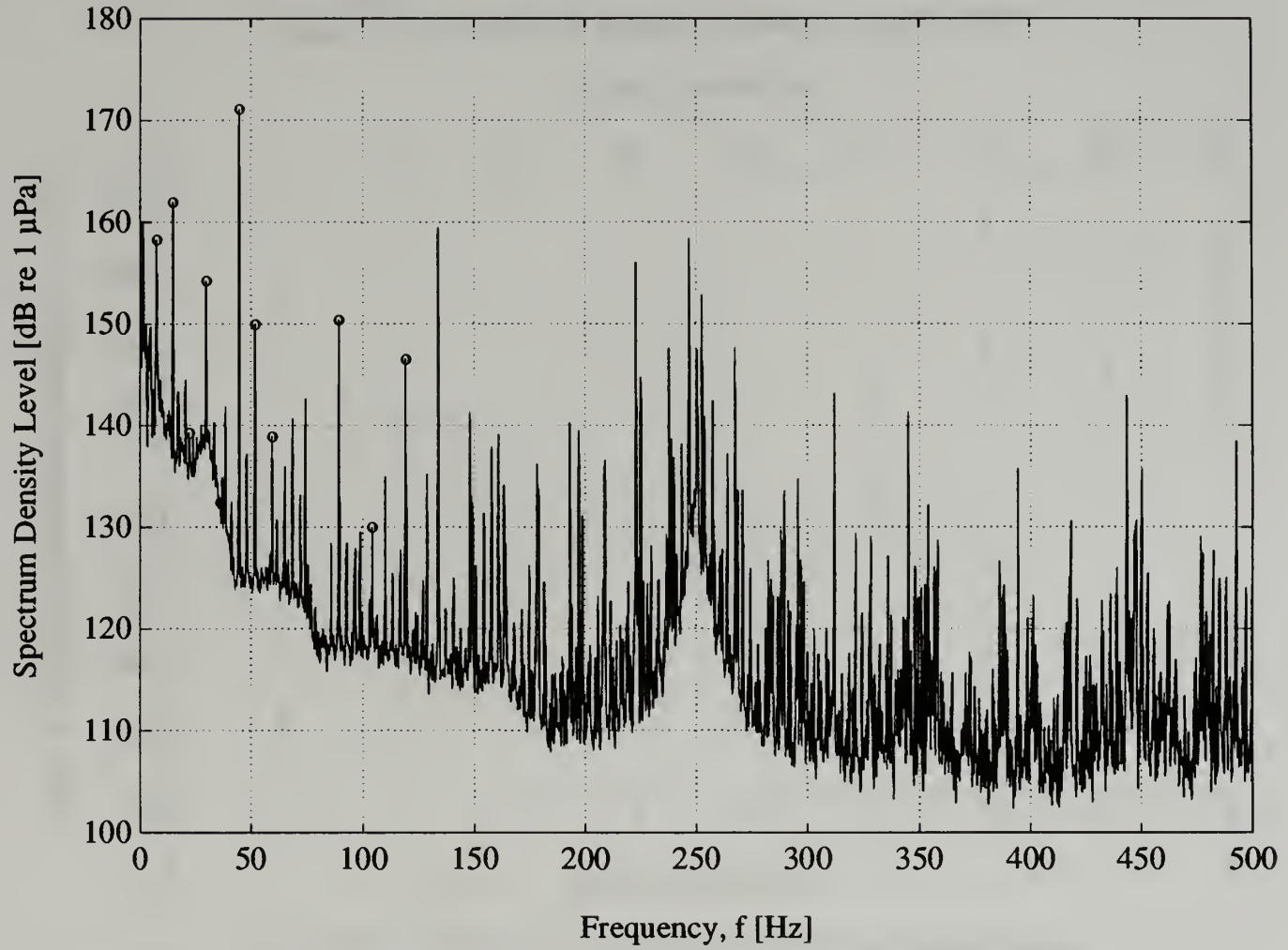

Figure D.16. Inlet Noise Spectrum, Low Throttle, 25% Speed, 28 GPM

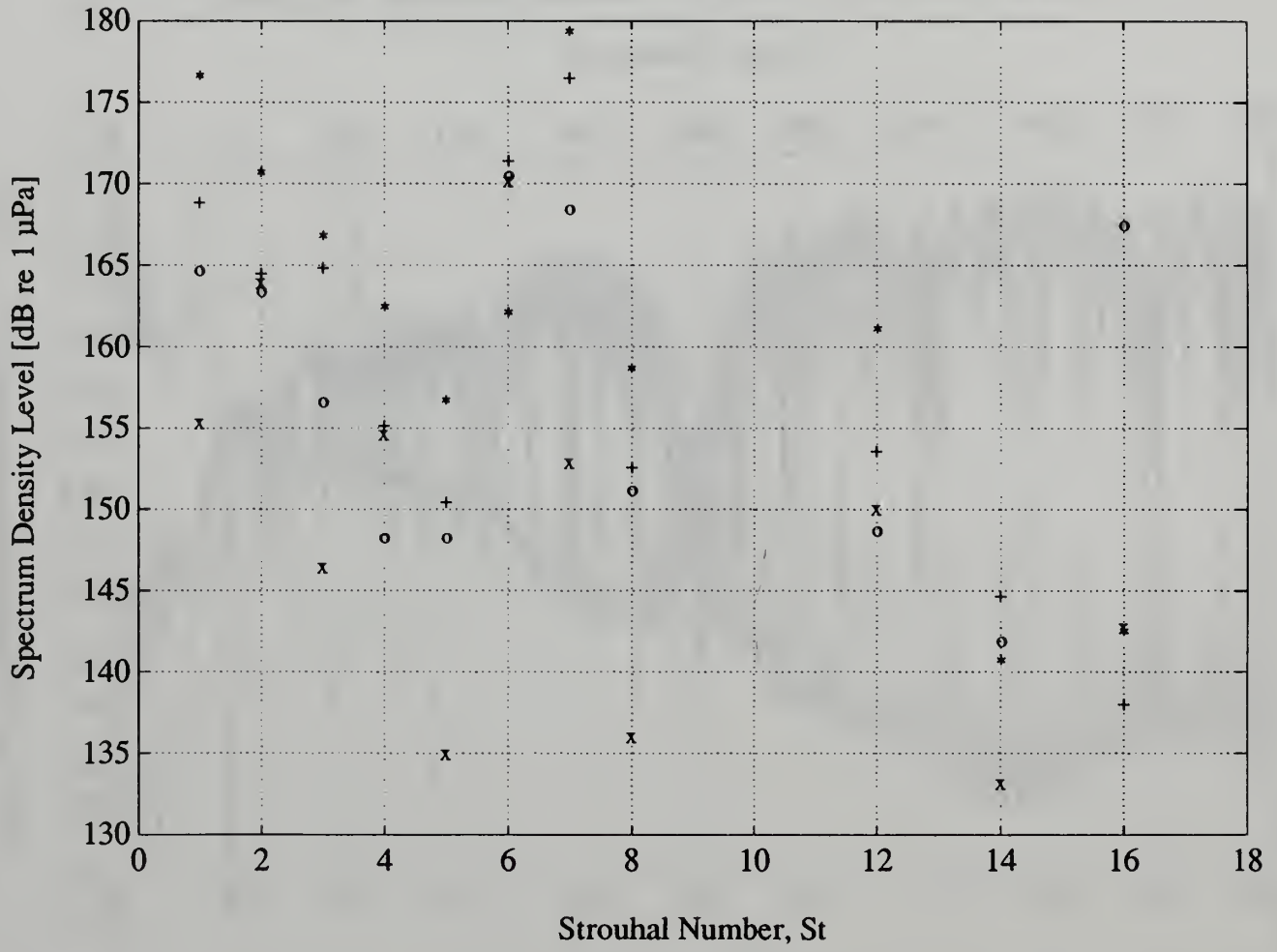

Figure D.17. Tonal Noise Levels, No Throttle, Varying Speed
(* : 100% Speed, + : 75% Speed, o : 50% Speed, x : 25% Speed)

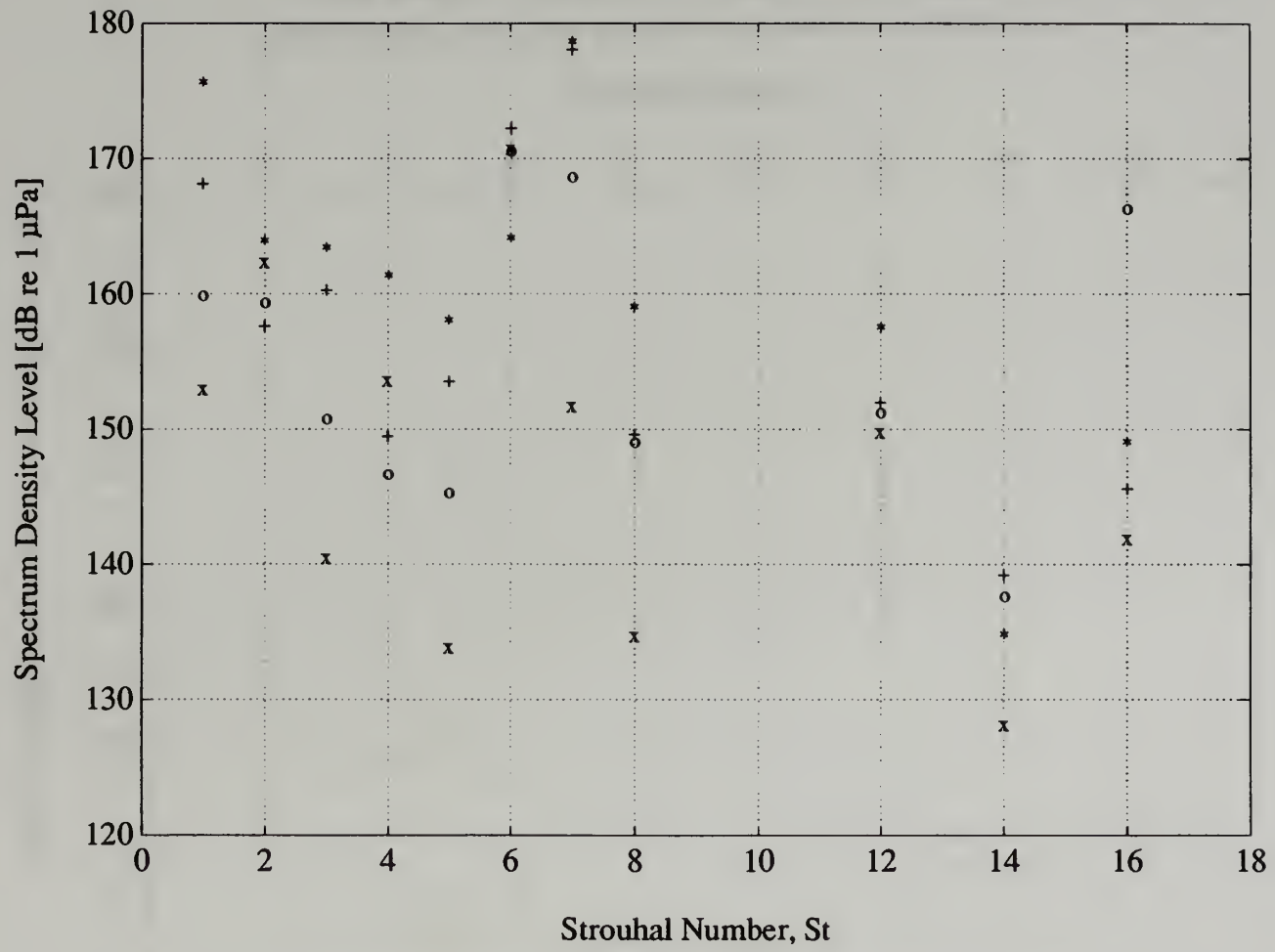

Figure D.18. Tonal Noise Levels, Medium Throttle, Varying Speed
(* : 100% Speed, + : 75% Speed, o : 50% Speed, x : 25% Speed)

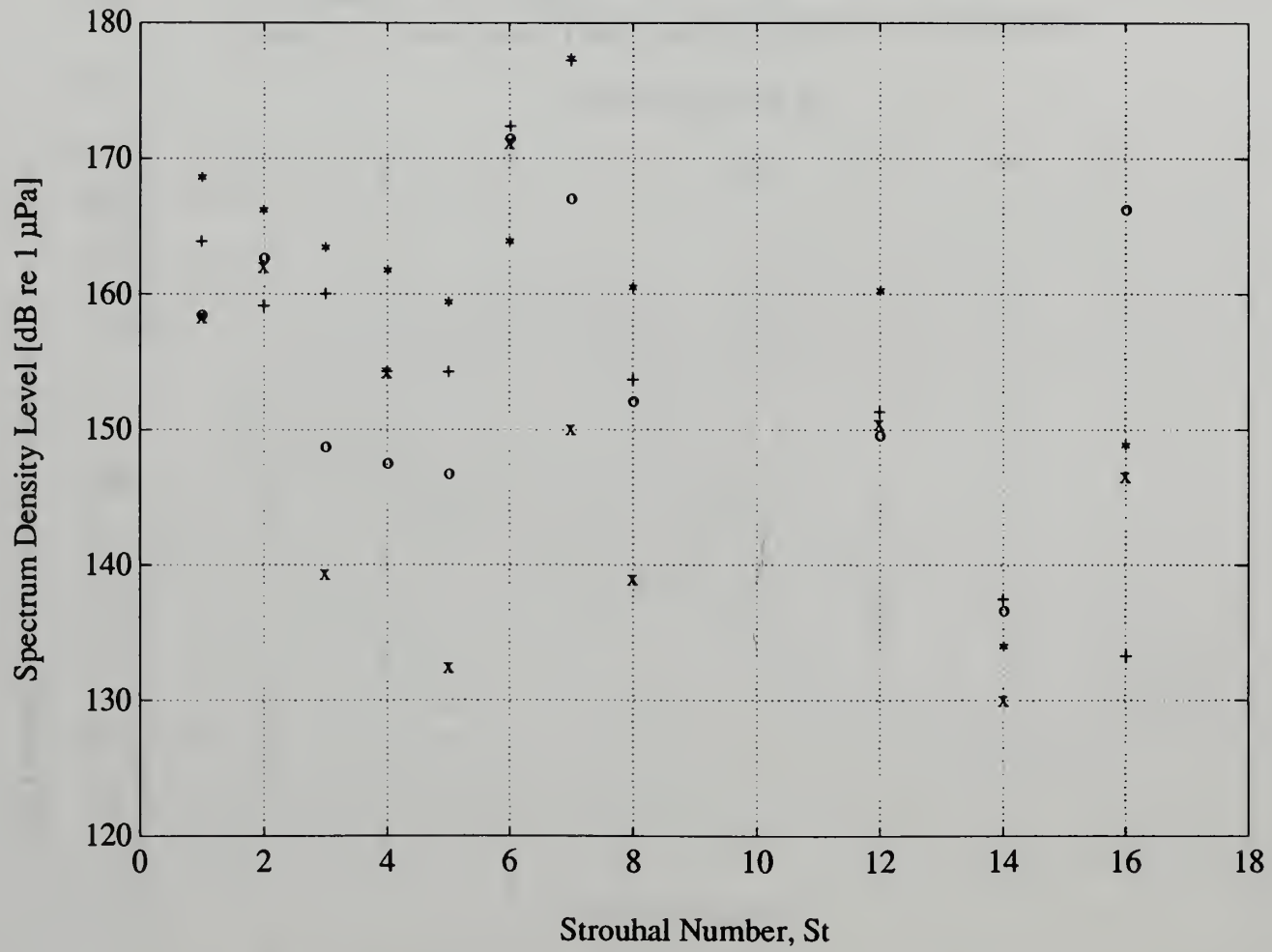

Figure D.19. Tonal Noise Levels, Low Throttle, Varying Speed
(* : 100% Speed, + : 75% Speed, o : 50% Speed, x : 25% Speed)

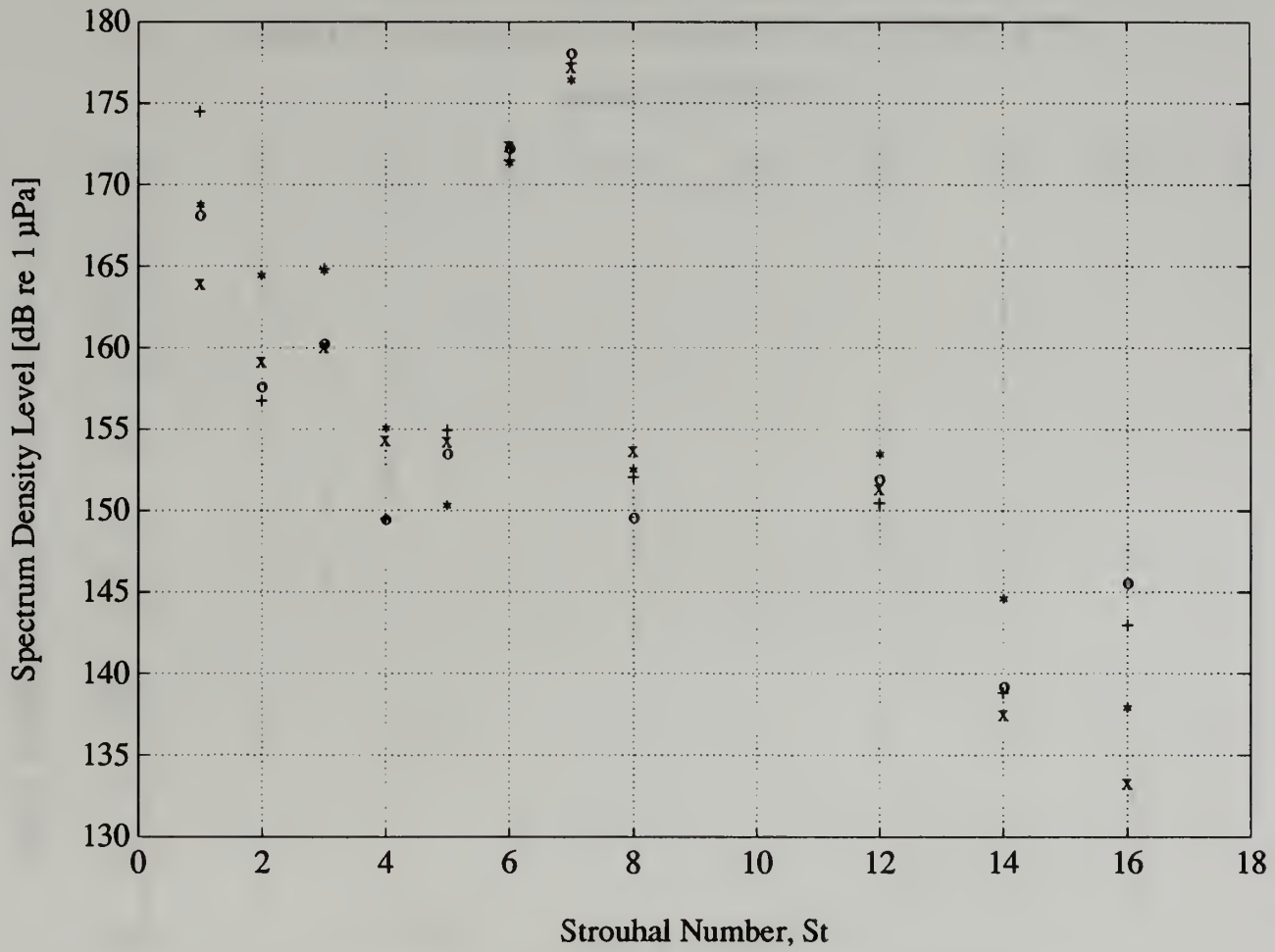

Figure D.20. Tonal Noise Levels, 75% Speed, Varying Flow Rate
(* : 359 GPM, + : 234 GPM, o : 155 GPM, x : 92 GPM)

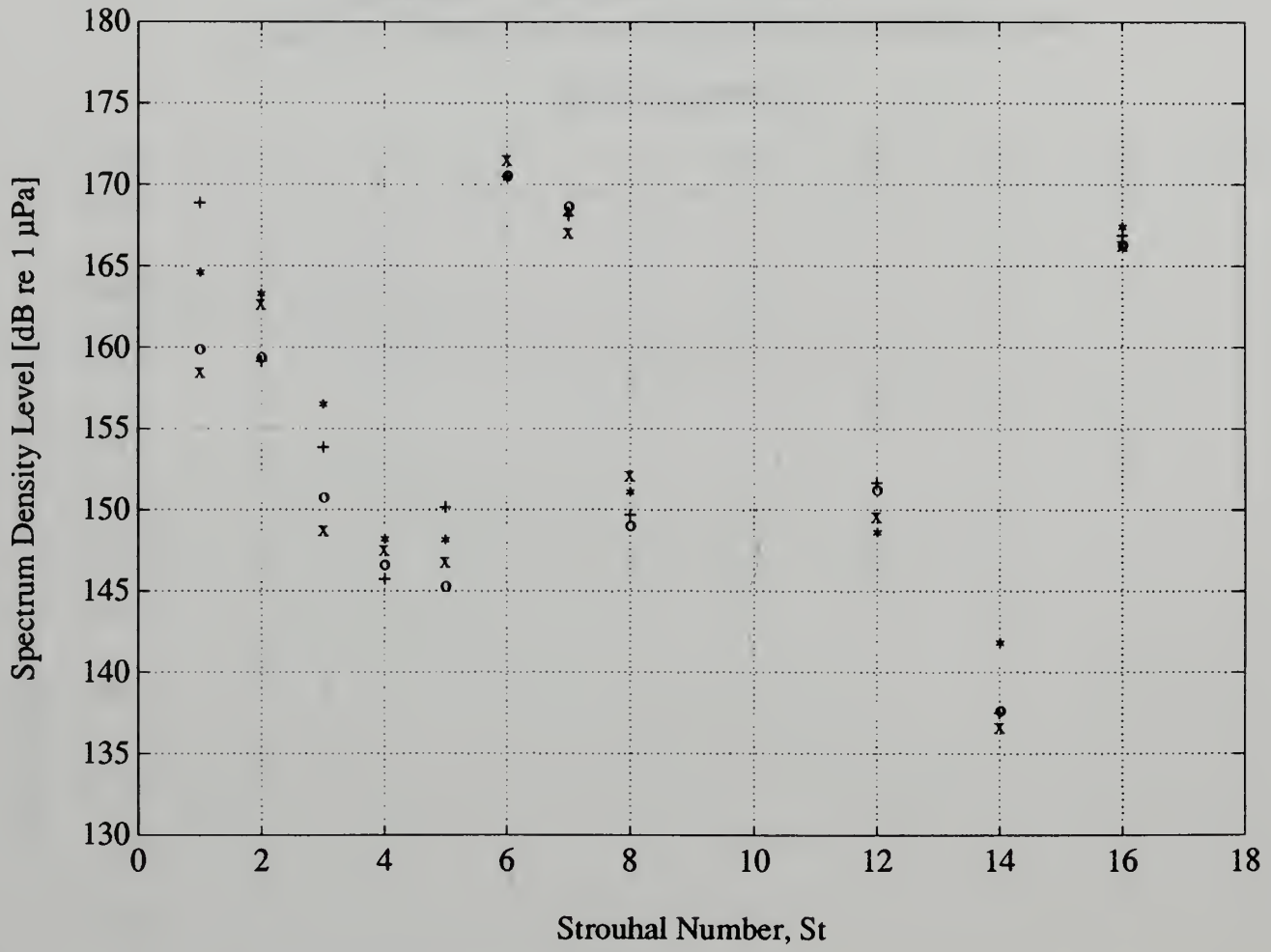

Figure D.21. Tonal Noise Levels, 50% Speed, Varying Flow Rate
(* : 223 GPM, + : 155 GPM, o : 100 GPM, x : 59 GPM)

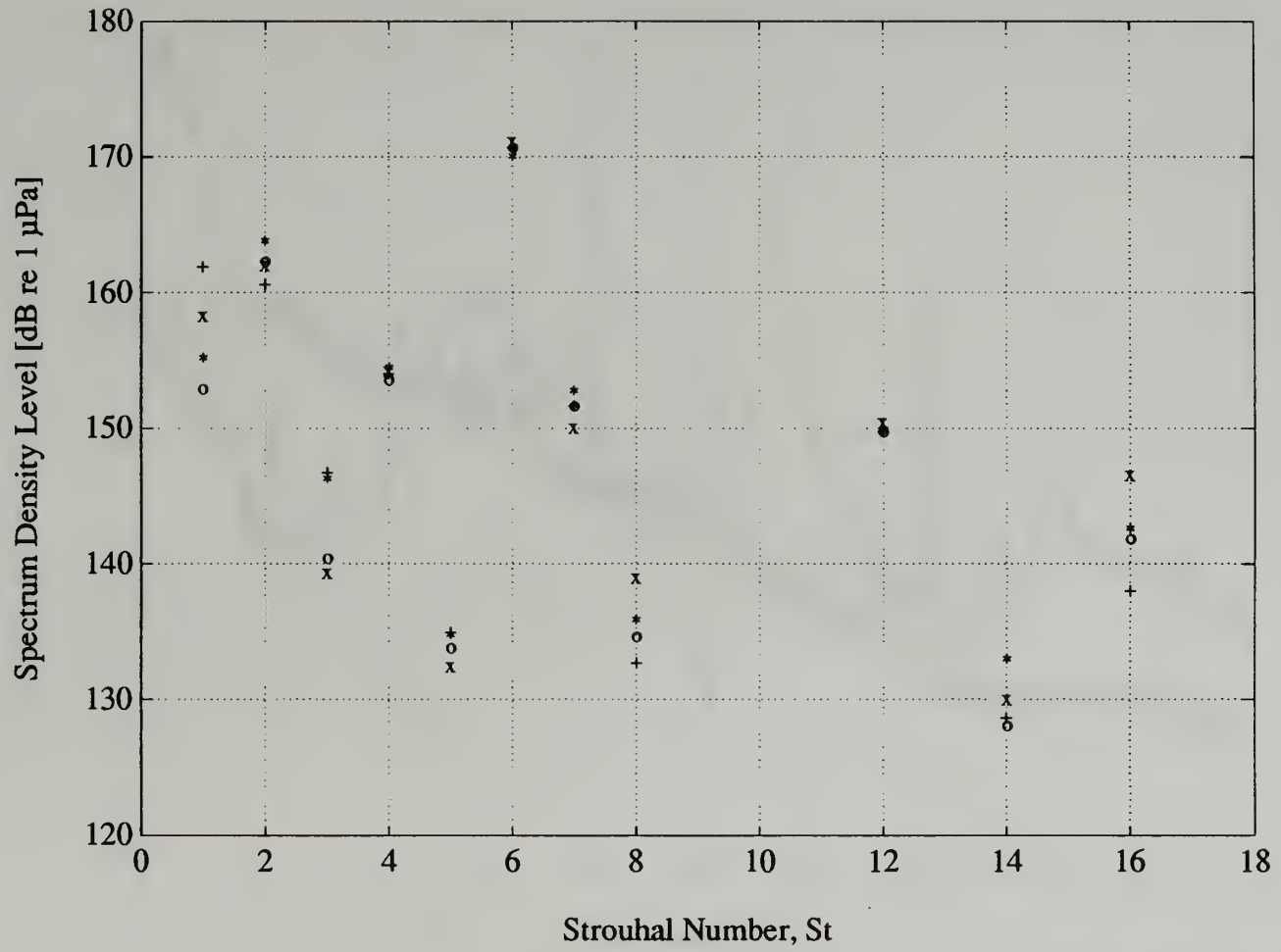

Figure D.22. Tonal Noise Levels, 25% Speed, Varying Flow Rate
(* : 155 GPM, + : 75 GPM, o : 47 GPM, x : 28 GPM)

E. Acoustic Results with the Experimental Diffuser

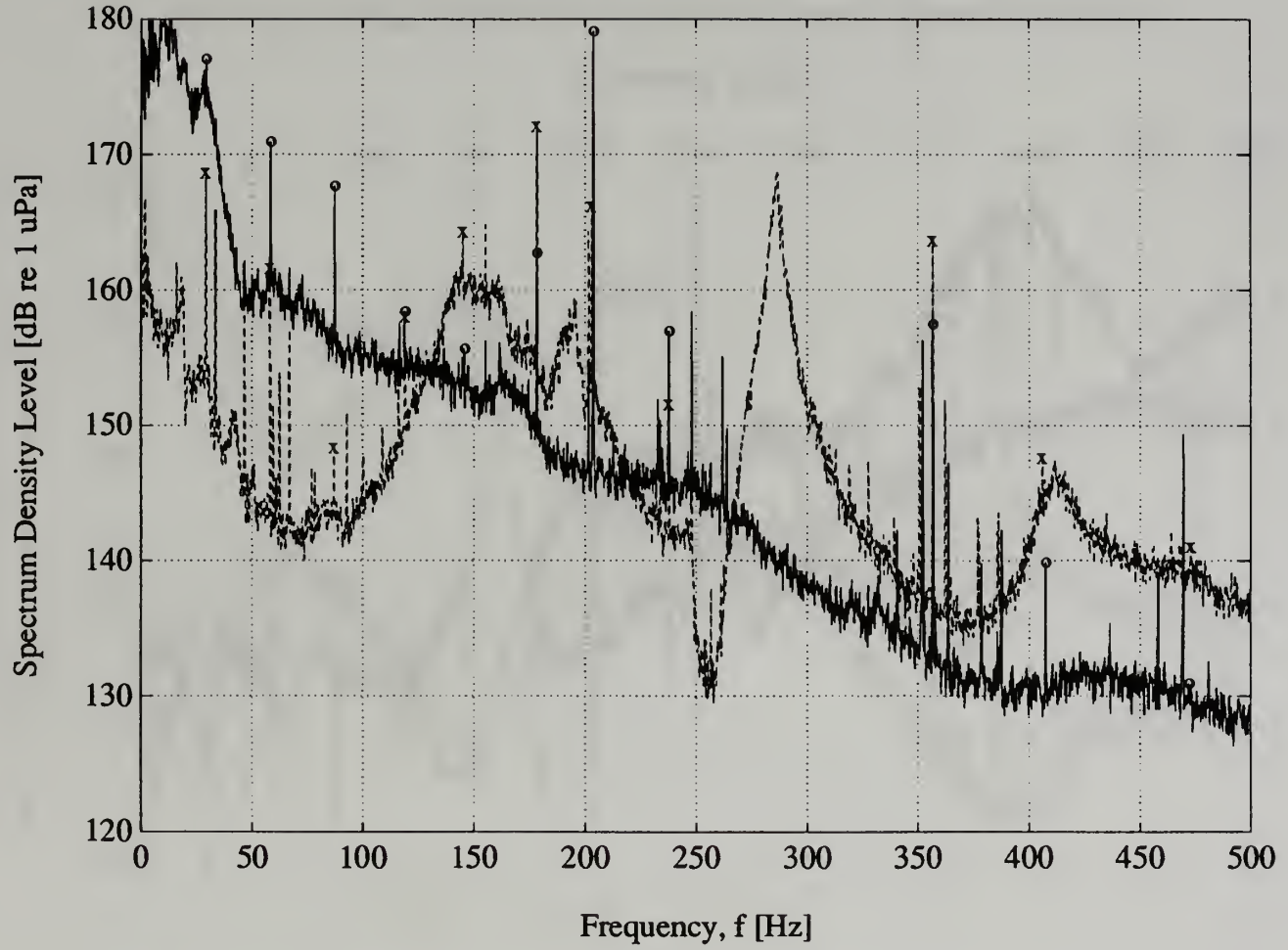

Figure E.1. Inlet Noise Spectra, 100% Speed, 490 GPM, Volute and Diffuser
(——, o : volute; — —, x : diffuser)

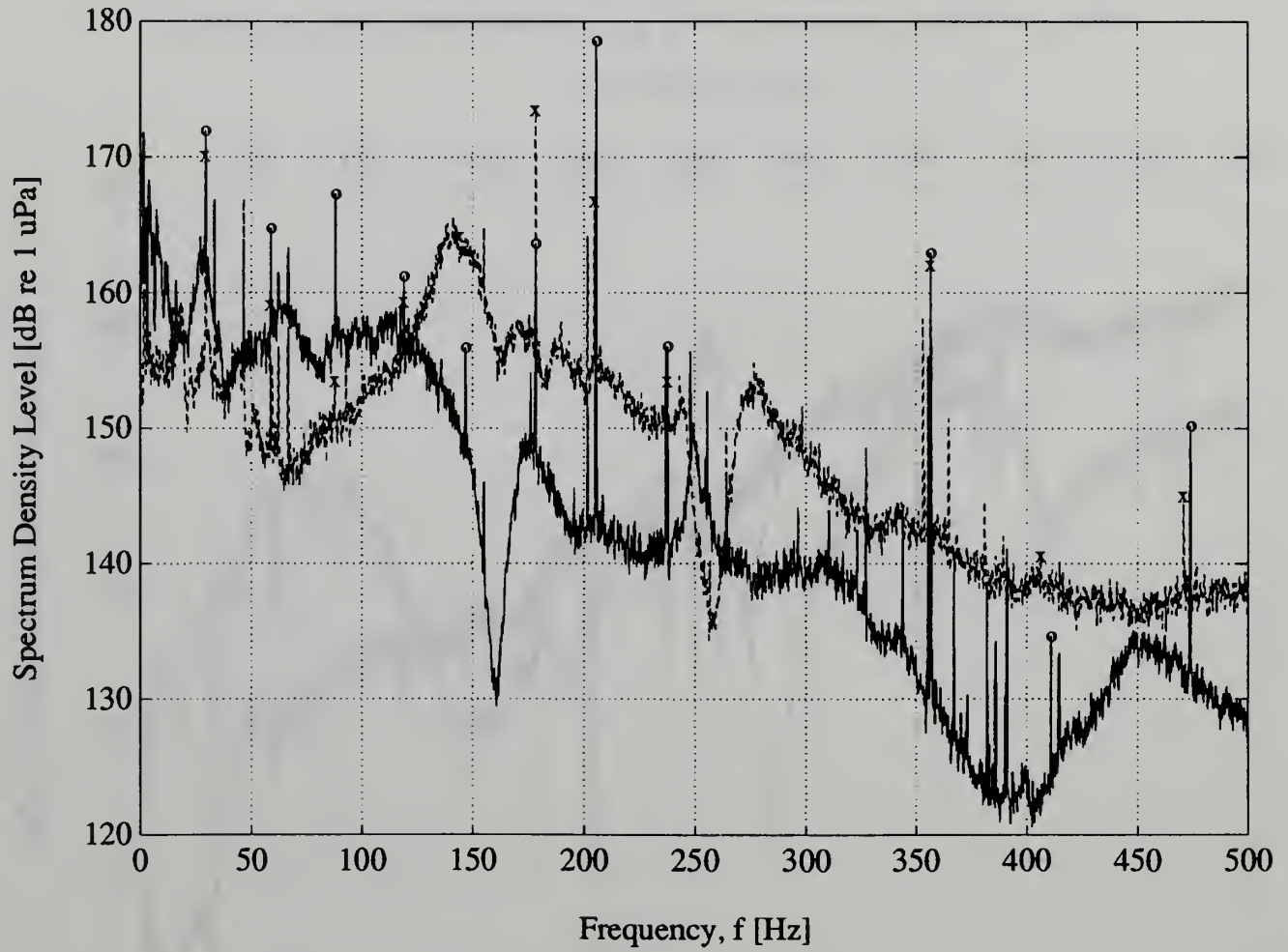

Figure E.2. Inlet Noise Spectra, 100% Speed, 220 GPM, Volute and Diffuser
(——, o : volute; — —, x : diffuser)

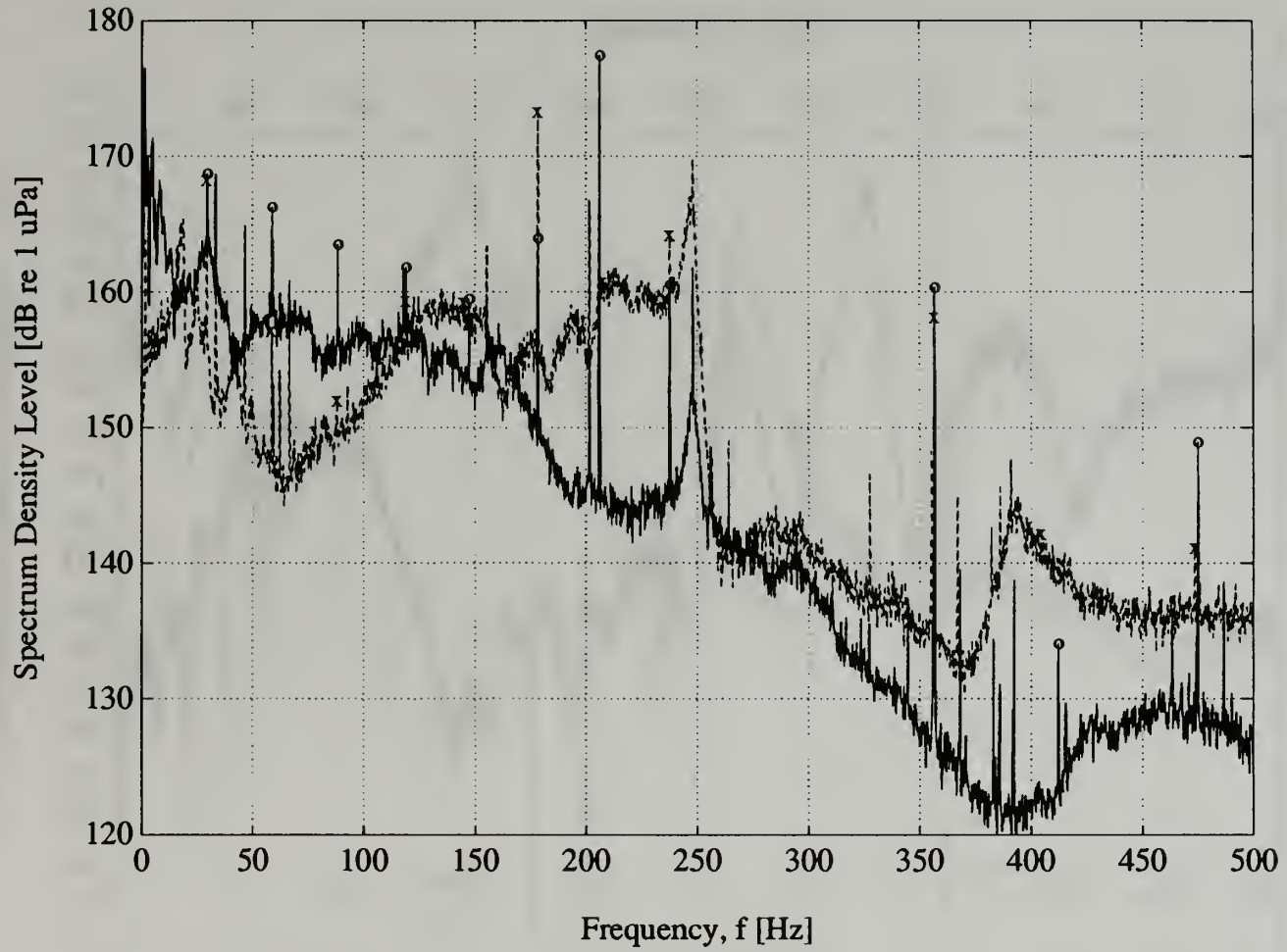

Figure E.3. Inlet Noise Spectra, 100% Speed, 127 GPM, Volute and Diffuser
(——, o : volute; — —, x : diffuser)

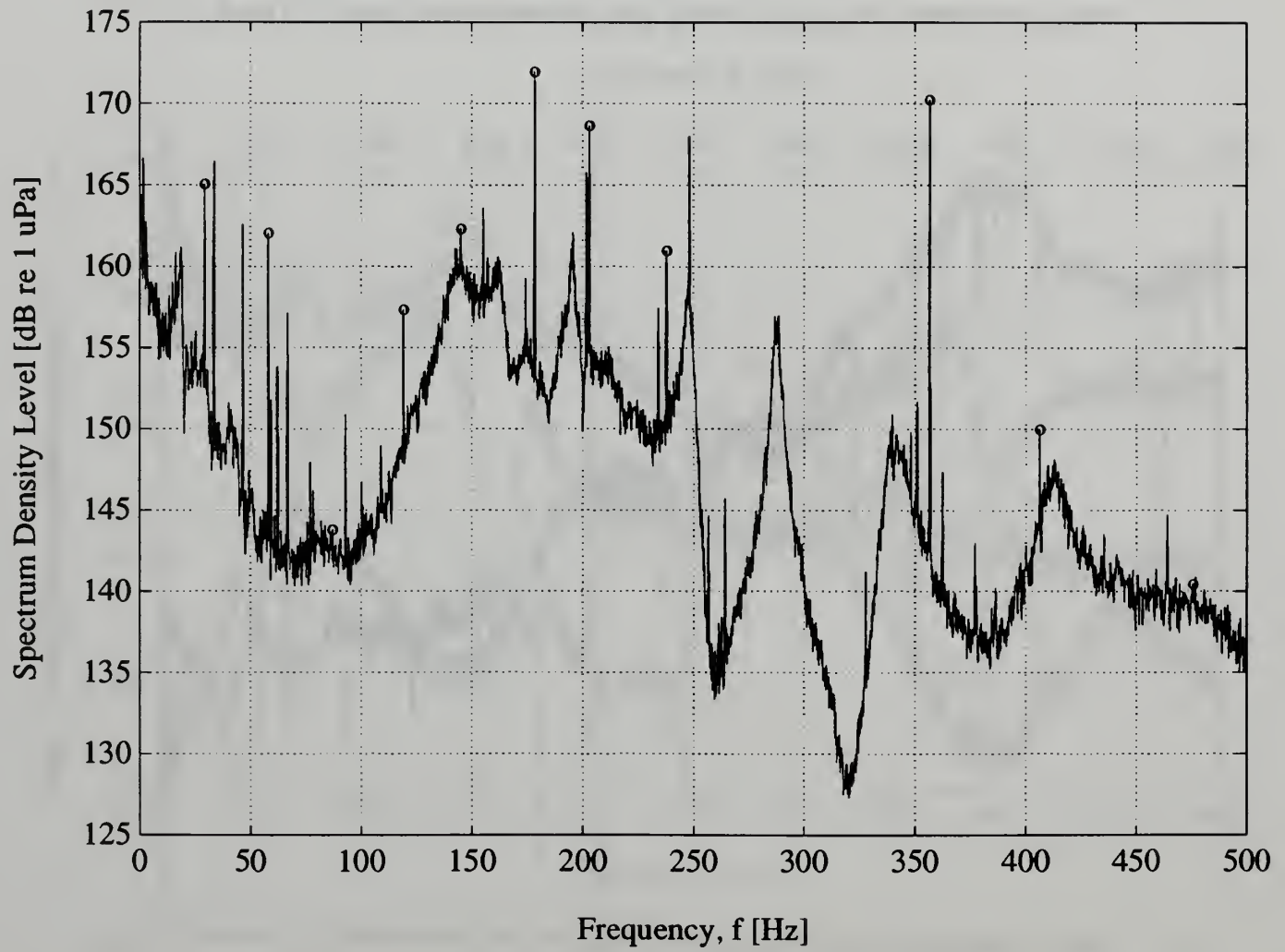

Figure E.4. Inlet Noise Spectrum, 100% Speed, 505 GPM

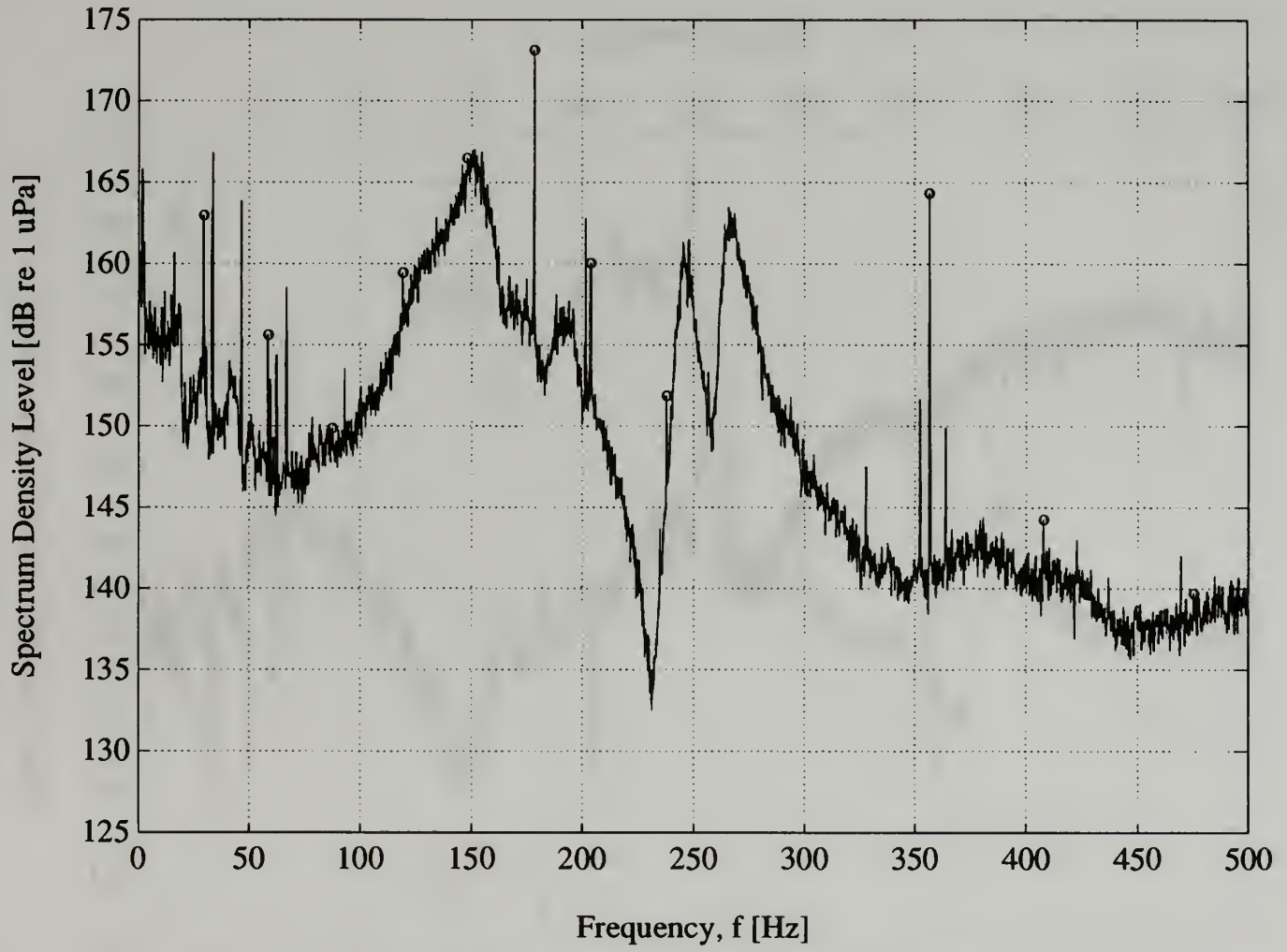

Figure E.5. Inlet Noise Spectrum, 100% Speed, 347 GPM

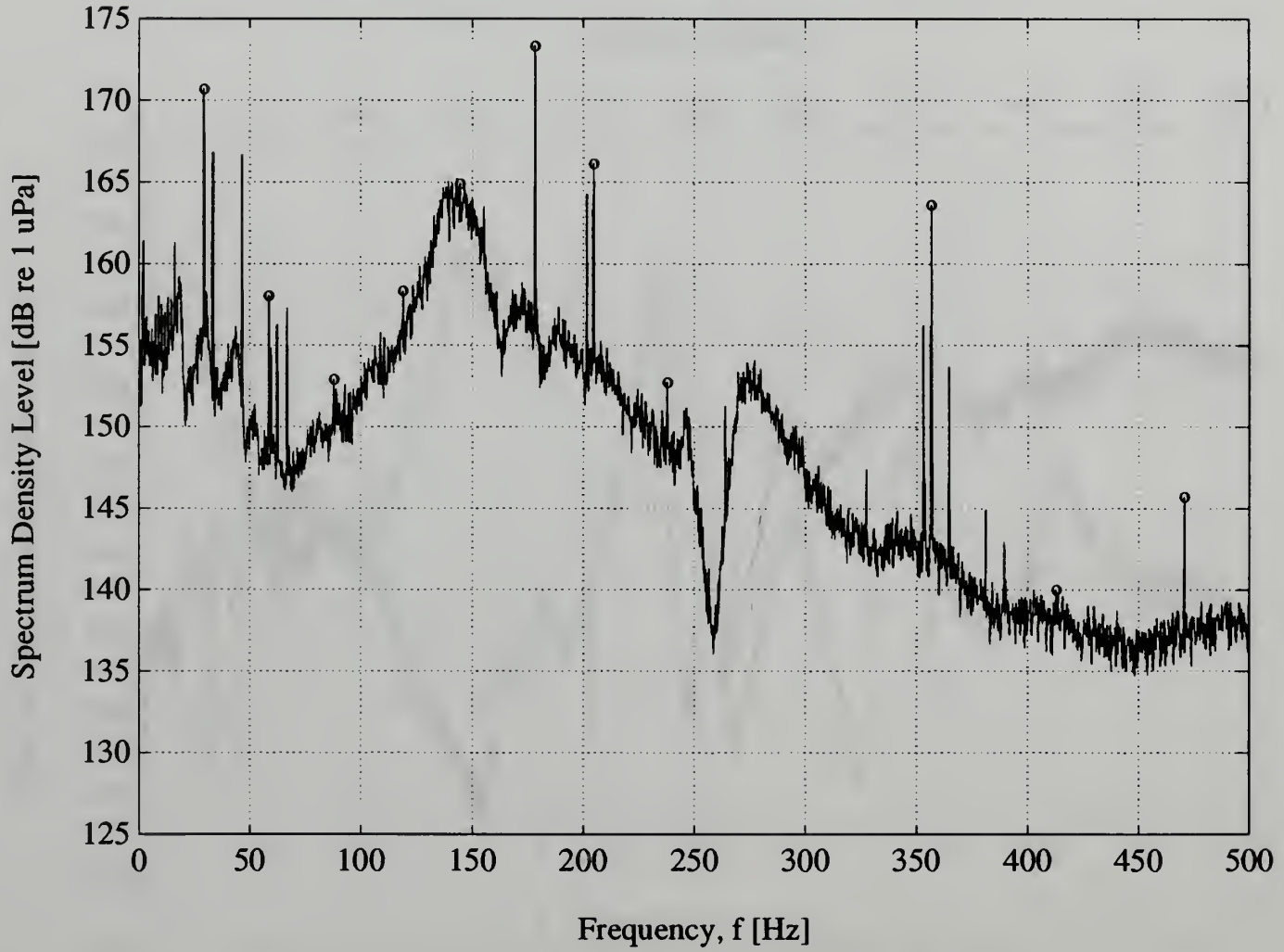

Figure E.6. Inlet Noise Spectrum, 100% Speed, 224 GPM

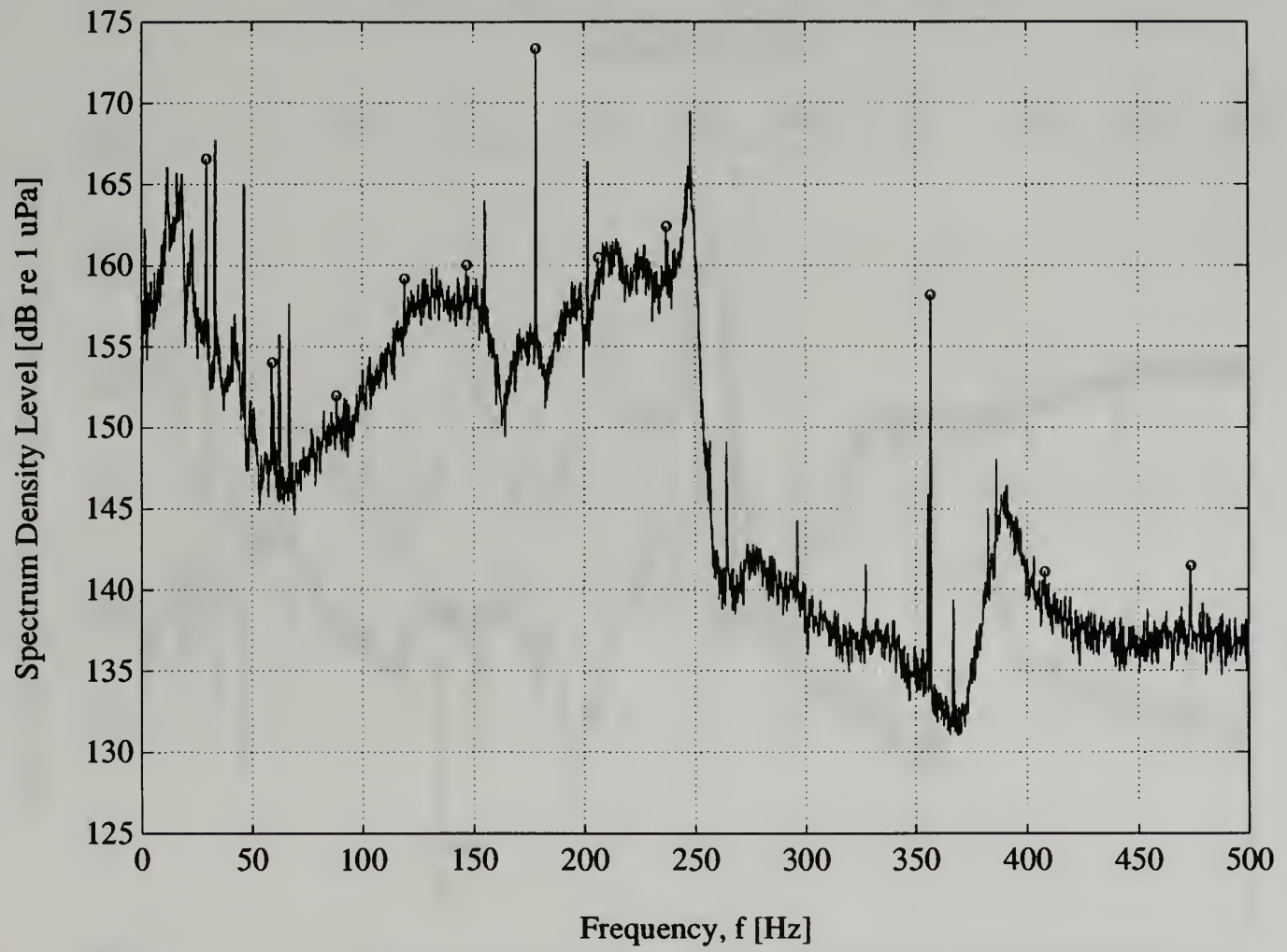

Figure E.7. Inlet Noise Spectrum, 100% Speed, 122 GPM

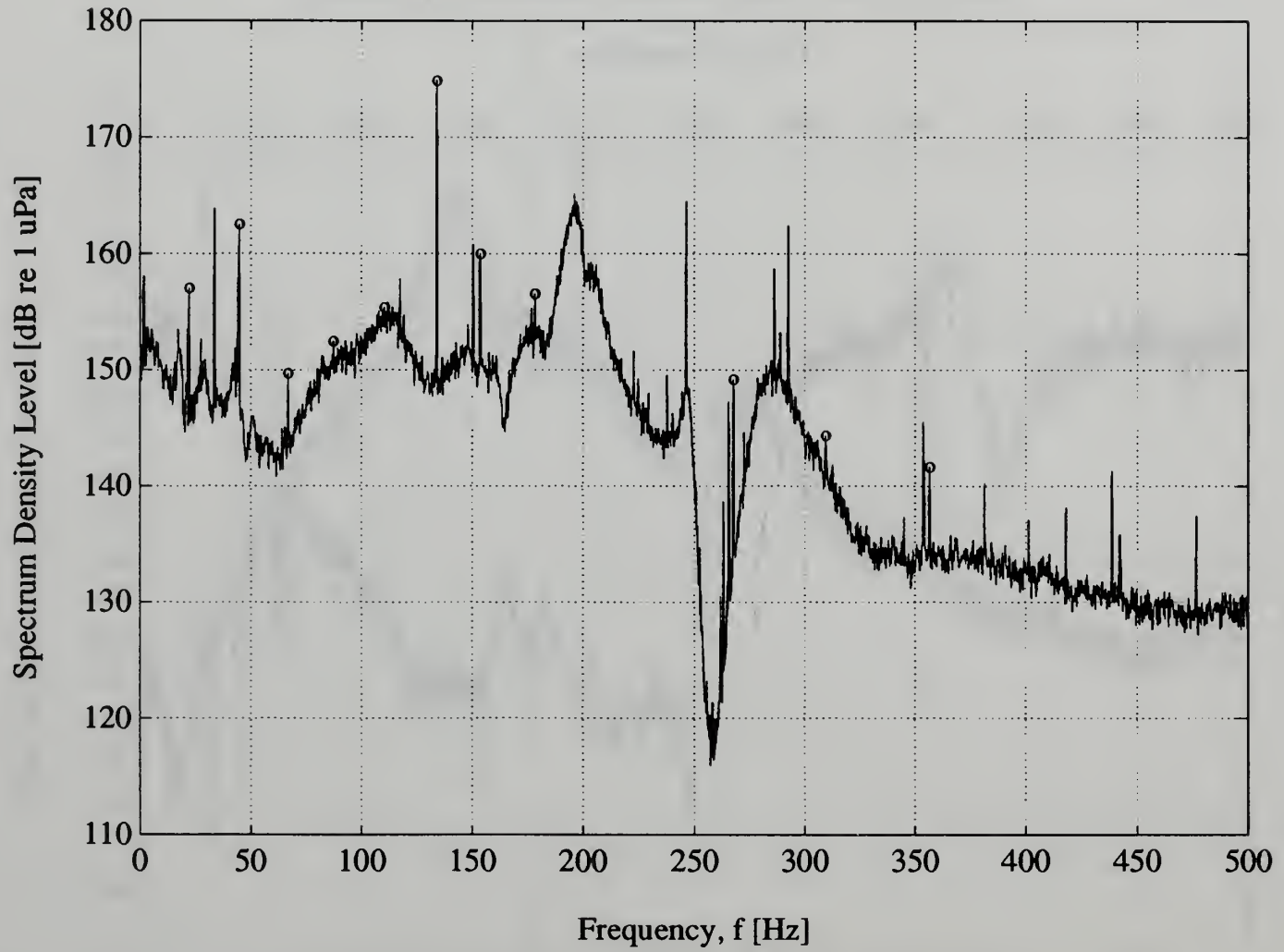

Figure E.8. Inlet Noise Spectrum, 75% Speed, 241 GPM

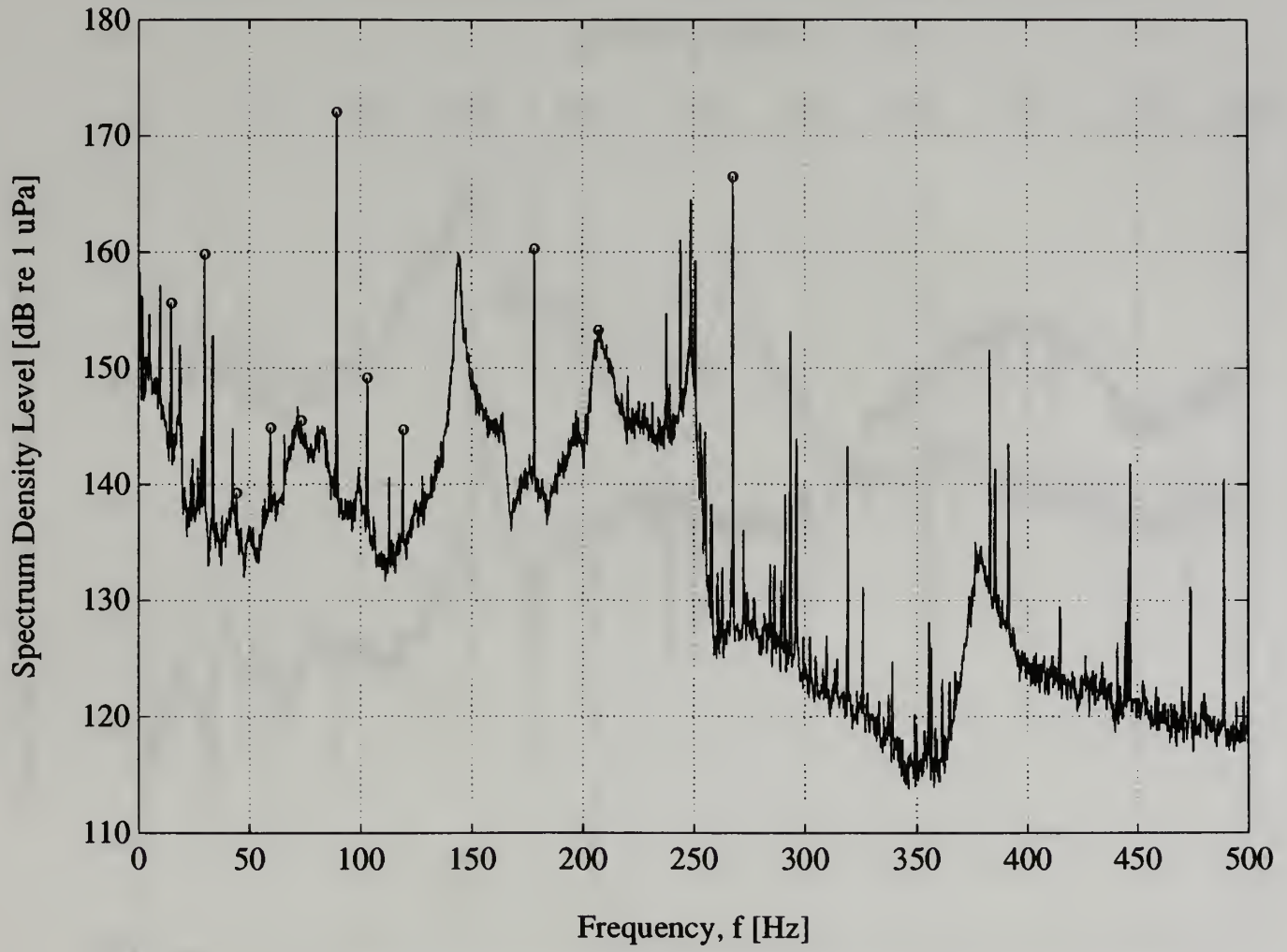

Figure E.9. Inlet Noise Spectrum, 50% Speed, 249 GPM

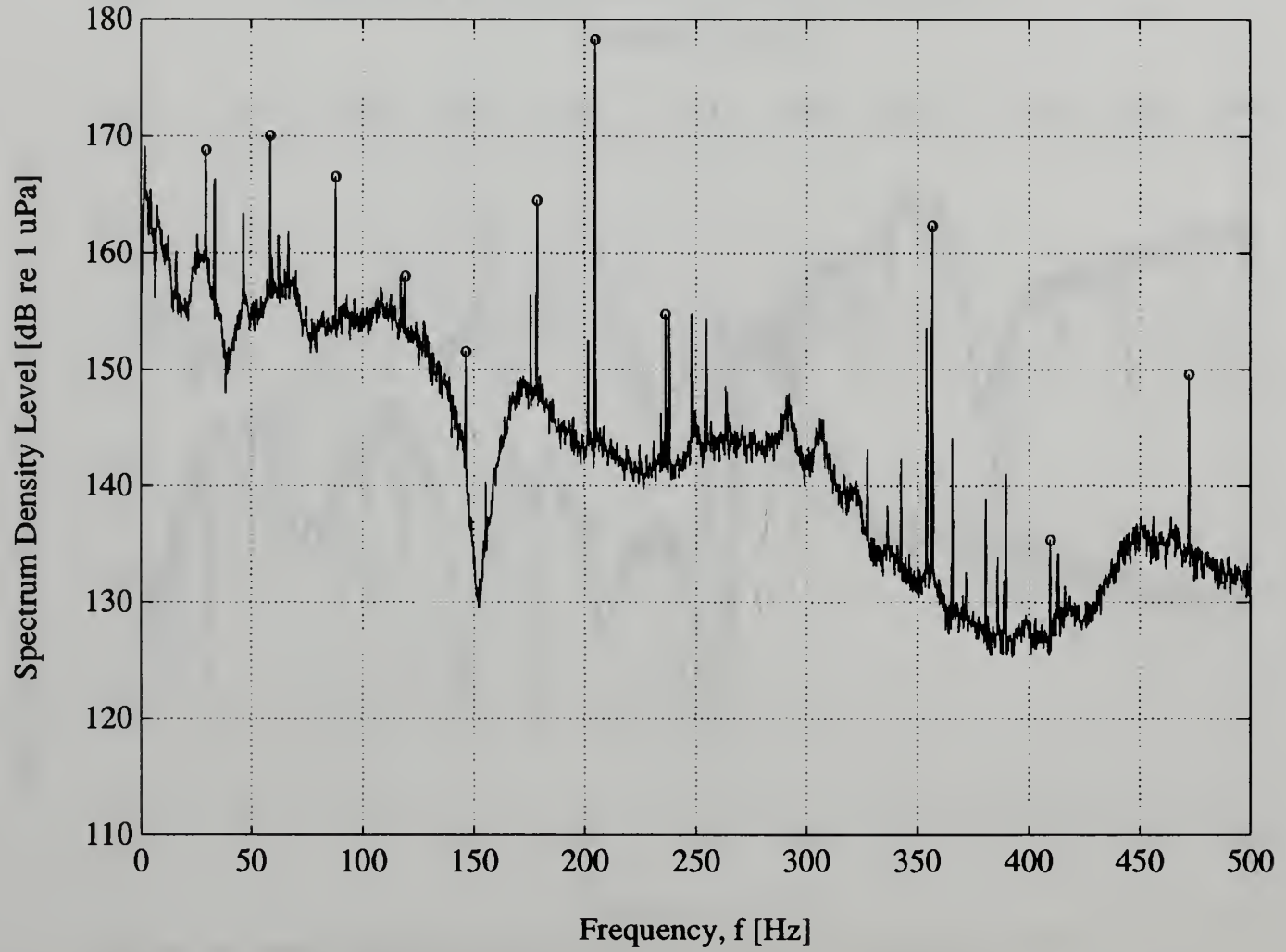

Figure E.10. Inlet Noise Spectrum, Volute Configuration, 100% Speed, 331 GPM

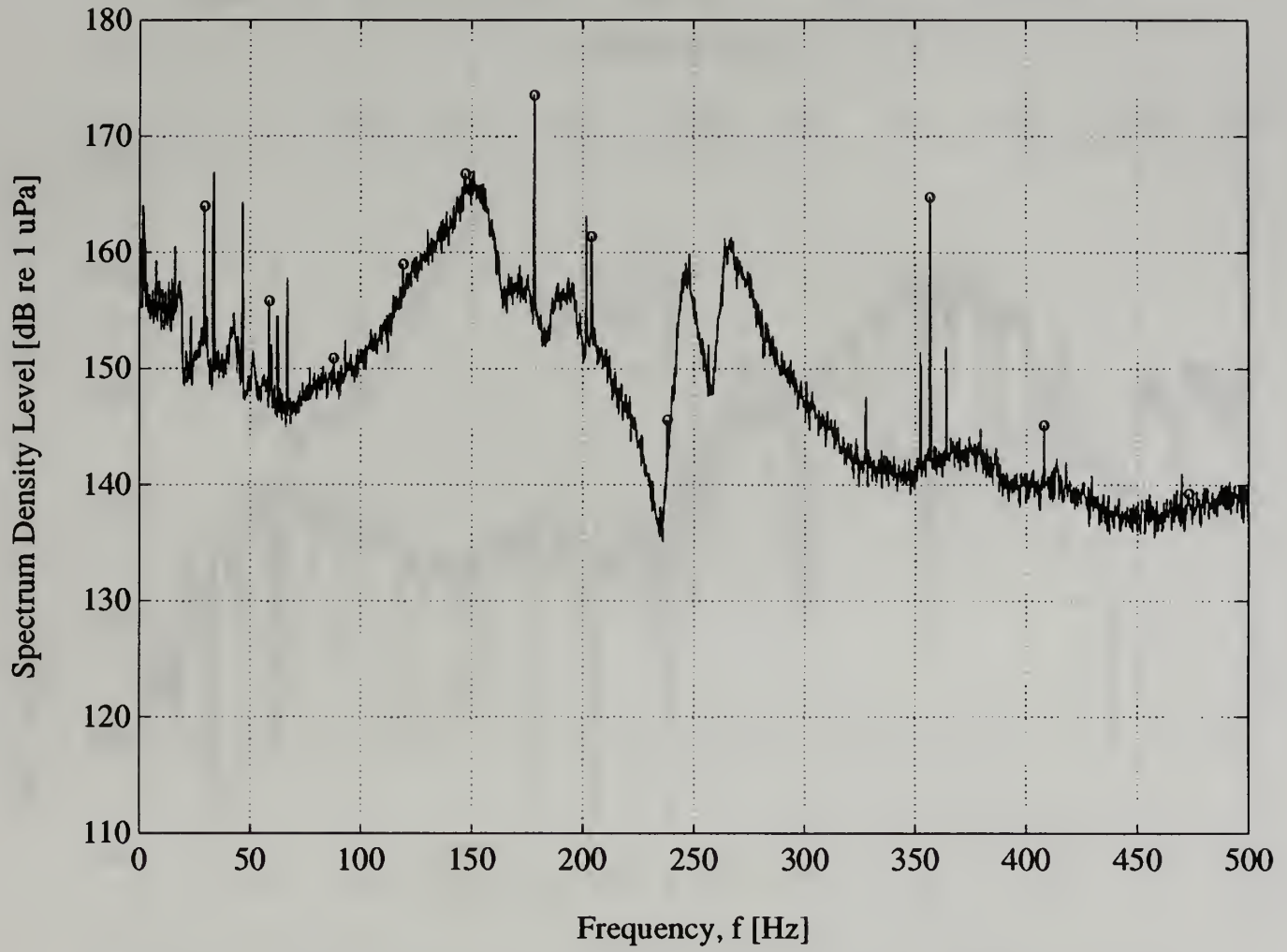

Figure E.11. Inlet Noise Spectrum, Diffuser Configuration, 100% Speed, 334 GPM

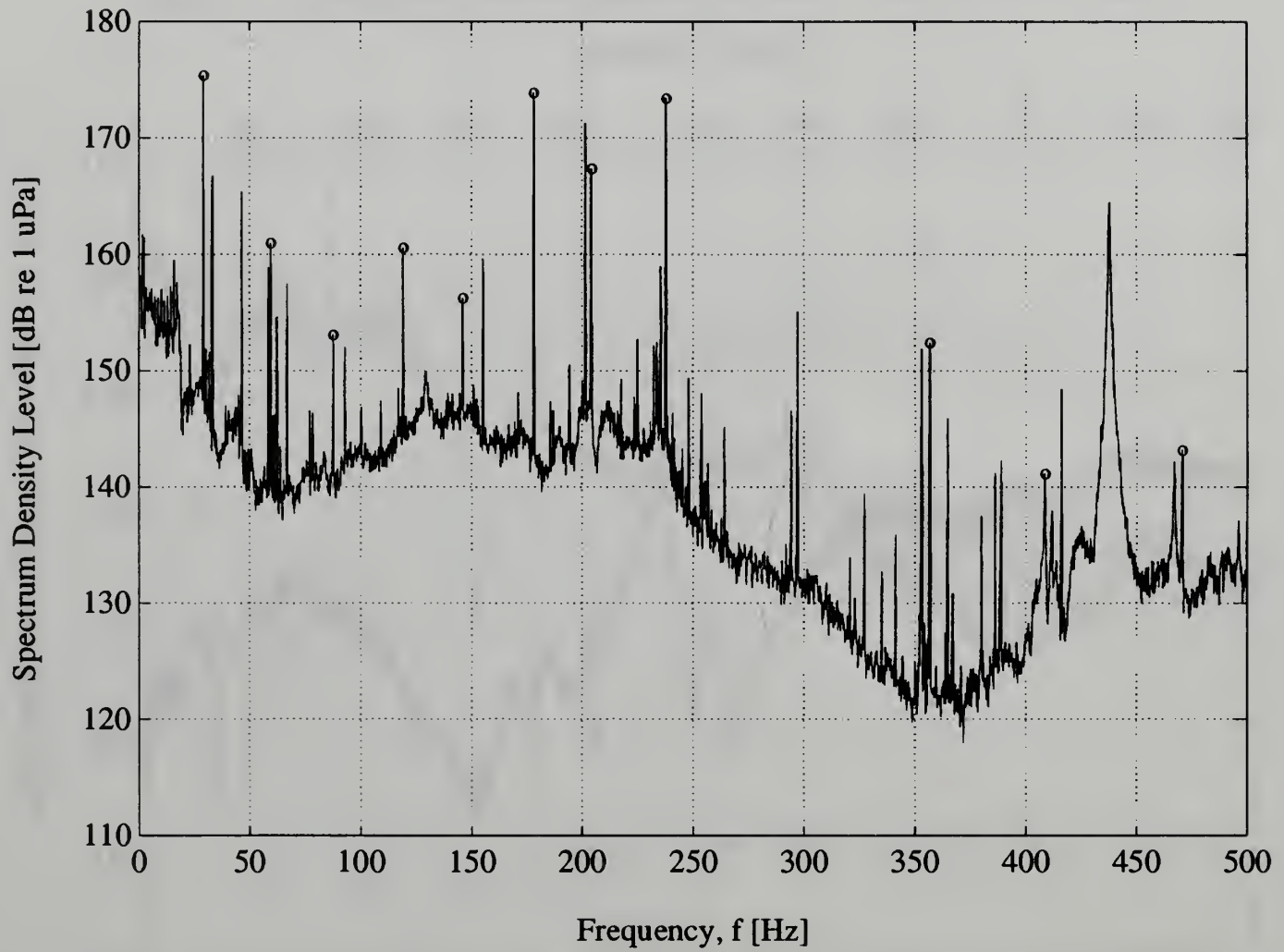

Figure E.12. Inlet Noise Spectrum, 180° Obstruction,100% Speed, 371 GPM

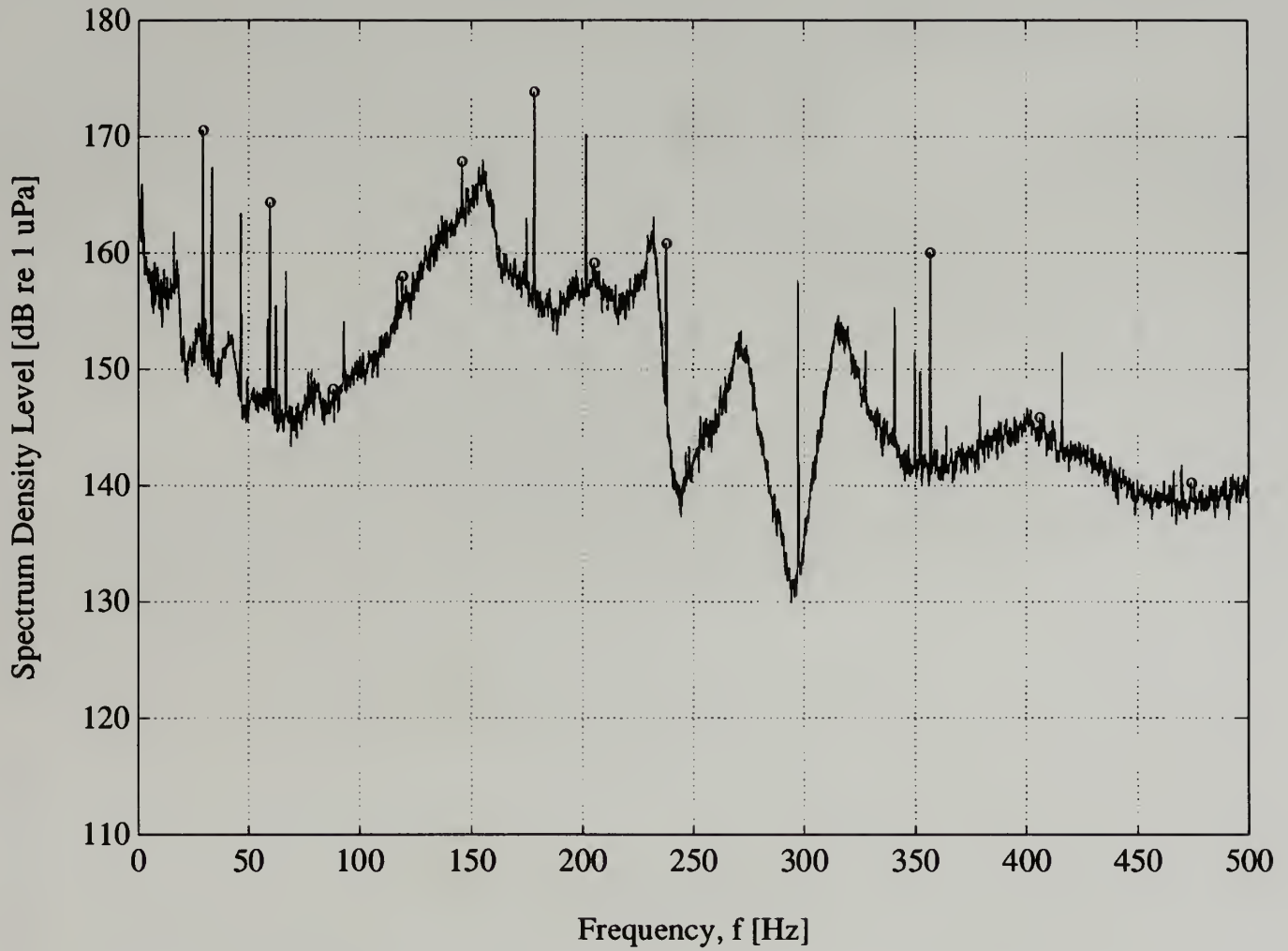

Figure E.13. Inlet Noise Spectrum, Diffuser Configuration (no basket), 100% Speed, 380 GPM

144-403